UNIVERSIDAD DE EXTREMADURA

TESIS DOCTORAL

SÍNTESIS Y APLICACIÓN DE CATALIZADORES MAGNÉTICOS EN PROCESOS DE OXIDACIÓN AVANZADA

JORGE LÓPEZ GALLEGO

MODELIZACIÓN Y EXPERIMENTACIÓN EN CIENCIA Y TECNOLOGÍA

Conformidad del director y codirectora:

Pedro Modesto Álvarez Peña **Ana Rey Barroso**

Esta Tesis cuenta con la autorización del director y codirectora de la misma y de la Comisión Académica del programa. Dichas autorizaciones constan en el Servicio de la Escuela Internacional de Doctorado de la Universidad de Extremadura.

2023

UNIVERSIDAD DE EXTREMADURA

TESIS DOCTORAL

SÍNTESIS Y APLICACIÓN DE CATALIZADORES MAGNÉTICOS EN PROCESOS DE OXIDACIÓN AVANZADA

SYNTHESIS AND APPLICATION OF MAGNETIC CATALYSTS IN ADVANCED OXIDATION PROCESSES

Memoria de Tesis depositada en la Universidad de Extremadura para aspirar al Grado de Doctor con mención internacional, presentada por:

JORGE LÓPEZ GALLEGO

Conformidad de los directores:

Director:
Pedro M. Álvarez Peña

Codirectora:
Ana Rey Barroso

Programa de Doctorado en:
MODELIZACIÓN Y EXPERIMENTACIÓN EN CIENCIA Y TECNOLOGÍA

BADAJOZ
2023

A mis padres, hermano
e Isabel

Este trabajo ha contado con el apoyo del Ministerio de Educación, Cultura y Deporte (actual Ministerio de Universidades, 2021) mediante una beca FPU (Resolución del 25 de septiembre de 2017, BOE nº14, 17/01/17) con número de referencia FPU16/03629. A su vez, también ha sido posible gracias al soporte económico recibido a través del Ministerio de Economía y Competitividad (MINECO) con el proyecto CTQ2015-64944-R, Junta de Extremadura, cofinanciados a su vez por los Fondos Europeos de Desarrollo Regional (FEDER).

GOBIERNO DE ESPAÑA MINISTERIO DE UNIVERSIDADES

GOBIERNO DE ESPAÑA MINISTERIO DE ECONOMÍA, INDUSTRIA Y COMPETITIVIDAD

JUNTA DE EXTREMADURA
Consejería de Economía e Infraestructuras

UNIÓN EUROPEA
Fondo Europeo de Desarrollo Regional
Una manera de hacer Europa

AGRADECIMIENTOS

De repente, y sin saber por qué, paras al pie de una enorme encina. Aunque vieja y algo desgastada por el inevitable paso del tiempo, se ve frondosa. Ya te habían hablado de ella, una encina milenaria con inscripciones en latín grabadas en la base. De este enorme árbol se han ido aprovechando generación tras generación los humanos y los animales de la zona. Por un lado, da cobijo cuando es necesario, alimento en épocas de hambruna y leña cuando las temperaturas son bajas. Ha ido creciendo lentamente, asimilando todos los nutrientes que las raíces extraían de la tierra y con el ser humano dando forma a su parte externa, para que generaciones posteriores la vieran como un símbolo de pasado, presente y futuro, el cual hay que cuidar y del que hay que aprender. Lamentablemente, hoy en día su existencia está en peligro de muerte. Se están intentado aprovechar de este árbol, talando sus ramas sin piedad, tomando sus frutos antes de madurar y construyendo bases con maderos podridos sobre las ramas. La idea es ampliarla, ayudarla a crecer de forma artificial y con unos cimientos sin consistencia. Tú por supuesto, quieres aportar tu granito de arena a la causa y ayudar a hacer crecer a la vieja encina.

Al mirar al tronco se aprecian unas pequeñas escaleras de madera atadas con cuerdas, las cuales invitan, sin ninguna duda, a subir rápidamente. Cuando comienzas el ascenso puedes escuchar los gritos de ánimo desde la parte superior, son los "constructores" de las llamas ramas artificiales, esas ampliaciones con maderos podridos que de lejos parecen totalmente seguras. Subes a una velocidad endiablada, aupado por la motivación inicial y las fuerzas que te aporta el mendrugo de pan que te dieron al desayunar por la mañana temprano. Sin dilación, apoyas toda tu masa en la primera plataforma que alcanzas, tu objetivo está cumplido piensas, pero en 2 segundos los maderos se desquebrajan y caes a plomo sobre el duro y pedregoso suelo. La hostia ha sido considerable, pero no

has muerto, ha sido una equivocación al apoyar y te decides a subir nuevamente, ahora con más cuidado. Pero de nuevo, al llegar a otra plataforma, te precipitas al vacío al ceder de nuevo los maderos. Antes incluso de golpear el suelo ya te das cuenta de que algo no cuadra. No te rindes y vuelves a intentar la escalada, esta vez, utilizas un arnés por si caes y subes guiado por la escalera, pero creando un nuevo camino ante las dudas de diseño. Buscas una rama sana y comienzas a construir tu plataforma, intentando en todo momento mantener la integridad de la vieja encina, pero, sobre todo, dando consistencia para futuros escaladores. **Apunte de última hora**: Justo antes de acabar, un rayo casi parte en dos la encina….

Este es el símil perfecto del camino de la ciencia que he vivido durante estos años y a la incertidumbre a la cual te enfrentas cuando empiezas a investigar en una rama concreta del conocimiento, la cual tiendes a pensar que está totalmente asentada. He de admitir que lo he conseguido superar por la ayuda inestimable de mucha gente, la cual expongo a continuación.

En primer lugar, me gustaría agradecer a Fernando Beltrán Novillo, por la confianza depositada a la hora de entrar en el grupo *Trataguas* desde que acabé la carrera. Aunque sea del Barca, le tengo mucho aprecio.

También a Pedro M. Álvarez Peña y Ana Rey Barroso, mis tutores y principales apoyos para llevar a buen puerto el barco. Sin ellos esto hubiera sido imposible. Gracias por las constantes reuniones para tomar decisiones, la guía continua en los experimentos y la transmisión de conocimientos a la largo de este viaje. Ambos son dos grandes investigadores, pero mejores personas.

No me puedo quedar sin agradecer su inestimable ayuda a mi compañera de penurias con los MOF, Ana M. Chávez Agüedo. Una gran persona, organizada e inteligente, siempre dispuesta a ayudar a cualquiera que lo necesite. Alguien indispensable en cualquier puesto de trabajo.

Emilio Viñuelas, por su soporte en la caracterización de materiales y su ánimo durante la Tesis.

A Adrián Da Silva y a Ana Rita Lado, las dos personas que hicieron posible mi estancia en Oporto. Dos investigadores de gran prestigio a los cuales quiero agradecer su predisposición a la hora de ayudarme durante los 3 meses que estuve.

De una forma u otra hay muchas otras personas que me han ayudado a completar el camino y a las cuales quiero hacer también una mención. Fany el primer año, no se olvidaba del impuesto revolucionario... Rafa, un gran investigador, muy organizado y experto en idiomas, siempre dispuesto a enseñar y ayudar cuando se le necesitaba. Anabel, con su inagotable alegría diaria. Checa, un buen bailarín, lástima que tu alumno fuera arrítmico. Figue, un compañero atento y siempre dispuesto a echar una mano. Sergio Correia, Sergio Nogales, Juan Carlos, Esther, Cristina, Pedro Molina y otros vecinos de laboratorio (que me perdonen los olvidados) los cuales de una forma u otra han aportado a la convivencia diaria.

No me puedo olvidar de las dos personas con las cuales más horas he pasado los últimos meses. Vicente Montes y Ana Martínez. El primero, siempre con la mente activa, ha sido una de las últimas personas en entrar al grupo, pero rápidamente se dio a querer por el enorme corazón que tiene. Ana, una pesadilla con la cual cuesta aburrirse, un apoyo total e inestimable durante las semanas anteriores a la presentación de la tesis.

En penúltimo lugar, quiero agradecer a todos los profesores que durante mi etapa de aprendizaje en la carrera me trasmitieron sus conocimientos, los cuales me han servido para poder llegar hoy hasta aquí.

Y, por último, a todos mis seres queridos y amigos, que de una forma u otra han contribuido a mi bienestar emocional para hacer posible que haya llegado de una pieza al final de esta bonita etapa.

"Si no sabes hacia qué puerto te diriges, ningún viento te será favorable"
Lucio Anneo Seneca
Corduba, 4 a. C.- Roma, 65 d. C.

INDEX

RESUMEN/ABSTRACT

RESUMEN

Existe una preocupación creciente acerca de los posibles efectos adversos para la salud y el medio ambiente de un elevado número de sustancias detectadas en el medio acuático, conocidas como contaminantes de preocupación emergente. Entre estos contaminantes se encuentran productos farmacéuticos y cosméticos, aditivos industriales, pesticidas, nanomateriales o microplásticos. Se trata de sustancias que, en general, se presentan en concentraciones bajas en el agua (μg L^{-1} a ng L^{-1}), pero de gran relevancia debido a sus potenciales efectos negativos a largo plazo sobre la salud y los ecosistemas.

Las estaciones de depuración de aguas residuales (EDAR) suponen, en muchos casos, la principal vía de entrada al medio acuático de numerosos contaminantes emergentes debido a que los tratamientos convencionales aplicados suelen presentar una baja eficacia en su eliminación, ya que se trata de sustancias persistentes y biorresistentes. Por este motivo, la degradación de contaminantes emergentes hasta sustancias inocuas (e.g., CO_2 y H_2O) supone uno de los principales desafíos en materia de tratamiento y calidad del agua. Así, en las últimas décadas se observa un interés creciente en la comunidad científica en investigar y desarrollar métodos de tratamiento complementarios que permitan una eliminación segura de contaminantes emergentes en las EDAR. En este campo, los procesos avanzados de oxidación (PAO) pueden considerarse una de las alternativas más prometedora por su efectividad. Sin embargo, su coste y su consumo energético suponen limitaciones importantes a superar para que lleguen a ser económicamente viables y sostenibles.

Los PAO se caracterizan por la generación de oxidantes secundarios muy potentes denominadas especies reactivas de oxígeno (Reactive Oxygen Species, ROS por sus siglas en inglés), entre las que destaca el radical hidroxilo ($HO^{\bullet}$,

E°=2.8 V). Esta especie es muy reactiva y poco selectiva, por lo que es capaz de degradar la mayoría de los contaminantes emergentes presentes en el agua. Entre los PAO más estudiados se encuentran algunos sistemas fotoquímicos como el foto-Fenton, UV/H_2O_2, UV/O_3 o la oxidación fotocatalítica con TiO_2.

Aunque los PAO fotoquímicos presentan, en general, un alto rendimiento de producción de oxidantes secundarios y, consecuentemente, una rápida degradación de contaminantes, su aplicación práctica a nivel industrial se ha visto limitada por razones económicas (coste de fuentes de radiación y consumo energético). Por ello, ha cobrado gran interés el estudio de PAO fotocatalíticos con radiación solar y fuentes de radiación LED de bajo consumo y larga duración. Uno de los principales retos en este sentido es la síntesis de catalizadores fotoactivos en el rango de longitudes de onda de la fuente de radiación empleada. Se requiere, además, que el fotocatalizador sea estable en el medio oxidante que se genera en estos procesos y pueda ser separado y reutilizado fácilmente.

La presente Tesis Doctoral se ha realizado fundamentalmente en Badajoz (España) entre octubre de 2017 y noviembre de 2022 en el seno del grupo de investigación "Tratamiento de Aguas-TRATAGUAS" del Departamento de Ingeniería Química y Química Física de la Universidad de Extremadura. Este grupo presenta una dilatada trayectoria en la investigación de PAO fotoquímicos y no fotoquímicos. Asimismo, una parte de la investigación se llevó a cabo en Facultad de Ingeniería de la Universidad de Oporto (Portugal) en el periodo de mayo a julio de 2021. En este contexto, la Tesis Doctoral se enfocó hacia la síntesis de nuevos fotocatalizadores para su uso en suspensión en PAO con radiación solar. Para facilitar la separación del catalizador se propuso dotar al mismo de propiedades magnéticas que permitiesen su recuperación del medio acuoso mediante la aplicación de un campo magnético externo. En un principio, la Tesis Doctoral se orientó hacia el uso de estructuras metal-orgánicas (Metal-Organic Frameworks, MOF, por sus siglas en inglés), que presentan excelentes propiedades para distintos procesos catalíticos. Sin embargo, se concluyó que la

estabilidad de los MOF estudiados se veía comprometida en las condiciones provocadas por la radiación y la presencia de oxidantes en el medio acuoso (parte 1). Por ello, la investigación se reorientó hacia la síntesis de fotocatalizadores magnéticos inorgánicos que resultaron ser estables bajo las condiciones de los PAO aplicados (partes 2 a 4).

Parte 1. Estructuras metal-orgánicas como potenciales fotocatalizadores solares en PAO: el caso de MIL-53(Fe)

La síntesis de nuevos catalizadores con actividad en el espectro UV-vis que puedan emplearse en PAO con radiación solar ha despertado un gran interés en la comunidad científica en los últimos años. El objetivo es desarrollar materiales con suficiente afinidad por los contaminantes objeto de estudio (e.g., contaminantes emergentes) y que cuando se exponen a la radiación solar o visible sean capaces de generar especies oxidantes en el medio acuoso (e.g., radical hidroxilo) en concentración suficiente para degradar de forma eficiente los contaminantes hasta productos inocuos. Para su aplicación práctica se requiere, además, una alta estabilidad del catalizador en las condiciones de reacción y capacidad para ser reutilizado sin pérdida de actividad. En este campo, los MOF han surgido como un grupo de materiales con extraordinarias propiedades como potenciales fotocatalizadores heterogéneos [1].

Los MOF constituyen una familia de materiales porosos y cristalinos formados por una extensa red de iones metálicos (clúster) combinados con compuestos orgánicos multifuncionales (ligandos) a través de enlaces de coordinación. La combinación de unidades inorgánicas y orgánicas en los MOF ofrece un extraordinario número de posibilidades estructurales para crear materiales con propiedades predefinidas que podrían hacerlos útiles en diversas aplicaciones, como el almacenamiento y la separación de gases, la detección molecular, la catálisis o la liberación controlada de fármacos [2]. Desde 2007, cuando Llabrés i Xamena y colaboradores demostraron la actividad fotocatalítica de MOF-5 para la degradación de fenol [3], se han investigado un número creciente de MOF para

la degradación de contaminantes orgánicos en agua mediante fotocatálisis [4-6]. Particularmente atractivos en este campo son los MOF basados en Fe, que pueden absorber luz visible debido a la excitación directa de los enlaces Fe-O [7]. Además, pueden funcionar como catalizadores heterogéneos para la activación de peróxido de hidrógeno (por ejemplo, en reacciones tipo Fenton) [8-10], persulfato [11,12] u ozono [13]. Entre los MOF basados en Fe se encuentra el MIL-53(Fe), un sólido tridimensional, flexible y poroso compuesto por clústeres de octaedros de $FeO_4(OH)_2$ conectados por enlaces de 1,4-bencenodicarboxilato (BDC), y que se presenta en la literatura científica reciente como potencial fotocatalizador activo bajo luz visible para la degradación de contaminantes orgánicos en agua. El MIL-53(Fe) ofrece las ventajas de una fácil preparación a partir de ácido tereftálico y sales de hierro comunes, estabilidad, no toxicidad y buena absorción de luz visible [14].

De acuerdo con las potenciales ventajas del material MIL-53(Fe) como fotocatalizador para PAO solares, el primer propósito de esta investigación fue utilizar este MOF, magnetizándolo para lograr mejorar su separación del medio acuoso tras su empleo. Sin embargo, ya se había demostrado anteriormente que otro MOF basado en Fe (MIL-100(Fe)) presentaba serios problemas de estabilidad dignos de ser considerados antes de proponerlo como catalizador para PAO solares [15]. En consecuencia, como primer paso de la investigación se decidió evaluar la estabilidad de MIL-53(Fe) en disolución acuosa bajo condiciones típicas de la oxidación fotocatalítica con luz solar simulada y en presencia de distintos oxidantes. Se evaluó la lixiviación del hierro y de materia orgánica del MOF en diferentes condiciones típicas de PAO, incluyendo la estabilidad en medio acuoso durante varios días y ante variaciones de pH. También se estudió la actividad fotocatalítica del MIL-53(Fe) mediante la degradación de fenol (Ph) y metoprolol (MTP) en presencia de diferentes aceptores de electrones (peróxido de hidrógeno, persulfato potásico y ozono).

El MIL-53(Fe) se sintetizó con éxito mediante un método solvotermal y se caracterizó completamente por difracción de rayos X (XRD), espectroscopia infrarroja por transformada de Fourier-reflectancia total atenuada (FTIR-ATR), isoterma de adsorción-desorción de nitrógeno, análisis termogravimétrico acoplado a espectrometría de masa (TGA-MS), espectroscopia UV-visible de reflectancia difusa (DRS), análisis elemental y fluorescencia de rayos X de dispersión de longitud de onda (WDXRF). La caracterización del material sintetizado concordaba con la bibliografía sobre el MIL-53(Fe). El material sintetizado presentaba una estabilidad relativamente buena en agua a pH 4, pero sufría una rápida hidrólisis en condiciones alcalinas. En suspensión acuosa a pH 4-5, la temperatura, la radiación solar y los oxidantes provocaron un efecto negativo sobre la estabilidad de la estructura metal-orgánica (MOF), dando lugar a cantidades nada despreciables del metal (hierro) y del ligando orgánico (ácido tereftálico, H_2BDC) lixiviados al medio, provenientes del MIL-53(Fe). En términos de actividad, el MIL-53(Fe) por sí solo eliminó menos del 10% de los contaminantes (MTP y Ph) tras 3 h de irradiación con luz solar simulada, mientras que, en presencia de ozono, persulfato o peróxido de hidrógeno, se consiguió la eliminación completa de los contaminantes tras 2 h de exposición. Sin embargo, la presencia de oxidantes y la formación de algunos intermedios de reacción (por ejemplo, ácidos carboxílicos de cadena corta) aceleraron la descarboxilación del MIL-53(Fe). Los resultados de este trabajo sugieren que el MIL-53(Fe) no debería recomendarse como fotocatalizador heterogéneo para el tratamiento de aguas debido a su inestabilidad en condiciones oxidantes. Por todo ello, se decidió que el MIL-53(Fe) no se magnetizaría para estudios posteriores.

Parte 2. Magnetización de metales, óxidos metálicos y materiales carbonosos

Algunos metales, óxidos metálicos y materiales carbonosos se han postulado como catalizadores útiles en diferentes tipos de PAO, como, por ejemplo, la ozonización catalítica [16]. El uso de sólidos inorgánicos en PAO catalíticos suele implicar su inmovilización sobre soportes estructurales (cerámicas, metales)

favoreciendo así su uso en procesos continuos (e.g., lechos fijos) o su separación en procesos con catalizador en suspensión [17]. Sin embargo, la inmovilización suele disminuir en gran medida la actividad catalítica debido a las limitaciones de transferencia de materia. Además, puede producirse cierta pérdida o deterioro del material catalítico con el tiempo, debido a las condiciones de funcionamiento (por ejemplo, temperatura, pH, agitación, entorno químico, etc.), lo que lleva a una pérdida de eficiencia tras su uso continuo o en varios ciclos de reutilización [18]. La magnetización del catalizador puede ofrecer ventajas prácticas frente a su inmovilización cuando se va a emplear en suspensión, por lo que actualmente es un tema de gran interés en investigación [19-22].

En la mayoría de los métodos de magnetización de catalizadores propuestos en la bibliografía se requieren altas temperaturas, así como reactivos tóxicos y caros. Además, el tratamiento de residuos es imprescindible tras la preparación del catalizador, lo que hace que el proceso en su conjunto resulte poco atractivo desde los puntos de vista económico y medioambiental. El objetivo de la investigación llevada a cabo en esta Tesis fue ofrecer una solución al problema técnico de "cómo magnetizar de forma barata y sostenible sólidos inorgánicos para producir catalizadores compuestos fácilmente recuperables por la acción de un imán/electroimán". El método propuesto comprendía los siguientes pasos:

(a) Disolver una sal de hierro (II) en agua. Pueden utilizarse haluros de hierro (II) o sulfatos de hierro (II). Se utilizó preferentemente $FeCl_2 \cdot 4H_2O$.
(b) Añadir la especie inorgánica que se desea magnetizar en forma de partículas en suspensión (tamaño de partícula < 250 μm) a la disolución obtenida en el paso (a). Los materiales inorgánicos deben ser estables y poder suspenderse en agua a pH básico. Algunas sustancias que cumplen estos requisitos y se han utilizado en este trabajo son las siguientes: TiO_2, TiO_2 /WO_3, CeO_2, Al_2O_3, Ru/Al_2O_3, Pt/Al_2O_3, grafeno, TiO_2 /grafeno, óxido de grafeno y carbón activado.
(c) Por separado, disolver el ácido tereftálico (H_2BDC) en una disolución acuosa

de NaOH 1M.

(d) Añadir la disolución obtenida en (c) a la solución obtenida en (b), manteniendo la temperatura constante en el intervalo de 10 °C a 70 °C durante un tiempo suficiente para producir óxido de hierro magnético (e.g., Fe_3O_4), obteniendo así una suspensión de un sólido inorgánico, compuesto y magnético.

(e) Separar las partículas de sólido obtenidas en la etapa (d) mediante un imán externo.

(f) Lavar varias veces con agua para eliminar trazas de H_2BDC del sólido magnético y separar posteriormente el sólido lavado con un imán externo.

(g) Secar el producto obtenido en la etapa (f).

(h) Recuperar el H_2BDC de la disolución obtenida en el paso (e) y reutilizar en (c).

Parte 3. Materiales magnéticos de carbono como fotocatalizadores solares en PAO: oxidación húmeda catalítica con peróxido de hidrógeno

Aprovechando que las propiedades magnéticas de la magnetita permiten una recuperación fácil, rápida y rentable del medio de reacción, junto con su estabilidad química, baja toxicidad y coste relativamente bajo, se han propuesto varios catalizadores basados en este material (magnetite-based catalysts, MBCs por sus siglas en inglés) para degradar contaminantes orgánicos acuosos mediante diferentes PAO [23]. Desde 2008, los procesos avanzados de oxidación más estudiados han sido los procesos catalíticos heterogéneos Fenton y foto-Fenton (catalytic wet peroxide oxidation, CWPO, por sus siglas en inglés) [24,25]. Aunque el mecanismo de descomposición de H_2O_2 sobre magnetita (Fe_3O_4) no está aun claramente dilucidado, existe un acuerdo general entre los científicos en que el Fe(II) superficial provoca la descomposición de H_2O_2 en $HO^{\bullet}$ [24-26]. La regeneración del Fe(II) superficial suele ser el paso limitante que controla la eficiencia global del proceso. Cuando se aplica radiación (es decir, proceso foto-Fenton heterogéneo), se favorece la velocidad de reducción del Fe(III),

aumentando la formación de HO• [25]. Para mejorar las propiedades catalíticas de la magnetita en las reacciones de CWPO, se ha propuesto emplear diferentes sólidos dando lugar a magnetita soportada o materiales compuestos [24]. Entre ellos, se han investigado algunos materiales de carbono (por ejemplo, carbón activado, nanotubos de carbono, grafeno, óxido de grafeno o nitruro de carbono grafítico) que resultan atractivos en los PAO debido a su elevada área superficial y a sus propiedades químicas superficiales [25,26]. Además de proporcionar una mayor área superficial, favorecer la dispersión de la magnetita y aumentar la adsorción de contaminantes orgánicos, las estructuras de carbono pueden promover la inyección de electrones hacia la magnetita, mejorando así la regeneración de los centros de Fe(II). Además, algunos materiales de carbono muestran por sí mismos actividad catalítica en el proceso CWPO [26].

Basándose en la estrategia descrita en la segunda parte de esta Tesis, en esta tercera se presenta un método de síntesis de MBC novedoso y respetuoso con el medio ambiente. El método emplea ácido tereftálico para dirigir la síntesis hacia la formación de magnetita sobre el soporte carbonoso. Se aplicó la filosofía de la química verde orientada hacia el uso de agentes no tóxicos y recuperables. Así, se logró la recuperación casi total del ácido tereftálico empelado. El método se utilizó con éxito para preparar magnetita pura y diferentes materiales compuestos de carbono (carbón activado, grafeno y óxido de grafeno) y magnetita. Se efectuó una caracterización completa de los MBC preparados y se llevó a cabo un estudio de su uso como catalizadores en CWPO solar empleando MTP como contaminante objetivo. Se hizo especial hincapié en los estudios de estabilidad, separabilidad, recuperación y reutilización del catalizador.

Se prepararon magnetita pura (Fe_3O_4) y algunos compuestos híbridos de magnetita y carbono (Fe_3O_4-G, Fe_3O_4-GO, y Fe_3O_4-AC). Como materiales de carbono de partida se utilizaron grafeno (G), óxido de grafeno (GO) y carbón activado (AC). El H_2BDC recuperado y los MBC sintetizados se caracterizaron completamente mediante XRD, FTIR, espectroscopia Raman, espectroscopía

fotoelectrónica de rayos X (XPS), magnetometría SQUID, TGA-DTA-MS, análisis elemental e isotermas de adsorción-desorción de N_2. Este H_2BDC recuperado tenía una pureza lo suficientemente alta como para ser reutilizado en la síntesis de nuevos MBC. Todos los catalizadores obtenidos presentaban la fase cristalina de nanopartículas de magnetita, un área superficial moderada (63-337 $m^2\ g^{-1}$) y propiedades magnéticas que permitían su fácil separación del medio acuoso mediante un imán externo (saturación magnética = 25-80 emu g^{-1}). Los MBC sintetizados fueron activos en los ensayos de CWPO asistida con luz solar simulada. Fe_3O_4-G y Fe_3O_4-GO mostraron una baja estabilidad en comparación con Fe_3O_4 y Fe_3O_4-AC. Además, este último catalizador presentó una actividad catalítica muy superior al Fe_3O_4 puro. Así, se alcanzaron conversiones de MTP y carbono orgánico total superiores al 90% y al 20%, respectivamente, tras 3 h de tratamiento con Fe_3O_4-AC a un pH inicial de 7 (el pH descendió hasta aproximadamente 4). A pH neutro, controlado durante el proceso, la eliminación de MTP con Fe_3O_4-AC fue más moderada (>60%), siendo este descenso de actividad una limitación típica en los tratamientos foto-Fenton. La mejor eficiencia en el uso de H_2O_2 fue de 0,23 mol de C eliminado por mol de H_2O_2 consumido, lo que supone aproximadamente un 60% de la máxima eficiencia alcanzable. El catalizador Fe_3O_4-AC pudo reutilizarse fácilmente en un experimento CWPO que comprendía nueve ciclos consecutivos recuperando el catalizador con un imán después de cada ciclo. Se observó una desactivación moderada del catalizador debida principalmente a la obstrucción de algunos microporos y/o a la pérdida de sitios catalíticos de Fe(II). No obstante, la desactivación a partir del cuarto ciclo fue insignificante y la separabilidad magnética siguió siendo muy satisfactoria.

Parte 4. Estructuras híbridas Fe_3O_4/TiO_2 como fotocatalizadores solares en PAO: oxidación fotocatalítica y ozonización fotocatalítica

Aunque hasta ahora se han propuesto muchos catalizadores para PAO solares, el TiO_2-P25 sigue considerándose el catalizador de referencia en este campo [27]. A pesar de no ser un fotocatalizador que funcione con luz visible, debido a su amplio salto de banda (3,2 eV), TiO_2-P25 suele proporcionar mayores tasas de fotodegradación de contaminantes acuosos bajo la luz solar que otros semiconductores clásicos (por ejemplo, ZnO) y nuevos materiales fotocatalíticos alternativos (por ejemplo, MOF) debido a la mayor generación de ROS [28]. Además, la producción de ROS puede mejorarse utilizando TiO_2-P25 en combinación con oxidantes como el peróxido de hidrógeno o el ozono [29,30]. Una de las principales limitaciones que impiden la aplicación práctica de la oxidación fotocatalítica con TiO_2-P25 como tratamiento terciario en EDAR es la dificultad para separar las partículas nanoestructuradas de TiO_2 del agua [31]. Para superar este problema, se puede considerar la inmovilización de TiO_2 en diferentes soportes, aunque normalmente es a costa de cierta pérdida de actividad fotocatalítica [32]. También se ha investigado ampliamente la preparación de materiales magnéticos con TiO_2 mediante la formación in situ de anatasa y óxidos de hierro magnéticos. Sin embargo, los métodos de síntesis, de múltiples pasos, utilizados para este fin suelen consumir mucha energía y requieren grandes cantidades de reactivos y disolventes tóxicos. Además, la actividad de los fotocatalizadores magnéticos de Fe_3O_4/TiO_2 preparados rara vez supera la de las nanopartículas de TiO_2-P25 [33]. Particularmente interesante parece el uso directo de TiO_2-P25 para producir nanopartículas (NP) magnéticas reutilizables [34].

De nuevo, siguiendo la estrategia de síntesis verde descrita en la segunda parte de esta Tesis, en esta cuarta parte se ha sintetizado un compuesto híbrido formado por Fe_3O_4 y TiO_2-P25, denominado Fe_3O_4@TiO_2-P25. Se aborda un estudio más detallado sobre la formación de este material por precipitación oxidativa de Fe(II)

en presencia de TiO_2 -P25 y BDC^{2-} . Se ha evaluado la estabilidad, la actividad fotocatalítica (utilizando O_2 y O_2/O_3 como aceptores de electrones) y la reutilización del catalizador para la eliminación de MTP en procesos de ozonación fotocatalítica.

Las partículas de Fe_3O_4, formadas in situ por precipitación oxidativa de Fe(II) en presencia de ácido tereftálico se lograron unir a nanopartículas de TiO_2-P25, dando lugar a una heteroestructura semiconductora acoplada con comportamiento superparamagnético a temperatura ambiente. El método de síntesis de Fe_3O_4@TiO_2 -P25 es interesante ya que se lleva a cabo en agua, a temperatura ambiente, con recuperación y reciclado casi total de H_2BDC. Los catalizadores preparados se caracterizaron completamente por XRD, FTIR, WDXRF, microscopía electrónica de barrido acoplada con espectrometría de dispersión de energía de rayos X (SEM/EDX), isotermas de adsorción-desorción de N_2, análisis elemental, XPS, DRS y SQUID. Las pruebas de estabilidad mostraron que el catalizador no sufre fotodisolución bajo radiación solar simulada y que es estable en medios fuertemente oxidantes. Por otro lado, los estudios de actividad fotocatalítica revelaron que el Fe_3O_4@TiO_2-P25 sintetizado muestra un mejor rendimiento fotocatalítico que dos materiales preparados anteriormente por el grupo de investigación (un material compuesto de carbón activado/Fe_3O_4/TiO_2 y un material híbrido Fe_3O_4/TiO_2 con estructura de núcleo y corteza) [35,36]. Por último, se demostró una favorable reutilización de Fe_3O_4@TiO_2-P25 mediante seis ciclos de ozonización fotocatalítica. Por lo tanto, la estructura sintetizada de Fe_3O_4@TiO_2-P25 puede considerarse como un prometedor fotocatalizador sostenible, eficaz y reciclable para los PAO.

Publicaciones y transferencia de resultados de esta investigación:

Los principales resultados de esta Tesis Doctoral ya han sido publicados o están listos para ser sometidos a revisión por pares. Además, se dispone de una patente concedida fruto de este trabajo.

- ✓ J. López, A.M. Chávez, A. Rey, P.M. Álvarez, Insights into the stability and activity of mil-53(Fe) in solar photocatalytic oxidation processes in water, Catalysts. 11 (2021). https://doi.org/10.3390/catal11040448

- ✓ J. López; A. Rey, J.F. García-Araya, P.M. Álvarez, Green synthesis of magnetite-based catalysts for solar-assisted catalytic wet peroxide oxidation. Catalysts, 12 (**2022**) 271. https://doi.org/10.3390/catal12030271

- ✓ J. López; A. Rey, E. Viñuela-Zahinos, P.M. Álvarez. Preparation of a new green magnetic Fe_3O_4@TiO_2-P25 photocatalyst for solar advanced oxidation processes in water. Preparado para su envío a publicación por revisión por pares.

- ✓ Patente ES2884450A1 "Método para la magnetización de sólidos inorgánicos". https://patents.google.com/patent/ES2884450A1/es

ABSTRACT

The awareness of the increasing occurrence of compounds of emerging concern or simply emerging contaminants (ECs) at trace levels in water systems, especially in populated areas of developed countries, has alerted about a high-concern threat to the environment and human health. Several types of EC are described in the literature including pharmaceuticals, personal care products, industrial additives, pesticides, nanomaterials and microplastics. Generally, they are chemicals that recently have been shown to occur widely in water bodies at low concentration level ($\mu g\ L^{-1}$ a $ng\ L^{-1}$) and yet have been identified as being a potential health and an environmental risk in the long-term.

Conventional biological and physical-chemical treatments usually applied at wastewater treatment plants (WWTPs) have been demonstrated rather ineffective for the removal of different ECs due to their recalcitrant and bio-refractory nature. Innovation in wastewater treatment adopting sustainable, cost-efficient technologies to achieve the goal of complete removal of ECs is becoming a must. In this sense, advanced oxidation processes (AOPs) are likely called to lead the battle against ECs in WWTPs. AOPs involve the generation of highly reactive oxygen species (ROS) such as hydroxyl radical ($HO^{\bullet}$, $E°=2.8$ V) that can degrade EC molecules eventually transforming them into harmless products. Among the most studied AOPs several photochemical processes can be cited including photo-Fenton, UV/H_2O_2, UV/O_3 and TiO_2 photocatalytic oxidation.

Photocatalytic AOPs are regarded as highly efficient processes in the production of ROS leading to fast degradation of ECs in water matrices. In spite of that, lowering the cost and energy consumption, as well as the sustainability and reusability of the catalyst remain as major challenges. As a consequence, today a great deal of research is devoted to photocatalytic AOPs driven by sunlight and light emitting diode (LED) as sources of radiation. The search for UV-vis photoactive catalysts with improved activity and reusability is the goal of many studies.

This Doctoral Thesis was conducted primarily in Badajoz (Spain) during October 2017- December 2022 at the Department of Chemical Engineering and Physical Chemistry of the University of Extremadura under the guidance of the TRATAGUAS research group. Besides, a three-month research stay was carried out in Portugal (Faculty of Engineering-University of Porto) from May to July 2021. TRATAGUAS group has vast experience in the study of classical and novel AOPs and is currently involved in several projects dealing with the topic of the synthesis of photocatalysts for AOPs. This Ph.D. work has been carried out in this context and it focuses on the preparation of magnetic recoverable photocatalysts for solar AOPs. A first attempt was made to develop UV-vis photoactive metal-organic frameworks (MOF). Unfortunately, the MOFs investigated were not stable enough in the AOP aqueous environment to be considered as promising photocatalysts for further magnetization studies (part 1). Then, the research was oriented towards the synthesis of magnetically recoverable inorganic materials (e.g., metal oxides, carbonaceous materials), which were found rather stable at the AOPs reaction conditions (parts 2 to 4)

Part 1. MOF as solar photocatalysts: the case of MIL-53(Fe)

There is a growing interest in developing new visible-light-responsive photocatalysts for the removal of contaminants from water with improved properties such as high adsorption capacity and photocatalytic activity under solar radiation or visible light, easy post-recovery and reusability. In this sense, some types of the so-called metal–organic frameworks (MOFs) are arising growing interest as potential heterogeneous photocatalysts [1].

MOFs constitute a class of porous, crystalline materials formed by an extended network of metal ions (clusters) coordinated to multifunctional organic ligands (linkers) through coordination bonds. The combination of inorganic and organic units in the MOF offers an outstanding number of structural possibilities for materials with predefined properties that might make them useful in a variety of applications such as gas storage and separation, molecular sensing, catalysis or

drug delivery [2]. Since 2007, when Llabrés i Xamena and co-workers showed the photocatalytic activity of MOF-5 for the degradation of phenol [3], an increasing number of MOFs have been researched as photocatalysts for the degradation of organic pollutants in water [4–6]. Particularly appealing in this field are Fe-based MOFs, which can absorb visible light due to the direct excitation of iron–oxo clusters [7]. Furthermore, they can work as heterogeneous catalysts for the activation of hydrogen peroxide (e.g., Fenton-like reactions) [8–10], persulfate [11,12] or ozone [13]. Among the Fe-based MOFs, MIL-53(Fe), a three-dimensional, flexible, porous solid composed of $FeO_4(OH)_2$ octahedra clusters connected by 1,4-benzenedicarboxylate (BDC) linkers, has gained special attention in the recent literature as a potential visible-light photocatalyst for the degradation of organic pollutants in water. MIL-53(Fe) offers the advantages of easy preparation from terephthalic acid and common iron salts, stability, non-toxicity and good visible light absorption [14].

Based on the potential advantages of MIL-53(Fe) as photocatalyst for solar AOPs was the primitive purpose of this research to functionalize MIL-53(Fe) as an effective magnetic heterojunction composite. However, we had shown previously that the stability of other Fe-based MOF (MIL-100(Fe)) is a critical aspect to take into account before proposing it as a catalyst candidate for solar AOPs [15]. Therefore, as a first research step was conceived to evaluate the stability of MIL-53(Fe) in aqueous solution under typical conditions of solar photocatalytic oxidation. Thus, leaching of iron and organic matter from the MOF were evaluated at different process conditions. Photocatalytic activity of MIL-53(Fe) towards the degradation of phenol (Ph) and metoprolol (MTP) in the presence of different electron acceptors (hydrogen peroxide, potassium persulfate and ozone) was also investigated.

MIL-53(Fe) was successfully synthesized by a solvothermal method and fully characterized by X-ray diffraction (XRD), attenuated total reflectance Fourier transform infrared spectroscopy (ATR-FTIR), N_2 adsorption–desorption

isotherm, thermogravimetric analysis coupled with mass spectrometry (TGA-MS), UV-visible diffuse reflectance spectroscopy (DRS), elemental analysis and wavelength dispersive X-ray fluorescence (WDXRF). The characterization of the synthetized material as MIL-53(Fe) was in good agreement with the literature. The as-synthetized MIL-53(Fe) exhibited relatively good stability in water at pH 4 but suffered fast hydrolysis at alkaline conditions. At pH 4–5, temperature, solar radiation and oxidants exerted negative effect on the stability of the metal–organic framework (MOF) in water, resulting in non-negligible amounts of metal (iron) and linker (terephthalic acid, H_2BDC) leached out from MIL-53(Fe). In terms of activity, MIL-53(Fe) on its own removed less than 10% of the pollutants (MTP and Ph) after 3 h of simulated sunlight irradiation, while in the presence of ozone, persulfate or hydrogen peroxide, complete elimination of pollutants was achieved within 2 h of exposure to radiation. However, the presence of oxidants and the formation of some reaction intermediates (e.g., short-chain carboxylic acids) accelerated MIL-53(Fe) decarboxylation. The findings of this work suggest that MIL-53(Fe) should not be recommended as a heterogeneous photocatalyst for water treatment due to its instability under oxidizing conditions. Therefore, MIL-53 was not magnetized for further studies.

Part 2. Magnetization of metal, metal oxides and carbonaceous materials

Some metal, metal oxides and carbonaceous materials are recognized as useful catalysts in different types of AOPs, as, for example, catalytic ozonation [16]. The use of inorganic solids in catalytic AOPs usually involves their immobilization on macro-structured supports (ceramics, metals), which favor their separation from the reaction medium [17]. However, the immobilization usually decreases the catalytic activity to a large extent due to mass transfer limitations. Also, some loss or deterioration of the catalytic material can occur over time, due to operating conditions (e.g., temperature, pH, agitation, chemical environment, etc.) [18]. Magnetization of the catalyst may offer practical advantages over its immobilization, so it is a subject of current research interest [19-22].

In most of the magnetization methods proposed in the literature, high temperature as well as toxic and expensive reagents are required. Moreover, waste treatment is a must after the catalyst preparation making the overall process unattractive from economic and environmental points of views. The aim of this piece of research carried out in this Thesis was to offer a solution to the technical problem of "how to functionalize different inorganic solids to produce magnetically recoverable composite catalysts in a cheap and sustainable way". The proposed method comprised the following steps:

(a) Dissolution of iron (II) salt in water. Either iron (II) halides or iron (II) sulfates can be used. $FeCl_2 \cdot 4H_2O$ was used preferentially.

(b) Addition of the inorganic species to be magnetized in particulate form (particle size < 250 μm) to the solution obtained in the step (a). Inorganic materials must be stable and able to be suspended in alkaline aqueous water. Examples of suitable substances are the following: TiO_2, TiO_2/WO_3, CeO_2, Al_2O_3, Ru/Al_2O_3, Pt/Al_2O_3, graphene, TiO_2/graphene, graphene oxide and activated carbon.

(c) Separately, to dissolve terephthalic acid (H_2BDC) in a 1M NaOH aqueous solution.

(d) Addition of the solution obtained in (c) to the solution obtained in (b), keeping temperature constant in the range from 10 °C to 70 °C for enough time to produce magnetic iron oxide (e.g., Fe_3O_4), thus obtaining a suspension of a magnetic composite solid.

(e) Separation of the particles of solid obtained in the step (d) by means of an external magnet.

(f) Washing several times with distilled water to remove traces of H_2BDC from the magnetic solid and subsequent separation with an external magnet.

(g) Drying of the product obtained in the step (f).

(h) Recovery of H_2BDC from the solution obtained in the step (e) and reuse in (c).

Part 3. Magnetic carbon materials as solar photocatalysts in AOPs: catalytic wet peroxide oxidation (CWPO)

Taking advantage of their magnetic properties that allow easy, fast, and cost-effective recovery from the reaction medium, together with their chemical stability, low toxicity, and relatively low cost, a number of magnetite-based catalysts (MBCs) has been proposed to degrade aqueous organic pollutants by different advanced oxidation processes (AOPs) [23]. By far, since 2008, the most studied AOPs using MBCs have been heterogeneous Fenton and photo-Fenton processes, also called catalytic wet peroxide oxidation (CWPO) [24,25]. Although the mechanism of H_2O_2 decomposition over magnetite (Fe_3O_4) has not been fully elucidated yet, there is general agreement that surface Fe(II) provokes the decomposition of H_2O_2 into $HO^{\bullet}$ [24-26]. Regeneration of surface Fe(II) is typically the limiting step that controls the overall process efficiency. When radiation is applied (i.e., heterogeneous photo-Fenton process), the reduction rate of Fe(III) is favored, increasing the formation rate of $HO^{\bullet}$ [25]. To enhance the catalytic properties of bare magnetite in CWPO reactions, several solids have been used to prepare supported or composite materials [24]. Among them, some carbon materials (e.g., activated carbon, biochar, carbon nanotubes, graphene, graphene oxide, or graphitic carbon nitride) have been investigated because of their high surface area and surface chemistry properties [25,26]. In addition to providing a greater surface area, favoring the dispersion of magnetite and increasing the adsorption of organic contaminants, carbon structures may promote electron injection towards magnetite, thus enhancing the regeneration

of Fe(II) sites. Moreover, some carbon materials exhibit catalytic activity in CWPO by themselves [26].

Based on the strategy described in the second part of this Thesis, this third presents a novel, environmentally friendly synthesis method of MBCs based on a terephthalate intermediate as structure director. Green chemistry philosophy towards circular use of resources was applied with an almost full recovery of the synthesis mediator, terephthalic acid (H_2BDC). The method was successfully used to prepare bare magnetite and different carbon-magnetite composites with activated carbon, graphene, and graphene oxide. Herein, fully characterization of the prepared MBCs and their use as catalysts in solar assisted-CWPO of aqueous solution of the drug metoprolol (MTP) were carried out. Emphasis was placed on catalyst stability, separability, recovery, and reusability.

Bare magnetite (Fe_3O_4) and some hybrid magnetite-carbon composites were prepared (Fe_3O_4-G, Fe_3O_4-GO, and Fe_3O_4-AC). Graphene (G), graphene oxide (GO), and activated carbon (AC) were used as starting carbon materials. The recovered H_2BDC and the as-synthetized MBCs were fully characterized by XRD, FTIR, Raman spectroscopy, XPS, SQUID magnetometry, TGA-DTA-MS, elemental analysis, and N_2 adsorption- desorption isotherms. The recovered H_2BDC was of purity high enough to be reused in the synthesis of MBCs. All the catalysts obtained presented the typical crystalline phase of magnetite nanoparticles, moderate surface area (63–337 $m^2\ g^{-1}$), and magnetic properties that allowed their easy separation from aqueous media by an external magnet (magnetization saturation = 25–80 emu g^{-1}). The as-synthesized MCBs were active for photo-CWPO, as demonstrated treating an aqueous solution of MTP. Fe_3O_4-G and Fe_3O_4-GO showed low stability compared with Fe_3O_4 and Fe_3O_4-AC. Moreover, the latter presented catalytic activity much superior to bare Fe_3O_4. MTP and TOC conversions higher than 90% and 20%, respectively, were achieved after 3 h of treatment with Fe_3O_4-AC at initial aqueous pH 7 (pH dropped to about 4). At circumneutral pH (pH was controlled at about 7

throughout the process) MTP removal was still moderate (>60%), this being a typical limiting issue in photo-Fenton treatments. The best efficiency in the use of H_2O_2 was 0.23 mol C eliminated per mol H_2O_2 consumed, which is about a 60% of the maximum attainable efficiency. Fe_3O_4-AC could be easily reused in a nine-consecutive CWPO experiment recovering the catalyst with a magnet after each cycle. Moderate catalyst deactivation was observed mainly due to the blockage of some micropores and/or loss of Fe^{2+} catalytic sites. Nevertheless, deactivation from the fourth cycle onwards was negligible and magnetic separability remained quite satisfactory.

Part 4. Fe_3O4/TiO_2 hybrid structures as solar photocatalysts in AOPs: photocatalytic oxidation and photocatalytic ozonation

Although many catalysts have been proposed for solar-driven AOPs so far, TiO_2-P25 is still considered the benchmark catalyst in this field [27]. Moreover, despite it is not a visible-light photocatalyst due to its wide band-gap (3.2 eV), TiO_2-P25 typically provides higher photodegradation rates of aqueous pollutants under sunlight than other classical semiconductors (e.g., ZnO) and alternative new photocatalytic materials (e.g., MOFs) because of larger generation of ROS [28]. Furthermore, ROS production can be improved using TiO_2-P25 in combination with oxidants such as hydrogen peroxide or ozone [29,30]. A main limitation impeding the widespread application of TiO_2-P25 photocatalytic oxidation in WWTPs is the difficulty in the separation of nanosized TiO_2 particles from water suspensions [31]. To overcome this separation problem, immobilization of TiO_2 on different supports can be considered, though typically at the expense of some loss of photocatalytic activity [32]. Extensive research has also been conducted on the preparation of TiO_2 magnetic reusable materials by in situ formation of anatase TiO_2 and magnetic iron oxides. However, the multi-step synthesis methods used for this purpose are usually high energy-consuming and require large amounts of toxic reagents and solvents. Moreover, the activity of the prepared magnetic Fe_3O_4/TiO_2 photocatalysts rarely surpasses that of bare

TiO_2-P25 nanoparticles [33]. Particularly interesting seems the direct use of TiO_2-P25 to produce robust magnetic reusable nanoparticles (NPs) [34].

Again, following the synthesis strategy outlined in the second part of this Thesis, a Fe_3O_4@TiO_2-P25 composite has been green-synthesized and fully characterized in this fourth part. Possible insights into the formation of this material by oxidative precipitation of Fe(II) in the presence of TiO_2-P25 and BDC^{2-} are addressed. The stability, photocatalytic activity (using O_2 and O_2/O_3 as electron acceptors) and reusability of the catalyst have been assessed for the removal of MTP.

Fe_3O_4 particles formed in situ by aerial oxidative precipitation of Fe(II) in the presence of terephthalic acid (H_2BDC) were bonded to TiO_2-P25 nanoparticles, giving rise to a coupled semiconductor heterostructure with superparamagnetic behavior at room temperature (Fe_3O_4@TiO_2-P25). The synthesis method is attractive as it is carried out in water at room temperature with almost full recovery and recycling of H_2BDC. The prepared samples were fully characterized by XRD, FTIR, WDXRF, SEM/EDX, N_2 adsorption-desorption, elemental analysis, XPS, DRS and SQUID. Photo-stability tests showed that the catalyst does not undergo photodissolution under simulated solar radiation. Photocatalytic activity studies revealed that Fe_3O_4@TiO_2-P25 shows better photocatalytic performance than an activated carbon/Fe_3O_4/TiO_2 composite and core-shell Fe_3O_4/TiO_2 NPs [35,36]. Finally, the reusability of the Fe_3O_4@TiO_2-P25 was demonstrated through six photocatalytic ozonation cycles reusing the catalyst sample. Therefore, the synthesized Fe_3O_4@TiO_2-P25 structure can be regarded as a promising sustainable, effective and recyclable photocatalyst for AOPs.

Output of this research:

The main findings of this Doctoral Thesis have been already published or are ready to be submitted for peer-review publication. In addition, the method of magnetization has been protected under a Spanish patent.

- J. López, A.M. Chávez, A. Rey, P.M. Álvarez, Insights into the stability and activity of mil-53(Fe) in solar photocatalytic oxidation processes in water, Catalysts. 11 (2021). https://doi.org/10.3390/catal11040448

- J. López; A. Rey, J.F. García-Araya, P.M. Álvarez, Green synthesis of magnetite-based catalysts for solar-assisted catalytic wet peroxide oxidation. Catalysts, 12 (**2022**) 271. https://doi.org/10.3390/catal12030271

- J. López; A. Rey, E. Viñuela-Zahinos, P.M. Álvarez. Preparation of a new green magnetic Fe_3O_4@TiO_2-P25 photocatalyst for solar advanced oxidation processes in water. To be submitted for peer-review publication.

- Patente ES2884450A1 "Método para la magnetización de sólidos inorgánicos". https://patents.google.com/patent/ES2884450A1/es

Bibliografía/References

[1] J. Gascón, A. Corma, F. Kapteijn, F.X. Llabrés i Xamena. Metal organic framework catalysis: quo vadis? ACS Catal., 4 (**2014**) 361-378.

[2] H. Furakawa, K.E. Cordova, M. O'Keeffe, O.M. Yaghi. The chemistry and applications of metal-organic frameworks. Science, 341 (**2013**) 974-986.

[3] F.X. Llabrés I Xamena, A. Corma, H. García. Applications for metal-organic frameworks (MOFs) as quantum dot semiconductors. J. Phys. Chem. C, 111 (**2007**) 80-85.

[4] C. Wang, J. Li, X. Lv, Y. Zhang, G. Guo. Photocatalytic organic pollutants degradation in metal-organic frameworks. Energy Environ. Sci., 7 (**2014**) 2831-2867.

[5] J. Bedia, V. Muelas-Ramos, M. Peñas-Garzón, A. Gómez-Avilés, J.J. Rodríguez, C. Belver. A review on the synthesis and characterization of metal organic frameworks for photocatalytic water purification. Catalysts, 9 (**2019**) 52.

[6] X. Zhang. J. Wang, X. Dong, Y. Lv. Functionalized metal-organic frameworks for photocatalytic degradation of organic pollutants in environment. Chemosphere, 242 (**2020**) 125144.

[7] D. Wang, Z. Li. Iron-based metal–organic frameworks (MOFs) for visible-light-induced photocatalysis. Res. Chem. Intermed., 43 (**2017**) 5169–5186.

[8] Q.Sun, M. Liu, K. Li, Y. Zuo, Y. Han, J. Wang, C. Song, G. Zhang, X. Guo. Facile synthesis of Fe-containing metal–organic frameworks as highly efficient catalysts for degradation of phenol at neutral pH and ambient temperature. Cryst. Eng.Comm, 17 (**2015**) 7160.

[9] Q. Sun, M. Liu, K. Li, Y. Han, Y. Zuo, J. Wang, C. Song, G. Zhang, X. Guo. Controlled synthesis of mixed-valent Fe-containing metal organic frameworks for the degradation of phenol under mild conditions. Dalton Trans., 45 (**2016**) 7952-7959.

[10] C. Gao, S. Chen, X. Quan, H. Yu, Y. Zhang. Enhanced Fenton-like catalysis by iron-based metal organic frameworks for degradation of organic pollutants. J. Catal., 356 (**2017**) 125-132.

[11] X. Li, W. Guo, Z. Liu, R.Wang, H. Liu. Fe-based MOFs for efficient adsorption and degradation of acid orange 7 in aqueous solution via persulfate activation. Appl. Surf. Sci., 369 (**2016**) 130-136.

[12] M. Pu, Z. Guand, Y. Ma, J. Wan, Y. Wang, M.L. Brusseau, H. Chi. Synthesis of iron-based metal-organic framework MIL-53 as an efficient catalyst to activate persulfate

for the degradation of Orange G in aqueous solution. Appl. Catal. A-Gen., 549 (**2018**) 82-92.

[13] D. Yu, M. Wu, Q. Hu, L. Wang, C.Lv, L. Zhang. Iron-based metal-organic frameworks as novel platforms for catalytic ozonation of organic pollutant: Efficiency and mechanism. J. Hazard. Mat., 367 (**2019**) 456-464.

[14] J.J. Du, Y.P. Yuan, J.X. Sun, F.M. Peng, X. Jiang, L.G. Qiu, A.J. Xie, Y.H. Shen, J.F. Zhu. New photocatalysts based on MIL-53 metal-organic frameworks for the decolorization of methylene blue dye. J. Hazard. Mat. 190 (**2011**) 945-951.

[15] A.M. Chávez, A. Rey, J. López, P.M. Álvarez, F.J.Beltrán. Critical aspects of the stability and catalytic activity of MIL-100(Fe) in different advanced oxidation processes. Sep. Purif. Technol., 255 (**2021**) 117660.

[16] J. Wang, H. Chen, Catalytic ozonation for water and wastewater treatment: Recent advances and perspective, Sci. Total Environ. 704 (**2020**) 135249.

[17] E.M. Rodríguez, A. Rey, E. Mena, F.J. Beltrán, Application of solar photocatalytic ozonation in water treatment using supported TiO_2, Appl. Catal. B Environ., 254 (**2019**) 237–245.

[18] J. Gomes, B. Maniezo, P. Alves, P. Ferreira, Martins, R. C. Immobilization of TiO_2 onto a polymeric support for photocatalytic oxidation of a paraben's mixture. J. Water Process Eng., 46 (**2022**) 102458.

[19] L. Zhu, X. Kong, C. Yang, B. Ren, Q. Tang. Fabrication and characterization of the magnetic separation photocatalyst C-TiO_2@Fe_3O_4/AC with enhanced photocatalytic performance under visible light irradiation. J. Hazard. Mater., 381 (**2020**) 120910.

[20] B. Fan, Y. Tan, J. Wang, B. Zhang, Y. Peng, C. Yuan, C. Guan, X. Gao, S. Cui. Application of magnetic composites in removal of tetracycline through adsorption and advanced oxidation processes (AOPs): A Review. Process., 9 (**2021**) 1644.

[21] A. Gallo-Cordova, J.J. Castro, E.L. Winkler, E. Lima, R.D. Zysler, M. del P. Morales, J.G. Ovejero, D.A. Streitwieser. Improving degradation of real wastewaters with self-heating magnetic nanocatalysts. J. Clean. Prod., 308 (**2021**) 127385.

[22] B. Jin, D. Zhao, H. Yu, W. Liu, C. Zhang, M. Wu. Rapid degradation of organic pollutants by Fe_3O_4@PDA/Ag catalyst in advanced oxidation process. Chemosphere, 307 (**2022**) 135791.

[23] A. Masudi, G.E. Harimisa, N.A. Ghafar, N.W.C. Jusoh. Magnetite-based catalysts for wastewater treatment. Environ. Sci. Pollut. Res., 27 (**2020**) 4664–4682.

[24] M. Muñoz, Z.M. de Pedro, J.A. Casas, J.J. Rodríguez. Preparation of magnetite-based catalysts and their application in heterogeneous Fenton oxidation-A Review. Appl. Catal. B Environ., 176-177 (**2015**) 249–265.

[25] N. Thomas, D.D. Dionysiou, S.C. Pillai. Heterogeneous Fenton Catalysts: A Review of Recent Advances. J. Hazard. Mater., 404 (**2021**) 124082.

[26] R.S. Ribeiro, A.M.T. Silva, J.L. Figueiredo, J.L. Faria, H.T. Gomes. Catalytic wet peroxide oxidation: a route towards the application of hybrid magnetic carbon nanocomposites for the degradation of organic pollutants. A Review. Appl. Catal. B Environ., 187 (**2016**) 428–460.

[27] J.M. Coronado, M.D. Hernández-Alonso, The keys of success: TiO_2 as a benchmark photocatalyst, Green Energy Technol., 71 (**2013**) 85-101.

[28] J. Carbajo, M. Jiménez, S. Miralles, S. Malato, M. Faraldos, A. Bahamonde, Study of application of titania catalysts on solar photocatalysis: Influence of type of pollutants and water matrices, Chem. Eng. J., 291 (**2016**) 64-73.

[29] J. Kelly, C. McDonnell, N. Skillen, P. Manesiotis, P.K.J. Robertson, Enhanced photocatalytic degradation of 2-methyl-4-chlorophenoxyacetic acid (MCPA) by the addition of H_2O_2, Chemosphere, 275 (**2021**) 130082.

[30] D. Bertagna Silva, A. Cruz-Alcalde, C. Sans, J. Giménez, S. Esplugas, Performance and kinetic modelling of photolytic and photocatalytic ozonation for enhanced micropollutants removal in municipal wastewaters, Appl. Catal. B Environ., 249 (**2019**) 211-217.

[31] L.K. Limbach, R. Bereiter, E. Müller, R. Krebs, R. Gälli, W.J. Stark, Removal of oxide nanoparticles in a model wastewater treatment plant: Influence of agglomeration and surfactants on clearing efficiency, Environ. Sci. Technol., 42 (**2008**) 5828-5833.

[32] A.Y. Shan, T.I.M. Ghazi, S.A. Rashid, Immobilisation of titanium dioxide onto supporting materials in heterogeneous photocatalysis: A review. Appl. Catal. A: Gen., 389 (**2010**) 1–8.

[33] R. Krakowiak, R. Frankowski, K. Mylkie, D.T. Mlynarczyk, M. Ziegler-Borowska, A. Zgoła-Grześkowiak, T. Goslinski, TiO_2–Fe_3O_4 composite systems. Preparation, physicochemical characterization, and an attempt to explain the limitations that arise in catalytic applications. Appl. Sci., 12 (**2022**) 8826.

[34] S. Sultana, A. Amirbahman, C.P. Tripp, A method to produce robust magnetic particles coated with TiO_2 nanoparticulates, Appl. Catal. B Environ., 273 (**2020**) 118935.

[35] P.M. Álvarez, J. Jaramillo, F. López-Piñero, P.K. Plucinski, Preparation and characterization of magnetic TiO_2 nanoparticles and their utilization for the degradation of emerging pollutants in water, Appl. Catal. B Environ. 100 (**2010**) 338-345.

[36] D. H. Quiñones, A, Rey, A.; P.M. Álvarez, F.J. Beltrán, P.K. Plucinski. Enhanced Activity and Reusability of TiO_2 Loaded Magnetic Activated Carbon for Solar Photocatalytic Ozonation. Appl. Catal. B Environ. 144 (**2014**) 96–106.

CHAPTER 1

INTRODUCTION AND OBJECTIVES

1.1 WATER REUSE: THE ISSUE OF CONTAMINANTS OF EMERGING CONCERN

Water is essential for life on the planet Earth. Although water covers about 70% of our planet, the available water resources for direct human use are not unlimited. Only 2.5% of the water in the planet is freshwater while the remaining 97.5% is saline water found in oceans, seas, lakes and as saline groundwater. Of the freshwater, only 2.5%, mainly belonging to surface water, is available and suitable for human activities (e.g., agriculture, industrial and domestic uses). In a scenario of fast growth of the worldwide population (8 billion people in November 2022) water scarcity is an increasing problem on every continent.

Wastewater reuse reveals itself as one of the measures to alleviate the water crisis following the circular economy principles. In Europe, medium and large wastewater treatment plants (WWTPs) were designed in the last century following Directive 91/271/EEC. Accordingly, physical/chemical and biological methods were adopted to remove particulate and biodegradable mater from wastewater before releasing it to the environment. The treatment sequence in WWTPs usually comprises pre-treatment, primary and secondary treatment. The pre-treatment aims at removing big objects, sand and grease that could otherwise harm any downstream equipment. Subsequently, the primary treatment is applied to allow the physical separation of suspended solids by different physical treatments such as coagulation-flocculation and decantation/flotation. Finally, the secondary treatment is a biological process in which a bacteria consortium (either aerobic or anaerobic) is capable of decomposing soluble and particulate organic matter, reducing carbon, nitrogen and phosphorous content of the wastewater [1]. However, if reclaimed water is required the WWTP must be equipped with advanced treatment (i.e., tertiary treatment) to further purify the effluent for any kind of reuse application [2–4]. For this purpose, different tertiary treatment technologies should be considered, including nitrogen and

phosphorous removal, chemical oxidation, adsorption and membrane separation processes and disinfection [3].

One of the most concerning aspects regarding wastewater reclamation is related to the presence in WWTP effluents of a vast number of refractory synthetic organic products of anthropogenic origin (e.g., pharmaceuticals, personal care products, pesticides, industrial additives, nanomaterials, microplastics, surfactants, etc.) that are used exponentially and on a global scale. Many of these substances fall into the category known as contaminants of emerging concern or simply emerging contaminants (ECs). They have been identified as being a potential human health and environmental risk. They are not properly degraded by primary and secondary treatment methods applied at WWTPs [2,3]. Currently, the Spanish legislation on water reuse (RD 1620/2007) does not contemplate the problem of ECs in the reuse of treated wastewater. There, only some biological and physicochemical quality parameters are considered (e.g., eggs from intestinal nematodes and *Escherichia coli*, suspended solids, turbidity, total nitrogen and total phosphorous). It is clear that these criteria should be upgraded to tackle the adverse effect of ECs. Then, WWTPs are called to adopt new treatment methods to efficiently remove ECs thus avoiding any further risk with reclaimed water [5,6].

There are discrepancies regarding the problems for public health and the natural environment generated by the presence of ECs in natural waters, mainly because the low concentration (typically at ng L^{-1} level) does not cause apparent effects in the short term. However, numerous toxicological studies have already demonstrated the ability of many ECs to alter the endocrine system, which is known as endocrine disrupting effect. Therefore, due to their continuous release to the environment, ECs represent a danger to most of the life cycles of living organisms, from fauna to flora [7]. Consequently, new management strategies are needed to safely remove ECs from wastewater, even if reclaimed water is not required.

The issue of micropollutants in surface water has prompted the European Union (EU) to a more stringent regulation regarding substances of concern due to their persistence, toxicity, bioaccumulation and widespread use and occurrence in water. Thus, the Directive 2013/39/EU extended the list of priority pollutants to 45 substances, including a more restrictive revision of the maximum concentration thresholds established in the environmental quality standards (EQS). This EU directive was adopted by Spain through the RD 817/2015. Later, in 2015, the Decision 2015/495/EU established a first watch list of 10 substances for Union-wide monitoring in the field of water policy. These compounds were considered as those that best met the definition of EC. The watch list has been periodically revised to update the list of substances of concern.

The strategy established in the Directive 2008/105/EC is to gain knowledge on the occurrence and effects of the substances of the watching list through exhaustive scientific studies. Then it is decided whether or not to include them in the list of priority pollutants. Loos et al. [8] wrote a report with the results obtained from the first year of monitoring the substances included in the watch list, evaluating the concentrations and toxicity to know the actual risk of each one of them. Based on this study, an update of the watch list was made (Decision 2018/840/EU), establishing a new list of 8 substances for observation. In addition, an update in 2020 (Decision (UE) 2020/1161) and another in 2022 (Decision (UE) 2022/1307), have greatly increased the number of substances to be monitored, while eliminating others for which sufficient information was available already.

1.2 ADVANCED OXIDATION PROCESSES (AOPs) FOR THE REMOVAL OF POLLUTANTS IN AQUEOUS MEDIA

To solve the problems addressed above concerning priority, emerging and other micropollutants, it is essential to apply tertiary treatments in WWTPs to obtain an effluent that is environmentally friendly and/or can be safely reused [9–11]. In general, tertiary treatments aimed at the removal of micropollutants include membrane, adsorption on solid materials and chemical oxidation technologies. The first two options do not degrade the pollutants but transfer them from the aqueous matrix to a solid phase (i.e., adsorbent or membrane) and/or a concentrated liquid phase (i.e., retentate), so the problem remains until an effective treatment of the solid and/or retentate is carried out. Chemical oxidation, on the other hand, can completely remove microcontaminants transforming them into harmless products.

Among the chemical oxidation methods, advanced oxidation processes (AOPs) can be highlighted. These processes involve the generation of powerful and relatively non-selective transient oxidizing species. These include primarily the hydroxyl radical ($HO^{\bullet}$) and other reactive oxygen species (ROS) such as $^1O_2$, $HO_2^{\bullet}$, $O_2^{\bullet-}$ and $O_3^{\bullet-}$.

ROS react non-selectively with the organic and inorganic compounds present in the aqueous matrix [12]. The hydroxyl radical has a high electrochemical oxidation potential (2.85 eV) showing high reactivities with most of the aqueous organic micropollutants (rate constants ranged in 10^7-10^{10} M^{-1} s^{-1}) [12].

Broadly speaking, AOPs can be classified according to the mechanism of ROS generation. **Table 1.1** gives a list of the main types of AOPs [13,14].

Table 1.1. Advanced Oxidation Processes (AOPs).

Homogeneous processes		
No energy input	• O_3 • O_3 /H_2 O_2 • Homogeneous Fenton: H_2 O_2 /Fe^{2+} • Homogeneous catalytic ozonation: O_3/Catalyst • Persulfate	
With energy supply	UV-vis radiation	• Photolytic ozonation: O_3/UV-vis • Photocatalytic ozonation: O_3/UV-vis/Catalyst in solution • Photo-Fenton, H_2 O_2 /UV-vis/Catalyst in solution • Ozone, hydrogen peroxide and radiation, O_3 /H_2 O_2 /UV-vis • Hydrogen peroxide and radiation, H_2 O_2 /UV-vis
	Electrochemical methods	• Electrochemical oxidation • Anodic oxidation • Electro-Fenton
	Others	• Ionizing radiation-based methods • Microwave-based methods • Wet air oxidation and supercritical oxidation • Sonochemical methods
Heterogeneous processes		
Heterogeneous photocatalysis • Heterogeneous catalytic ozonation • Heterogeneous photocatalytic ozonation • Heterogeneous photo-Fenton • Heterogeneous Fenton		

Figure 1.1 shows the results of a search made in the SCOPUS database under the criterion "advanced oxidation processes". It can be seen an exponential increase in the number of published documents (articles, books, book chapters and conference papers) with over 30,000 accumulated in the last 30 years. This reveals the growing interest of the scientific community in classical and novel AOPs.

However, implementation of AOPs at industrial scale is still mostly limited O_3, O_3/H_2O_2 and O_3/UV processes.

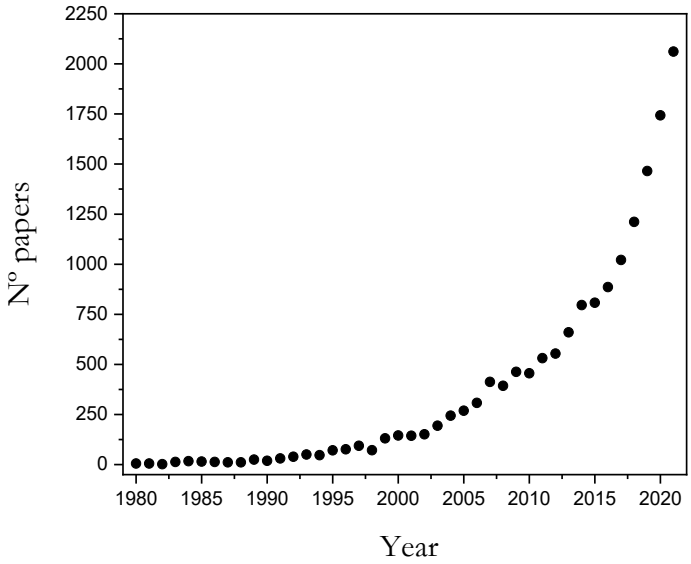

Figure 1.1. Result of a search with the database Scopus under the search criterion "advanced oxidation processes".

In short, despite the potential of AOPs and the numerous scientific papers published so far, further studies are still needed to better understand the reaction mechanisms, the effect of the aqueous matrix, the accumulation of reaction by-

products of adverse effects, etc. Moreover, photocatalytic AOPs still have considerable room for improvement through the use of cheap light sources (e.g. solar radiation, LEDs) and the synthesis of new photoactive catalysts with improved properties [15]. In this Thesis the following AOPs have been investigated: heterogeneous photocatalysis, ozonation, photolytic ozonation, photocatalytic ozonation, Fenton, photo-Fenton and photocatalytic oxidation with persulfate.

1.2.1 Heterogeneous photocatalysis

The heterogeneous photocatalysis process comprises a set of chemical reactions induced by the photo-excitation of a solid semiconductor used as catalyst (e.g. TiO_2, CdS, ZnO, etc.).

Figure 1.2 depicts an illustration of the photocatalysis phenomenon on a semiconductor material.

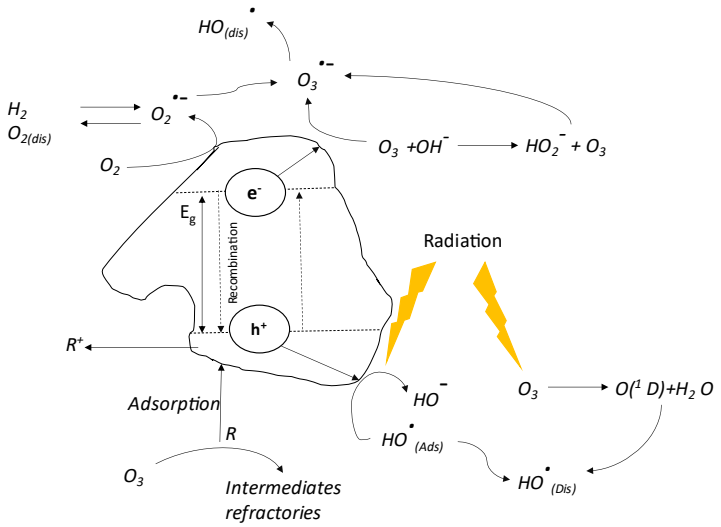

Figure 1.2. Energy band diagram and electron/hole

The photocatalytic process begins when the photocatalyst absorbs a photon with energy higher than the band gap energy of the semiconductor, producing the excitation of an electron from the valence band (VB) to the conduction band (CB) (**Figure 1.2.a**). This generates an electron-hole pair capable of migrating toward the surface of the catalyst, where oxidation-reduction reactions can take place (**Figure 1.2.b).** In the case of titanium dioxide as photocatalyst, equation (1.1) represents the electron-hole formation:

$$TiO_2 + hv \rightarrow TiO_2\ (e^-, h^+) \quad (1.1)$$

The excitation of the semiconductor can take place not only directly (by absorbing the photons that reach its surface), but also through the initial excitation of molecules adsorbed on the surface of the catalyst which, in turn, are capable of injecting charges (electrons) into the semiconductor.

The holes generated in the valence layer are powerful oxidants (oxidation potential of 2.53 V), capable of reacting with electron-giving substances. Thus, they can react directly with a pollutant B adsorbed on the catalyst through reaction (1.2), or with water or hydroxide anions, depending on the pH of the medium, generating $HO^{\bullet}$ according to reactions (1.3) and (1.4):

$$B_{ad} + h^+ \longrightarrow B_{ad}^{\bullet +} \quad (1.2)$$

$$H_2O_{ad} + h^+ \longrightarrow HO_{ad}^{\bullet} + H^+ \quad (1.3)$$

$$HO_{ad}^- + h^+ \longrightarrow HO_{ad}^{\bullet} \quad (1.4)$$

On the other hand, the electrons present in the conduction band are reducing species (+0.5 to -1.5 V) than can be taken by electron acceptor compounds such as oxygen, present in the medium when the process takes place under aerobic conditions. In this way, oxygen acts as an electron acceptor, generating the

superoxide free radical ((1.5)) which, depending on the pH and according to the equilibrium (1.6), can be found in its protonated form (hydroperoxide free radical). The presence of electron acceptors prevents ineffective recombination of the electron-hole pair, thus increasing the effectiveness of the photocatalytic process.

$$O_2 + e^- \xrightarrow{1{,}8\times10^{10}M^{-1}s^{-1}} O_2^{\bullet-} \quad (1.5)$$

$$O_2^{\bullet-} + H^+ \rightleftarrows HO_2^{\bullet} \qquad (pK_a = 4{,}8) \quad (1.6)$$

On the other hand, the recombination of hydroperoxide or superoxide radicals generates hydrogen peroxide through (1.7) and (1.8), respectively. In turn, hydrogen peroxide can lead to the formation of hydroxyl radical, either by acting as an electron acceptor through reaction (1.9) or through its reaction with the superoxide/hydroperoxide radical (1.10). In addition, hydrogen peroxide can react with hydroxyl radical via (1.11), regenerating the $O_2^{\bullet-}$ /$HO_2^{\bullet}$ pair.

$$HO_2^{\bullet} + HO_2^{\bullet} \xrightarrow{8{,}3x10^{5}M^{-1}s^{-1}} H_2O_2 + O_2 \quad (1.7)$$

$$O_2^{\bullet-} + O_2^{\bullet-} + 2H^+ \xrightarrow{9{,}7x10^{7}M^{-1}s^{-1}} H_2O_2 + O_2 \quad (1.8)$$

$$H_2O_2 + e^- \longrightarrow HO^{\bullet} + HO^- \quad (1.9)$$

$$HO_2^{\bullet}(o\ O_2^{\bullet-}) + H_2O_2 \longrightarrow O_2 + H_2O(o\ OH^-) + HO^{\bullet} \quad (1.10)$$

$$H_2O_2 + HO^{\bullet} \xrightarrow{2{,}7\times10^{7}M^{-1}s^{-1}} O_2^{\bullet-} + H^+ \quad (1.11)$$

In summary, a series of ROS with the ability to oxidize aqueous micropollutants are generated in the photocatalytic oxidation process.

1.2.2 Single, photolytic and photocatalytic ozonation

a) Single ozonation

Ozone is an allotropic form of oxygen that has a high redox potential (1.07 V). In drinking water treatment, it is currently used as a disinfectant to kill bacteria and viruses; as an oxidant to remove natural organic matter and micropollutants; and as aid of coagulation-flocculation process [16]. Also, it is recommended to be used as pre-treatment of refractory wastewater as it increases the biodegradability of recalcitrant compounds by oxidizing them and converting them into other molecules of easy biodegradation [17].

As an oxidant, ozone can be defined as a selective reactant because it preferentially attacks some organic moieties as unsaturated bonds or aromatic rings while the reactivity towards aldehyde or carboxylic acid functional groups is much slower as shown in **Table 1.2** [18,19].

Table 1.2. Reactivity of ozone towards different functional groups

Functional groups	Reactivity
$-OH^-$,$-O^-$,$-NH_2$, -NHR, $-NR_2$, $-NO_2$, $-NR_3^+$	High
-OR, -NHCOR, -C≡N, -CHO, -COOH	Media
$-C_6H_5$, -alkyl, -F, -Cl, -Br, -I	Low

Apart from the direct reaction with organic compounds, ozone can decompose in water and generate $HO^{\bullet}$ and other ROS, which reacts fast with most of organic functional groups. The reaction mechanism of ozone decomposition in water is shown in **Table 1.3** [19]. As it can be seen, the initiation of ozone decomposition to give $HO^{\bullet}$ is favored by the presence of the OH^{-}, so pH is a key parameter in the efficiency of ozone reactions in water to degrade aqueous pollutants [19].

Table 1.3. Decomposition mechanisms of ozone in pure water.

Reaction	Reaction constant	Reaction Nº
Initiation reaction		
$O_3 + OH^- \xrightarrow{k} HO_2^\bullet + O_2^{-\bullet}$	70 M^{-1} s^{-1}	(1.12)
Propagation reactions		
$HO_2^\bullet \xrightarrow{k2} H^+ + O_2^{-\bullet}$	7.9x10^{-5} M^{-1} s^{-1}	(1.13)
$O_2^{-\bullet} + H^+ \xrightarrow{k3} HO_2^\bullet$	5.0x10^{10} M^{-1} s^{-1}	(1.14)
$O_3 + O_2^{-\bullet} \xrightarrow{k4} O_3^{-\bullet} + O_2$	1.6x10^{9} M^{-1} s^{-1}	(1.16)
$O_3^{-\bullet} + H^+ \xrightarrow{k5} HO_3^\bullet$	5.2x10^{10} M^{-1} s^{-1}	(1.17)
$HO_3^\bullet \xrightarrow{k6} O_3^{-\bullet} + H^+$	3,3x10^{2} M^{-1} s^{-1}	(1.18)
$HO_3^\bullet \xrightarrow{k7} HO^\bullet + O_2$	1.1x10^{5} M^{-1} s^{-1}	(1.19)
$O_3 + HO^\bullet \xrightarrow{k8} HO_4^\bullet$	2.0x10^{9} M^{-1} s^{-1}	(1.20)
$HO_4^\bullet \xrightarrow{k9} HO_2^\bullet + O_2$	2.8x10^{4} M^{-1} s^{-1}	(1.21)
Termination reactions		
$HO_4^\bullet + HO_4^\bullet \xrightarrow{k10} H_2O_2^\bullet + 2O_3$	5x10^{9} M^{-1} s^{-1}	(1.22)
$HO_4^\bullet + HO_3^\bullet \xrightarrow{k11} H_2O_2^\bullet + O_2 + O_3$	5x10^{9} M^{-1} s^{-1}	(1.23)

b) Photolytic ozonation

Processes involving ozone and UV-vis radiation, referred to as photolytic ozonation processes, are also widely studied [20]. It has been shown that the UV/O_3 AOP highly increase the $HO^\bullet$ formation rate compared to O_3 alone. As a result, the mineralization of aqueous pollutants is improved by the presence of UV radiation [21,22]. Both aqueous pH and the radiation wavelength are parameters influencing the O_3/UV efficiency. High pH and radiation of

wavelength lower than 310 nm (UVC and UVB) favor ozone decomposition according to:

$$O_3 \xrightarrow{h\nu\ (\lambda \leq 310nm)} O_2 + O(\,^1D) \tag{1.24}$$

$$O(\,^1D) + H_2O \longrightarrow 2HO^{\bullet} \tag{1.25}$$

The species O(^{1} D) corresponds to atomic oxygen in an excited state, which not only reacts with water but also has high reactivity with most organic compounds [19].

Although ozone decomposes preferentially under UVB and UVC radiation, UVA-vis radiation has been proven also useful for ozone decomposition into H_2O_2 and other ROS [22].

c) Photocatalytic ozonation

The combined use of ozone, radiation and a photocatalyst constitutes an AOP called photocatalytic ozonation. In addition to the direct ozone reactions and its decomposition into ROS initiated by OH^- and radiation, ozone can also act as an electron acceptor on the surface of the photocatalyst, thus preventing electron-hole recombination.

Ozone captures the electron of the catalyst and gives rise to the formation of the ozonide free radical ($O_3^{\bullet -}$) which can be further transformed into $HO^{\bullet}$ (equations (1.26) and (1.27)). Consequently, it drastically increases the production of $HO^{\bullet}$ compared to photocatalysis or photolytic ozonation, leading to an enhanced degradation of aqueous pollutants, especially those refractories to O_3.

$$O_{3(ad)} + e^- \longrightarrow O_3^{\bullet -} \tag{1.26}$$

$$O_3^{\bullet -} + H^+ \longrightarrow HO_3^{\bullet} \longrightarrow HO^{\bullet} + O_2 \tag{1.27}$$

Figure 1.3 shows a scheme of the heterogeneous photocatalytic ozonation process.

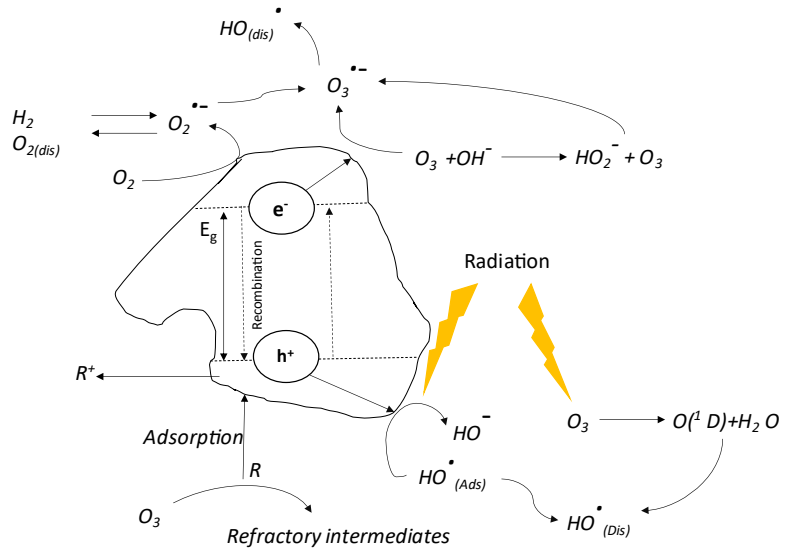

Figure 1.3. Photochemical reactions during the photocatalytic ozonation process.

1.2.3 Fenton and photo-Fenton AOPs

a) Fenton AOP

The AOP known as "Fenton" was first described in 1894 by Henry J. Fenton, who discovered that H_2O_2 could be activated with ferrous ions to oxidize tartaric acid [23]. The process involves the decomposition of H_2O_2 in the presence of Fe(II) salts with formation of $HO^{\bullet}$. This process is favored at low pH (i.e., around 3). The main reactions of the Fenton mechanism are given by equations (1.28) and (1.29) [23–26]. The regeneration reaction (1.29) is considered to be the limiting step of the process.

$$Fe^{2+} + H_2O_2 \longrightarrow Fe^{3+} + OH^- + OH^{\bullet} \quad (1.28)$$

$$Fe^{3+} + H_2O_2 \longrightarrow Fe^{2+} + H^+ + HO_2^{\bullet} \quad (1.29)$$

It is important to consider a series of HO• consuming reactions in the process (**Table 1.4**), which has a negative impact on the efficiency of the treatment (reactions (1.30) to (1.33)). To avoid as much as possible these undesirable reactions, dosage of H_2O_2 at optimum conditions is required.

Table 1.4. HO• consumption reactions in Fenton process.

$H_2O_2 + OH^{\bullet} \longrightarrow OH_2^{\bullet} + H_2O$	(1.30)
$Fe^{2+} + OH^{\bullet} \longrightarrow Fe^{3+} + OH^-$	(1.31)
$OH^{\bullet} + OH^{\bullet} \longrightarrow H_2O_2$	(1.32)
$OH^{\bullet} + OH_2^{\bullet} \longrightarrow H_2O + O_2$	(1.33)

Iron can be added to the process in its ferrous (Fe^{2+}) or ferric (Fe^{3+}) sate forms. For the latter, the process is known as "Fenton-like", Although, Fe(II) salts are more expensive than Fe(III) salts, the first are typically the preferred choice as they lead to a faster generation of HO• [24,25].

b) Photo-Fenton AOP

When the Fenton process is combined with UV-vis radiation, the process becomes known as photo-Fenton and significantly increases its efficiency [24].

This is due to reaction (1.34), which accelerates the regeneration of Fe^{2+} and it is an additional pathway for the production of HO• [23].

$$Fe^{3+} + H_2O + hv \longrightarrow Fe^{2+} + H^+ + HO^\bullet \quad (1.34)$$

This is explained by the formation of aqueous Fe^{3+} complexes [$Fe(OH)^{2+}$] at acidic pH, capable of absorbing UV and visible radiation, undergoing photo-reduction and producing HO• [23,27,28].

Fenton and photo-Fenton AOPs can also be carried out using copper or cobalt ions as well as iron oxides as heterogenous catalysts [29–32].

1.2.4 Monopersulfate-driven AOPs

Persulfate is another strong oxidant useful for the degradation of aqueous pollutants given its high oxidation potential of 2.12 V [33,34].

$$S_2O_8^{-2} + 2H^+ + 2e^- \longrightarrow 2HSO_4^- \quad (1.35)$$

However, the persulfate anion has slow oxidative kinetics at room temperature for most pollutants, being only effective against a limited number of organic compounds [34]. The decomposition of persulfate into persulfate free radical is generally accelerated under certain conditions (i.e, heat and high pH) or in the presence of reagents (e.g., H_2O_2) and/or catalysts (e,g, some Fe-containing catalysts) [33–35].

$$S_2O_8^{-2} + \text{activator} \longrightarrow SO_4^{\bullet -} + (SO_4^{\bullet -} \text{ o } SO_4^{-2}) \quad (1.36)$$

Under acidic conditions, the persulfate anion can undergo hydrolysis to form hydrogen peroxide:

$$S_2O_8^{-2} + 2H_2O \longrightarrow H_2O_2 + 2HSO_4^- \quad (1.37)$$

Under strong acidic conditions, persulfate can form peroxymonopersulfate anions, with an oxidation potential of 1.44 V. As a result, persulfate solutions can contain several different oxidant species [36].

$$S_2O_8^{-2} + 2H_2O \longrightarrow HSO_5^- + HSO_4^- \quad (1.38)$$

A positive consequence of this mixture of oxidant species is that multiple pathways may exist for pollutant oxidation, which increases the likelihood of reducing pollutant concentrations [33,35].

1.3 CATALYSTS

Next, some relevant aspects of the AOP catalysts used in this work as well as some alternatives for their improvement are discussed.

1.3.1 TiO_2-P25

Today, TiO_2-P25 is considered a benchmark photocatalyst for photocatalytic oxidation processes of pollutants in water, due to its high photocatalytic activity in the presence of UV radiation, stability, no toxicity and expensiveness [37–39]. This semiconductor is typically used as suspended nanoparticles (NPs) to maximize the surface area exposed to radiation.

Figure 1.4. TiO_2-P25 powder (Evonik).

The best-known and most widely used material is Aeroxide TiO_2- P25 (Evonik Industries), consisting of 20% rutile and 80% anatase with a specific surface area of 50 m^2 g^{-1} and an average crystalline particle size of 20 to 40 nm [40]. It has been widely demonstrated that it is one of the most active materials in photocatalysis reactions in aqueous media for the degradation of pollutants using UV radiation sources [41–43]. It has also been proven quite effective in photocatalytic ozonation processes, greatly improving the mineralization of pollutants compared to simple ozonation [44,45].

Despite all, TiO_2-P25 NPs have several drawbacks such as i) large band gap energy (3.2 eV), which makes that the photocatalyst is excited only by UV radiation, ii) fast recombination of the pair e^-/h^+, greatly decreasing its kinetic efficiency and iii) difficult separation from the reaction medium due to the low particle size.

Given these limitations, efforts are being made to develop photocatalyst with improved properties over TiO_2-P25. As main lines of research the following can

be cited: alternative photocatalysts (other than TiO_2), hybrid materials (e.g, heterojunction composites), use of metal and non-metal doping agents, and immobilization/magnetization of catalysts.

1.3.2 MOFs as alternative photocatalysts

A relatively recent field of study in catalysis is the synthesis of metal-organic frameworks (MOFs) as photocatalysts. These types of materials have aroused great interest in the scientific community due to their potential applications in various areas such as chemical synthesis, energy production and storage or decontamination processes. Proof of the enormous current interest in MOFs is the number of scientific papers recently published about these structures. Thus, a search in the Scopus database under the term "MOF" yields more than 30,000 documents in the last 6 years.

These MOF structures constitute a new class of materials that has generated great expectations among researchers and technological companies. They are crystalline, porous materials with a high specific surface area that combine in the same structure metal centers (metal ions or clusters) that act as nodes, and organic ligands that act as bridges between nodes, thus generating structures that extend in space in several dimensions. As an example, **Figure 1.5** shows the structure of MIL-53, which represents one of the most studied compounds of the family of MOFs called MIL (Materiaux de l'Institut Lavoisier) based on trivalent cations and aromatic carboxylic acids [46,47].

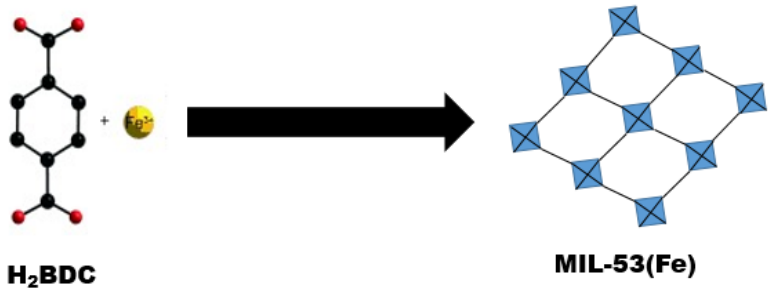

Figure 1.5. Structure of MIL-53(Fe) from the organic ligand 1,4-BDC (1,4-benzene dicarboxylic acid) and Fe^{3+}.

The combination of organic and inorganic units in MOFs offers a myriad of structural possibilities to obtain materials with predefined properties that make them useful for specific applications [48–51]. Some of the most outstanding applications so far include gas storage and separation (e.g. CO_2 capture, CH_4 and H_2 storage [52]), applications in electronics (e.g., photovoltaic cells [53]) or in heterogeneous catalysis (e.g., tandem reactions [54]). One of the advantages of using MOFs as heterogeneous catalysts is their high porosity which allows easy diffusion of reagents and products through the pores so that a larger number of active centers are accessible. On the other hand, the hybrid nature of MOFs allows the incorporation of active sites in the metal centers and the organic ligands. The use of different MOFs in photocatalytic processes has been proposed, given their capacity to absorb UV-visible radiation and carry out different photochemical processes such as water splitting [55], reduction of CO_2 to organic compounds of interest [56,57] or the photocatalytic oxidation of water and air pollutants [58–60].

In the present work, MIL-53(Fe) was synthesized and studied as solar photocatalyst for the degradation of organic pollutants in water. Previous research studies have shown this MOF as promising for this purpose [61–64]. As with most MOFs, however, there is a lack of studies on the stability of MIL-53(Fe) under the strongly oxidizing conditions generated in photocatalytic processes.

1.3.3 Composite catalysts

Many studies on the use of structures combining various materials (i.e., composite materials) as photocatalyst have demonstrated their improved properties. In particular, extending the light absorption spectrum, preventing electron-hole recombination and facilitating the separation of the catalyst from the aqueous phase are typical aims of hybrid materials. Some of the hybrid materials recently studied for photocatalytic AOPs are combinations of TiO_2 with carbonaceous structures, such as graphene, graphene oxide (GO) or activated carbon (AC) [65]. Graphene is an allotropic form of carbon, which is usually produced by the exfoliation of graphite sheets by different methods [66,67]. It was discovered in 2004 by Russian researchers Andre Geim and Konstantin Novoselov. Among its most interesting characteristics are high mechanical strength and flexibility, high optical transmittance, high specific surface area (approximately 2630 $m^2 g^{-1}$) and high thermal conductivity (5000 $W m^{-1} K^{-1}$), but the most important is its high charge (electron) mobility at room temperature (200000 $cm^2 V^{-1} s^{-1}$) [68]. Quickly from its discovery, it aroused the interest of scientists for its potential use as photocatalyst. The idea is that graphene can prevent the recombination e^-/h^+ in semiconductors such as TiO_2 [65]. Research has also begun on the use of the oxidized form of graphene, GO, which is composed of carbon, oxygen and hydrogen in variable proportions. GO is obtained by the treatment of graphite with a strong oxidant. This material consists of only one or a few layers, being a very exfoliated material [69,70]. In combination with semiconductors, GO hybrid materials are promising as visible photocatalysts [71]. AC, a highly porous material has also been investigated in photochemical and non-photochemical AOPs [53]. Unlike graphene and graphene oxide, the use of activated carbon is widespread worldwide, and its cost is much lower [72,73].

In the composite catalysts, the inclusion of magnetic iron oxides (Fe_xO_y), especially magnetite (Fe_3O_4), in their structure is also of special relevance. The

presence of this iron oxide, besides providing magnetic properties to the solid may favor the AOP photocatalytic process through enhanced carrier transfer through the heterojuction preventing electron-hole recombination. Also, Fenton and photo-Fenton reactions can develop [74].

1.4 RESEARCH OBJECTIVES AND ORGANIZATION OF THIS THESIS

UV-vis photocatalytic detoxification of wastewater is one of the technology research areas of the Doctoral Program "Modelización y Experimentación en Ciencia y Tecnología" offered by the University of Extremadura. In line with this, the research group TRATAGUAS, coordinated by Professor Beltrán, has completed a project on the study of different catalysts for UV-vis photocatalytic AOPs (CTQ2015-64944-R). In 2017, I was granted by the Spanish Ministry of Education, Culture and Sports to join the TRATAGUAS group and carry out my Ph.D. on the subject of this project. Particularly, this Thesis focusses on powdered photocatalysts with magnetic properties to be used in slurry reactors. At the planning stage, the following areas and objectives of the research were identified:

Research area 1: Some MOFs were being investigated worldwide as promising heterogeneous UV-visible photocatalysts for the removal of water pollutants. Among them, Fe-based MOFs were particularly appealing as visible light responsive photocatalysts due to the existence of iron-oxo clusters. Moreover, some of these structures had been demonstrated to be effective heterogeneous photo-Fenton catalysts for the degradation of organic pollutants. However, the available literature lacked studies about stability under the AOP environment, separability and reusability of Fe-based MOFs.

Research objective 1: preparation and characterization of MIL-53 as a Fe-based MOF of potential use in solar photocatalytic oxidation.

Specific objectives of this area of research were:

1.1. Successfully synthetize and characterize MIL-53(Fe).

1.2. Evaluate the stability of MIL-53(Fe) in water: effect of pH, temperature and UV-vis radiation.

1.3. Study the effects of oxidants typically used in AOPs (hydrogen peroxide, ozone and persulfate) on the structure and properties of MIL-53(Fe).

1.4. Asses the photocatalytic activity of MIL-53(Fe) under solar radiation.

1.5. If promising results were obtained in the specific objectives 1.1 to 1.4, synthetize a magnetically recoverable MIL-53(Fe) composite to improve its reusability in solar AOPs.

Research area 2: A main concern about the use of some nanosized metal oxides (e.g., TiO_2) as photocatalyst in slurry reactors arises from their difficult separation from the aqueous media upon photoreaction completion. As a result, the photocatalyst reusability is poor and there is a risk of water contamination associated with nanoparticles. Magnetically recoverable photocatalysts offer a good solution to this limitation. However, most of the methods developed so far for the magnetization of nanoparticles involve the use of toxic solvents and/or reagents and high temperatures making the process unsuitable from economic and environmental points of view.

Research objective 2: develop a green method for the magnetization of various metals, metal oxides and carbonaceous materials through the formation of magnetite containing composites.

Specific objectives of this area of research were:

2.1. Study a green method for the magnetization of various inorganic solids based on the formation of magnetite composites by aerial oxidation of iron salts at low temperature.

2.2. Characterization of the magnetic materials synthesized with a focus on their saturation magnetization.

Research area 3: some magnetite-based catalysts (MBCs) have been proposed in the literature as catalysts for the degradation of organic pollutants by Fenton and photo-Fenton AOPs (i.e., catalytic wet peroxide oxidation, CWPO). Particularly, appealing are composite MBCs that contain carbonaceous materials, which provide high surface area for pollutant adsorption and may have improved photoresponse performance.

Research objective 3: preparation and characterization of magnetite-based carbonaceous materials as photocatalysts for solar wet peroxide oxidation (i.e., solar radiation/H_2O_2).

Specific objectives of this area of research were:

3.1. Following research objective 2, preparation and characterization of MBCs containing graphene (G), graphene oxide (GO) and activated carbon (AC).
3.2. Characterize the synthesized MBCs.
3.3. Evaluate the stability of the prepared MBCs in aqueous solution: effect of pH, radiation and presence of H_2O_2.
3.4. Study the photocatalytic activity of the obtained MBCs in CWPO processes both in the dark and in the presence of solar radiation.
3.5. Examine the reusability of MBCs in CWPO processes.

Research area 4: Commercial powdered titanium dioxide TiO_2-P25 is considered a benchmark photocatalyst for the degradation of aqueous pollutants under UV radiation. However, main drawbacks on the use of TiO_2-P25 in solar detoxification processes arise from the facts that (i) it is not a visible-light photocatalyst due to its wide band-gap (3.2 eV) and (ii) it is difficult to remove from water suspensions by coagulation or filtration methods. As mentioned above, this is a critical issue regarding the adverse impact associated with the release of nanomaterials to the environment. With the aim of overcoming the limitations of TiO_2-P25 for practical applications of solar AOPs, different approaches are being conducted worldwide to produce photocatalysts with

improved properties. Among them, the coupling of TiO_2 and Fe_3O_4 semiconductors to produce magnetically recoverable hybrid heterojunction structures (Fe_3O_4/TiO_2) can be highlighted.

Research objective 4: preparation and characterization of a Fe_3O_4@TiO_2-P25 composite with enhanced properties as photocatalyst for AOPs.

Specific objectives of this area of research were:

4.1. Following the research objective 2, preparation and characterization of a magnetically recoverable Fe_3O_4@TiO_2-P25 composite

4.2. Characterize the synthesized Fe_3O_4@TiO_2-P25 composite.

4.3. Evaluate the stability of the prepared Fe_3O_4@TiO_2-P25 composite in aqueous solution: effect of pH, radiation and presence of oxidants (e.g., H_2O_2 and O_3).

4.4. Study the photocatalytic activity of the obtained Fe_3O_4@TiO_2-P25 in solar photocatalytic oxidation and solar photocatalytic ozonation.

4.5. Examine the reusability of Fe_3O_4@TiO_2-P25 in solar photocatalytic AOPs.

The next chapters of this Thesis present the research efforts made to achieve the aforementioned objectives. Chapter 2 describes materials and methods for solids characterization and reaction monitoring. Chapters 3 to 6 are written in a self-containing manner so the reader can find the experimental work, results and discussion of each objective separately. Chapter 3 deals with the synthesis, stability and photoactivity of MIL-53(Fe). Chapter 4 aims to develop a green method for the magnetization of inorganic solids. Chapter 5 focuses on the performance of carbonaceous MBCs in CWPO processes. Finally, Chapter 6 covers the synthesis, characterization and performance in solar photocatalytic AOPs of a Fe_3O_4@TiO_2-P25 hybrid material.

References

[1] L. Chen, W. Fu, Y. Tan, X. Zhang, Emerging organic contaminants and odorous compounds in secondary effluent wastewater: Identification and advanced treatment, J. Hazard. Mater., 408 (**2021**) 124817.

[2] S. Gupta, Y. Mittal, R. Panja, K.B. Prajapati, A.K. Yadav, Conventional wastewater treatment technologies, Curr. Dev. Biotechnol. Bioeng., (**2021**) 47–75.

[3] P.R. Rout, T.C. Zhang, P. Bhunia, R.Y. Surampalli, Treatment technologies for emerging contaminants in wastewater treatment plants: A review, Sci. Total Environ., 753 (**2021**) 141990.

[4] J. Hollender, S.G. Zimmermann, S. Koepke, M. Krauss, C.S. Mcardell, C. Ort, H. Singer, U. Von Gunten, H. Siegrist, Elimination of organic micropollutants in a municipal wastewater treatment plant upgraded with a full-scale post-ozonation followed by sand filtration, Environ. Sci. Technol., 43 (**2009**) 7862–7869.

[5] K. Sharma, N. Sen Sarma, A. Devi, Paper mill effluents: identification of emerging pollutants in taranga beel of assam, India, (**2021**) 89–96.

[6] Y. Choi, J.H. Lee, K. Kim, H. Mun, N. Park, J. Jeon, Identification, quantification, and prioritization of new emerging pollutants in domestic and industrial effluents, Korea: Application of LC-HRMS based suspect and non-target screening, J. Hazard. Mater., 402 (**2021**) 123706.

[7] M. Gavrilescu, K. Demnerová, J. Aamand, S. Agathos, F. Fava, Emerging pollutants in the environment: present and future challenges in biomonitoring, ecological risks and bioremediation, N. Biotechnol., 32 (**2015**) 147–156.

[8] R. Loos, D. Marinov, I. Sanseverino, D. Napierska, T. Lettieri, Review of the 1 st watch list under the water framework directive and recommendations for the 2 nd watch list, JCR Tech. Reports., (**2018**).

[9] M.F. Hamoda, I. Al-Ghusain, N.Z. AL-Mutairi, Sand filtration of wastewater for

tertiary treatment and water reuse, Desalination., 164 (**2004**) 203–211.

[10] G. Tchobanoglous, J. Darby, K. Bourgeous, J. McArdle, P. Genest, M. Tylla, Ultrafiltration as an advanced tertiary treatment process for municipal wastewater, Desalination., 119 (**1998**) 315–321.

[11] A. Bernabeu, R.F. Vercher, L. Santos-Juanes, P.J. Simón, C. Lardín, M.A. Martínez, J.A. Vicente, R. González, C. Llosá, A. Arques, A.M. Amat, Solar photocatalysis as a tertiary treatment to remove emerging pollutants from wastewater treatment plant effluents, Catal. Today., 161 (**2011**) 235–240.

[12] W.H. Glaze, J.W. Kang, D.H. Chapin, The chemistry of water treatment processes involving ozone, hydrogen peroxide and ultraviolet radiation, 9 (**2008**) 335–352.

[13] M.A. Oturan, J.J. Aaron, Advanced oxidation processes in water/wastewater treatment: principles and applications. A Review, 44 (**2014**) 2577–2641.

[14] D.B. Miklos, C. Remy, M. Jekel, K.G. Linden, J.E. Drewes, U. Hübner, Evaluation of advanced oxidation processes for water and wastewater treatment – A critical review, Water Res., 139 (**2018**) 118–131.

[15] S. Pierucci, J.J. Klemeš, L. Piazza, S. Bakalis, V. Vaiano, O. Sacco, D. Sannino, G. Di Capua, N. Femia, Enhanced performances of a photocatalytic reactor for wastewater treatment using controlled modulation of LEDs light, Chem. Eng. Trans., 57 (**2017**).

[16] S.T. Oyama, Chemical and catalytic properties of ozone, 42 (**2007**) 279–322.

[17] J. Hoigné, Chemistry of aqueous ozone and transformation of pollutants by ozonation and advanced oxidation processes, (**1998**) 83–141.

[18] J.L. Sotelo, F.J. Beltran, F.J. Benitez, J. Beltran-Heredia, Ozone decomposition in water: kinetic study, Ind. Eng. Chem. Res., 26 (**1987**) 39–43.

[19] F. Beltran, Ozone reaction kinetics for water and wastewater systems, (**2003**).

[20] G.R. Peyton, W.H. Glaze, Mechanism of photolytic ozonation., Natl. Meet. - Am. Chem. Soc. Div. Environ. Chem., 25 (**1985**) 299–301.

[21] L. Sánchez, X. Domènech, J. Casado, J. Peral, Solar activated ozonation of phenol and malic acid, Chemosphere., 50 (**2003**) 1085–1093.

[22] A.M. Chávez, A. Rey, F.J. Beltrán, P.M. Álvarez, Solar photo-ozonation: A novel treatment method for the degradation of water pollutants, J. Hazard. Mater., 317 (**2016**) 36–43.

[23] J.J. Pignatello, E. Oliveros, A. MacKay, Advanced oxidation processes for organic contaminant destruction based on the fenton reaction and related chemistry, Crit. Rev. Environ. Sci. Technol., 36 (**2006**) 1–84.

[24] W. Gernjak, M. Fuerhacker, P. Fernández-Ibañez, J. Blanco, S. Malato, Solar photo-Fenton treatment - Process parameters and process control, Appl. Catal. B Environ., 64 (**2006**) 121–130.

[25] M. hui Zhang, H. Dong, L. Zhao, D. xi Wang, D. Meng, A review on Fenton process for organic wastewater treatment based on optimization perspective, Sci. Total Environ., 670 (**2019**) 110–121.

[26] E. Neyens, J. Baeyens, A review of classic Fenton's peroxidation as an advanced oxidation technique, J. Hazard. Mater., 98 (**2003**) 33–50.

[27] A.P.S. Batista, R.F.P. Nogueira, Parameters affecting sulfonamide photo-Fenton degradation - Iron complexation and substituent group, J. Photochem. Photobiol. A Chem., 232 (**2012**) 8–13.

[28] V. Kavitha, K. Palanivelu, The role of ferrous ion in Fenton and photo-Fenton processes for the degradation of phenol, Chemosphere., 55 (**2004**) 1235–1243.

[29] X. Liu, Y. Li, X. Fan, F. Zhang, G. Zhang, W. Peng, Photo-accelerated Co3+/Co2+transformation on cobalt and phosphorus co-doped g-C3N4for Fenton-like reaction, J. Mater. Chem. A., 9 (**2021**) 22399–22409.

[30] C. Wang, H. Liu, Z. Sun, Heterogeneous photo-Fenton reaction catalyzed by

nanosized iron oxides for water treatment, Int. J. Photoenergy., 2012 (**2012**).

[31] D.A. Nichela, A.M. Berkovic, M.R. Costante, M.P. Juliarena, F.S. García Einschlag, Nitrobenzene degradation in Fenton-like systems using Cu(II) as catalyst. Comparison between Cu(II)- and Fe(III)-based systems, Chem. Eng. J., 228 (**2013**) 1148–1157.

[32] G. Ghiselli, W.F. Jardim, M.I. Litter, H.D. Mansilla, Destruction of EDTA using Fenton and photo-Fenton-like reactions under UV-A irradiation, J. Photochem. Photobiol. A Chem., 167 (**2004**) 59–67.

[33] R.R. Solís, F.J. Rivas, M. Tierno, Monopersulfate photocatalysis under 365 nm radiation. Direct oxidation and monopersulfate promoted photocatalysis of the herbicide tembotrione, J. Environ. Manage., 181 (**2016**) 385–394.

[34] F.J. Rivas, Monopersulfate in water treatment: Kinetics, J. Hazard. Mater., 430 (**2022**) 128383.

[35] J.M. Dangwang Dikdim, Y. Gong, G.B. Noumi, J.M. Sieliechi, X. Zhao, N. Ma, M. Yang, J.B. Tchatchueng, Peroxymonosulfate improved photocatalytic degradation of atrazine by activated carbon/graphitic carbon nitride composite under visible light irradiation, Chemosphere., 217 (**2019**) 833–842.

[36] S. Wacławek, H. V. Lutze, K. Grübel, V.V.T. Padil, M. Černík, D.D. Dionysiou, Chemistry of persulfates in water and wastewater treatment: A review, Chem. Eng. J., 330 (**2017**) 44–62.

[37] I. García-Fernández, I. Fernández-Calderero, M. Inmaculada Polo-López, P. Fernández-Ibáñez, Disinfection of urban effluents using solar TiO_2 photocatalysis: A study of significance of dissolved oxygen, temperature, type of microorganism and water matrix, Catal. Today., 240 (**2015**) 30–38.

[38] E.M. Rodríguez, G. Márquez, M. Tena, P.M. Álvarez, F.J. Beltrán, Determination of main species involved in the first steps of TiO_2 photocatalytic degradation of organics with the use of scavengers: The case of ofloxacin, Appl. Catal. B Environ., 178 (**2014**) 44–53.

[39] A. Rey, E. Mena, A.M. Chávez, F.J. Beltrán, F. Medina, Influence of structural properties on the activity of WO_3 catalysts for visible light photocatalytic ozonation, Chem. Eng. Sci., 126 (**2015**) 80–90.

[40] M.A. Henderson, A surface science perspective on TiO_2 photocatalysis, Surf. Sci. Rep., 66 (**2011**) 185–297.

[41] J. Araña, J.A. Herrera Melián, J.M. Doña Rodríguez, O. González Díaz, A. Viera, J. Pérez Peña, P.M. Marrero Sosa, V. Espino Jiménez, TiO_2-photocatalysis as a tertiary treatment of naturally treated wastewater, Catal. Today., 76 (**2002**) 279–289.

[42] J. Chen, F. Qiu, W. Xu, S. Cao, H. Zhu, Recent progress in enhancing photocatalytic efficiency of TiO2-based materials, Appl. Catal. A Gen., 495 (**2015**) 131–140.

[43] C. Reyes, J. Fernández, J. Freer, M.A. Mondaca, C. Zaror, S. Malato, H.D. Mansilla, Degradation and inactivation of tetracycline by TiO_2 photocatalysis, J. Photochem. Photobiol. A Chem., 184 (**2006**) 141–146.

[44] E.M. Rodríguez, A. Rey, E. Mena, F.J. Beltrán, Application of solar photocatalytic ozonation in water treatment using supported TiO_2, Appl. Catal. B Environ., 254 (**2019**) 237–245.

[45] F.J. Beltrán, A. Aguinaco, A. Rey, J.F. García-Araya, Kinetic studies on black light photocatalytic ozonation of diclofenac and sulfamethoxazole in water, Ind. Eng. Chem. Res., 51 (**2012**) 4533–4544.

[46] G. Férey, Hybrid porous solids: Past, present, future, Chem. Soc. Rev., 37 (**2008**) 191–214.

[47] P. Horcajada, C. Serre, G. Maurin, N.A. Ramsahye, F. Balas, M. Vallet-Regí, M. Sebban, F. Taulelle, G. Férey, Flexible porous metal-organic frameworks for a controlled drug delivery, J. Am. Chem. Soc., 130 (**2008**) 6774–6780.

[48] M. Feng, P. Zhang, H.C. Zhou, V.K. Sharma, Water-stable metal-organic

frameworks for aqueous removal of heavy metals and radionuclides: A review, Chemosphere., 209 (**2018**) 783–800.

[49] Y. Fang, Y. Ma, M. Zheng, P. Yang, A.M. Asiri, X. Wang, Metal–organic frameworks for solar energy conversion by photoredox catalysis, Coord. Chem. Rev., 373 (**2018**) 83–115.

[50] C.C. Wang, X.H. Yi, P. Wang, Powerful combination of MOFs and C_3N_4 for enhanced photocatalytic performance, Appl. Catal. B Environ., 247 (**2019**) 24–48.

[51] W. Zhan, L. Sun, X. Han, Recent progress on engineering highly efficient porous semiconductor photocatalysts derived from metal–organic frameworks, Nano-Micro Lett., 11 (**2019**).

[52] G. Orcajo, H. Montes-Andrés, J.A. Villajos, C. Martos, J.A. Botas, G. Calleja, Li-Crown ether complex inclusion in MOF materials for enhanced H_2 volumetric storage capacity at room temperature, Int. J. Hydrogen Energy., 44 (**2019**) 19285–19293.

[53] C.-C. Lee, C.-I. Chen, Y.-T. Liao, K.C.-W. Wu, C.-C. Chueh, Enhancing efficiency and stability of photovoltaic cells by using perovskite/Zr-MOF heterojunction including bilayer and hybrid structures, Adv. Sci., 6 (**2019**) 1801715.

[54] X. Liao, W. Wei, Y. Zhou, M. Zhang, Y. Cai, H. Liu, Y. Yao, S. Lu, Q. Hao, A Ti-based bi-MOF for the tandem reaction of H2O2 generation and catalytic oxidative desulfurization, Catal. Sci. Technol., 10 (**2020**) 1015–1022.

[55] K. Meyer, S. Bashir, J. Llorca, H. Idriss, M. Ranocchiari, J.A. van Bokhoven, Photocatalyzed hydrogen evolution from water by a composite catalyst of NH_2-MIL-125(Ti) and Surface Nickel(II) Species, Chem. - A Eur. J., 22 (**2016**) 13894–13899.

[56] C. Liu, W. Wang, B. Liu, J. Qiao, L. Lv, X. Gao, X. Zhang, D. Xu, W. Liu, J. Liu, Y. Jiang, Z. Wang, L. Wu, F. Wang, Recent advances in MOF-based nanocatalysts

for photo-promoted CO_2 Reduction Applications, Catal., 9 (**2019**) 658.

[57] X.-J. Kong, T. He, J. Zhou, C. Zhao, T.-C. Li, X.-Q. Wu, K. Wang, J.-R. Li, X. Kong, T. He, J. Zhou, C. Zhao, T. Li, X. Wu, K. Wang, J. Li, In situ porphyrin substitution in a Zr(IV)-MOF for stability enhancement and photocatalytic CO_2 Reduction, Small., 17 (**2021**) 2005357.

[58] S. Abdpour, E. Kowsari, M.R.A. Moghaddam, Synthesis of MIL-100(Fe)@MIL-53(Fe) as a novel hybrid photocatalyst and evaluation photocatalytic and photoelectrochemical performance under visible light irradiation, J. Solid State Chem., 262 (**2018**) 172–180.

[59] C.M. Navarathna, N.B. Dewage, A.G. Karunanayake, E.L. Farmer, F. Perez, E.B. Hassan, T.E. Mlsna, C.U. Pittman, Rhodamine B Adsorptive Removal and Photocatalytic Degradation on MIL-53-Fe MOF/Magnetic Magnetite/Biochar Composites, J. Inorg. Organomet. Polym. Mater., 30 (**2020**) 214–229.

[60] R. Liang, F. Jing, L. Shen, N. Qin, L. Wu, MIL-53(Fe) as a highly efficient bifunctional photocatalyst for the simultaneous reduction of Cr(VI) and oxidation of dyes, J. Hazard. Mater., 287 (**2015**) 364–372.

[61] Y. Zhang, G. Li, H. Lu, Q. Lv, Z. Sun, Synthesis, characterization and photocatalytic properties of MIL-53(Fe)-graphene hybrid materials, RSC Adv., 4 (**2014**) 7594–7600..

[62] C. Zhang, L. Ai, J. Jiang, Solvothermal synthesis of MIL-53(Fe) hybrid magnetic composites for photoelectrochemical water oxidation and organic pollutant photodegradation under visible light, J. Mater. Chem. A., 3 (**2015**) 3074–3081.

[63] C. Zhang, L. Ai, J. Jiang, Solvothermal synthesis of MIL-53(Fe) hybrid magnetic composites for photoelectrochemical water oxidation and organic pollutant photodegradation under visible light, J. Mater. Chem. A. , 3 (**2015**) 3074–3081.

[64] J.J. Du, Y.P. Yuan, J.X. Sun, F.M. Peng, X. Jiang, L.G. Qiu, A.J. Xie, Y.H. Shen, J.F. Zhu, New photocatalysts based on MIL-53 metal-organic frameworks for the decolorization of methylene blue dye, J. Hazard. Mater., 190 (**2011**) 945–951.

[65] F.J. Beltrán, M. Checa, Comparison of graphene oxide titania catalysts for their use in photocatalytic ozonation of water contaminants: Application to oxalic acid removal, Chem. Eng. J. , 385 (**2020**) 123922.

[66] A. Islam, B. Mukherjee, K.K. Pandey, A.K. Keshri, Ultra-Fast, Chemical-free, mass production of high quality exfoliated graphene, ACS Nano. , 15 (**2021**) 1775–1784.

[67] N. Kumar, R. Salehiyan, V. Chauke, O. Joseph Botlhoko, K. Setshedi, M. Scriba, M. Masukume, S. Sinha Ray, Top-down synthesis of graphene: A comprehensive review, FlatChem. , 27 (**2021**) 100224.

[68] A.K. Geim, K.S. Novoselov, The rise of graphene, Nanosci. Technol. A Collect. Rev. from Nat. Journals., (**2009**) 11–19.

[69] L. Shahriary, A. a. Athawale, Graphene Oxide synthesized by using modified hummers approach, Int. J. Renew. Energy Environ. Eng., 2 (**2014**) 58–63.

[70] L. Zhang, J. Liang, Y. Huang, Y. Ma, Y. Wang, Y. Chen, Size-controlled synthesis of graphene oxide sheets on a large scale using chemical exfoliation, Carbon N. Y. , 47 (**2009**) 3365–3368.

[71] L.K. Putri, L.L. Tan, W.J. Ong, W.S. Chang, S.P. Chai, Graphene oxide: Exploiting its unique properties toward visible-light-driven photocatalysis, Appl. Mater. Today., 4 (**2016**) 9–16.

[72] S. Rawal, B. Joshi, Y. Kumar, Synthesis and characterization of activated carbon from the biomass of Saccharum bengalense for electrochemical supercapacitors, J. Energy Storage., 20 (**2018**) 418–426.

[73] A.A. Mamun, Y.M. Ahmed, S.A. Muyibi, M.F.R. Al-Khatib, A.T. Jameel, M.A. AlSaadi, Synthesis of carbon nanofibers on impregnated powdered activated carbon as cheap substrate, Arab. J. Chem., 9 (**2016**) 532–536.

[74] S. Navalon, A. Dhakshinamoorthy, M. Alvaro, H. Garcia, Heterogeneous fenton catalysts based on activated carbon and related materials, ChemSusChem., 4 (**2011**) 1712–1730.

[75] J. López, A.M. Chávez, A. Rey, P.M. Álvarez, Insights into the stability and activity of MIL-53(Fe) in solar photocatalytic oxidation processes in water, Catalysts. , 11 (**2021**).

[76] A.M. Chávez, A. Rey, J. López, P.M. Álvarez, F.J. Beltrán, Critical aspects of the stability and catalytic activity of MIL-100(Fe) in different advanced oxidation processes, Sep. Purif. Technol., 255 (**2021**) 117660.

CHAPTER 2

EXPERIMENTAL SECTION

This chapter is dedicated to compiling and giving an overview of the reagents, analytical and characterization techniques and procedures followed during the experimental part of this Doctoral Thesis. Additionally, the subsequent chapters contain the details of their specific experimental work.

2.1 REAGENTS

Table 2.1 lists the reagents used, classified according to their application. Semi-pure water (resistivity 10 MΩ cm) obtained from the RiOs-DI® equipment and ultrapure water (resistivity 18.2 MΩ cm) produced by the Milli-Q Reference® device, both from Merck-Millipore, were used to prepare aqueous solutions.

Table 2.1. Reagents used.

Reactive (State)	Formula	CAS	Supplier	Purity
Reagents and materials for analysis				
Glacial acetic acid (l)	C_2H_4O	64-19-7	Fischer	99.0%
Acetonitrile (l)	C_2H_3N	75-05-8	Panreac	99.99%
tert-butanol (l)	$C_4H_{10}O$	75-65-0	Panreac	99.0%
Cobalt chloride hexahydrate (s)	$CoCl_2$-$6H_2O$	7791-13-1	Panreac	99.0%
Dichloroacetic acid (l)	$C_2H_2Cl_2O_2$	2156-56-1	Merck	98.0%
Formic acid (l)	CH_2O_2	64-18-6	Panreac	98.0%
Fumaric acid (s)	$C_4H_4O_4$	110-17-8	Merck	99.0%
Hydrochloric acid (l)	HCl	7647-01-0	Fischer	37.0%
Hydrogen peroxide (l)	H_2O_2	7722-84-1	Panreac	33.0%
Iron test, Spectroquant® (l)	-	-	Merck	-
Malonic acid (s)	$C_2H_2O_4$	141-82-2	Merck	99.0%
Mercury (II) sulfate (s)	$HgSO_4$	7783-35-9	Merck	98.0%
Methanol (l)	CH_4O	67-56-1	Panreac	99.99%
trans, trans- Muconic acid (s)	$C_6H_6O_4$	3588-17-8	Merck	98.0%
Ortho-phosphoric acid (l)	H_3PO_4	7664-38-2	Panreac	85.0%
Oxalic acid dihydrate (s)	$C_2H_6O_4$-$2H_2O$	144-62-7	Merck	99.5%
Perchloric acid (l)	$HClO_4$	7601-90-3	Panreac	70.0%
Potassium bromide (s)	KBr	7758-02-3	Merck	99.0%
Potassium dichromate (s)	$K_2Cr_2O_7$	7778-50-9	Panreac	99.5%
Potassium hydrogen phthalate (s)	$C_8H_5KO_4$	877-24-7	Merck	99.95%
Potassium trisulfonate indigo(s)	$C_{16}H_7K_3N_2O_{11}S_3$	67627-18-3	Merck	98.0%

Table 2.1 (Continued). Reagents used.

Reactive (State)	Formula	CAS	Supplier	Purity
Potassium hydrogen phthalate (s)	K_2HPO_4	7758-11-4	Panreac	99.0%
Propionic acid (l)	$C_3H_6O_2$	79-09-4	Panreac	99.5%
Pyruvic acid sodium salt (s)	$C_3H_3NaO_3$	113-24-6	Merck	98.0%
Sodium hydrogen carbonate (s)	$NaHCO_3$	144-55-8	Panreac	99.7%
Sodium chloride (s)	NaCl	7647-14-5	Panreac	99.0%
Sodium hydroxide (s)	NaOH	1310-73-2	Panreac	98.0%
Sodium nitrite (s)	$NaNO_2$	7632-00-2	Panreac	98.0%
Sodium nitrate(s)	$NaNO_3$	7631-99-4	Panreac	99.0%
Sodium polyphosphate (s)	Na(PO3)n	50813-16-6	Merck	96.0%
Sodium sulfate (s)	Na_2SO4	7757-82-6	Panreac	99.0%
Succinic acid (s)	$C_4H_6O_4$	110-15-6	Merck	99.5%
Sulfuric acid (l)	H_2SO_4	7664-93-9	Panreac	98.0%
Titanium (IV) oxysulfate in H_2SO_4	$TiSO_5$-xH_2SO_4	123334-00-9	Merck	27.0%
Gases and solvents				
Acetone (l)	C_3H_6O	67-64-1	Panreac	99.5%
Ethanol (l)	C_2H_6O	64-17-5	Panreac	99.5%
Oxygen (g)	O_2	7782-44-7	Linde	99.5%
Nitrogen (g)	N_2	7727-37-9	Linde	99.99%
Synthetic air (g)	80%N_2 + 20%O_2	-	Linde	-
Ultrapure water(l)	H_2O	-	Merck	-
Acetone (l)	C_3H_6O	67-64-1	Panreac	99.5%
Ethanol (l)	C_2H_6O	64-17-5	Panreac	99.5%
Oxygen (g)	O_2	7782-44-7	Linde	99.5%
Nitrogen (g)	N_2	7727-37-9	Linde	99.99%
Reagents and materials for synthesis				
Carbón active DARCO (12-20 mesh) (s)	-	7440-44-0	Merck	-
Graphene nanoplatelets 750 m^2 g^{-1}(s)	-	7782-42-5	Merck	99.0%
Iron (II) chloride 4-hydate (s)	$FeCl_2 \cdot 4H_2O$	13478-10-9	Panreac	98.0%
Iron (III) chloride 6-hydate (s)	$FeCl_3 \cdot 6H_2O$	7705-08-0	Panreac	97.0%
Titanium dioxide, Aeroxide P25(s)	TiO_2	13463-67-7	Evonik	-
Tereftalic acic (s)	$C_8H_6O_4$	100-21-9	Merck	98.0%
Graphene oxide (s)	-	7782-42-5	Graphenea	99.0%
Contaminants				
Metoprolol tartrate salt (s)	$C_{34}H_{56}N_2O_{12}$	56392-17-7	Merck	99.0%
Fenol (s)	C_6H_6O	67-64-1	Merck	99.5%

2.2 AQUEOUS SOLUTIONS OF TARGET COMPOUNDS

Metoprolol tartrate (MTP) and phenol (Ph) were used as target compounds in the AOPs studied, to check the catalytic activity of the different materials. In general, ultrapure water solutions with concentrations of 50 mg L^{-1} of MTP (natural pH 7) and 25 mg L^{-1} of Ph (natural pH 5.6) were used, varying these concentrations in some experiments (detailed in the operating conditions of the corresponding chapter).

- MTP

Metoprolol is a β-blocker used in the treatment of severe diseases of the cardiovascular system, especially hypertension and acute myocardial infarction. It is marketed under the name Lopressor, by Novartis, and Toprol-XL. The active compound metoprolol is used as metoprolol succinate or metoprolol tartrate, and is formulated as an extended-release or conventional-release compound. Concentrations detected in sewage treatment plant effluents are currently between 38-5762 ng L^{-1} [1].

Exposure to low concentrations of MTP for long periods can result in bradycardias, dizziness, numbness and tingling, sexual dysfunction, respiratory distress, hair loss, and mood swings, among others [2-5].

This work was carried out with metoprolol tartrate, $C_{34}H_{56}N_2O_{12}$ and its structure is shown in **Figure 2.1**.

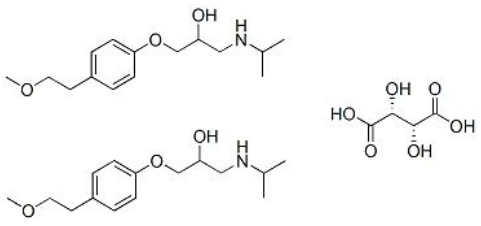

Figure 2.1. Metoprolol tartrate molecule.

- PHENOL

Pure phenol (C_6H_6O, see structure in **Figure 2.2**) is a white-colorless crystalline solid at room temperature. It is also known as phenic acid. It is one of the main wastes from the petrochemical and coal industries so phenol can end up in the water cycle and, eventually, can come into contact with chlorine forming chlorophenols during water disinfection, compounds highly soluble and cytotoxic. If ingested in high concentrations, these compounds can cause poisoning, vomiting, skin discoloration and respiratory irritation [6,7]. Phenol concentration can reach values between 1700-7000 mg L^{-1} in coal industries, as well as 40-185 mg L^{-1} in refinery effluents. Many other industries (textile, biomass gasification, etc.) can lead to high phenol concentrations in their effluents in the order of 100 mg L^{-1} [8].

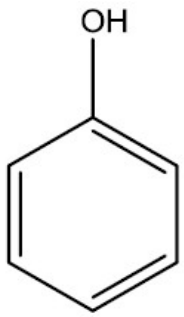

Figure 2.2. Phenol molecule.

2.3 CATALYSTS AND CATALYTIC COMPONENTS

Different materials have been used as catalysts or as catalytic precursors. Their use was always in suspension in the aqueous medium to be treated. Some data of the synthesis or main properties and application of these materials are briefly summarized in **Table 2.2** and deeply discussed in the subsequent sections (Chapters 3, 4, 5 and 6).

Table 2.2. Catalysts and catalytic precursors

Material	Supplier	Main properties
MIL-53(Fe)	This work	MOF with iron nodes and terephthalate linker (Chapter 3), Synthesis method solvothermal [9]
Aeroxide TiO_2-P25	Evonik	Anatase/Rutile 80/20, S_{BET}= 60.4 m^2 g^{-1}; Vpore=0.19 cm^3 g^{-1}, 21 nm crystal size
TiO_2-WO_3	This work	WO_3 of 3.8 wt %, S_{BET}= 49 m^2 g^{-1} [10]
NC-CeO_2	This work	87.4 % Ce(IV) 12.6 % Ce(III), S_{BET}= 14 m^2 g^{-1} [11]
Al_2O_3 corundum	Sigma-Aldrich	Powder (purity ≥ 98 %)
Ru/Al_2O_3	Alfa Aesar	0.5 wt. % of Ru, powder
Pt/Al_2O_3	Sigma-Aldrich	1 wt. % of Pt, powder
Graphene (G)	Sigma-Aldrich	S_{BET}=760 m^2 g^{-1}, Particle size<2 μm
Graphene oxide (GO)	Graphenea	S_{BET}=142 m^2 g^{-1}, %C: 49 – 56%, O: 41 – 50%
Activated carbon (AC)	Sigma-Aldrich	S_{BET}=644 m^2 g^{-1}, 12-20 mesh, Density = 1.8 – 2.1 g cm^{-3}
Fe_3O_4-magnetized materials		
Fe_3O_4	This work	Magnetic materials with variable composition and textural properties, used as catalysts for different AOPs: photocatalysis, heterogeneous Fenton and photo-Fenton, ozonation and photocatalytic ozonation. For properties and applications see Chapters 4, 5 and 6.
Fe_3O_4-TiO_2		
Fe_3O_4-TiO_2-WO_3		
Fe_3O_4-CeO_2		
Fe_3O_4-Al_2O_3		
Fe_3O_4-Ru/Al_2O_3		
Fe_3O_4-Pt/Al_2O_3		
Fe_3O_4-G		
Fe_3O_4-GO		
Fe_3O_4-AC		

Hydrothermal and solvothermal syntheses of MIL-53(Fe), CeO_2 and TiO_2-WO_3 were carried out in a 125 mL Teflon-lined autoclave (Parr Instruments) using a P-Selecta programable oven for temperature control.

The synthesis of magnetic catalysts is the scope of the subsequent chapters, where a detailed description is provided.

2.4 EXPERIMENTAL SET-UP FOR CATALYTIC ACTIVITY AND STABILITY STUDIES

2.4.1 Simulated solar radiation and ozonation system

Experiments to examine the activity of the catalysts and their stability under simulated solar radiation were performed in the experimental set-up depicted in **Figure 2.3**.

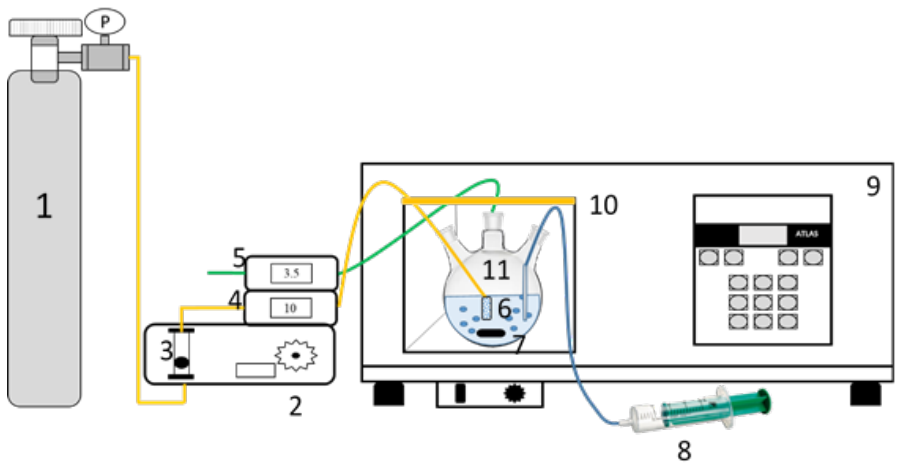

Figure 2.3. Experimental set-up for solar simulated radiation tests. 1: Oxygen bottle; 2: Ozone generator; 3: Rotameter; 4: Inlet ozone meter; 5: Outlet ozone meter; 6: Inlet gas diffuser/bubbler; 7: Magnetic stirrer; 8: Sample port; 9: Solar simulator; 10: Xenon lamp; 11: Borosilicate glass reactor.

The experimental set-up consisted of a solar simulator Suntest CPS+ (Atlas) with dimensions of 90x35x35 cm coupled to an ozonation system comprising gas supply, ozone generator, flowmeter and ozone analyzers. The photoreactor was placed in the solar box chamber to be irradiated by a 1500 W air-cooled xenon lamp, with an exposure area of 560 cm^2. In addition, the lamp has quartz and glass filters that restrict the emission spectrum to wavelengths longer than 300 nm. The temperature of the chamber reached 40 ºC during the experiments.

Figure 2.4 shows the comparison of the spectrum of the simulated solar radiation at the reactor level with natural sunlight, both obtained using the compact fiber optic UV-Vis spectroradiometer (Black-Comet model C from StellarNet). At the nominal irradiance used of 550 W m^{-2}, the UV-irradiance (300-400 nm) was 62.0 W m^{-2}, similar to 61.4 W m^{-2} of natural sunlight (11 am, 07/01/2019).

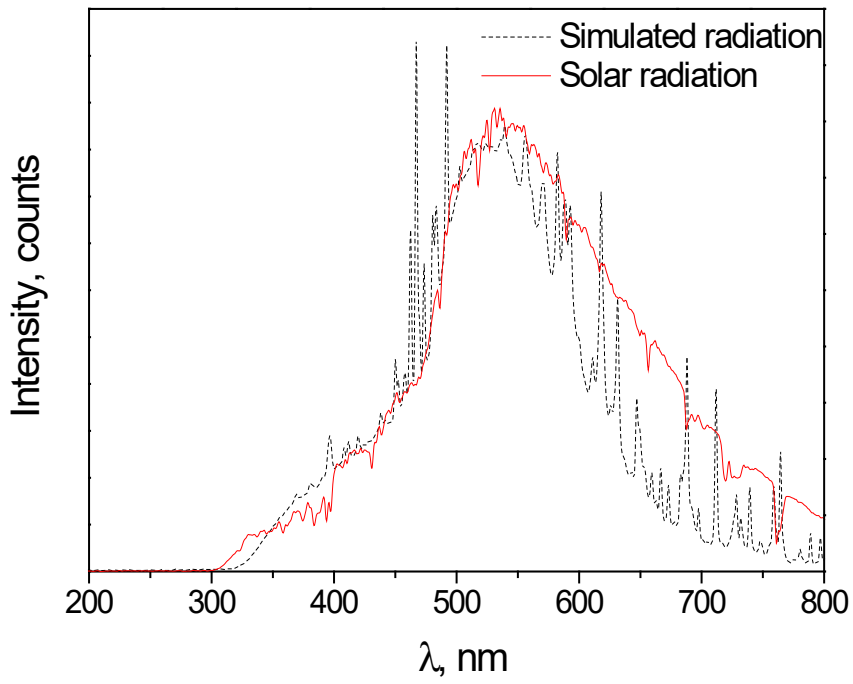

Figure 2.4. Comparison of simulated and natural solar radiation spectra.

The reactor was a spherical borosilicate glass 3.3 beaker, of 300 mL with a working volume of 250 mL. It had three inlets, one for oxygen or oxygen/ozone inlet, one for exhaust gases and the last one for sampling during the experiments. The agitation of the aqueous medium was performed by Teflon-coated magnets and a magnetic stirrer (Raypa AG-1) with adjustable speed.

The gas flow rate was controlled by a Cole Parmer PMR-1 rotameter and entered the reactor through ceramic diffuser. Ozone was generated in a Sander Labor-Ozonisator (model 301.7) ozone generator. Ozone analyzers Anseros GM-600-OEM and Anseros Ozomat GM6000 Pro were used to measure ozone concentration in the gases entering and leaving the reactor.

For the AOPs studied, the catalytic activity tests carried out and their main operating conditions are summarized in **Table 2.3**. On the other hand, the main information for stability studies under oxidizing conditions are summarized in **Table 2.4**. More details on the procedures used are described in the corresponding sections of chapters 3-6.

Table 2.3. Catalytic activity tests.

Process	Catalyst	Oxidant	Simulated solar radiation	Other conditions:
Persulfate (PS)	---	PS; 2.5 mM	---	V_R = 250 mL Target: MTP 50 mg L^{-1}; Ph 25 mg L^{-1} pH = 5-7
H_2O_2	---	H_2O_2; 6.5-50 mM	---	
O_3 Ozonation	---	O_3; 6 mg L^{-1}; Q = 10 L h^{-1}	---	
Adsorption	MIL-53(Fe); 0.6 g L^{-1} Fe_3O_4-C (MBCs); 0.2 g L^{-1} Fe_3O_4-TiO_2; 0.2-0.4 g L^{-1}	---	---	V_R = 250 mL Target: MTP 50 mg L^{-1}; Ph 25 mg L^{-1} pH = 5-7
Catalytic PS decomposition	MIL-53(Fe) 0.6 g L^{-1}	PS; 2.5 mM	---	V_R = 250 mL Target: MTP 50 mg L^{-1}; Ph 25 mg L^{-1} pH = 5-7
Catalytic H_2O_2 decomposition **Het. Fenton-like** **CWPO**	MIL-53(Fe) 0.6 g L^{-1} Fe_3O_4-C (MBCs) 0.2 g L^{-1}	H_2O_2; 6.5-50 mM	---	V_R = 250 mL Target: MTP 50 mg L^{-1}; Ph 25 mg L^{-1} pH = 5-7
Catalytic O_3 decomposition **Catalytic ozonation**	MIL-53(Fe) 0.6 g L^{-1} Fe_3O_4-TiO_2; 0.2-0.4 g L^{-1}	O_3; 6 mg L^{-1}; Q = 10 L h^{-1}	---	V_R = 250 mL Target: MTP 50 mg L^{-1}; Ph 25 mg L^{-1} pH = 5-7
Photolysis + O_2	---	O_2; 10 L h^{-1}	I = 580 W m^{-2}, 3 h	V_R = 250 mL Target: MTP 50 mg L^{-1}; Ph 25 mg L^{-1} pH = 5-7
Photolysis + PS	---	PS; 2.5 mM	I = 580 W m^{-2}, 3 h	
Photolysis + H_2O_2	---	H_2O_2; 6.5-50 mM	I = 580 W m^{-2}, 3 h	
Photolysis + O_3 **Photolytic ozonation**	---	O_3; 6 mg L^{-1}; Q = 10 L h^{-1}	I = 580 W m^{-2}, 3 h	
Photocatalysis	MIL-53(Fe) 0.6 g L^{-1} Fe_3O_4-C (MBCs) 0.2 g L^{-1} Fe_3O_4-TiO_2; 0.2-0.4 g L^{-1}	O_2; 10 L h^{-1}	I = 580 W m^{-2}, 3 h	V_R = 250 mL Target: MTP 50 mg L^{-1}; Ph 25 mg L^{-1} pH = 5-7
Photocatalysis + PS	MIL-53(Fe) 0.6 g L^{-1}	PS; 2.5 mM	I = 580 W m^{-2}, 3 h	V_R = 250 mL Target: MTP 50 mg L^{-1}; Ph 25 mg L^{-1} pH = 5-7
Photocatalysis + H_2O_2 **Het. photo-Fenton-like** **Photo-CWPO**	MIL-53(Fe) 0.6 g L^{-1} Fe_3O_4-C (MBCs) 0.2 g L^{-1}	H_2O_2; 6.5-50 mM	I = 580 W m^{-2}, 3 h	V_R = 250 mL Target: MTP 50 mg L^{-1}; Ph 25 mg L^{-1} pH = 5-7
Photocatalysis + O_3 **Photocatalytic ozonation**	MIL-53(Fe) 0.6 g L^{-1} Fe_3O_4-TiO_2; 0.2-0.4 g L^{-1}	O_3; 6 mg L^{-1}; Q = 10 L h^{-1}	I = 580 W m^{-2}, 3 h	V_R = 250 mL Target: MTP 50 mg L^{-1}; Ph 25 mg L^{-1} pH = 5-7

Table 2.4. Stability tests under oxidizing conditions and radiation

Catalyst	Loading ($g\ L^{-1}$)	pH_0	Volume (mL)	T (°C)	Time (h)	Treatment and conditions	Analyses
MIL-53(Fe)	1	7-7.5	250	25, 40	3	O_2 + Radiation H_2O_2 + Radiation PS + Radiation O_3 + Radiation	Liquid phase: Total and dissolved Fe TOC H_2BDC pH Solid: -XRD -FTIR
Fe_3O_4-C (MBCs)	0.2	7-7.5	250	40	3	O_2 + Radiation H_2O_2 + Radiation	Liquid phase: Total and dissolved Fe TOC H_2BDC pH Solid: -XRD -FTIR
Fe_3O_4-TiO_2	0.5	7-7.5	250	40	3	O_2 + Radiation H_2O_2 + Radiation O_3 + Radiation	Liquid phase: Total and dissolved Fe TOC H_2BDC pH Solid: -XRD -FTIR

2.4.2 Long-term stability tests at different pH values

The stability of catalytic materials was tested at different pH using 50 mL stoppered glass vials placed in a thermostatic bath with orbital shaking (PSelecta Unitronic OR). **Table 2.5** summarizes the main operating conditions used, and a detailed description of the procedure is shown in the corresponding sections of chapters 3-6.

Table. 2.5. Long-term stability tests at different pH in dark conditions.

Catalyst	Loading ($g\ L^{-1}$)	pH	Volume (mL)	T (ºC)	Time (days)	Analyses
MIL-53(Fe)	1	4, 6, 7, 8, 10	20	25	20	Liquid phase: -Total and dissolved Fe -TOC -H_2BDC -pH Solid: -XRD -FTIR
Fe_3O_4-C (MBCs)	1	4, 6, 7, 8, 10	20	25	7	Liquid phase: -Total and dissolved Fe -TOC -H_2BDC -pH Solid: -XRD -FTIR
Fe_3O_4-TiO_2	1	4, 6, 7, 8, 10	20	25	7	Liquid phase: Total and dissolved Fe TOC H_2BDC pH Solid: -XRD -FTIR

2.5 ANALYTICAL TECHNIQUES FOR SOLIDS CHARACTERIZATION

The physicochemical properties of the catalysts have been deeply studied through the characterization techniques summarized in **Table 2.6**. The analyses were mainly performed with the help of "Solid and Surface Analysis and Characterization Service (SACSS)" and the "Elemental and Molecular Analysis Service (SAEM)" belonging to the "Research Support Services of the University

of Extremadura (SAIUEX)", UV-visible diffuse reflectance spectroscopy and magnetometry analysis were performed by the Research Support Unit of the Institute of Catalysis and Petrochemistry (ICP) of the Spanish National Research Council (CSIC) and the "Unit of Magnetic Measurements of the Centre of Science and Technology, University of Barcelona", respectively. Exceptionally, X-ray photoelectron spectroscopy (XPS) analyses were performed by the Central Research Support Services (SCAI) of the University of Málaga. This section shows the most relevant aspects of the techniques used.

Table 2.6. Summary of properties, techniques and equipment used in the characterization of catalyst samples.

Property	Technique	Equipment
Surface morphology	Scanning Electron Microscopy (SEM)	SEM 3D, Quanta (FEI).
Crystallinity **Structural composition** **Crystal size**	X-ray diffraction (XRD)	X-Ray diffractometer D8 advance, Bruker@
Funcional groups **Chemical composition** **Structural features**	Fourier Transform Infrared Spectroscopy (FTIR)	Nicolet iS10, Thermo Scientific
	Raman Spectroscopy	Nicolet Almega XR, dispersive Raman spectrometer, Thermo Scientific
Adsorption-desorption isotherms **BET surface** **Pore volume**	N_2 adsorption-desorption	Autosorb iQ2-C, Quantachrome@
Elemental composition	Wavelength dispersive X-ray fluorescence (WDXRF)	S8 Tiger 4K, Bruker@
Thermal stability **Chemical composition**	Thermogravimetric analysis-coupled to mass spectrometry (TG-DTA-MS)	SETSYS Evolution-16, Setaram
Surface composition **Chemical Bonding** **Oxidation state**	X-Ray Photoelectron Spectroscopy (XPS)	XPS K, Thermo Scientific
Optical properties **UV-Vis absorption** **Band Gap**	The reflectance spectrum of UV-vis diffuse radiation	UV-vis-NIR Cary 5000, Varian
Magnetic hysteresis loop	Superconducting Quantum Interference (SQUID)	SQUID MPMS CL-7, Quantum Design

2.5.1 Scanning electron microscopy (SEM)

Scanning electron microscopy (SEM) is a common technique used to determine the morphology of a sample. The principle of the analysis is based on passing a beam of incident electrons on the surface of the sample and measuring its interactions which generate several signals: secondary electrons, reflected or backscattered electrons, characteristic X-rays, Auger electrons and cathodoluminescence photons (See **Figure 2.5**).

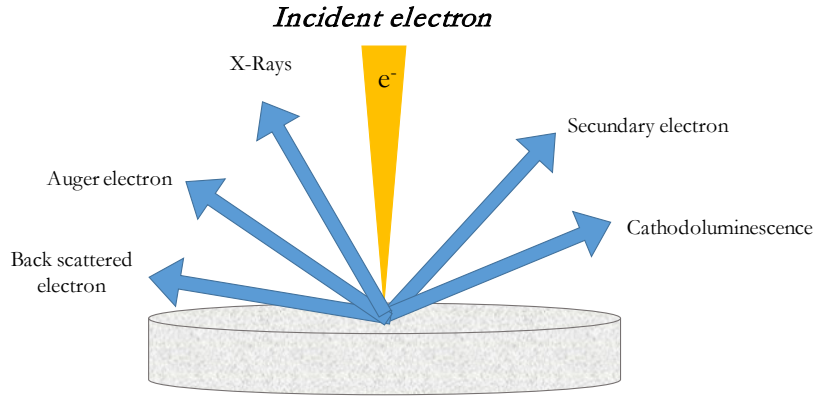

Figure 2.5. Scheme of signals generated as a result of irradiating a sample surface with an electron beam in a SEM analysis.

Thus, depending on the selected signal, different information can be obtained. For example, backscattered electrons are commonly used to represent a 2-D image with contrast in composition, while secondary electrons are useful to show the morphology of the sample. In addition, characteristic X-rays can also be detected by energy-dispersive X-ray spectroscopy (EDX) coupled to the microscope, which allows to semi-quantify the abundance of different elements in the sample.

SEM analyses were performed on a Hitachi S-4800 SEM device working at 20 kV accelerating voltage and 120-10000x magnification. Finally, the catalysts were examined by EDX for surface chemical composition and distribution. An SSD XFlash 5010 detector (Bruker) was used for this purpose. The samples were prepared by powder dispersion on carbon strips.

2.5.2 X-Ray diffraction (XRD)

X-ray diffraction (XRD) is a technique that allows obtaining information about the crystalline structure of a material. It is based on the phenomenon of scattering an incident beam of monochromatic X-rays, with a certain angle and intensity, on the material under study, complying with Bragg's law. This states that crystals will reflect X-rays of specific wavelengths and incident angles when the wavelengths of the scattered X-rays interfere constructively. Thus, the graphical representation of the intensity of the radiation versus the diffracted angle constitutes a diffractogram or XRD pattern, typical of each crystalline material. In general, most materials are composed of randomly oriented microcrystals, also called polycrystalline aggregates [12]. Therefore, crystalline phases of polycrystalline aggregates could be identified by comparing the experimental diffraction pattern with the single crystal patterns recorded in the International Centre for Diffraction Data (ICDD) database.

Moreover, this technique allows to determine the mean crystal size using the Scherrer's equation (2.1) attending usually to the main peak of the diffractogram [13].

$$d = \frac{k \cdot \alpha}{\beta \cdot cos\,\theta} \tag{2.1}$$

Where d is the crystal size (nm); K is a numerical factor referring to the crystal shape (usually K = 0.9 for spherical-shaped particles [13]); λ the wavelength used

in the analysis (nm); β the width of the main peak at half height in radians; and θ the Bragg angle in radians.

XRD analyses were performed on a D8 Advance microcrystalline powder diffractometer (Bruker ©) using a Cu Kα radiation (λ = 0.1541 nm) and a linear VANTEC detector with an aperture up to 12°. Data were collected between 2° and 80° at a scanning speed of $0.1°s^{-1}$.

2.5.3 Fourier transform infrared spectroscopy (FTIR)

IR spectroscopy is a technique sensitive to the presence of functional groups in a molecule as a higher energy vibrational state is generated when a functional group absorbs photons belonging to a certain IR region, which can identify a functional group with the frequency (wavenumber) at the maximum absorbance value. Thus, the representation of intensity (e.g. transmittance) versus wavenumber results in a spectrum that is used as a fingerprint of a sample. Like any other spectroscopy technique, the intensity of the signal at each wavenumber is related to the concentration of the species in the sample [14].

FTIR spectra were obtained on a Nicolet iS10 spectrometer (Thermo Scientific) using KBr wafers or using the attenuated total reflectance (ATR) accessory. When KBr was used, a solid mixture containing 10 mg of sample and KBr powder was prepared. Subsequently, the mixture was homogenized and pressed to obtain a thin film. Then, IR light is passed through the pellet and the intensity of the transmitted beam is detected and recorded using OMNIC software. In the case of the ATR accessory, no pretreatment was necessary. The sample was placed directly on the ATR plate and the infrared radiation undergoes multiple internal reflections on the glass. Generally, data were acquired in the range 400-4000 cm^{-1} (with the KBr tablet) or 550-4000 cm^{-1} (with the ATR) with a resolution of 1 cm^{-1}.

2.5.4 Raman spectroscopy

Raman spectroscopy is a non-destructive technique that provides detailed information on chemical structure, phase and polymorphism, crystallinity and molecular interactions in a sample. This technique is often used as a complement to IR spectroscopy results.

It is based on the interaction of a laser light source with the chemical bonds of the elements in the sample. A monochromatic beam is used as the radiation source, and different wavelengths can be used, from UV to infrared. When the photons interact with the molecules of a sample, they emit other radiation, usually of lower energy and of a specific spectrum (increasing wavelength and decreasing frequency), obtaining a fingerprint of the sample. The signal intensity of the resulting spectrum makes possible to quantify the concentration of the different species in the sample [15].

The equipment used to record the Raman spectra was the Nicolet Almega XR dispersive Raman spectrometer (Thermo Scientific), equipped with two objectives for focusing the sample: MPlan 10x BD and MPlan 50Xbd. In addition, it is equipped with a laser at 630 nm as a radiation source and fluorescence effects were corrected in the spectral range of 1288-92 cm^{-1}. The spot size was μ2.5 m. Spectra were recorded and processed with OMNIC software (Thermo Scientific).

2.5.5 Adsorption-desorption isotherms of N_2

The techniques related to adsorption and desorption of gases allow the analysis of the textural properties of a solid, including specific surface area, pore size distribution and pore volume. They are based on the physical phenomenon of adsorption where an adsorbate (usually N_2) is distributed on the surface of the adsorbent by Van der Walls forces [12]. The higher the pressure applied, the

greater the amount of gas adsorbed by the solid, thus filling the micropores (smaller than 2 nm), mesopores (2-50 nm) and macropores (larger than 50 nm). Plotting the adsorbed volume versus normalized pressure yields the adsorption isotherm from which all the above information is extracted. If, in addition, the desorbed gas is represented as the relative pressure decreases, the adsorption-desorption isotherms are obtained, which allow to determine some characteristics of the material under study. The isotherms are classified into six types according to their shape (type I: microporous material, type II, III, VI: non-porous and type IV and V: mesoporous material) [12]. The specific BET surface area (S_{BET}) is determined by the data collected by forming a monolayer of adsorbed gas on the surface according to the model of Brunauer, Emmet and Teller (2.2):

$$\frac{1}{V[(P_0/P)-1]} = \frac{C-1}{V_m C P_0}\frac{P}{P_0} + \frac{1}{V_m C} \qquad (2.2)$$

V is the volume of gas adsorbed per gram (mL g^{-1}) at a relative pressure (P/P_0), V_m is the volume of gas in the monolayer (mL g^{-1}) and C is a constant related to the adsorbate-adsorbent interaction and, consequently, to the heat of adsorption.

Consequently, V_m and C can be obtained from the linear regression of equation (2.2) of the monolayer data. Furthermore, when using N_2 as the adsorbate gas, the BET surface area (S_{BET}), expressed as $m^2\ g^{-1}$, is obtained from the following expression (2.3):

$$S_{BET} = 4.37 V_m \qquad (2.3)$$

The external surface area (S_{ext}), micropore volume (V_{micro}) and the multilayer thickness of the standard nonporous solid (t) are evaluated by the t-plot method [12]. Then, the S_{ext} of the sample can be derived from the slope of the gas volume and y-values, while the intersection of the t-plot is related to the micropore volume (V_{micro}).

All the analyses of nitrogen adsorption-desorption isotherms performed in this work were carried out using the Autosorb iQ2-C (Quantachrome) equipment. To eliminate possible gases or adsorbed molecules, previous degassing was carried out at 150 ºC for 12 hours with a residual pressure of $1x10^{-3}$–$4x10^{-4}$ Torr. The ASiQwin software was used for data acquisition and processing.

2.5.6 Wavelength dispersive X-ray fluorescence (WDXRF)

X-ray fluorescence (XRF) is an analytical technique used to determine the chemical composition of materials. The analysis is fast, accurate, non-destructive and does not require a large amount of sample. Two different XRF methods are distinguished: energy dispersive (EDXRF) and wavelength dispersive (WDXRF) systems [16]. A wider range of elements is detected by the latter.

XRF analysis is based on the fact that all elements produce secondary "fluorescent" X-rays of characteristic energy when exposed to X-rays of a given higher energy. The higher the atomic weight of an element, the higher the energy required to induce the fluorescence energy. WDXRF systems are based on Bragg's law, where photons emitted by the sample diffract before reaching the detector.

WDXRF analyses were performed on a Brucker S8 Tiger 4K WDXRF spectrometer equipped with a 4 kW rhodium excitation X-ray source operating at maximum voltage and intensity, 60 kV and 170 mA, respectively. Elemental composition was evaluated in a helium atmosphere, using different mask sizes (28 or 8 mm) and crystals (XS-5S, PET and LiF (200)) according to the energy range and measurable elements. Experimental data were evaluated with Spectra Plus software (version 3).

2.5.7 Thermogravimetric analysis (TGA-DTA)

Thermogravimetric analysis (TGA) and differential thermal analysis (DTA) are included in the thermal analysis techniques, which are based on the changes that a sample undergoes when subjected to gradual increases in temperature [12].

In thermogravimetric analysis, the TG curve shows the weight loss or gain of a substance with increasing temperature under a specific atmosphere. Therefore, the thermal stability and chemical composition of a sample can be intuited by analyzing also the products produced in the mass losses and the final product.

DTA analysis is based on the difference between the sample temperature and the reference temperature under a specific atmosphere. As a result, a DTA curve is obtained that describes the amount of heat absorbed or released by a sample at a given temperature. Thus, exothermic processes (energy release) or endothermic processes (energy requirement) are recorded on the DTA curve.

By analyzing TG and DTA plots together, adsorbed water, decomposition of substances and chemical transformations can be determined. Both analyses are performed on a thermobalance which consisted of an oven, a precision balance device and a sample holder (made of platinum, alumina or quartz crucibles) where the sample is placed [12].

TG-DTA analyses were performed in a SETARAM thermobalance (SETSYS Evolution-16) at a heating rate of 10 °C min^{-1} under 100 mL min^{-1} of O_2/Argon (80/20) and in the temperature range between 40 to 950 °C. To determine and quantify the species produced during heating, an QMS 403D Aëolos III-Netzsch SETSYS Evolution-16 mass spectrometer coupled to the outlet of the thermobalance gas stream was used. H_2O, CO and CO_2 have been quantified during TGA-DTA-MS tests.

2.5.8 X-Ray photoelectron spectroscopy (XPS)

X-ray photoelectron spectroscopy (XPS) is a surface quantitative technique used to evaluate the surface composition, chemical state and oxidation state of material elements [17]. It is based on irradiating the sample with a beam of radiation and observing the emission of photoelectrons from the surface. The photoelectrons have a specific kinetic energy (KE), which can be measured during analysis by an electron energy detector. This is a surface technique, with a depth range in the sample down to about 4 nm.

Chemical composition, chemical bonds and oxidation states were evaluated with a PHI VersaProbe II Scanning XPS Microprobe spectrometer using Al Kα radiation (hν=1486.68 eV) under vacuum conditions. The voltage and intensity were 12 kV and 6 mA, respectively. In addition, the radiation source was tilted 30° concerning the horizontal of the sample. The deviation of the spectrum energy was 0.9 % of the value set in the step energy. Anyway, binding energy (BE) was corrected to the C1s peak at 284.6 eV. The data acquired for specific atomic levels in detail spectra were deconvoluted into different peaks in the form of Gaussian and Lorentzian functions using Shirley baseline using XPSpeak 4.1 software. The chemical composition of the surface was estimated from the peak areas.

2.5.9 Diffuse reflectance UV-visible spectroscopy

This technique has been used to observe the transition of electrons in a material from the valence band to the conduction band, and calculate the band gap energy. For semiconductors, this transition occurs in the UV-visible region of the electromagnetic radiation spectrum (wavelengths between 190-800 nm). If the electronic jump has a high energy requirement, the precise wavelengths will be those in the UV part of the spectrum.

The analyses were carried out using a Cary 5000 (Agilent) UV-Vis-NIR spectrophotometer equipped with an integrating sphere, in the range of 200-800 nm. The diffuse reflectance spectra were collected by the equipment and subsequently transformed into apparent absorbance spectra using the Kulbelka-Munk (F(R)) function. The band gap in eV of the materials was determined by constructing Tauc's plots plotting $(F(R)hv)^n$ versus hv, being n=1/2, for semiconductors with an indirect transition.

2.5.10 SQUID Magnetometry

Superconducting quantum interference devices (SQUID) magnetometry is one of the most effective and sensitive tests for measuring the magnetic properties. The sample magnetic signal is obtained employing a 4-winding superconducting pickup coil. As the sample moves up and down, it produces an alternating magnetic flux in the pickup coil, which generates an alternating output voltage from the SQUID. The voltage is subsequently amplified and recorded by the magnetometer [18].

A Quantum Design MPMS XL-7 SQUID equipment was used for the measurements at room temperature. The maximum magnetization is obtained with the maximum value of the asymptotic curve of the magnetic moment M versus the applied magnetic field (H).

2.5.11 Elemental analysis

Elemental analysis is a technique for determining carbon, hydrogen, nitrogen and sulfur contents of a given material. CHNS analysis requires the combustion of the material in an atmosphere of pure oxygen, resulting in the transformation of C, H, N and S into the species CO_2, H_2O, NO_x and SO_2, respectively. NO_x is

subsequently reduced to N_2 and the gases generated are entrained in the oxygen stream and analyzed with IR, thermal conductivity, or high selectivity detectors. The analytical determination was performed on a CHNS-932 LECO-1100 analyzer. This technique was complementary to X-ray fluorescence for the quantification of the other elements present in the sample.

2.6 ANALYTICAL METHODS FOR WATER CHARACTERIZATION

This section describes the analytical methods used in the monitoring of the aqueous phase during the oxidation and stability experiments. **Table 2.7** shows the analytical techniques according to the parameter to be determined.

Table 2.7. Analytical techniques according to the parameter to be determined.

Parameter	Technique	Equipment
Concentration of contaminants in water	High-performance liquid chromatography (HPLC)	HPLC-UV-Vis Agilent 1100 series
Temperature and pH	Thermometer/Potentiometry	pH-Meter, GLP21+Crison
Conductivity	Conductimetry	Conductivity-Meter, pH-Meter , GLP21+Crison
Turbidity	Nephelometry	Turbidity-meter, HI 93414 Hanna
Concentration of low molecular weight carboxylic acids/dissolved inorganic anions	Ion chromatography	881 Compact IC pro, Metrohm
Dissolved ozone concentration	Oxidation + spectrophotometry	Helios, Thermo Spectronic T60, PG Instruments
Gas phase ozone concentration	Spectrophotometry	Ozomat GM-6000 / Anseros Ozomat GM6000 Pro
Concentration of organic and inorganic carbon in an aqueous solution	Oxidation + infrared spectroscopy	TOC-V VCSH (Shimadzu)
Concentration of H_2O_2 in water	Oxidation/Complexation + spectrophotometry	Helios, Thermo Spectronic
Total dissolved iron concentration	Oxidation/Complexation + spectrophotometry	Spectroquant iron test, Merck Helios , Thermo Spectronic
Iron concentration (II)	Complexation + spectrophotometry	Helios, Thermo Spectronic
Persulfate	Spectrophotometry	Helios, Thermo Spectronic

2.6.1 Determination of the concentration of contaminants in water

The determination of the concentration of the contaminants MTP and phenol in an aqueous solution was carried out using the high-performance liquid chromatography (HPLC) technique and an absorbance detector (UV/Vis). In addition, H_2BDC, present in the aqueous medium was also analyzed. First, the UV-visible absorbance spectrum of each compound was recorded to evaluate the optimal detection wavelength. Calibration curves were then performed using different standard concentrations.

The HPLC used was the Agilent 1100 Series model, equipped with a quaternary pump, degasser, automatic sampler and UV-visible detector. For data recording and processing, the equipment is equipped with ChemStation software. A Kromasil C18 column (150 x 4.0 mm, 5 m) was used as the stationary phase. A mixture of water with phosphoric acid and acetonitrile was used as the mobile phase. In the following experimental chapters, the methods used for the analysis of the target compounds will be detailed.

2.6.2 Determination of temperature and pH

The pH measurements were performed with a pH meter GLP 21+, provided with electrode 50 21T, characterized by a ground diaphragm that improves the electrolyte flow, Ag/AgCl dissolution in the electrode, an Ag^+ cartridge barrier and a temperature sensor with which the temperature was measured when necessary. This pH meter is suitable for wastewater and low conductivity water samples in a pH range between 0 and 14 and at temperatures from 0 to 60 °C. The electrode was filled with KCl electrolyte solution (1 M, Crison) when necessary.

Calibration was performed daily with 4.01, 7.00 and 9.21 buffered standard solutions.

2.6.3 Turbidity determination

The turbidity of aqueous samples is due to suspended solids. It is an optical property caused by the absorption and scattering of a light beam instead of being transmitted.

The turbidity values were obtained by the nephelometric method [20] using a HI 93414 turbidity meter (Hanna), which is suitable for use in drinking water and wastewater up to 1000 NTU (Nephelometric Turbidity Units). Specifically, the HI 93414 turbidity meter is based on an optical system inside a tungsten filament to irradiate the cuvette containing the sample, detectors to measure scattered and transmitted light and a microprocessor to calculate the NTU value utilizing an internal algorithm. The device was calibrated with standards (< 0.1, 15, 100 and 750 NTU) supplied by Hanna.

2.6.4 Determination of the concentration of low molecular weight carboxylic acids and dissolved inorganic anions

The detection and quantification of inorganic anions and short-chain carboxylic acids were carried out by ion chromatography, using a Metrohm model 881 compact IC Pro ion chromatograph equipped with a chemical suppressor and conductivity detector. It also has a dosing unit (800 Dosino) coupled to an 863 Compact autosampler. A Metrosep A Supp 7 anion column (250mmLx4.0 mmID), thermostated at 45°C, with polyvinyl alcohol particles and ammonium groups was used as the stationary phase. The mobile phase consisted of a gradient sodium carbonate solution at a constant flow rate of 0.7 mL min^{-1}, varying the carbonate concentration from 0.6 to 14.6 mM in 50 min, with 10 min being the equilibration time. The injection volume in all cases was set at 20 μL. The

chemical suppression had a 250 mM dilution in H_2SO_4 and 23.6 mM in oxalic acid for system regeneration. The data were processed with Magic IC Net™ software.

This method can separate inorganic anions and some short-chain organic acids. The calibration curves (0.1-10 mg L^{-1}) were verified with an external standard, as shown in **Figure 2.6** where the retention times are also shown.

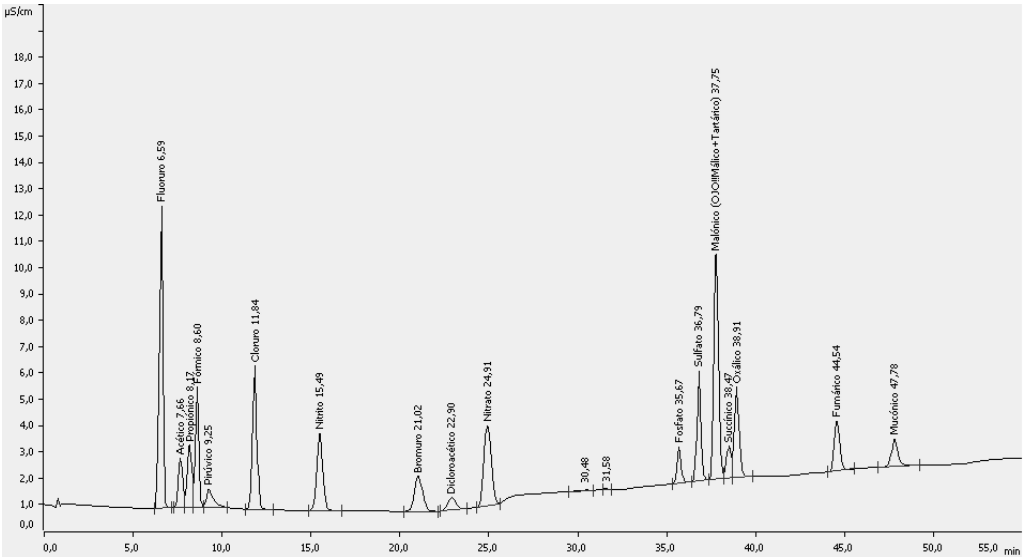

Figure 2.6. Extracted chromatogram of the external standard (5 mg L^{-1}) from the ion chromatograph.

2.6.5 Determination of dissolved ozone concentration

The colorimetric method proposed by Bader and Hoigné was used to quantify the ozone concentration in aqueous solution [20]. It is based on the decolorization of potassium 5,5,7-indigo trisulfonate when oxidized with ozone under acidic conditions. The wavelength for measurement in the spectrophotometer (Helios, Thermo Spectronic) was 600 nm, corresponding to blue samples. The ozone concentration was evaluated spectrophotometrically from the difference between a blank sample (intense blue without ozone) and the partially colorless samples due to the oxidation of the indigo by ozone dissolved

in the sample. This method allows the determination of ozone concentrations in the range between $1.0x10^{-7}$ and $6.3x10^{-4}$ M.

The indigo solution (10^{-4} M) was prepared by mixing 100 mL of a 10^{-3} M solution of indigo and $2x10^{-3}$ M in H_3PO_4, with 900 mL of a pH 2 buffer solution containing 35 g L^{-1} of H_3PO_4 and 28 g L^{-1} of KH_2PO_4.

To proceed with the analysis, in a vial containing the indigo solution (V_{IA}), usually 4 mL, a given sample volume (V_m), usually 1 mL, was added and the absorbance of the mixture was rapidly measured at 600 nm in a plastic cuvette with a 1 cm optical path. Similarly, a blank was prepared for comparison by replacing the sample volume with a similar volume of ultrapure water or water to be treated prior ozonation. According to the Lambert-Beer's law, knowing the absorbance values of the blank (A_b) and the sample (A_m), considering the volumes V_{IA} and V_m together with the molar extinction coefficient of indigo at 600 nm (ε_{600nm} =20000 M^{-1} cm^{-1}), the concentration of dissolved ozone was determined by the equation (2.4). By employing 1 cm optical path cuvettes the analytical method has a minimum sensitivity of 0.05 mg L^{-1} of dissolved ozone.

$$C_{O_{3,d}}(M) = \frac{A_b - A_m}{\varepsilon_{600nm}} \frac{V_m + V_{IA}}{V_m} \quad (2.4)$$

2.6.6 Determination of ozone concentration in gas phase

The ozone gas concentration during ozonation experiments, was analyzed by means of two ozone detectors: Anseros GM-6000-OEM (0-200 mg L^{-1}) and Anseros GM-PRO (0-200 mg L^{-1}) models for inlet and outlet streams, respectively. The measurement is based on the ozone radiation absorption with a maximum at 253.7 nm.

2.6.7 Determination of the concentration of organic and inorganic carbon in aqueous solution

Total carbon (TC) in an aqueous sample includes total organic carbon (TOC) from organic matter, and inorganic carbon (IC), i.e. carbonate and bicarbonate ions. TC, TOC and IC were determined on a Shimadzu TOC-VCSH analyzer coupled to an ASI-V automatic sample injector. The measurement data of TC, IC and consequently TOC values were automatically recorded and processed by the TOC-Control V™ software.

The equipment first performs the TC analysis. The aqueous sample is introduced into a quartz combustion tube filled with a catalyst (platinum supported on 2 mm alumina beads, 33 g). A flow of synthetic air (150 mL min^{-1}) passes continuously through the reactor heated by an oven at 680 °C, which allows the oxidation of the organic content of the sample into carbon dioxide. Thus, the CO_2 produced in the combustion process, previously cooled and dehumidified, is analyzed by non-dispersive infrared detector (*NDIR*) spectroscopy. The signal is processed by TOC-Control V software that associates the peak area with a calibration curve for quantification purposes.

On the other hand, the IC concentration is quantified by acidification with H_3PO_4 (25%) so that carbonate and bicarbonate ions are transformed into CO_2, to be measured by NDIR spectroscopy. As for TC analysis, the signals are correlated to a calibration curve. The TOC value is calculated by the difference between TC and IC values.

The calibration curves for TC and IC (0.1-20 mgTC L^{-1}, 20-100 mgTC L^{-1} and 0.1-20 mgIC L^{-1}) were prepared using potassium hydrogen phthalate and a mixture of sodium hydrogen carbonate and sodium carbonate as standards, respectively, and were periodically checked.

2.6.8 Determination of the concentration of H_2O_2 in water

H_2O_2 in aqueous solution was quantified using two methods of analysis depending on the concentration values to be determined.

a) High hydrogen peroxide concentration (10^{-3} M>C>10^{-5} M)

The method proposed by Eisenberg (1943) was used when the concentration of H_2O_2 was relatively high [20]. This is based on the colorimetric determination at 405 nm of yellow pertitanic acid. Generally, this method was used in Fenton and photo-Fenton experiments, where H_2O_2 was added to the experiment.

Typically, 0.5 mL of commercial titanium (IV) oxysulfate in sulfuric acid solution was mixed with 4.4 mL of ultrapure water and 0.1 mL of sample. For solutions with a lower concentration of H_2O_2 the volume of the sample was increased and the volume of water was decreased so that the value obtained was within the detection range. After a few minutes, the mixture was transferred directly to a plastic cuvette and measured at 405 nm. According to Lambert-Beer's law, equation (2.5) was used to calculate the concentration of H_2O_2:

$$C_{H_2O_2}(M) = \frac{A_m - A_b}{\varepsilon_{425nm} \cdot b} \frac{V_{Reagents} + V_m}{V_m} \quad (2.5)$$

where H_2O_2 is the concentration of hydrogen peroxide in M; A_b and A_m are the absorbances at 405 nm of the blank (determined by replacing the sample volume with the same volume of ultrapure water) and the sample, respectively; ε_{405} is the molar extinction coefficient at 405 nm (720 M^{-1} cm^{-1}); b the cell length (1 cm) and $V_{reagents}$ and V_m the volume of titanium oxysulfate (IV) reagent and sample volume, respectively.

b) Low hydrogen peroxide concentration (C<10^{-5} M)

For H_2O_2 concentration values below 10^{-5} M, the method of cobalt carbonate proposed by Maschelein et al. (1977) was selected [21]. It is based on the oxidation

of the Co (II) cation to Co (III) in the presence of H_2O_2, giving rise to Co (III)-bicarbonate complexes with maximum of absorbances at 260, 440 and 665 nm. Quantification was performed at 260 nm since it is the wavelength with the highest molar extinction coefficient. The detection limit was estimated at $3x10^{-7}$ M. In a typical test, 1 mL of sample was added to a vial containing 11 mL of the determination mixture.

For the preparation of the mixture described above, three stock solutions were first prepared: one of 16.1 g L^{-1} of $CoCl_2$, another containing 10 g L^{-1} of sodium polyphosphate (Calgon, $(NaPO_3)_n$) and a third supersaturated solution of HCO_3^-. Once prepared, 0.5 mL of the cobalt solution, 0.5 mL of the Calgon solution and 10 mL of the HCO_3^- were added to the vial, resulting in the aforementioned 11 mL of the mixture. Since the organic content can cause a positive interference in the determination at 260 nm, it was necessary to prepare another vial with the mixture where the cobalt (II) chloride solution was replaced by ultrapure water. After waiting at least 15 minutes, the mixture was transferred to a 1 cm quartz cell and its absorbance at 260 nm was measured. In addition, two blank vials were prepared using 1 mL of ultrapure water, instead of 1 mL of the test sample. Therefore, according to the Lambert-Beer's law, the concentration of H_2O_2 was determined by applying equation (2.6):

$$C_{H_2O_2}(M) = \frac{(A_{m,Co} - A_{m,without\ Co}) - (A_{b,Co} - A_{b,without\ Co})}{\varepsilon_{260nm} \cdot b} \cdot \frac{V_{Reagents} + V_m}{V_m} \qquad (2.6)$$

$A_{m,\,Co}$ and $A_{m,without\ Co}$ are the absorbance values at 260 nm of the vials with the sample with and without the cobalt solution, respectively. $A_{b,Co}$ and $A_{b,without\ Co}$ are the absorbance values of the blanks. $_{260nm}$ the molar extinction coefficient at 260 nm (26645 M^{-1} cm^{-1}) and b the optical path of the quartz cuvette (1 cm). $V_{Reagents}$ the volume of the titration mixture (11 mL) and V_m the sample volume (1 mL).

2.6.9 Determination of total dissolved iron concentration

The concentration of total iron in an aqueous solution was evaluated spectrophotometrically at 565 nm following the specifications of the Spectroquant® iron test (Merck 1.14761.0001), based on the transformation of Fe(III) to Fe(II) and the sudden formation of a purple complex between Fe(II) and ferrozine in a thioglycolate buffered medium. The analysis was performed by adding 3 drops of iron test reagent to 5 mL of sample. After waiting 3 min, absorbance was evaluated at 565 nm in a 1 cm plastic cuvette. The concentration in mg L^{-1} can be obtained directly by multiplying the absorbance value (Absorbance of the sample minus that of the corresponding blank) by a factor of 2.08 (ε_{Fe} =27044 M^{-1} cm^{-1} and M_{Fe} =55.845 g mol^{-1}). The minimum and maximum limits of quantification are 0.05 and 5 mg L^{-1}, respectively.

$$C_{Fe}(mg\ L^{-1}) = 2.08 \cdot Abs \tag{2.7}$$

2.6.10 Determination of dissolved iron (II) concentration

To quantify the ratio of iron species present in the aqueous medium (Fe(II)/Fe(III)), the Fe(II) concentration was determined and compared with the total Fe concentration. This method, described by Zuo in 1995 [22] is based on the formation of the colored complex of Fe(II) and o-phenanthroline in an acidic medium (acetic/acetate) with a pH between 3 and 4. This complex absorbs radiation at 510 nm (ε_{510} =11023 M^{-1} cm^{-1} [23]).

To proceed with the analysis, first, a vial was prepared with 1.5 mL of 0.1 M acetic acid/acetate buffer at pH = 3 and 1 mL of 0.2 wt.% of o-phenanthroline. The above volumes were added to a third, 5 mL of filtered sample for analysis (0.45 μm Millex-HV Millipore PVDF hydrophilic membrane filters). After shaking, 1 mL of ammonium fluoride (NH_4F) was added and shaken. After 20 min, the absorbance was measured at 510 nm using a 1-cm quartz cuvette. In

each analysis, a blank was prepared by adding 5 mL of ultrapure water (Milli-Q) instead of the sample.

According to Beer's Law, as seen in previous sections, the Fe(II) concentration can be determined by equation (2.8):

$$C_{Fe(II)}, M = \frac{A_m - A_b}{\varepsilon_{510nm} \cdot b} \frac{V_T}{V_m} \quad (2.8)$$

where $C_{Fe(II)}$ is the molar concentration of Fe(II) in solution; A_m is the absorbance of the sample at 510 nm, A_b is the absorbance of the blank at 510 nm, ε_{510} is the molar absorptivity of the complex formed at 510 nm; b, the optical path (1 cm); V_T, the total volume of the vial (8.5 mL) and V_m, the volume of sample added (5 mL).

2.6.11 Determination of persulfate concentration

For the determination of persulfate concentration with a detection limit of $3x10^{-4}$ -$5x10^{-5}$ M, the method proposed by Wahba et al. (1959) was used [24]. A 0.05 M phosphoric acid solution A was prepared and soda was added up to pH = 6. On the other hand, a solution B with 1 wt.% of n-n-diethyl-p-phenylenediamine (DPD) and 0.1 M H_2SO_4 was prepared. For the measurement, 0.1 mL of filtered sample (0.45 μm Millex-HV Millipore PVDF) was added to a vial containing 9.9 mL of solution A, after which 0.1 mL of solution B was added and shaken for 10 sec. Finally, it was left to stand for exactly 30 min and the absorbance of the sample was analyzed at 551 nm in a spectrophotometer with a quartz cuvette of 1 cm. A calibration curve with known concentrations of persulfate was prepared beforehand to determine the concentration of the target sample. For each analysis a blank was taken, adding 0.1 mL of Milli-Q water, instead of the sample, to subtract the signal.

References

[1] R. Loos, D. Marinov, I. Sanseverino, D. Napierska, T. Lettieri, Review of the 1 st watch list under the water framework directive and recommendations for the 2 nd watch list, JCR Tech. Reports., (**2018**).

[2] T.P. Rohrig, D.A. Rundle, Fatality resulting from metoprolol overdose, J. Anal. Toxicol., 11 (**1987**) 231–232.

[3] J. Richard, A. Boergers, C. vom Eyser, K. Bester, J. Tuerk, Toxicity of the micropollutants Bisphenol A, Ciprofloxacin, Metoprolol and Sulfamethoxazole in water samples before and after the oxidative treatment, Int. J. Hyg. Environ. Health., 217 (**2014**) 506–514.

[4] J.N. Love, β-Blocker toxicity: A clinical diagnosis, Am. J. Emerg. Med., 12 (**1994**) 356–357.

[5] H. Arslan, Invited Response on: "Several opinions on effects of insulin, metoprolol and deferoxamine on fat graft," Aesthetic Plast. Surg., 43 (**2019**) 1413–1414.

[6] M.L. Davì, F. Gnudi, Phenolic compounds in surface water, Water Res., 33 (**1999**) 3213–3219.

[7] R.H. Burttschell, A.A. Rosen, F.M. Middleton, M.B. Ettinger, Chlorine derivatives of phenol causing taste and odor, J. Am. Water Works Assoc., 51 (**1959**) 205–214.

[8] W.H. Saputera, A.S. Putrie, A.A. Esmailpour, D. Sasongko, V. Suendo, R.R. Mukti, Technology advances in phenol removals: current progress and future perspectives, Catalysts., 11 (**2021**) 998.

[9] M. Al Haydar, H.R. Abid, B. Sunderland, S. Wang, Metal organic frameworks as a drug delivery system for flurbiprofen, Drug Des. Devel. Ther., 11 (**2017**) 2685–2695.

[10] A. Rey, P. García-Muñoz, M.D. Hernández-Alonso, E. Mena, S. García-Rodríguez, F.J. Beltrán, WO_3–TiO_2 based catalysts for the simulated solar radiation assisted photocatalytic ozonation of emerging contaminants in a municipal wastewater treatment plant effluent, Appl. Catal. B Environ., 154–155 (**2014**) 274–284.

[11] E. Mena, A. Rey, E.M. Rodríguez, F.J. Beltrán, Nanostructured CeO_2 as catalysts for different AOPs based in the application of ozone and simulated solar radiation, Catal. Today., 280 (**2017**) 74–79.

[12] M. Faraldos, C. Goberna, Técnicas de análisis y caracterización de materiales, Consejo Su, Consejo Superior de Investigaciones Científicas, (**2021**).

[13] B. Ohtani, Photocatalysis A to Z-What we know and what we do not know in a scientific sense, J. Photochem. Photobiol. C Photochem. Rev., 11 (**2010**) 157–178.

[14] B.C. Smith, Fundamentals of fourier transform infrared spectroscopy, CRC Press, (**2011**).

[15] B. Dietzek, D. Cialla, M. Schmitt, J. Popp, Introduction to the fundamentals of raman spectroscopy, in: Springer Ser. Surf. Sci., Springer Verlag, (**2018**) 47–68.

[16] P. Brouwer, Theory of XRF, (**2010**).

[17] J. Sharma, B.C. Beard, Fundamentals of x-ray photoelectron spectroscopy(xps) and its applications to explosives and propellants, in: Chem. Phys. Energ. Mater., Springer Netherlands, (**1990**) 569–585.

[18] S. Srinath, A Review of: "The SQUID Handbook: Fundamentals and technology of SQUIDS and SQUID systems," Mater. Manuf. Process., 21 (**2006**) 583–583.

[19] E.W. Rice, R.B. Baird, Methods for the examination of water and wastewater, AWWA (American Water Works Association), (**2017**).

[20] R.B. Baird, A.D. Eaton, E.W. Rice, standard methods for the examination of water and wastewater, (**2017)**.

[21] W. Masschelein, M. Denis, R. Ledent, Spectrophotometric determination of redisual hydrogen peroxide, Water Sew. Work., (**1977**).

[22] Y. Zuo, Kinetics of photochemical/chemical cycling of iron coupled with organic substances in cloud and fog droplets, Geochim. Cosmochim. Acta., 59 (**1995**) 3123–3130.

[23] E. Rodríguez, M. Mimbrero, F.J. Masa, F.J. Beltrán, Homogeneous iron-catalyzed photochemical degradation of muconic acid in water, Water Res., 41 (**2007**) 1325–1333.

[24] N. Wahba, M.F. El Asmar, M.M. El Sadr, Iodometric method for determination of persulfates, Anal. Chem., 31 (**1959**) 1870–1871.

CHAPTER 3

INSIGHTS INTO THE STABILITY AND ACTIVITY OF MIL-53(Fe) IN SOLAR PHOTOCATALYTIC OXIDATION PROCESSES IN WATER

3.1 INTRODUCTION

3.1.1 State of the art

Advanced oxidation processes (AOPs) have been extensively used for the degradation of organic pollutants in water. In these processes, combinations of oxidants, catalysts and/or radiation of different wavelengths produce powerful secondary oxidizing species (e.g., free radicals such as hydroxyl radical, HO•), which can even mineralize organic contaminants. In the last decades a great deal of research on AOPs has been devoted to photocatalytic processes mediated by solar radiation or low-cost energy sources (e.g. visible LED lamps) seeking for cleaner, more efficient and economically viable processes [1]. Efforts have been focused on developing new visible-light-responsive photocatalysts for the removal of contaminants from water with improved properties such as high adsorption capacity and photocatalytic activity under solar radiation or visible light, easy post-recovery and reusability. In this sense, some types of the so-called metal-organic-frameworks (MOFs) are arising growing interest as potential heterogeneous photocatalysts [2].

MOFs constitute a new class of porous, crystalline materials formed by an extended network of metal ions (clusters) coordinated to multifunctional organic ligands (linkers) through coordination bonds. The combination of inorganic and organic units in the MOF offers an outstanding number of structural possibilities for materials with predefined properties that might make them useful in a variety of applications such as gas storage and separation, molecular sensing, catalysis or drug delivery [3]. Since 2007, when Llabrés i Xamena and co-workers showed the photocatalytic activity of MOF-5 for the degradation of phenol [4], an increasing number of MOFs are being researched as photocatalysts for the degradation of organic pollutants in water [5-7]. Particularly appealing in this field are Fe-based MOFs, which can absorb visible light due to the direct excitation of iron-oxo clusters [8]. Furthermore, they can work as heterogeneous catalysts for the activation of hydrogen peroxide (e.g., Fenton-like reactions) [9-11], persulfate

[12-13] or ozone [14]. Among the Fe-based MOFs, MIL-53(Fe), a three-dimensional, flexible, porous solid composed of $FeO_4(OH)_2$ octahedra clusters connected by 1,4-benzenedicarboxylate (BDC) linkers, has gained special attention in the recent literature as a potential visible-light photocatalyst for the degradation of organic pollutants in water [15-44]. MIL-53(Fe) offers the advantages of easy preparation from terephtalic acid (TA) and common iron salts, stability, non-toxicity and good visible light absorption [15]. As shown in **Table 3.1**, the photocatalytic activity of MIL-53(Fe) has been mainly demonstrated in the decolorization of dyes, such as methylene blue, rhodamine B or acid orange 7, though there are also studies about the photodegradation of other types of pollutants like some pharmaceuticals and herbicides and on the photocatalytic reduction of Cr(VI) to Cr(III) [21, 32, 45-47]. It has been reported that MIL-53(Fe) mediated photodegradation of organic pollutants takes place mainly through photogenerated holes (h^+) and reactive oxygen species (ROS) such as singlet oxygen ($^1O_2$), superoxide radical ($^{\bullet}O_2^-$) and, especially, hydroxyl radical ($HO^{\bullet}$) [48]. However, as a general rule, photodegradation of organic contaminants mediated by bare MIL-53(Fe) is a rather slow process due to fast electron-hole recombination, though this can be prevented to some extent by controlling the Fe(II)/Fe(III) ratio in the MOF structure [49]. The photocatalytic performance of MIL-53(Fe) can be enhanced in hybrid materials [17-19, 22 ,25-28, 32, 34, 35, 37-41, 43, 44], by acid modulation [36] and/or using electron acceptors, such as hydrogen peroxide [15, 16, 18-20, 23, 40, 43], persulfate [15, 24, 35, 42], percarbonate/Fe(III) [30] or peroxymonosulfate [31]. Contrarily, little information is found in the available literature regarding the use of ozone in photodegradation processes catalyzed by MIL-53(Fe) or other MOFs despite that some Fe-based MOFs has been recently reported as useful catalysts for the ozonation of Rhodamine B and salicylic acid [14, 50]. The studies carried out so far on the photodegradation of aqueous pollutants by MIL-53(Fe) have been mainly focused on the characterization and photocatalytic activity of the materials. However, much less attention has been paid to the MOF stability under

the oxidizing photocatalytic environment. Some authors claimed that MIL-53(Fe) is rather photostable after reusing a catalyst sample in some batch photodegradation cycles with minor loss of activity [15, 16, 21, 23, 24, 31] while others observed from moderate to serious decrease in the photocatalytic activity upon recycling [25-28, 32, 35, 36]. In most of these works, results of FTIR and XRD revealed no significant changes in the chemical and crystal structure of the catalyst after recycling. However, from little to no information was provided about iron leaching and stability of the linker (BDC) under photocatalytic conditions despite the fact that MIL-53(Fe) may decompose in water at a rate that depends on the pH and temperature of the media [51]. In addition, H_2BDC is known to react fast with photochemically generated hydroxyl radical ($k_{HO^{\bullet}}=4.4\times10^{9}$ $M^{-1}s^{-1}$) [52]. Accordingly, during MIL-53(Fe)-mediated photocatalytic processes, the BDC linker could be at risk of photogenerated $HO^{\bullet}$ attack, which might result in instability of the MOF. Recently, we have shown that the stability of other Fe-based MOF (MIL-100(Fe)) is a critical aspect to take into account before proposing it as a catalyst candidate for AOPs [53]. Therefore, it would be of interest to further investigate the stability of MIL-53(Fe) in order to explore its applications as photocatalyst in aqueous media.

3.1.2 Objectives and scope of this chapter

This study was conceived to evaluate the stability of MIL-53(Fe) in aqueous solution under typical conditions of solar photocatalytic oxidation. Thus, leaching of iron and organic matter from the MOF are evaluated at different process conditions. Photocatalytic activity of MIL-53(Fe) towards the degradation of phenol (Ph) and metoprolol (MTP) in the presence of different electron acceptors (hydrogen peroxide, potassium persulfate and ozone) is also addressed.

Table 3.1. Literature review on the performance of MIL-53(Fe) and MIL-53(Fe)-based composites as visible photocatalysts for the degradation of aqueous organic pollutants.

Catalyst	Radiation source	Catalyst conc.	Pollutant	Pollutant initial conc.	Irradiation time	Added oxidants (electron acceptors)	Pollutant removal	Fe leaching	Linker stability	Ref.
MIL-53(Fe)	Vis (λ>420 nm) (500 W Xe lamp)	10 mg L^{-1}	MB	0.4 mM	60 min	None H_2O_2 (0.01 mM) $(NH_4)_2S_2O_8$ (0.01 mM) $KBrO_3$ (0.01 mM)	~2% ~30% ~40% ~3%	NM	NM	[15]
MIL-53(Fe)	Vis (λ>420 nm) (500 W lamp)	0.4 g L^{-1}	RhB	10 mg L^{-1}	50 min	None H_2O_2 (20 mM)	62% 98%	NM	NM	[16]
MIL-53(Fe) MIL-53(Fe)/rGO (2.5 wt% rGO)	Vis (λ>420 nm) (250 W Na lamp)	5 mg L^{-1}	MB	30 mg L^{-1}	420 min	None	32% 49%	NM	NM	[17]
MIL-53(Fe)/rGO (5 wt% rGO)	Vis (λ>420 nm) (500 W Xe lamp)	0.4 g L^{-1}	RhB	10 mg L^{-1}	60 min	None H_2O_2 (20 mM)	42% ~100%	NM	NM	[18]
MIL-53(Fe)/Fe_3O_4	Vis (λ>420 nm) (500 W lamp)	0.4 g L^{-1}	RhB	10 mg L^{-1}	70 min	None H_2O_2 (20 mM)	55% 99%	NM	NM	[19]
MIL-53(Fe)	Vis (λ>410 nm) (300 W Xe lamp)	15 mg L^{-1}	MB	10 mg L^{-1}	100 min	None H_2O_2 (conc. NI)	~40% 70-100%			[20]
MIL-53(Fe)	Vis (λ>420 nm) (300 W Xe lamp)	1.0 g L^{-1}	MG	20 mg L^{-1}	40 min	None Cr(VI) (20 mg L^{-1})	25% ~100%	< 1.0 mg L^{-1} (pH=4)	NM	[21]
			RhB			None Cr(VI) (20 mg L^{-1})	44% 83%			
MIL-53(Fe) MIL-53(Fe)/Fe_3O_4 (11 wt% Fe_3O_4)	Vis (8 W lamp)	0.2 g L^{-1}	MB	10 mg L^{-1}	60 min	None	30% 52%	NM	NM	[22]
MIL-53(Fe)	Vis (λ>420 nm) (500 W Xe lamp)	0.1 g L^{-1}	CA	40 mg L^{-1}	240 min	None H_2O_2 (20 mM)	20% 98%	NM	NM	[23]
			CBZ			None H_2O_2 (20 mM)	7% 90%			
MIL-53(Fe)	Vis (λ=455 nm) LED lamp	0.6 g L^{-1}	AO7	0.05 mM	90 min	None $Na_2S_2O_8$ (2 mM)	24% >98%	0.37 mg L^{-1} (pH=6)	NM	[24]
MIL-53(Fe) MIL-53(Fe)/AER MIL-53(Fe)/CER	Vis (λ>420 nm) (400 W Xe lamp)	0.17 g L^{-1}	SRhB RhB SRh B RhB	3.3 mM	120 min	None	24% 85% 96% 97%	D/NQ	NM	[25]

Table 3.1 (Contd)

Catalyst	Radiation source	Catalyst conc.	Pollutant	Pollutant initial conc.	Irradiation time	Added oxidants (electron acceptors)	Pollutant removal	Fe leaching	Linker stability	Ref.
MIL-53(Fe)	Vis (λ>420 nm) (500 W Xe lamp	0.4 g L^{-1}	MB	10 mg L^{-1}	240 min	None	87%	NM	NM	[26]
MIL-53(Fe)/ γ-Fe_2O_3							72%			
MIL-53(Fe)	Vis (λ>400 nm) (500 W Xe lamp)	0.4 g L^{-1}	RhB	10 mg L^{-1}	120 min	None	<5%	NM	NM	[27]
MIL-53(Fe)/CdS (1:1.5 mass ratio)		1.0 g L^{-1}					86%			
MIL-53(Fe)	Vis (λ>420 nm) (300 W Xe lamp)	0.3 g L^{-1}	RhB	0.01 mM	120 min	None	~70%	NM	NM	[28]
MIL-53(Fe)/AgI (2:1 molar ratio)							~95%			
MIL-53(Fe)	Vis (λ>420 nm) (300 W Xe lamp)	0.5 g L^{-1}	TC	50 mg L^{-1}	180 min	None	41%	NM	NM	[29]
MIL-53(Fe)	Vis (λ=455 nm) LED lamp	0.2 g L^{-1}	SMT	0.02 mM	60 min	None	12%	NM	NM	[30]
						$Na_2CO_3 \cdot 1.5H_2O_2$/Fe(III) (0.2 mM/0.3 mM)	91%			
MIL-53(Fe)	Vis (LED lamp)	0.2 g L^{-1}	RhB	40 mg L^{-1}	20 min	None	~30%	NM	NM	[31]
						$KHSO_5$ (100 mgL^{-1})	~100%			
MIL-53(Fe)	Sunlight	0.5 g L^{-1}	2,4-D	45 mg L^{-1}	240 min	None	58%	D/NQ	NM	[32]
MIL-53(Fe)/WO_3							~100%			
MIL-53(Fe)	Vis (λ>420 nm) (500 W Xe lamp	0.4 g L^{-1}	RhB	10 mg L^{-1}	180 min	H_2O_2 (20 mM)	50-90%	NM	NM	[33]
MIL-53(Fe)	Vis (λ>420 nm) (500 W Xe lamp)	0.4 g L^{-1}	IBP	10 mg L^{-1}	120 min	None	~50%	NM	NM	[34]
MIL-53(Fe)/1T-MoS_2							~100%			
MIL-53(Fe)	Vis (λ>420 nm) (350 W Xe lamp)	0.5 g L^{-1}	RhB	20 mg L^{-1}	30 min	None	24%	NM	NM	[35]
						$K_2S_2O_8$ (0.5 gL^{-1})	50%			
MIL-53(Fe)/BiOCl						None	59%	NM	NM	
						$K_2S_2O_8$ (0.5 gL^{-1})	>99%			
MIL-53(Fe)	Vis (λ>420 nm) (300 W Xe lamp)	0.5 g L^{-1}	TC	20 mg L^{-1}	150 min	None	60%	NM	NM	[36]
MIL-53(Fe) (HCl modulated)							37-90%			
MIL-53(Fe)	Vis (λ>420 nm) (300 W Xe lamp	0.4 g L^{-1}	RhB	10 mg L^{-1}	72 min	None	~70%	NM	NM	[37]
			CBZ		100 min		80-95%			
MIL-53(Fe)/ BiOBr			RhB		72 min		~30%			
			CBZ		100 min		60-85%			

Table 3.1 (Contd)

Catalyst	Radiation source	Catalyst conc.	Pollutant	Pollutant initial conc.	Irradiation time	Added oxidants (electron acceptors)	Pollutant removal	Fe leaching	Linker stability	Ref.
MIL-53(Fe)	Vis (λ>420 nm) (35 W Xe lamp)	0.4 g L^{-1}	AB10B	10 mg L^{-1}	60 min	None	~85%	NM	NM	[38]
MIL-53(Fe)/α-Bi_2O_3/g-C_3N_4 (32% wt. MIL-53)							100%			
MIL-53(Fe)	Vis (λ>420 nm) (300 W Xe lamp	NI	TC	20 mg L^{-1}	60 min	None	25%	NM	NM	[39]
MIL-53(Fe)/Ag_3PO_4 (10:1 mass ratio)							76%			
MIL-53(Fe)	Vis (λ>420 nm) (500 W Xe lamp	0.4 g L^{-1}	IBP	10 mg L^{-1}	180 min	H_2O_2 (20 mM)	51%	NM	NM	[40]
MIL-53(Fe)/Fe_3O_4							78-100%			
MIL-53(Fe)	Vis (λ>420 nm) (500 W Xe lamp)	0.2 g L^{-1}	NOR	10 mg L^{-1}	90 min	None	42%	NM	NM	[41]
MIL-53(Fe)/GO/γ-Fe_2O_3							92%			
MIL-53(Fe)	Vis (λ>420 nm) (300 W Xe lamp)	0.2 g L^{-1}	TC-HCl	300 mgL^{-1}	80 min	None	17%	NM	NM	[42]
						$Na_2S_2O_8$ (8 mM)	~100%			
MIL-53(Fe)	Simulated sunlight (300 W Xe lamp)	0.66 g L^{-1}	RhB	20 mg L^{-1}	60 min	None	38%	NM	NM	[43]
						H_2O_2 (conc.NI)	52%			
			TC			None	78%			
						H_2O_2 (conc.NI)	88%			
MIL-53(Fe)/Ag_2S (1:0.3 mass ratio)			RhB			None	96%			
						H_2O_2 (conc.NI)	~100%			
			TC			None	94%			
						H_2O_2 (conc.NI)	~100%			
MIL-53(Fe)	Vis (λ>400 nm) (100 W High-pressure mercury vapor lamp)	0.2 g L^{-1}	MB	20 mg L^{-1}	120 min	None	61%	NM	NM	[44]
S^{2-}-doped MIL-53(Fe) (1% wt. S^{2-})							97%	NM	NM	

Nomenclature: Catalyst: GO= graphene oxide; rGO= reduced graphene oxide; AER=anionic exchange resin (Amberlite IRA-200); CER=cationic exchange resin (Amberlite IRA900)

Contaminant: MB= methylene blue; RhB= rhodamine B; MG= malachite green; CA= clofibric acid; CBZ= carbamazepine; AO7= Acid orange 7; 2,4-D=2,4-dichhlorophenoxyacetic acid; TC=tetracycline; TC-HCl= tetracycline hydrochloride; SRhB= sulforhodamine B; SMT= sulfamethazine; IBP=ibuprofen; NOR= norfloxacin;AB10B=amido black 10B

NM= Not measured; D/NQ= Detected but not quantified; NI= Not indicated

3.2 MATERIALS AND METHODS

3.2.1 Materials

All solvents and reagents were used as received without further purification. Iron (III) chloride 6-hydrate (>97%, CAS number 10025-77-1, Panreac), 1,4-benzenedicarboxylic acid (H_2BDC) (98%, CAS number 100-21-0, Sigma-Aldrich) and N,N-Dimethylformamide (DMF) (99%, CAS number 68-12-2, Panreac) were used in the synthesis of MIL-53(Fe). Metoprolol tartrate (>97%, CAS number 56392-17-7, Sigma-Aldrich) and phenol (>97%, CAS number 604-001-00-7, Sigma-Aldrich) were used as organic water pollutants in photodegradation runs. Hydrogen peroxide (30% w/v, CAS number 7722-84-1, Panreac) and potassium persulfate (>99%, CAS number 7727-21-1, Sigma-Aldrich) and ozone were used in some MIL-53(Fe) mediated photocatalytic tests. Ozone was produced in situ from pure oxygen by an ozone generator (Anseros Ozomat, COM-AD-02 model) and its concentration in the gas stream was measured with an Anseros Ozomat GM-6000Pro gas analyzer. All solutions were prepared in ultrapure water (Milli-Q Academic, Millipore, 18.2 MΩ cm).

3.2.2 Synthesis of MIL-53(Fe)

MIL-53(Fe) was prepared using a solvothermal method adapted from the literature [48]. A mixture of $FeCl_3 \cdot 6H_2O$ (10 mmol, 2.7 g), H_2BDC (10 mmol, 1.66 g) and DMF (50 mL) were stirred at room temperature for 30 min. Then, the mixture was introduced into a 125 mL Teflon-lined stainless steel autoclave (Parr Instrument Company), which was placed in an oven (P-Selecta) to be heated at 20 ºC min^{-1} up to 150 ºC and held at this temperature for 64 hours. After that, the reaction vessel was removed from the oven and allowed to cool down to

room temperature before recovering the solid by centrifugation at 4000 rpm for 5 min. The solid was thoroughly washed, first with methanol and then repeatedly with Milli-Q water. Then, it was suspended in 200 mL of Milli-Q water overnight to remove substances still retained in the pores. Finally, the obtained solid sample was dried in a rotary evaporator at 75 ºC under vacuum and then in an oven at 100 ºC for 1 h. The as-prepared catalyst was stored in a glass desiccator until further use.

3.2.3 Characterization of MIL-53(Fe)

Powder X-ray diffraction (XRD) was carried out on a Bruker D8 Advance diffractometer with Cu Kα radiation (λ=0.1541 nm). The XRD patterns were recorded in the 2θ range of 5-30º at a scan rate of 0.02 s^{-1} and time of accumulation of 1 s per point. Attenuated total reflectance mode- Fourier transform infrared transmission spectra (ATR-FTIR) were recorded in a Nicolet iS10 apparatus using KBr pellets containing about 10 mg of sample. The spectra were recorded in the wavelength 550-4000 cm^{-1} range at a resolution of 1 cm^{-1}. The BET surface area and porous structure of the synthesized MIL-53(Fe) were determined from N_2 adsorption-desorption isotherms obtained at -196ºC on an Autosorb 1 apparatus (Quantachrome). Prior to the analysis, the sample was outgassed in vacuum (<10^{-4} Pa) at 150 ºC for 10 h. Thermogravimetric analysis mass spectrometry (TGA-MS) was carried out on a thermobalance (STA 449 F3 Jupiter®, Netzsch) coupled with a spectrometer (QMS 403D Aëolos III, Netzsch) from 40 to 950 ºC using 50 mL min^{-1} of Ar/O_2 mixture (80/20 v/v) at a heating rate of 10 °C min^{-1}. UV-vis diffuse reflectance spectroscopy (UV-vis-DRS) measurements were carried out with a UV-vis-NIR Cary 500 spectrophotometer (Varian-Agilent Technologies) equipped with an integrating sphere device. Carbon and hydrogen contents of the MOF were determined using an elemental analyzer (TruSpec Micro, LECO) while iron content was analyzed

by wavelength dispersive X-ray fluorescence (S8 Tiger, Bruker). The morphology of samples was examined with a Hitachi S-4800 field-emission scanning electron microscope.

3.2.4 MIL-53(Fe) stability experiments

Stability tests of MIL-53(Fe) in water were performed in a 300 mL borosilicate glass vessel provided with magnetic agitation and ports for gas inlet, gas outlet and liquid sampling. This vessel was placed in the chamber of a solar box (Suntest CPS+, Atlas Material Testing Technology LLC) equipped with a 1500 W air-cooled Xe lamp. The overall irradiance (λ= 300-800 nm) at the photoreactor level was measured with a UV-vis spectrometer (Black Comet C, StellarNet) to be 581.4 W m^{-2}. In some instances, cut-off filters were used to restrict radiation to the visible range (λ=390-800 nm). The temperature of the simulator chamber was controlled at either 25 ºC or 40 ºC. Typically, the vessel was charged with 250 mL of Milli-Q water. If required, the initial pH of the solution was then adjusted to the desired value by adding aqueous solutions of 0.1 M H_2SO_4 or 0.1 M NaOH. Then, an amount of MIL-53(Fe) was added and the suspension was agitated by means of a magnetic stirrer. In some experiments, hydrogen peroxide or potassium persulfate was also added to the mixture. After that, the lamp of the solar box was turn on (if illumination was required) and, simultaneously, a 10 L h^{-1} gas flowrate of air or an oxygen-ozone mixture (c.a. 6 mg L^{-1} ozone concentration) was bubbled into the vessel through a porous diffuser. If illumination was not required in the experiment, the vessel was covered in aluminum foil. Once the runtime was elapsed, the solid was separated from the solution by vacuum filtration and dried overnight in an oven at 100 ºC. The supernatant aqueous solution was analyzed for pH, dissolved organic carbon (DOC), iron, H_2BDC and short-chain carboxylic acids (SCCAs). The recovered solid was analyzed by XRD and ATR-FTIR.

3.2.5 Photodegradation experiments

Photodegradation of aqueous solutions of Ph (25 mg L^{-1}) or MTP (50 mg L^{-1}) were carried out in the experimental device described above for MIL-53(Fe) stability tests. The procedure was also similar to that followed in stability tests though a 30-min dark stage (lamp switched off) was considered to allow for Ph or MTP adsorption onto the catalyst before starting the photodegradation stage [54]. Samples were periodically withdrawn from the reactor, filtered through 0.2 μm PET membranes and analyzed for pH, pollutant concentration (either Ph or MTP), DOC, H_2BDC and iron. If hydrogen peroxide, potassium persulfate or ozone was used as oxidant, its concertation in samples was also measured. Blank runs (i.e., without radiation or without catalyst) were also carried out.

3.2.6 Analytical methods

Liquid samples from stability and photodegradation runs were analyzed by different techniques: (i) H_2BDC, Ph and MTP concentrations were analyzed by an HPLC apparatus provided with a UV-vis detector set at 225 nm (HP 1100 Series chromatograph). A Kromasil C-18 column (5 μm, 150 mm length, 4 mm diameter) was used as stationary phase while the mobile phase consisted of a mixture of 0.1% vol. formic acid in ultrapure water (solvent A) and acetonitrile (solvent B) at a constant flowrate of 1 mL min^{-1}. The mobile phase program used for the analysis was as follows: start at 20% B; 0-6 min, linear gradient of B in A (20-27.5% B); 6-7 min, hold at 27.5% B, 7-8 min, linear gradient (27.5-20% B); 8-9 min, hold at 20% B. The retention times were 3.4 min (BDC), 4.1 min (MTP) and 6.5 min (Ph). (ii) DOC was analyzed with a Shimadzu apparatus (TOC-V CSH model). (iii) Some SCCAs (e.g. oxalic acid) were analyzed by ion chromatography using a Metrohm apparatus (881 Compact IC Pro model) provided with suppressor and conductivity detector. A MetroSep A Supp 5 column (150 mm length, 4 mm diameter), thermoregulated at 45 ºC, was used as

stationary phase. A 0.7 mL min^{-1} flowrate of aqueous Na_2CO_3 (linear gradient program at 20 min from 0.6 mM to 14.6 mM Na_2CO_3 in 50-minute analysis and 10 min post-time equilibration) was the mobile phase. (iv) Iron concentration was determined by a photometric method based on the formation of a trizaine derivative using the Spectroquant Iron Test (Merck Millipore). (v) Hydrogen peroxide was analyzed either by the cobalt carbonate method (conc. < 0.1 mg L^{-1}) or by the titanium sulfate method (conc. 0.1-50 mg L^{-1}) [55-56]. (vi) Persulfate concentration was measured by the iodometric titration method [57]. (vii) Ozone in aqueous solution was measured following the indigo trisulfonate colorimetric method [58]. (viii) Measurements of pH were made with a pH-meter (Crison GLP21+). All UV-vis spectrophotometric determinations were recorded on a Thermo Spectronic Helios α device (Thermo Fisher Scientific).

3.3 RESULTS AND DISCUSSION

3.3.1 Characterization of MIL-53(Fe)

Figure 3.1 shows the XRD patterns of the pale-orange powder synthesized in this work and three simulated MIL-53s, designated as MIL-53(Fe)-ht (anhydrous), MIL-53(Fe)-int (metastable anhydrous phase) and MIL-53(Fe)-It (hydrated) [59]. Simulation was carried out using the Mercury program from the Cambridge Crystallographic Data Center (CCDC). As can be seen, XRD peaks of the synthesized material match well with those of the hydrated MIL-53(Fe)-It at 2θ of 9.2º, 12.6º; 17.6º; 18.2º; 18.5º and 25.4º. The recorded XRD pattern is also in good agreement with those obtained by other authors for MIL-53(Fe) materials with visible-light photocatalytic activity [15, 21] and/or ability to activate the decomposition of hydrogen peroxide [9], persulfate [11, 13], peroxymonosulfate [31] or ozone [14] into ROS.

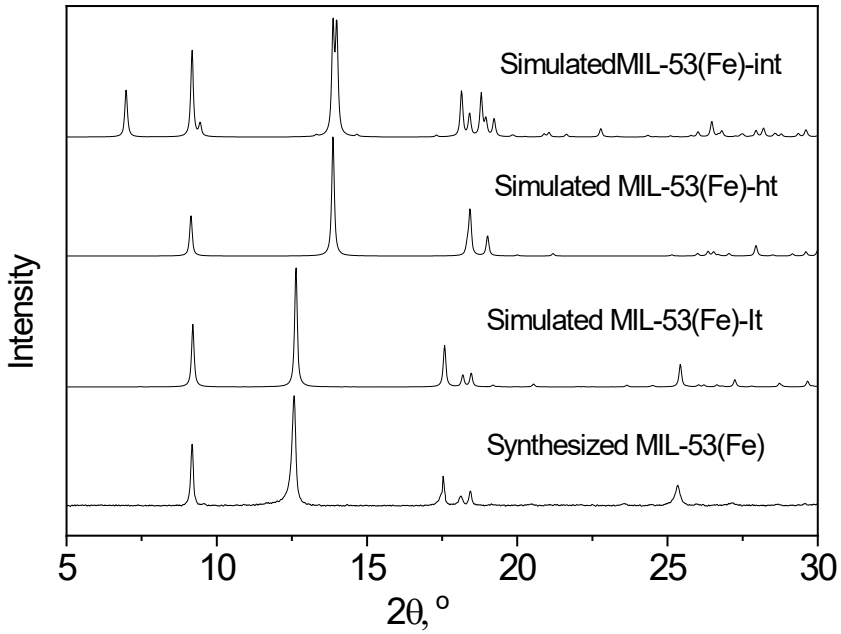

Figure 3.1. XRD patterns of the synthesized and three simulated MIL-53(Fe).

The nitrogen adsorption-desorption isotherm of the as-synthesized MIL-53(Fe) is presented in **Figure 3.2**. It displays the profile of mixed type I and IV isotherms, characteristic of microporous and mesoporous materials, respectively. The specific BET surface area (S_{BET}=79 $m^2 g^{-1}$) was obtained applying the BET equation to the section of the isotherm in the relative pressure range of 0.05-0.35, the microporous volume (V_{micro} = 0.012 $cm^3 g^{-1}$) and external surface area (S_{ext}=19 $m^2 g^{-1}$) were calculated by the t-plot method, and the total pore volume (V_T = 0.124 $cm^3 g^{-1}$) was estimated as the volume corresponding to the branch of desorption of the isotherm at a relative pressure of 0.96. In general, these values agree well with those reported in the literature for MIL-53(Fe), typically, with S_{BET} and V_T in the 15-90 $m^2 g^{-1}$ and 0.01-0.3 $cm^3 g^{-1}$ ranges, respectively [13].

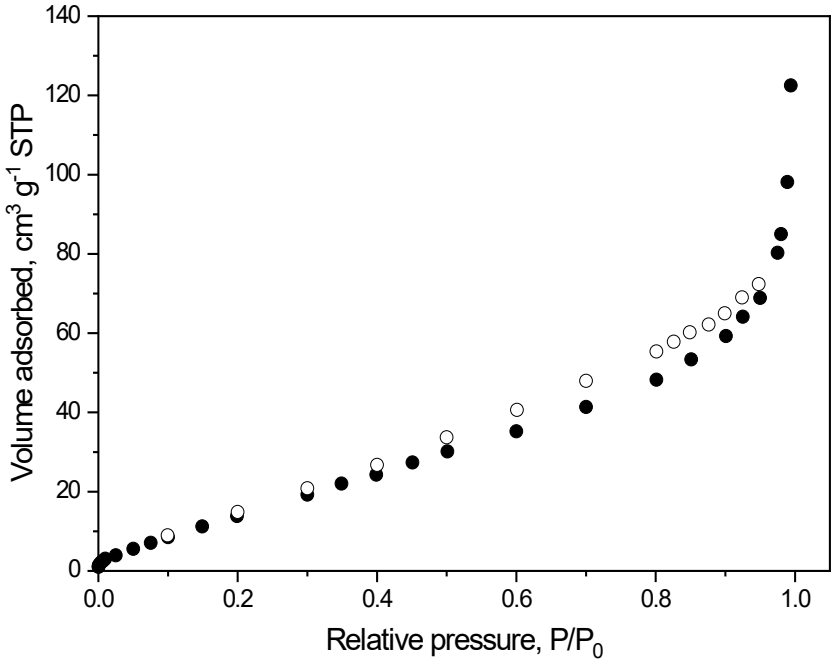

Figure 3.2. N_2 adsorption–desorption isotherm at −196 °C of the as-prepared MIL-53(Fe). Solid symbols: adsorption branch; Open symbols: desorption branch.

The morphology and particle size of the synthetized MIL-53(Fe) was evaluated by scanning electron microscopy (SEM). **Figure 3.3** reveals well-defined rod-like particles at micrometric scale in addition to smaller bulky irregular fragments, which is in agreement with MIL-53(Fe) polycrystals synthetized under solvothermal conditions, according to previously reported studies [9].

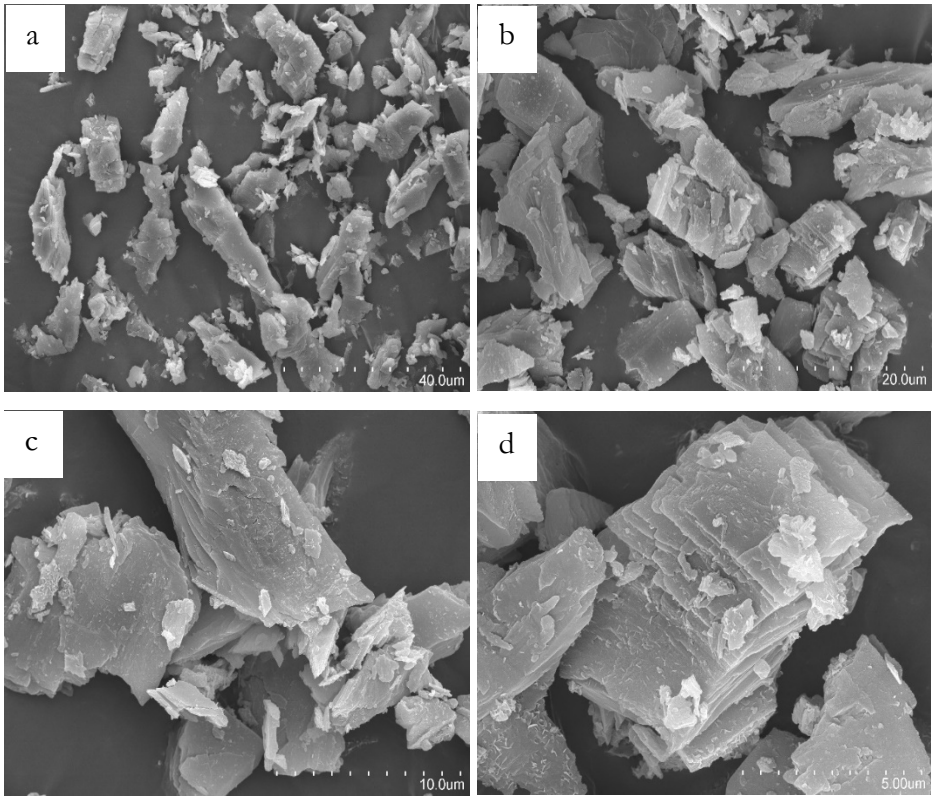

Figure 3.3. SEM images of the as-prepared MIL-53. Scale bar: (a) 40 μm; (b) 20 μm; (c) 10 μm; (d) 5 μm

Carbon and iron contents of the prepared MIL-53(Fe) were found to be 38.0 wt.% and 21.2 wt.%, as determined by elemental analysis and WDXRF, respectively, resulting in a Fe/C ratio of 0.558, which is slightly lower than the theoretical 0.581 corresponding to pure MIL-53(Fe)-It (i.e., $Fe^{III}(OH)[BDC]\cdot H_2O$). This suggests the presence of some free H_2BDC trapped in the MOF structure (c.a. 0.03 g free H_2BDC/g pure MIL-53(Fe)). The TGA profile presented in **Figure 3.4** shows a small gradual decrease of mass up to ca. 150 ºC due to the evaporation of adsorbed water (< 1% weight) and a sharp weight loss in the temperature range of 350-440 ºC. This latter is primarily associated with dehydration of MIL-53(Fe) and combustion of the framework as

deduced from the nature of evolved gases. Thus, the amount of carbon released as CO and CO_2 accounted for 38.5 wt.% of the initial mass, which is in close agreement with the elemental composition of the synthetized MOF. Moreover, the percentage of iron in the prepared MIL-53(Fe) estimated from the final residue of Fe_2O_3 was 21.0 wt.%, which is in agreement with WDXRF results.

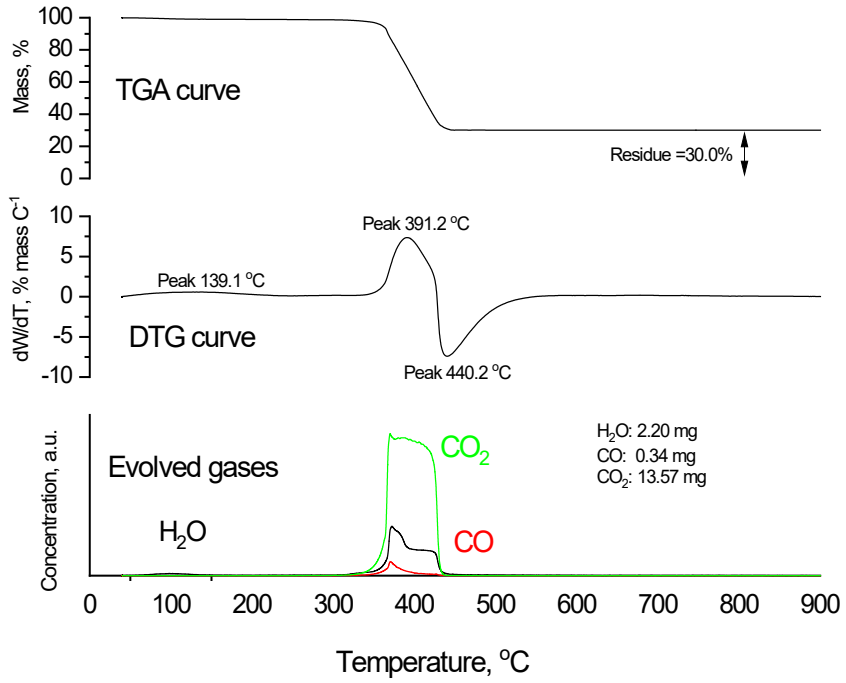

Figure 3.4. Thermal analysis of the as-prepared MIL-53(Fe).

Figure 3.5 shows the ATR-FTIR spectra of as-synthesized MIL-53(Fe) and H_2BDC samples in the 500-2000 cm^{-1} wavenumber range. In accordance with previous studies, a number of characteristic peaks due to different surface groups can be distinguished in the spectrum of MIL-53(Fe) [21, 30]. Thus, the band centered at 538 cm^{-1} corresponds to the stretching vibration of Fe-O bonds between the carboxylic group of the ligand and Fe(III); the sharp peak at 747 cm^{-1} is due to the C-H bending vibration of benzene rings of the linker; the broad

bands centered at 1380 cm^{-1} and 1535 cm^{-1} are ascribable to symmetric and asymmetric stretching vibrations of C-O bonds in carboxylic groups, respectively; the peak at 1632 cm^{-1} can be assigned to the C=O stretching vibration of carboxylic groups. In addition, the weak peak at 1694 cm^{-1} could be tentatively ascribed to a slight shift of the ν(C=O) vibration of carboxylic groups in free H_2BDC occluded within the pores of MIL-53(Fe) [60].

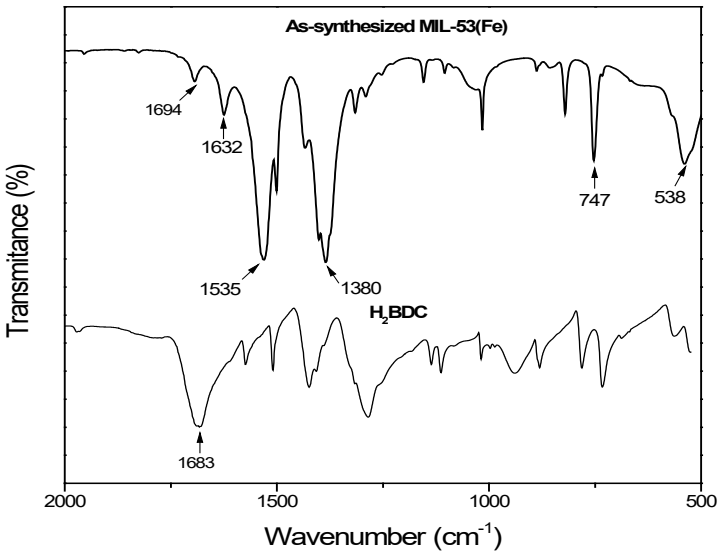

Figure 3.5. ATR-FTIR spectra of the as-synthesized MIL-53(Fe) and H_2BDC samples.

The UV-vis-DRS of the obtained MIL-53(Fe) shown in **Figure 3.6** displays two main absorption bands at ca. 220 nm and 445 nm, which can be ascribed to the ligand-to-metal charge transfer and to the spin-allowed d-d transition ($^6A_{1g} \rightarrow {}^4A_{1g} + {}^4E_g(G)$) of octahedral Fe^{3+} in MIL-53(Fe) [15, 25, 41]. The optical band gap energy (E_g) was estimated from a plot of $(\alpha h\nu)^2$ vs. the energy of absorbed light (inset of **Figure 3.6**) to be 2.7 eV, which reveals the ability of the MOF to

harvest visible light. This E_g value agrees with most of the previous studies of optical properties of pure MIL-53(Fe) [15, 18, 20-23, 25, 27, 28, 32, 34, 40-42, 46].

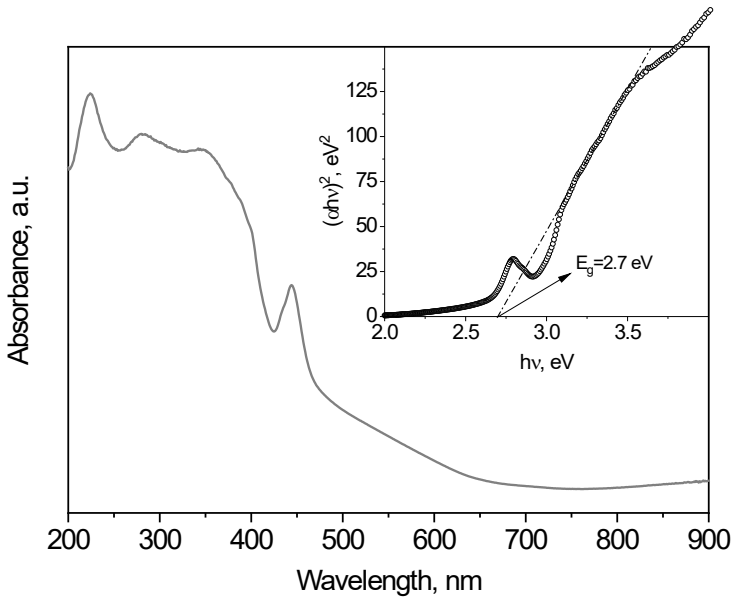

Figure 3.6. UV-vis diffuse reflectance spectrum of the as-prepared MIL-53(Fe).

Based on the characterization data shown above, which are in good agreement with the literature on the MIL-53 (Fe) framework, it can be concluded that MIL-53(Fe) was successfully synthesized, though some free H_2BDC remained clogged in the pore network of the MOF.

3.3.2 Stability of MIL-53(Fe) in Water. Effect of pH, Radiation and Presence of Oxidants

MIL-53(Fe) has been generally considered to be an iron-carboxylate framework with appreciable stability in water. Consequently, this MOF has been investigated in adsorption and photocatalytic degradation of aqueous pollutants

[6-7, 61]. However, it has also been observed that MIL-53(Fe) may undergo hydrolysis to some extent in deionized water at 50 ºC and in a controlled pH = 7 aqueous solution at ambient temperature, according to Eq. (3.1) [51]:

$$2\ Fe(OH)[BDC]\cdot H_2O + 3\ H_2O \rightarrow Fe_2O_3\cdot 2\ H_2O + 2\ H_2BDC \qquad (3.1)$$

To further explore this controversy, which would affect the potential application of MIL-53(Fe) as photocatalyst for the degradation of water pollutants, a series of MIL-53(Fe) stability experiments were carried out in water.

3.3.2.1 Effect of Aqueous pH

First, the effect of pH on the stability of MIL-53(Fe) in water at 25 ºC was investigated. **Figure 3.7** displays XRD results of samples after being soaked in different pH Milli-Q water for 20 days. Regardless of the initial pH, the XRD patterns remained unchanged after exposure of MIL-53(Fe) to water, suggesting retained crystallinity. Additionally, no drastic changes were appreciated in FT-IR results. However, a noticeable color change of the solid, from pale-orange to reddish-brown, was observed after the test carried out at initial pH = 10 (**Figure 3.7**), which is a sign of the formation of hydrated iron species.

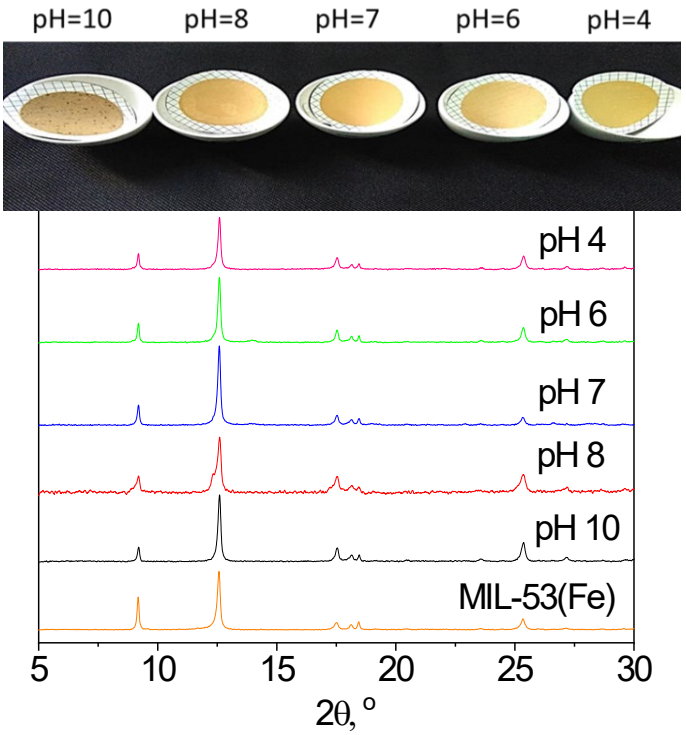

Figure 3.7. Effect of initial pH on the color transformation (up) and XRD patterns (down) of the synthesized MIL-53(Fe) before and after exposure to water at 25 ºC for 20 days.

Figure 3.8 shows the percentages of iron and carbon leached out from MIL-53(Fe) samples after prolonged contact with water. All DOC found in solution in each experiment was due only to H_2BDC molecules displaced from the solid, thus ruling out the formation of other carbonaceous products from the hydrolysis reaction. From **Figure 3.8,** it is apparent that MIL-53(Fe) stability decreased with initial pH, as the hydrolysis reaction of the MIL-53 structure was favored at alkaline conditions [62]. Thus, as much as 5% and 12% of iron and carbon, respectively, were leached out from the solid at pH = 10, whereas at pH = 4 little DOC (1.8 mg L^{-1}, i.e., 3.1 mg L^{-1} H_2BDC) and negligible iron (< 0.15 mg L^{-1}) were found in solution. Nevertheless, it should be taken into account that iron in solution might underestimate the actual amount of this metal withdrawn from

the MIL-53(Fe) structure since small papers of free iron oxides species (e.g., amorphous oxyhydroxides) resulting from partial hydrolysis of the framework could be deposited on the surface of MIL-53(Fe) [51]. The negative effect of the pH on the water stability of MIL-53(Fe) here found agrees with that recently reported for other iron-carboxylate MOF, namely MIL-100(Fe) [53]. Accordingly, pH must be controlled in the acidic range to hinder the hydrolysis of iron-carboxylate frameworks to some extent.

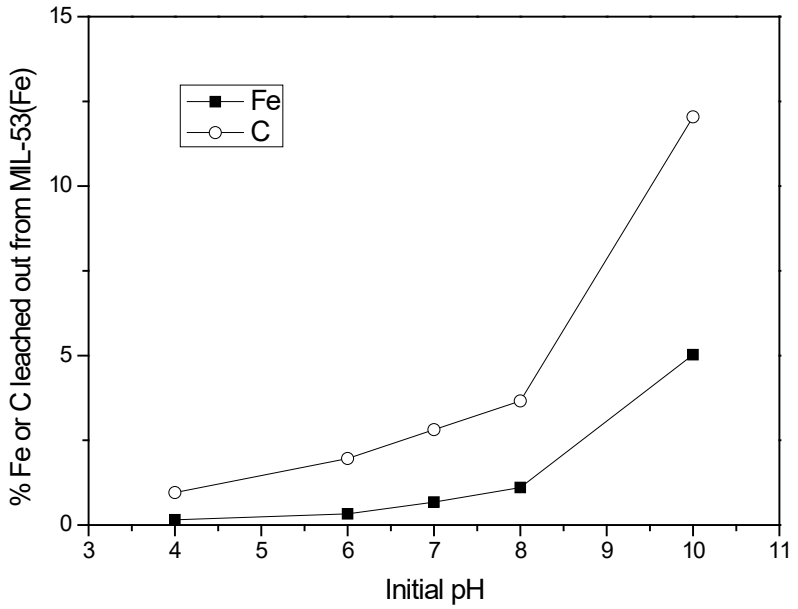

Figure 3.8. Effect of initial pH on the percentages of iron and carbon leached out from MIL-53(Fe) after exposure to water at 25ºC for 20 days.

3.3.2.2 Effect of UV-vis Radiation and Temperature

A series of experiments where MIL-53(Fe) samples were soaked in Milli-Q water at initial pH = 4.5 and constant temperature for 7 h was carried out to examine the impact of temperature (25 ºC and 40 ºC) and radiation (solar and visible radiation) on the stability of MIL-53(Fe). Aqueous pH slightly decreased

throughout all the tests in the 4.5-4.1 range. As shown in **Figure 3.9**, the amounts of iron and carbon leached out from MIL-53(Fe) were affected by both temperature and radiation. In the absence of radiation, temperature exerted a negative impact on MIL-53(Fe) stability likely because of increases in the rate of the hydrolysis reaction (3.1) and in H_2BDC solubility. Both, visible and simulated solar radiation, also accelerated the leaching of carbon and iron from the framework structure, being the effect of solar radiation stronger. This suggests that the photogeneration of holes (h^+) and ROS from MIL-53(Fe) activation under visible or solar radiation might contribute to decarboxylation of the MOF to some extent:

$$\text{MIL-53(Fe)} + h\cdot\nu \rightarrow \text{MIL-53(Fe)}\ (e^-,h^+) \quad (3.2)$$

$$H_2O + h^+ \rightarrow HO^\bullet + H^+ \quad (3.3)$$

$$O_2 + e^- \rightarrow {}^\bullet O_2^- \quad (3.4)$$

$$2\ {}^\bullet O_2^- + 2\ H^+ \rightarrow H_2O_2 + O_2 \quad (3.5)$$

$$H_2O_2 + {}^\bullet O_2^- \rightarrow OH^- + HO^\bullet + O_2 \quad (3.6)$$

$$H_2O_2 + e^- \rightarrow OH^- + HO^\bullet \quad (3.7)$$

$$Fe(OH)[BDC]\cdot H_2O + h+/{}^\bullet O_2^-/\ HO^\bullet \rightarrow H_2BDC + \text{Iron oxide species} \quad (3.8)$$

Furthermore, photogenerated $HO^\bullet$ would attack aqueous H_2BDC to form intermediate products such as SCCAs eventually yielding CO_2 and H_2O [52]:

$$H_2BDC + HO^\bullet \rightarrow H_2BDC\text{-}OH \rightarrow \ldots \rightarrow \text{SCCAs} \rightarrow CO_2 + H_2O \quad (3.9)$$

It is interesting to note that in the runs carried out in the dark, all DOC belonged to aqueous H_2BDC, while in experiments carried out in the presence of visible and simulated solar radiation, H_2BDC in solution accounted for 86.3 %

and 82.4 % of overall DOC, respectively. Accordingly, accumulation of some H_2BDC degradation products (e.g., SCCAs) took place to some extent only in irradiated runs, suggesting the formation of $HO^{\bullet}$ upon MIL-53(Fe) illumination. It should be mentioned that the generated SCCAs might also contribute to iron leaching through organic complexation of Fe(III) (e.g., ferric-oxalate complexes) [63]. To investigate this effect, another MIL-53(Fe) stability run was conducted at 25 ºC in the dark adding 2.5 mg L^{-1} oxalic acid to the solution. **Figure 3.9** reveals that the presence of oxalic acid three folded and ten folded the amounts of carbon and iron released from MIL-53(Fe) to water compared to the blank run. Moreover, the H_2BDC/Fe molar ratio found in solution after the run carried out with oxalic acid was 1.1 (close to the 1:1 MIL-53(Fe) stoichiometry) while in the absence of oxalic acid the ratio was as high as 6.7 (25 ºC) and 6.0 (40 ºC). This clearly suggests that in the presence of oxalic acid all iron extracted from MIL-53(Fe) was transferred to the aqueous phase as highly soluble ferric-oxalate complexes.

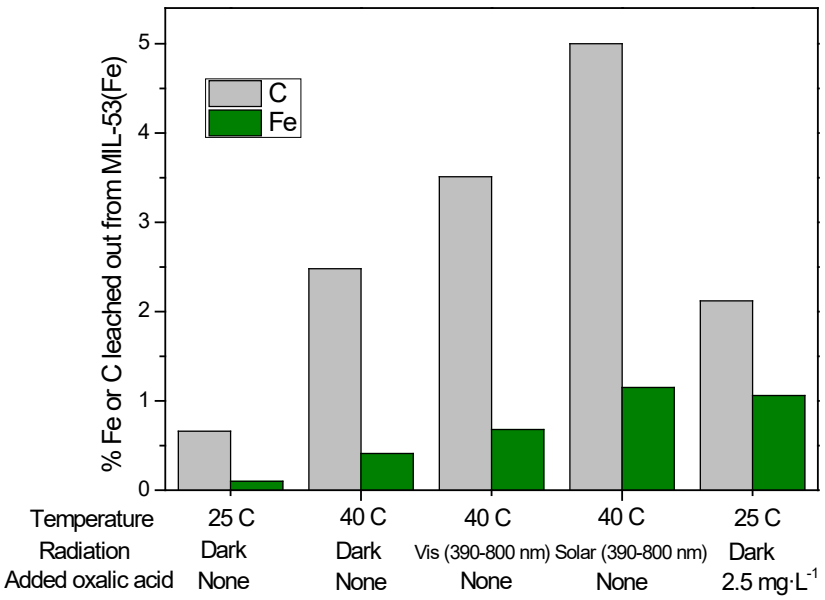

Figure 3.9. Effect of temperature and radiation on the percentage of iron and carbon leached out from MIL-53(Fe) after exposure to water for 7 h.

Despite the clear evidence of photo-decarboxylation of the BDC linker, XRD patterns and FTIR spectra peaks of an irradiated MIL-53(Fe) sample exhibited no apparent changes in the position and relative intensity respect to fresh MIL-53(Fe) as shown in **Figure 3.10**. In agreement with these results, other researchers have also found that decarboxylation of terephthalate-based MOFs is not frequently reflected in XRD and FTIR results [64].

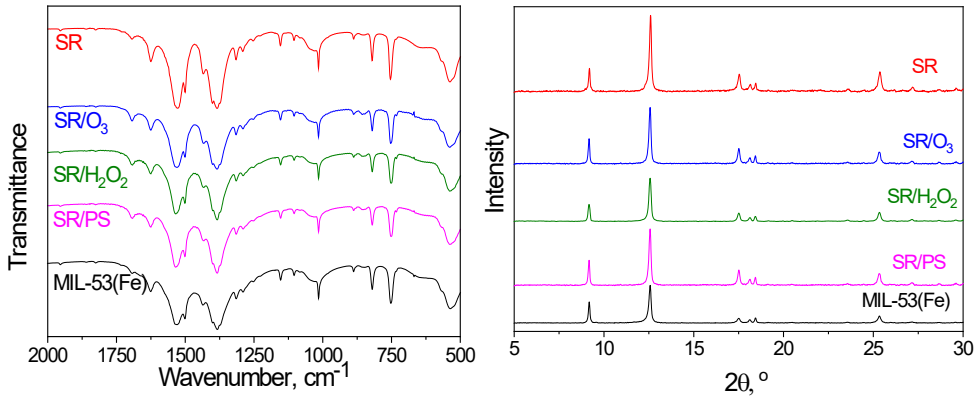

(a) **(b)**

Figure 3.10. ATR-FTIR spectra (a) and XRD patterns (b) of MIL-53(Fe) after exposure to radiation and oxidants. MIL-53(Fe) treatment conditions: SR = Simulated solar radiation for 7 h; SR/O_3 = Simulated solar radiation/ozone (1 mg min^{-1}) for 1 h; SR/H_2O_2 = Simulated solar radiation/hydrogen peroxide (75 mM) for 1 h; SR/PS= Simulated solar radiation/potassium persulfate (2.5 mM) for 1 h.

3.3.2.3 Effect of Oxidants: Hydrogen Peroxide, Persulfate and Ozone

The fast recombination of photogenerated electrons and holes in MIL-53(Fe) usually leads to unsatisfactory photocatalytic efficiency. To reduce this charge carrier recombination the use of some oxidants (i.e., electron acceptors), such as hydrogen peroxide or persulfate, has been frequently considered in research studies to enhance the photodegradation of water pollutants (see **Table 3.1**). However, the oxidation power of these species and the enhanced generation of ROS might compromise MIL-53(Fe) stability. **Figure 3.11** shows the evolution

of the concentrations of aqueous iron, H_2BDC and SCCAs during MIL-53(Fe) photostability tests performed at 40 ºC and pH = 4.0-4.5 under simulated solar radiation in the presence of hydrogen peroxide, persulfate (PS) or ozone. Results clearly demonstrate that all the tested oxidants accelerated the leaching of iron and H_2BDC out of MIL-53(Fe). In the absence of added oxidant, solar radiation provoked a steadily release of both linker and metal with a constant H_2BDC/Fe molar ratio of about 4 and negligible formation of SCCAs as oxidation products. However, the incorporation of electron acceptors (i.e., H_2O_2, PS or O_3) to the photocatalytic process led to an increased generation of ROS, particularly $HO^{\bullet}$ and, as a consequence, partial removal of the released linker. Accordingly, H_2BDC concentration profiles in **Figure 3.11** show a peak concentration at the beginning of the experiments followed by a continuous decline likely due to $HO^{\bullet}$ attack to H_2BDC, which is a known probe for photochemically generated hydroxyl radicals [52]. In addition to reactions (3.2) to (3.7), the production of ROS in MIL-53(Fe) photocatalytic processes aided by oxidants can be explained by the following sets of reactions:

Hydrogen peroxide [16]:

$$\text{MIL-53}(Fe^{3+}) + H_2O_2 \rightarrow \text{MIL-53}(Fe^{2+}) + H^+ + HO_2^{\bullet} \quad (3.10)$$

$$\text{MIL-53}(Fe^{2+}) + H_2O_2 \rightarrow \text{MIL-53}(Fe^{3+}) + OH^- + HO^{\bullet} \quad (3.11)$$

$$HO_2^{\bullet} + OH^- \rightarrow {}^{\bullet}O_2^- + H_2O \quad (3.12)$$

Persulfate [42]:

$$\text{MIL-53}(Fe^{3+}) + S_2O_8^{2-} \rightarrow \text{MIL-53}(Fe^{2+}) + S_2O_8^{-\bullet} \quad (3.13)$$

$$\text{MIL-53}(Fe^{2+}) + S_2O_8^{2-} \rightarrow \text{MIL-53}(Fe^{2+}) + SO_4^{-\bullet} + SO_4^{2-} \quad (3.14)$$

$$S_2O_8^{2-} + e^- \rightarrow SO_4^{-\bullet} + SO_4^{2-} \quad (3.15)$$

$$SO_4^{-\bullet} + H_2O \rightarrow SO_4^{2-} + HO^{\bullet} + H^+ \quad (3.16)$$

$$S_2O_8^{2-} + h\upsilon \rightarrow 2\,SO_4^{-\bullet} \quad (3.17)$$

Ozone [53,60]:

$$\text{MIL-53}(Fe^{3+}) + O_3 + OH^- \rightarrow \text{MIL-53}(Fe^{2+}) + HO_2^{\bullet} + {}^1O_2 \quad (3.18)$$

$$\text{MIL-53}(Fe^{2+}) + O_3 + H_2O \rightarrow \text{MIL-53}(Fe^{3+}) + OH^- + HO^{\bullet} + O_2 \quad (3.19)$$

$$O_3 + e^- + H_2O \rightarrow {}^1O_2 + {}^{\bullet}O_2^- + HO^{\bullet} \quad (3.20)$$

$$O_3 + H_2O + h\upsilon \rightarrow {}^1O_2 + H_2O_2 \quad (3.21)$$

The degradation of aqueous H_2BDC by ROS resulted in the accumulation of SCCAs in solution as shown in **Figure 3.11**. This is in agreement with previous studies where some SCCAs such as muconic acid, fumaric acid, maleic acid or oxalic acid were identified as products of advanced oxidation of aqueous H_2BDC [66, 67]. The generated SCCAs might also contribute to prevent iron precipitation and to enhance the production of ROS through organic complexation of Fe(III) (e.g., ferric-oxalate complexes). Under UV-vis radiation, Fe(III)-carboxylate complexes can undergo photolysis with formation of $HO^{\bullet}$ and $HO_2^{\bullet}/{}^{\bullet}O_2^-$ [68], activate PS decomposition into $SO_4^{\bullet-}$ and $HO^{\bullet}$ [69] or improve the $HO^{\bullet}$ yield in photo-Fenton-like and photo-ozonation processes [70, 71]. Moreover, as discussed above, some SCCAs such as oxalate have the ability to extract iron from solids through complex formation. In line with this, **Figure 3.11** shows that dissolved iron concentration in runs carried out in the presence of oxidants increased specially after 20 min when the concentration of SCCAs started to be significant.

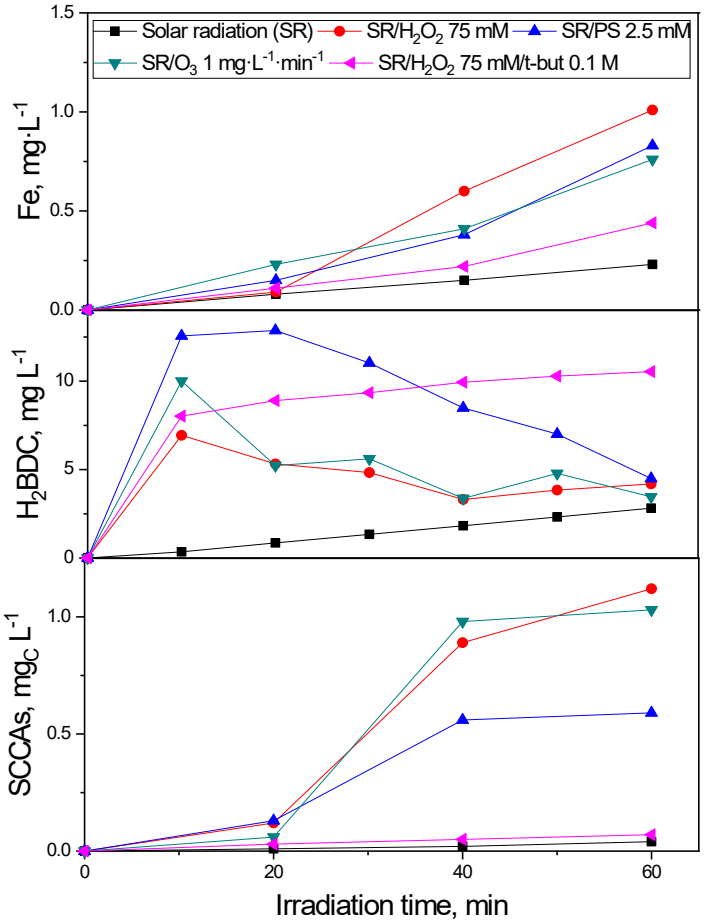

Figure 3.11. Effect of oxidants on the photostability of MIL-53(Fe) in water. Nomenclature of runs as in **Figure 3.10**.

To further investigate the effect of photogenerated HO• on MIL-53(Fe) stability, a test was run under solar radiation with added H_2O_2 (75 mM) and tert-butanol (100 mM), a powerful HO• scavenger. As it can be seen in **Figure 3.11**, the quenching of HO• by tert-butanol drastically decreased the amount of iron released from MIL-53(Fe) to que aqueous medium compared to the parallel experiment carried out with H_2O_2 but in the absence of tert-butanol. Moreover, because of the HO• scavenging effect of tert-butanol a steadily accumulation of H_2BDC and practically no formation of SCCAs were observed along the experiment. These findings suggest that photogenerated HO• might attack iron nodes of MIL-53(Fe) leading to the release of both iron and linker to solution.

Samples of MIL-53(Fe) were examined by XRD and ATR-FTIR after being exposed to solar radiation and H_2O_2, PS or O_3 for 1 h. The results displayed in **Figure 3.10** show no appreciable changes in XRD patterns and ATR-FTIR spectra compared to those of fresh MIL-53(Fe). Therefore, the observed instability of MIL-53(Fe) under oxidizing environment evidenced in **Figure 3.11** is not appreciated in XRD and ATR-FTIR results.

3.3.3 Photocatalytic Activity of MIL-53(Fe) under Simulated Solar Radiation

The photocatalytic performance of the as-prepared MIL-53(Fe) was evaluated by the removal of aqueous Ph and MTP. Hydrogen peroxide, persulfate and ozone were used in some experiments to accelerate the degradation process. **Figure 3.12** shows the removal of both target pollutants during 3 h of exposure to simulated solar radiation. Before irradiation, an initial stage was considered in the absence of simulated solar radiation and oxidant to allow for Ph or MTP adsorption onto MIL-53(Fe). However, as little as 1.1 mg Ph/g MIL-53(Fe) and 2.1 mg MTP/g MIL-53(Fe) (average values) were adsorbed onto MIL-53(Fe) after the 30-minute dark stage. Moreover, the synthetized MIL-53(Fe) demonstrated low photocatalytic activity towards the degradation of Ph and MTP under simulated solar radiation in the absence of added oxidants with only 8.5% Ph removal and 9.5% MTP removal after 3 h of irradiation. This low photodegradation rate can be ascribed to a fast electron-hole recombination [15]. The addition of any oxidant greatly enhanced the photodegradation rate leading to complete removal of Ph and MTP in less than 2 h. The added oxidants (H_2O_2, PS or O_3) might play several roles leading to the acceleration of Ph and MTP removal rates: (i) direct attack of the oxidant to the target pollutants; (ii) MIL-53(Fe) mediated catalytic degradation of pollutants (non-photocatalytic routes); (iii) enhancement of photocatalytic degradation routes.

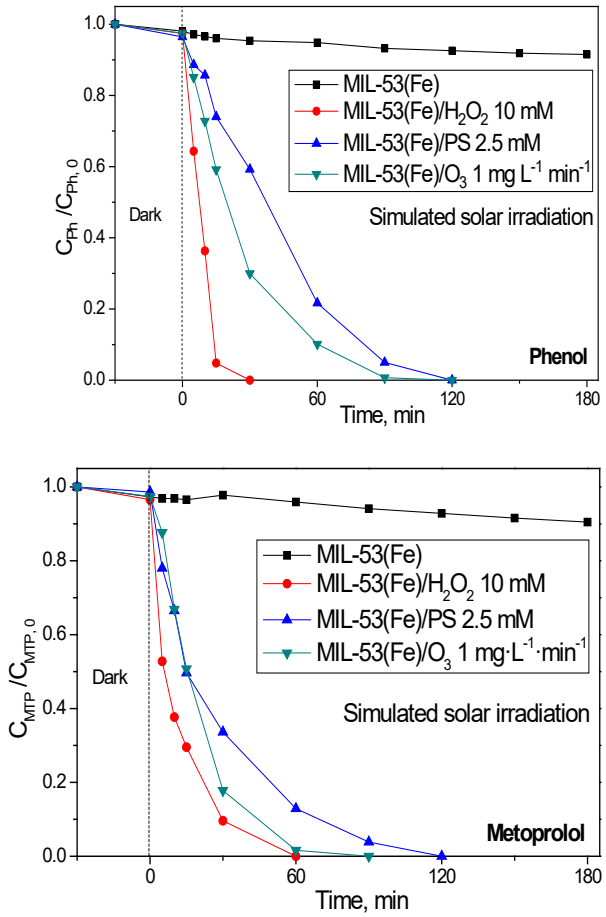

Figure 3.12. Photodegradation of phenol (Ph) and metoprolol (MTP) under simulated solar radiation in different MIL-53(Fe) catalytic systems. Experimental conditions: MIL-53(Fe) concentration =0.6 g L^{-1}; Pollutant initial concentration: Ph 25 mg L^{-1}, MTP 50 mg L^{-1}; pH = 4-5.

In **Figure 3.13** it can be appreciated that neither simulated solar radiation nor MIL-53(Fe) had any improving effect on the removal rate of Ph and MTP by ozonation. Taking into account the high rate constants between molecular ozone and both organic compounds at the working pH (i.e., 1.3 mM^{-1} s^{-1} and 1.4 mM^{-1} s^{-1} for Ph and MTP, respectively [72, 73]), the results of **Figure 3.13** clearly suggest that both contaminants were primarily removed by direct ozonation. Moreover, no ozone was found in solution during the first 60 min of reaction indicating that a fast kinetic regime of ozone absorption developed in this period.

Accordingly, reactions would take place in the liquid film close to the gas-liquid interface regardless of the irradiation or the use of MIL-53(Fe) as photocatalyst. At reaction time longer than ca. 1 h, when fast-reacting ozone compounds were eliminated, ozone started to accumulate in solution. Then, ROS formation from ozone reactions in water (3.18) to (3.21) would develop. Accordingly, both solar radiation and MIL-53(Fe) would favor the generation of ROS involved in the degradation mechanism [14, 67]. As a result, irradiation enhanced DOC removal, as can be observed in **Figure 3.13,** and low concentration of SCCAs was found in the treated water (not shown). However, **Figure 3.13** evidences poorer results in terms of DOC removal for the MIL-53(Fe)/SR/O_3 system than for the SR/O_3. The negative effect of MIL-53(Fe) can be ascribed to the decarboxylation of the MOF in the presence of ozone as discussed in Section 3.3.2.3. The leaching of H_2BDC ligand molecules out of the solid led to an increased content of organic matter in solution, which competed with Ph or MTP degradation products for ROS.

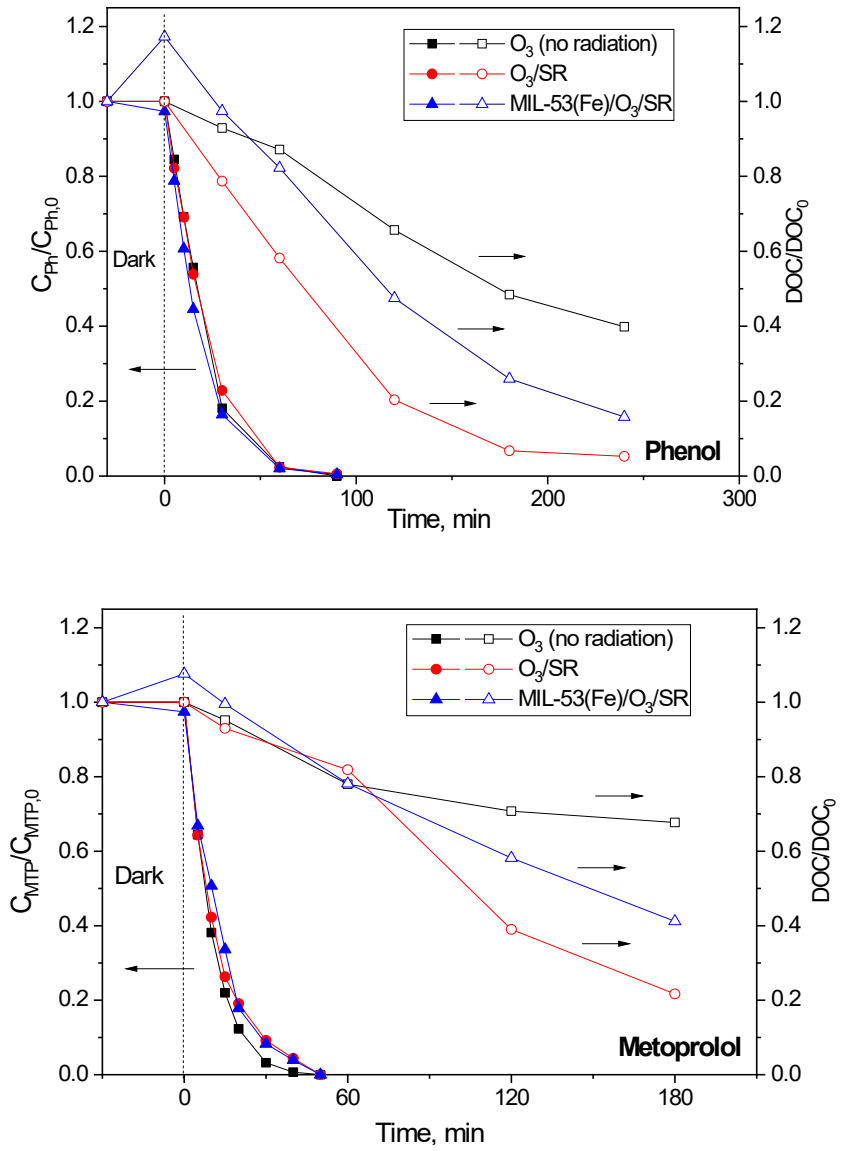

Figure 3.13. Effect of simulated solar radiation and MIL-53(Fe) on the ozonation of aqueous phenol (Ph) and metoprolol (MTP). Experimental conditions: MIL-53(Fe) concentration (if used) =0.6 g L^{-1}; initial concentration: Ph 25 mg L^{-1}, MTP 50 mg L^{-1}; pH = 4-5; Ozone dosage: 1 mg min^{-1}.

Figure 3.14 reveals that PS on its own (PS/dark) could not remove Ph or MTP to any extent. However, simulated solar light activated PS leading to almost complete disappearance of Ph and MTP after 3 h of irradiation. At the working

pH (4-5), $SO_4^{-\bullet}$ is believed to be the major contributing radical responsible for the destruction of the organic contaminants in the PS/SR system [74]. Accordingly, both Ph and MTP, with comparable $SO_4^{-\bullet}$ rate constant values ($k_{Ph} = 8.8\times10^{10}$ M^{-1} s^{-1} [75] and $k_{MTP} = 1.0\times10^{10}$ M^{-1} s^{-1} [76]), showed similar removal profiles. When MIL-53(Fe) was used in combination with simulated solar radiation and PS, better photocatalytic performance in terms of Ph and MTP removal rates was obtained as illustrated in **Figure 3.14**. MIL-53(Fe) is reported to directly activate PS leading to $SO_4^{-\bullet}$, $^{\bullet}O_2^-$ and $HO^{\bullet}$ in aqueous acidic media [13]. However, PS activation could also be induced by Fe(III) species leached out from MIL-53(Fe) such as iron oxyhydroxides and dissolved Fe^{3+} [77]. Furthermore, electron-hole recombination is avoided to some extent through reaction (3.15) [24, 35]. As a consequence, the formation of ROS with the MIL-53(Fe)/PS/RS combination was favored compared to MIL-53(Fe)/SR, MIL-53(Fe)/PS or PS/SR systems.

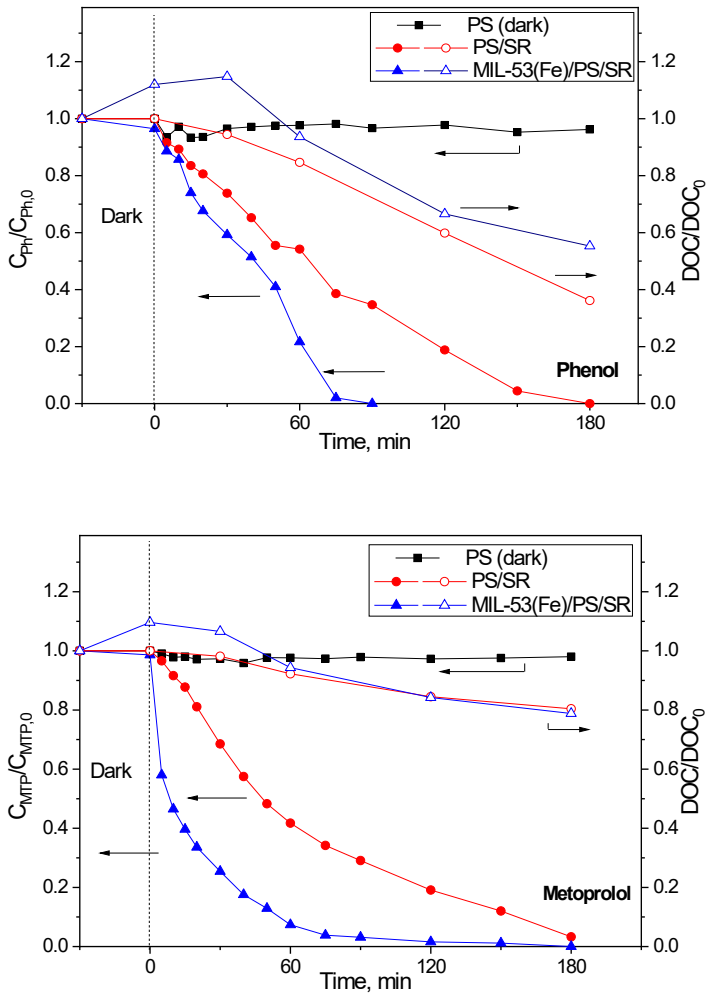

Figure 3.14. Effect of simulated solar radiation and MIL-53(Fe) on the oxidation of aqueous phenol (Ph) and metoprolol (MTP) by PS. Experimental conditions: MIL-53(Fe) concentration (if used) =0.6 g L^{-1}; initial concentration: Ph 25 mg L^{-1}, MTP 50 mg L^{-1}; pH = 4-5; PS initial concentration= 2.5 mM.

The effect of H_2O_2 on the degradation of Ph and MTP is illustrated in **Figure 3.15**. It is clearly seen that the H_2O_2/SR system barely eliminated 10% of the target pollutants in 3 h of reaction despite the fact that hydrogen peroxide may undergo photolytic breakdown into ROS under illumination by solar radiation [65]. However, the MIL-53(Fe)/H_2O_2 processes both in the dark and under

simulated solar radiation led to complete removal of the pollutants in less than 2 h and 1 h, respectively.

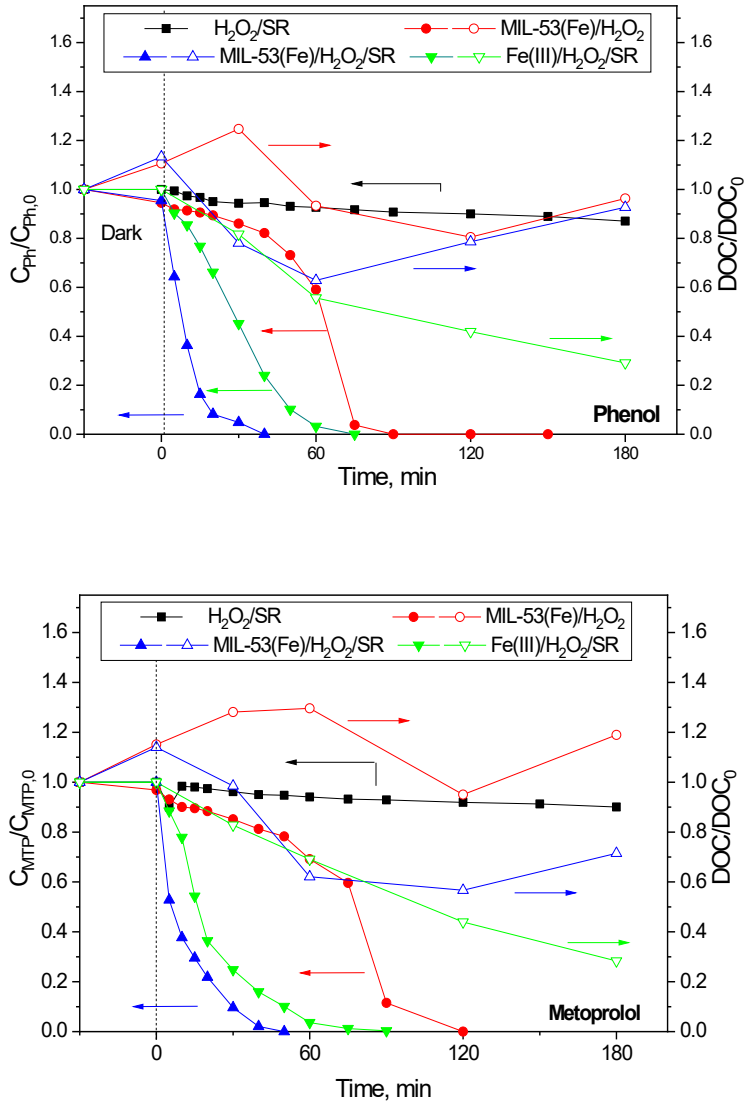

Figure 3.15. Degradation of aqueous phenol (Ph) and metoprolol (MTP) by H_2O_2 assisted catalytic and photocatalytic processes. Experimental conditions: MIL-53(Fe) concentration (if used) =0.6 g L^{-1}; initial concentration: Ph 25 mg L^{-1}, MTP 50 mg L^{-1}; pH = 4-5; H_2O_2 initial concentration: 10 mM; Fe(III) initial concentration (if used): 0.5 mg L^{-1}.

It is interesting to note in **Figure 3.15** that the shape of any pollutant decay profile differs significantly between Fenton-like (MIL-53(Fe)/H_2O_2) and photo-Fenton like (MIL-53(Fe)/H_2O_2/SR) experiments. Such difference is also reflected in the H_2O_2 concentration profiles shown in **Figure 3.16.** The inverted S-shaped curve observed in MIL-53(Fe)/H_2O_2 runs carried in the dark suggests that the role of MIL-53(Fe) as a heterogeneous Fenton-like catalysts was not significant (i.e., reactions (3.10) and (3.11) would be rather slow). Accordingly, minor pollutant removal and H_2O_2 consumption were observed within the first 30 minutes of reaction when the concentration of iron in solution was still low (< 0.5 mg L^{-1}) (see **Figure 3.16**). As the run progressed, increasing amounts of iron leached out from MIL-53(Fe) into solution, thus favoring the homogeneous Fenton-like reactions [78]:

$$Fe^{3+} + H_2O_2 \rightarrow Fe^{2+} + HO_2^{\bullet} + H^+ \ (k_{22} = 10^{-2}\ M^{-1}\ s^{-1}) \qquad (3.22)$$

$$Fe^{2+} + H_2O_2 \rightarrow Fe^{3+} + OH^- + HO^{\bullet} \ (k_{23} = 76\ M^{-1}\ s^{-1}) \qquad (3.23)$$

$$Fe^{2+} + HO^{\bullet} \rightarrow Fe^{2+} + OH^- \quad (k_{24} = 4.3\times10^{8}\ M^{-1}\ s^{-1}) \qquad (3.24)$$

Furthermore, partial oxidation of the parent compound (i.e., Ph or MTP) by generated ROS (i.e., $HO^{\bullet}$ and $HO_2^{\bullet}$) would produce some intermediate products (e.g. hydroquinone and quinone-type products) acting as reducing agents ($Fe^{3+} \rightarrow Fe^{2+}$) or electron-transfer catalysts, making the process auto-catalytic [78]. Some authors have reported enhanced Fenton-like catalysis by MIL-53(Fe) for the degradation of phenol [9-11]. However, in line with our results, from their conversion-time plots it is inferred that phenol was hardly degraded within the first 30 min of the MIL-53(Fe)/H_2O_2 oxidation experiments when dissolved iron concentration was found below 0.6 mg L^{-1} [11] The relatively low number of coordinatively unsaturated iron sites in MIL-53(Fe) could explain such limited catalytic activity [11]. On the other hand, apparent first-order kinetics without lag phase is observed in **Figure 3.15** for both Ph (k_{obs} = 0.107 min^{-1}, R^2 = 0.970) and MTP (k_{obs} = 0.089 min^{-1}, R^2 = 0.966) removals in the MIL-53(Fe) photo-assisted

runs, which agrees with previous studies on the photodegradation of water pollutants by MIL-53(Fe)/H_2O_2 under UV-visible or visible light irradiation [15-17, 20, 23, 33, 40]. The absence of lag phase in pollutant conversion and fast decomposition of H_2O_2 from the beginning of MIL-53(Fe)/H_2O_2/SR experiments when the dissolved iron concentration was small (see **Figure 3.16**) are signs of some heterogeneous photocatalytic ability of MIL-53(Fe) for the degradation of Ph and MTP through H_2O_2 mediated reactions.

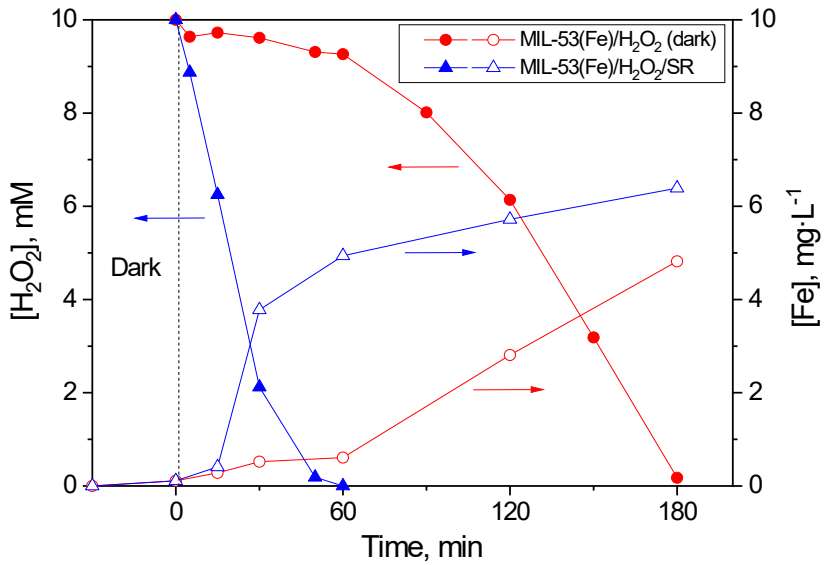

Figure 3.16. Hydrogen peroxide and iron concentration profiles during the degradation of phenol by H_2O_2 assisted catalytic and photocatalytic processes using MIL-53(Fe). Experimental conditions: MIL-53(Fe) concentration =0.6 g L^{-1}; initial concentration: Ph 25 mg L^{-1}, pH = 4-5; H_2O_2 initial concentration: 10 mM.

In addition to the role of MIL-53(Fe) as heterogeneous catalyst to activate H_2O_2 under sunlight, its instability under the reaction conditions and the resulting release of iron and H_2BDC into solution might have an impact on the pollutant degradation. On one hand, aqueous iron could significantly contribute to ROS

generation via homogeneous photo-Fenton-like mechanism initiated by photogeneration of Fe(II):

$$[Fe^{III}(H_2O)]^{3+} + h\cdot\nu \rightarrow Fe^{2+} + HO^{\bullet} + H^{+} \quad (3.25)$$

Some SCCAs (e.g., oxalic acid) are typically viewed as intermediates of organic molecules oxidation by ROS (e.g., see as an example reference [79] for Ph degradation). In the MIL-53(Fe)/H_2O_2/SR experiments conducted in this work, concentrations of SCCAs as high as 8.4 and 5.1 mgC L^{-1} were measured during the degradation of Ph and MTP, respectively. In the absence of radiation (i.e., MIL-53(Fe)/H_2O_2 experiments) the accumulation of SCCAs was much lower with peak concentrations at longer reaction times. As discussed before, some SCCAs have the ability of both extracting iron from solid species and forming iron complexes with photochemical activity under UV-vis radiation leading to ROS generation [63,68]:

$$[Fe^{III}RCOO]^{2+} + h\cdot\nu \rightarrow Fe^{2+} + CO_2 + R^{\bullet} \quad (3.26)$$

$$R^{\bullet} + O_2 \rightarrow \ldots \rightarrow ROS \quad (3.27)$$

As an example, **Figure 3.16** shows a dramatic increase of iron in solution beginning at 15 min of irradiation time in a MIL-53(Fe)/H_2O_2/SR run treating aqueous phenol. The maximum concentration of SCCAs, particularly oxalic acid (10.1 mg L^{-1}) was detected at 30 min irradiation time. Therefore, ferric-carboxylate complexes had likely a primary role in iron dissolution and ROS formation in the MIL-53(Fe)/H_2O_2/SR AOP. The enhanced generation of ROS is reflected in the DOC removal presented in **Figure 3.15** for both Ph and MTP experiments. Thus, despite the continuous leaching of BDC linker from MIL-53(Fe), DOC decreased significantly during the first hour of irradiation. At longer times when H_2O_2 was completely consumed (see **Figure 3.16**), ROS generation would decrease drastically and, as a result, DOC increased because the accumulation of H_2BDC and oxidation products in solution.

From the discussion above, it is clear that homogeneous photo-Fenton-like reactions might likely be a leading oxidation mechanism in the MIL-53(Fe)/H_2O_2/SR process. Fe(III)/H_2O_2/SR runs were carried out to provide experimental proof of such contribution to Ph and MTP degradation. **Figure 3.15** shows that the removal rates of Ph and MTP by Fe(III)/H_2O_2/SR were only slightly lower than those observed in the corresponding heterogeneous runs (i.e., MIL-53(Fe)/H_2O_2/SR) despite the relatively low concentration of Fe(III) used (i.e., 0.5 mg L^{-1}). Moreover, DOC removals in homogeneous photo-Fenton runs followed similar trends than in heterogeneous runs during the first hour of reaction, when H_2O_2 was still present. After that time, very low concentration of H_2O_2 remained in solution but further DOC removal was observed in the Fe(III)/H_2O_2/SR runs, likely due to oxidation by ROS produced through reactions (3.25) to (3.27).

3.4 CONCLUSIONS

The metal organic framework MIL-53(Fe) has been successfully prepared via a facile solvothermal method. The characterization of the resulting material is in good agreement with the literature. The as-prepared MIL-53(Fe) is relatively stable in water at pH = 4 but undergoes partial decomposition at alkaline conditions yielding H_2BDC and amorphous oxyhydroxide species as hydrolysis products. At weakly acidic conditions (pH = 4-5) the MOF shows increasing instability with temperature, exposure to UV-vis radiation and presence of oxidants such as ozone, persulfate and hydrogen peroxide. The photostability of MIL-53(Fe) under simulated solar radiation illumination in the presence of oxidants is compromised by the enhanced generation of ROS, which might attack the MOF structure leading to its decarboxylation (i.e, release of H_2BDC and iron species to solution). The as-synthetized MIL-53(Fe) on its own shows limited photocatalytic activity for the removal of aqueous Ph and MTP under simulated

radiation, though the removal efficiency can be greatly improved in the presence of added oxidants (i.e., ozone, persulfate or hydrogen peroxide). However, the enhanced removal of Ph and MTP cannot be primarily ascribed to the MIL-53(Fe) role as heterogeneous catalyst but to other reaction pathways such as direct attack of the oxidant (case of ozone) or the homogeneous catalytic effect of aqueous iron species (case of H_2O_2).

The findings of this study suggest that caution should be taken when proposing MIL-53(Fe) as a heterogeneous photocatalyst for the degradation of water pollutants. MOF photostability at actual reaction conditions is a critical issue that needs to be considered before recommendation of the material for its utilization in photocatalytic treatments of water and wastewater.

References

[1] D. Robert, S. Malato. Solar photocatalysis: a clean process for water detoxification. Sci. Total Environ., 291 (**2002**) 85-97.

[2] J. Gascón, A. Corma, F. Kapteijn, F.X. Llabrés i Xamena. Metal organic framework catalysis: quo vadis? ACS Catal., 4 (**2014**) 361-378.

[3] H. Furakawa, K.E. Cordova, M. O'Keeffe, O.M. Yaghi. The chemistry and applications of metal-organic frameworks. Science, 341 (**2013**) 974-986.

[4] F.X. Llabrés I Xamena, A. Corma, H. García. Applications for metal-organic frameworks (MOFs) as quantum dot semiconductors. J. Phys. Chem. C, 111 (**2007**) 80-85.

[5] C. Wang, J. Li, X. Lv, Y. Zhang, G. Guo. Photocatalytic organic pollutants degradation in metal-organic frameworks. Energy Environ. Sci., 7 (**2014**) 2831-2867.

[6] J. Bedia, V. Muelas-Ramos, M. Peñas-Garzón, A. Gómez-Avilés, J.J. Rodríguez, C. Belver. A review on the synthesis and characterization of metal organic frameworks for photocatalytic water purification. Catalysts, 9 (**2019**) 52.

[7] X. Zhang. J. Wang, X. Dong, Y. Lv. Functionalized metal-organic frameworks for photocatalytic degradation of organic pollutants in environment. Chemosphere, 242 (**2020**) 125144.

[8] D. Wang, Z. Li. Iron-based metal–organic frameworks (MOFs) for visible-light-induced photocatalysis. Res. Chem. Intermed., 43 (**2017**) 5169–5186.

[9] Q.Sun, M. Liu, K. Li, Y. Zuo, Y. Han, J. Wang, C. Song, G. Zhang, X. Guo. Facile synthesis of Fe-containing metal–organic frameworks as highly efficient catalysts for degradation of phenol at neutral pH and ambient temperature. Cryst. Eng.Comm, 17 (**2015**) 7160.

[10] Q. Sun, M. Liu, K. Li, Y. Han, Y. Zuo, J. Wang, C. Song, G. Zhang, X. Guo. Controlled synthesis of mixed-valent Fe-containing metal organic frameworks for the degradation of phenol under mild conditions. Dalton Trans., 45 (**2016**) 7952-7959.

[11] C. Gao, S. Chen, X. Quan, H. Yu, Y. Zhang. Enhanced Fenton-like catalysis by iron-based metal organic frameworks for degradation of organic pollutants. J. Catal., 356 (**2017**) 125-132.

[12] X. Li, W. Guo, Z. Liu, R.Wang, H. Liu. Fe-based MOFs for efficient adsorption and degradation of acid orange 7 in aqueous solution via persulfate activation. Appl. Surf. Sci., 369 (**2016**) 130-136.

[13] M. Pu, Z. Guand, Y. Ma, J. Wan, Y. Wang, M.L. Brusseau, H. Chi. Synthesis of iron-based metal-organic framework MIL-53 as an efficient catalyst to activate persulfate for the degradation of Orange G in aqueous solution. Appl. Catal. A-Gen., 549 (**2018**) 82-92.

[14] D. Yu, M. Wu, Q. Hu, L. Wang, C.Lv, L. Zhang. Iron-based metal-organic frameworks as novel platforms for catalytic ozonation of organic pollutant: Efficiency and mechanism. J. Hazard. Mat., 367 (**2019**) 456-464.

[15] J.J. Du, Y.P. Yuan, J.X. Sun, F.M. Peng, X. Jiang, L.G. Qiu, A.J. Xie, Y.H. Shen, J.F. Zhu. New photocatalysts based on MIL-53 metal-organic frameworks for the decolorization of methylene blue dye. J. Hazard. Mat. 190 (**2011**) 945-951.

[16] L. Ai, C. Zhang, L. Li, J. Jiang. Iron terephthalate metal–organic framework: Revealing the effective activation of hydrogen peroxide for the degradation of organic dye under visible light irradiation. Appl. Catal. B- Environ., 148-149 (**2014**) 191-200.

[17] Y. Zhang, G. Li, H. Lu, Q. Lv, Z. Sun. Synthesis, characterization and photocatalytic properties of MIL-53(Fe)-graphene hybrid materials. RSC Adv., 4 (**2014**) 7594-7600.

[18] C. Zhang, L. Ai, J. Jiang. Graphene hybridized photoactive iron terephthalate with enhanced photocatalytic activity for the degradation of rhodamine B under visible light. Ind. Eng. Chem. Res. 54 (**2015**) 153-163.

[19] C. Zhang, L. Ai, J. Jiang. Solvothermal synthesis of MIL-53(Fe) hybrid magnetic composites for photoelectrochemical water oxidation and organic pollutant photodegradation under visible light. J. Mat. Chem. A. 3 (**2015**) 3074-3081.

[20] N.D. Trinh, S Hong. Photocatalytic decomposition of methylene blue over MIL-53(Fe) prepared using microwave-assisted process under visible light irradiation. J. Nanosci. Nanotechnol., 15 (**2015**) 5450-5454.

[21] R. Liang, F. Jing, L. Shen, N. Qin, L. Wu. MIL-53(Fe) as a highly efficient bifunctional photocatalyst for the simultaneous reduction of Cr(VI) and oxidation of dyes. J. Hazard. Mat., 287 (**2015**) 364-372.

[22] R. Panda, S. Rahut, J.K. Basu. Preparation of a Fe_2O_3/MIL-53(Fe) composite by partial thermal decomposition of MIL-53(Fe) nanorods and their photocatalytic activity. RSC Adv., 6 (**2016**) 80981-80985.

[23] Y. Gao, G. Yu, K. Liu, S. Deng, B. Wang, J. Huang, Y. Wang. Integrated adsorption and visible-light photodegradation of aqueous clofibric acid and carbamazepine by a Fe-based metal-organic framework. Chem. Eng. J. 330 (**2017**) 157-165.

[24] Y. Gao, S. Li, Y. Li, L. Yao, H. Zhang. Accelerated photocatalytic degradation of organic pollutant over metal-organic framework MIL-53(Fe) under visible LED light mediated by persulfate. Appl. Catal. B- Environ., 202 **(2017**) 165-174.

[25] T. Araya, M. Jia, J. Yang, P. Zhao, K. Cai, W.Ma, Y. Huang. Resin modified MIL-53 (Fe) MOF for improvement of photocatalytic performance. Appl. Catal. B-Environ., 203 (**2017**) 768-777.

[26] X. Feng, X., H. Chen, F. Jiang. In-situ ethylenediamine-assisted synthesis of a magnetic iron-based metal-organic framework MIL-53(Fe) for visible light photocatalysis. J. Colloid. Interf. Sci., 494 (**2017**) 32-37.

[27] L. Hu, G. Deng, W. Lu, S. Pang, X. Hu. Deposition of CdS nanoparticles on MIL-53(Fe) metal-organic framework with enhanced photocatalytic degradation of RhB under visible light irradiation. Appl. Surf. Sci., 410 (**2017**) 401-413.

[28] Y. Han, C. Bai, L. Zhang, J.Wu, H. Meng, J. Xu, Y.Xu, Z. Liang, X. Zhang. A facile strategy for fabricating AgI-MIL-53(Fe) composites: Superior interfacial contact and enhanced visible light photocatalytic performance. New J. Chem., 42 (**2018**) 3799-3807.

[29] D. Wang, F. Jia, H. Wang, F. Chen, Y. Fang, W. Dong, G. Zeng, X. Li, Q. Yang, X. Yuan. Simultaneously efficient adsorption and photocatalytic degradation of tetracycline by Fe-based MOFs. J. Colloid Interf. Sci., 519 (**2018**) 273-284.

[30] R. Li, Z. Chen, M. Cai, J. Huang, P. Chen, G. Liu, W. Lv. Improvement of sulfamethazine photodegradation by Fe(III) assisted MIL-53(Fe)/percarbonate system. Appl. Surf. Sci. 457 (**2018**) 726-734.

[31] W. Mei, D. Li, H. Xu, J. Zan, L. Sun, Q. Li, B. Zhang, Y. Wang, D. Xia. Effect of electronic migration of MIL-53(Fe) on the activation of peroxymonosulfate under visible light. Chem. Phys. Lett., 706 (**2018**) 694-701.

[32] A.A. Oladipo. MIL-53 (Fe)-based photo-sensitive composite for degradation of organochlorinated herbicide and enhanced reduction of Cr(VI). Process Saf. Environ., 116 (**2018**) 413-423.

[33] N. Liu, C. Jing, Z. Li, W. Huang, B. Gao, F. You, X. Zhang. Effect of synthesis conditions on the photocatalytic degradation of Rhodamine B of MIL-53(Fe). Mater. Lett., 237 (**2019**) 92-95.

[34] N. Liu, W. Huang, M. Tang, C. Yin, B. Gao, Z. Li, L. Tang, J. Lei, L. Cui, X. Zhang. In-situ fabrication of needle-shaped MIL-53(Fe) with 1T-MoS_2 and study on its enhanced photocatalytic mechanism of ibuprofen. Chem. Eng. J., 359 (**2019**) 254-264.

[35] S. Miao, Z. Zha, Y. Li, X. Geng, J. Yang, S. Cui, J. Yang. Visible-light-driven MIL-53(Fe)/BiOCl composite assisted by persulfate: Photocatalytic performance and mechanism. J. Photochem. Photobiol. A-Chem., 380 (**2019**) 111862.

[36] D. Jiang, Y. Zhu, M. Chen, B. Huang, G. Zeng, D. Huang, B. Song, L. Qin, H. Wang, W. Wei. Modified crystal structure and improved photocatalytic activity of MIL-53 via inorganic acid modulator. Appl. Catal. B-Environ., 255 (**2019**) 117746.

[37] L. Tang, Z.Q. Lv, Y.C. Xue, L. Xu, W.H. Qiu, C.M. Zheng, W.Q. Chen, M.H. Wu. MIL-53(Fe) incorporated in the lamellar BiOBr: Promoting the visible-light catalytic capability on the degradation of rhodamine B and carbamazepine. Chem. Eng. J., 374 (**2019**) 975-982.

[38] Y. Cui, L.C. Nengzi, J. Gou, Y. Huang, B. Li, X. Cheng. Fabrication of dual Z-scheme MIL-53(Fe)/A-Bi_2O_3/g-C_3N_4 ternary composite with enhanced visible light photocatalytic performance. Sep. Purif. Technol., 232, (**2020**) 115959.

[39] X. Li, Z. Zeng, G. Zeng, D. Wang, R. Xiao, Y. Wang, C. Zhou, H. Yi, S. Ye, Y. Yang, W. Xiong. A "bottle-around-ship" like method synthesized yolk-shell Ag_3PO_4@MIL-53(Fe) Z-scheme photocatalysts for enhanced tetracycline removal. J. Colloid Interface Sci., 561 (**2020**) 501-511.

[40] N. Liu, J. Wang, J. Wu, Z. Li, W. Huang, Y. Zheng, J. Lei, X. Zhang, L. Tang. Magnetic Fe_3O_4@MIL-53(Fe) nanocomposites derived from MIL-53(Fe) for the photocatalytic degradation of ibuprofen under visible light irradiation. Mater. Res. Bull., 132 (**2020**) 111000.

[41] Q. Wu, Y. Liu, H. Jing, H. Yu, Y. Lu, M. Huo, H. Huo. Peculiar synergetic effect of γ-Fe_2O_3 nanoparticles and graphene oxide on MIL-53 (Fe) for boosting photocatalysis. Chem. Eng. J., 390 (**2020**) 124615.

[42] Y. Zhang, J. Zhou, J. Chen, X. Feng, W. Cai. Rapid degradation of tetracycline hydrochloride by heterogeneous photocatalysis coupling persulfate oxidation with MIL-53(Fe) under visible light irradiation. J. Hazard. Mater., 392 (**2020**) 122315.

[43] L. Deng, D. Yin, K.K. Khaing, S. Xiao, L. Li, X. Guo, J. Wang, Y. Zhang. The facile boosting sunlight-driven photocatalytic performance of a metal-organic-framework through coupling with Ag_2S nanoparticles. New J. Chem., 44 (**2020**) 12568-12578.

[44] P. George, P. Chowdhury. Enhanced photocatalytic performance of novel S_2-doped MIL-53(Fe) under visible light. J. Alloy. Compd., 850 (**2021**) 156578.

[45] R. Liang, L. Shen, F. Jing, N. Qin, L. Wu. Preparation of MIL-53(Fe)-reduced graphene oxide nanocomposites by a simple self-assembly strategy for increasing interfacial contact: efficient visible-light photocatalysts. ACS Appl. Mater. Interfaces, 7 **(2015**) 9507–9515.

[46] W. Huang, N. Liu, X. Zhang, M. Wu, L.Tang. Metal organic framework g-C_3N_4/MIL-53(Fe) heterojunctions with enhanced photocatalytic activity for Cr(VI) reduction under visible light. Appl. Surf. Sci., 425 (**2017**) 107-116.

[47] Q. Xia, B. Huang, X. Yuan, X, H. Wang, Z. Wu, L. Jiang, T. Xiong, J. Zhang, G. Zeng, H. Wang. Modified stannous sulfide nanoparticles with metal-organic framework: Toward efficient and enhanced photocatalytic reduction of chromium (VI) under visible light. J. Colloid Interf. Sci., 530 (**2018**) 481-492.

[48] K. Liu, Y. Gao, J. Liu, Y. Wen, Y. Zhao, K. Zhang, G. Yu. Photoreactivity of metal-organic frameworks in aqueous solutions: metal dependence of reactive oxygen species production. Environ. Sci. Technol., 50 (**2016**) 3634-3640.

[49] H. Chen, Y. Liu, T. Cai, W. Dong, L. Tang, X. Xia, L. Wang, T. Li. Boosting photocatalytic performance in mixed-valence MIL-53(Fe) by changing Fe^{II}/Fe^{III} ratio. ACS Appl. Mater. Interfaces, 11 (**2019**) 28791-28800.

[50] D. Yu, L. Wang, T. Yang, G. Yang, D. Wang, H. Ni, M. Wu. Tuning Lewis acidity of iron-based metal-organic frameworks for enhanced catalytic ozonation. Chem. Eng. J., 404 (**2021**) 127075.

[51] I. Bezverkhyy, G. Weber, J.P. Bellat. Degradation of fluoride-free MIL-100(Fe) and MIL-53(Fe) in water: Effect of temperature and pH. Micropor. Mesopor. Mat., 219 (**2016**) 117-124.

[52] S.E. Page, Arnold, W.A., McNeill, K. Terephthalate as a probe for photochemically generated hydroxyl radical. J. Environ. Monitor., 12 (**2010**) 1658-1665.

[53] A.M. Chávez, A. Rey, J. López, P.M. Álvarez, F.J.Beltrán. Critical aspects of the stability and catalytic activity of MIL-100(Fe) in different advanced oxidation processes. Sep. Purif. Technol., 255 (**2021**) 117660.

[54] D.H. Quiñones, A. Rey, P.M. Álvarez, F.J. Beltrán, P.K. Plucinski. Enhanced activity and reusability of TiO_2 loaded magnetic activated carbon for solar photocatalytic ozonation. Appl. Catal. B - Environ., 144 (**2014**) 96-106.

[55] W. Masschelein, M. Denis, R. Ledent. Spectrophotometric determination of residual hydrogen peroxide. Water Sewage Works, 124 (**1977**) 69-72.

[56] G.M. Eisenberg, G.M. Colorimetric determination of hydrogen peroxide, Ind. Eng. Chem. Res., 15 (**1942**) 327–328.

[57] N. Wahba, M.F. El Asmar, M.M. El Sadr. Iodometric method for determination of persulfates. Anal. Chem., 31 (**1959**) 1870-1871.

[58] H. Bader, J. Hoigné. Determination of ozone in water by the indigo method. Water Res., 15 (**1981**) 449-456.

[59] F. Millange, N. Guillou, R.I. Walton, J. Grenèche, I. Margiolaki, G. Férey. Effect of the nature of the metal on the breathing steps in MOFs with dynamic frameworks. Chem. Commun., 130 (**2008**) 4732-4734

[60] M.T.H. Nguyen, Q.T. Nguyen. Efficient refinement of a metal-organic framework MIL-53(Fe) by UV-vis irradiation in aqueous hydrogen peroxide solution. J. Photoch. Photobio. A. 288 (**2014**) 55-59.

[61] S. Dhaka, R. Kumar, A. Deep, M.B. Kurade, S.W. Ji, B.H. Jeon. Metal–organic frameworks (MOFs) for the removal of emerging contaminants from aquatic environments. Coord. Chem. Rev., 380 (**2019**) 330-352.

[62] X. Qian, B.Yadian, R. Wub, Y.Long, K. Zhou, B. Zhu, Y. Huang. Structure stability of metal-organic framework MIL-53 (Al) in aqueous solutions. Int. J. Hydrog. Energy, 38 (**2013**) 16710-16715.

[63] E.M. Rodríguez, G. Fernández, P.M. Álvarez, R. Hernández, F.J. Beltrán. Photocatalytic degradation of organics in water in the presence of iron oxides: Effects of pH and light source. Appl. Catal. B-Environ., 102 (**2011**) 572-583.

[64] D. Mateo, A. Santiago-Protillo, J. Albero, S. Navalón, M. Álvaro, H. García. Long-term photostability in terephtalate metal-organic frameworks. Angew. Chemie - Int Ed 58 (**2019**), 17843.

[65] A.M. Chávez, A. Rey, F.J. Beltrán, P.M. Álvarez. Solar photo-ozonation: A novel treatment method for the degradation of water pollutants. J. Hazard. Mat. 317 **(2016**) 36-43.

[66] R. Thiruvenkatachari, T.O. Kwon, J.C. Jun, S. Balaji, M. Matheswaran, I.S. Moon. Application of several advanced oxidation processes for the destruction of terephthalic acid (TPA). J. Hazard. Mater., 142 (**2007**) 308-314.

[67] I. Fuentes, J.L. Rodríguez, T. Poznyak, I. Chairez. Photocatalytic ozonation of terephtalic acid: a by-product-oriented decomposition study. Environ Sci. Pollut. Res. 21 (**2014**) 12241-12248.

[68] B.S. Faust, R.G. Zepp. Photochemistry of aqueous iron(III)-polycarboxylate complexes: roles in the chemistry of atmospheric and surface waters. Environ. Sci. Technol., 27 (**1993**) 2517-2522.

[69] L. Rao, Y. Yang, X. Liu, Y. Huang, M. Chen, Y. Yao, W. Wang. Heterogeneous activation of persulfate by supporting ferric oxalate onto activated carbon fibers for organic contaminants removal. Mater. Res. Bull., 130 (**2020**) 110919.

[70] G. Zhang, Q. Wang, W. Zhang, T. Li, Y. Yuan, P. Wang. Effects of organic acids and initial solution pH on photocatalytic degradation of bisphenol A (BPA) in a photo-Fenton-like process using goethite (α-FeOOH). Photochem. Photobiol. Sci., 15 (**2016**) 1046-1053.

[71] E.M. Rodríguez, G. Fernández, P.M. Alvarez, F.J. Beltrán. TiO_2 and Fe (III) photocatalytic ozonation processes of a mixture of emergent contaminants of water. Water Res., 46 (**2012**) 152-166.

[72] J. Hoigné, H. Bader. Rate constants of reactions of ozone with organic and inorganic compounds in water-II: Dissociating organic compounds. Water Res., 17 (**1983**) 185-194.

[73] F.J. Benítez, J.L. Acero, F.J. Real, G. Roldán, Ozonation of pharmaceutical compounds: rate constants and elimination in various water matrices. Chemosphere, 77 (**2009**) 53-59.

[74] J.Yang, M. Zhu, D.D .Dionysiou. What is the role of light in persulfate-based advanced oxidation for water treatment? Water Res., 189 (**2021**) 116627.

[75] Q. Mei, J. Sun, D. Han, B. Wei, Z. An, X. Wang, J. Xie, J. Zhan, M. He. Sulfate and hydroxyl radicals-initiated degradation reaction on phenolic contaminants in the aqueous phase: Mechanisms, kinetics and toxicity assessment. Chem. Eng. J., 373 (**2019**) 668-676.

[76] K.S. Tay, N.S.B. Ismail. Degradation of β-blockers in water by sulfate radical-based oxidation: kinetics, mechanism and ecotoxicity assessment. J. Environ. Sci. Technol., 13 (**2016**) 2495-2504.

[77] Y. Wu, R. Prulho, M. Brigante, W. Dong, K. Hanna, G.Mailhot. Activation of persulfate by Fe(III) species: Implications for 4-tert-butylphenol degradation. J. Hazard. Mater., 322 (**2017**) 380-386.

[78] R. Chen, J.J. Pignatello. Role of quinone intermediates as electron shuttles in Fenton and photoassisted Fenton oxidations of aromatic compounds. Environ. Sci. Technol., 31 (**1997**) 2399-2406.

[79] T.Olmez-Hanci, I. Arslan-Alaton. Comparison of sulfate and hydroxyl radical based advanced oxidation of phenol. Chem. Eng. J., 22 (**2013**) 10-16.

CHAPTER 4:

MAGNETIZATION OF INORGANIC SOLIDS

4.1 INTRODUCTION

4.1.1 State of the art

Nowadays inorganic solids are used as catalysts in many chemical processes to increase their reaction rate or their selectivity and/or to operate under milder conditions, which results in a substantial improvement of the process economy. Ideally, the materials used should be easily recovered and reused to avoid the loss of the catalyst giving place to a better economic and environmental viability.

In water treatment, the use of catalysts in slurry has been shown to greatly improve the efficiency of different processes mainly due to minor mass transfer limitations and higher exposed areas, especially in photocatalytic treatments. However, the recovery of the catalyst, although technically possible, is often not economically viable and the catalytic particles can cause additional contamination [1].

Some metal, metal oxides and carbonaceous materials are useful catalysts in different types of AOPs. Examples of these catalysts are TiO_2 in photocatalysis and Al_2O_3 or activated carbon for ozonation [2,3]. The use of inorganic solids in catalytic AOPs usually involves their immobilization on macro-structured supports (ceramics, metals), which favors their separation from the reaction medium [4-7]. However, the immobilization usually decreases the catalytic activity to a great extent due to mass transfer limitations. Also, some loss or deterioration of the catalytic material can occur over time due to operating conditions (e.g., temperature, pH, agitation and fluid erosion, chemical environment, etc.) [8,9].

Another attractive alternative to improve the separability of the catalyst is to endow it with magnetic properties that allow the separation from the reaction medium by an external magnetic field. In terms of exposed active sites or mass transfer limitations, magnetization of the catalyst is expected to have advantages over its immobilization, being currently a research area of growing interest [9-16].

Some magnetization methods have been protected under patents, e.g., US20130052140A1 [14], where TiO_2 and magnetite Fe_3O_4 were coprecipitated in acidic media at temperatures above 65 °C using $TiCl_4$ as a precursor of TiO_2. The material obtained was easily separable but presented a low photocatalytic activity due to non-optimized structural characteristics [17]. Kim et al. (2013) prepared different TiO_2-coated magnetite clusters ($nFe_3O_4@TiO_2$) as anode materials for Li-ion batteries. The synthesis was performed in two steps. Firstly, magnetite was obtained from $FeCl_2$, $FeCl_3$ and NH_4OH at 70 °C. Then, 3-aminopropyltrimethylsilanate and tetraethyl orthotitanate were mixed in ethanol and heated at 500 °C for 2 h [18]. Qi et al. (2019) synthesized novel magnetic superstructures of TiO_2 mesocrystal composites with enhanced visible-light photocatalytic activity using graphene oxide (GO) and magnetite. The purpose of GO was to widen the light absorption spectrum, thus exploiting the visible range of the solar spectrum. Despite the good photocatalytic performance of the materials, the multi-step synthesis prodedure required a number of toxic reagents and relatively temperature, resulting in a complex and expensive method [19]. Another example is the work carried out by Ro and Kim (2019) where Pt nanoparticles encapsulated in $Fe_3O_4@SiO_2@TiO_2$ were prepared and tested for hydrogen generation. Again, numerous reagents were used (povidone, 3-aminopropyl, 3-aminopropyl, triethoxysilane, titanium butoxide, ethanol, hydroxypropyl cellulose and ammonia) and the magnetite was synthesized in a different step. The whole process involved temperatures of 70 ºC for 12h, 85 ºC for 1h, drying at 60 ºC and a final calcination at 450 ºC for 2h [11]. There are also some review publications in the literature dealing with magnetic catalysts for water and wastewater treatment that compile similar intricated synthesis protocols [20,21]. In summary, most of the magnetization method proposed in the literature require high temperature and the use of toxic and expensive reagents. Moreover, waste treatment is a must after the catalyst preparation, making the overall process unattractive from economic and environmental points of views.

4.1.2 Objectives and scope of this chapter

The following chapter is devoted to the development of a novel method of magnetization of different inorganic materials to offer a solution to the technical problem of "how to functionalize different inorganic solids to synthesize magnetically recoverable composite catalysts cheaply and sustainably". To achieve this objective, the method was developed under the philosophy of green synthesis procedures using water as solvent, mild temperature, non-toxic reagents, with recovery and reuse. This method has been protected under the Spanish patent "Method for the magnetization of inorganic solids" ES2884450B2 [22].

The method was applied to prepare magnetized TiO_2, TiO_2/WO_3, CeO_2, Ru/Al_2O_3, Pt/Al_2O_3, corundum, graphene, TiO_2/graphene, graphene oxide and activated carbon. The synthesis procedure and the main specific properties of the materials are addressed. The complete characterization, the optimization of the synthesis conditions and the application of some of these materials in different AOPs are part of the scope of Chapters 5 and 6.

4.2 MATERIALS AND METHODS

4.2.1 Materials

Terephthalic acid (1,4-benzene dicarboxylic acid, $C_6H_4(COOH)_2$, purity ≥ 98%, H_2BDC in this work), iron (II) chloride tetrahydrate ($FeCl_2 \cdot 4H_2O$; purity ≥ 98%), sodium hydroxide (NaOH, purity ≥ 98% purity) and hydrochloric acid (HCl, 37% wt.) were used as received from commercial suppliers (Sigma-Aldrich and Panreac) without any further purification. Ultrapure water (UP) was produced by a Milli-Q academic system (Millipore). Aeroxide® TiO_2-P25 NPs were directly obtained from the manufacturer (Evonik Industries); Commercial Darco 12-20 granular activated carbon (AC) from Sigma-Aldrich was milled to

obtain particle size < 125 μm before use (specific surface area 650 m^2 g^{-1}); commercial xGnP graphene nanoplatelets (G) from Sigma-Aldrich was used as received (particle size < 2 μm, thickness few nm, specific surface area 750 $m^2 g^{-1}$); Platinum on alumina from Sigma-Aldrich (1 wt. % of Pt powder); Corundum in powder from Sigma-Aldrich (purity ≥ 98 %); Ruthenium supported on alumina from Alfa Aesar (molted tablets, purity ≥ 98 %) and graphene oxide powder (GO) from Graphenea (particle size <25-28 μm, specific surface area > 100 m^2 g^{-1}) were used for catalyst synthesis. TiO_2 impregnated with WO_3 was prepared as described elsewhere [23]. CeO_2 catalyst was synthesized by a hydrothermal method according to the literature [24].

4.2.2 Synthesis of magnetic solids

The proposed magnetization method, described more detail in the Spanish Patent Nº ES2884450B2 [22] comprised the following steps:

a) Dissolution of an iron(II) salt in water. Either iron(II) halides or iron(II) sulfates can be used. $FeCl_2 \cdot 4H_2O$ was used preferentially in this work. Usually, 1 g of this salt was dissolved in 50 mL of deionized water in a 100 mL beaker.
b) Addition of the inorganic species to be magnetized with particle size less than 250 μm to the solution obtained in the step (a). Inorganic materials must be stable and able to be suspended in alkaline aqueous media. Examples of suitable substances are the following: TiO_2, TiO_2/WO_3, CeO_2, Ru/Al_2O_3, Pt/Al_2O_3, corundum, graphene, TiO_2/graphene, graphene oxide, activated carbon. A variable amount of 1-2 g of solids was added to the solution (a) and was either stirred in an ultrasound bath or vigorously shaken.
c) Separately, dissolution of terephthalic acid (H_2BDC) in a 1 M NaOH aqueous solution. Generally, 0.835 g of H_2BDC were used in 15-20 mL

of NaOH, which represents a molar ratio of 1:1 Fe/H_2BDC. The volume of NaOH added was varied.

d) Addition of the solution obtained in (c) to the solution obtained in (b), keeping the temperature constant in the range from 10 °C to 70 °C for enough time to produce magnetic iron oxide (e.g., Fe_3O_4), thus obtaining a suspension of a magnetic composite solid. The addition speed of the solution (c) to the solution (b) was around 1 mL s^{-1}, then the mixture was covered but allowing air contact.
e) Separation of the particles of solid obtained in the step (d) by means of an external magnet.
f) Washing of the solid with different amounts of deionized water, usually 2-5 batches with 250 mL for 12 h.
g) Drying of the product obtained in the step (f) in an oven under static air at 60-100 ºC.
h) Recovery of H_2BDC from the solution obtained in the step (e) by adding acid to promote H_2BDC precipitation and a subsequent filtration.

The products obtained by the method are denoted as $(M)_x(Fe)_{T\text{-}z}$, where M is the inorganic solid to be magnetized, x is the molar ratio between the inorganic solid and terephthalic acid (H_2BDC), T is the synthesis temperature in ºC and z is the liters of NaOH (1 M) per mole of H_2BDC.

4.2.3 Characterization of magnetic solids

X-ray diffraction (XRD) patterns of the samples were obtained in the range of $2\theta = 5° - 70°$ with a step size of 0.01° and 0.5 s of sampling per point using a powder Bruker D8 Advance XRD diffractometer with a Cu $K\alpha_1$ radiation (λ =0.1541 nm) and a linear detector VANTEC (aperture 3º). The morphology of the composites was examined by scanning electron microscopy (SEM) using a Hitachi S-4800 apparatus working at 20–30 kV accelerating voltage and 500–2000

magnification. Fourier-transformed infrared spectroscopy in attenuated total reflectance mode (ATR-FTIR) analyses were performed on a Nicolet is10 spectrometer (Thermo Scientific). Sampling resolution was set at 4 cm^{-1} and 32 scans from 600 to 4000 cm^{-1} wavenumber range. Spectra were processed using Thermo Scientific Omnic 3.2v software. Magnetic measurements were performed using a Quantum Design MPMS XL-7 Superconducting Quantum Interference Device (SQUID). The magnetic moment *M* was measured as a function of the applied magnetic field *H* at room temperature.

4.3 RESULTS AND DISCUSSION

The procedure described was used to prepare different magnetic composites in order to demonstrate its versatility for different applications. The optimization of the synthesis temperature, drying temperature, NaOH/Fe ratio, H_2BDC/Fe ratio and inorganic solid/Fe ratio was carried out but the main results are presented as a case-study in Chapter 6. During the synthesis, also the stirring velocity was studied. With vigorous stirring, the time required for complete synthesis was lower than 24 h whereas with gentle agitation 3 days were required to ensure the maximum yield, which was in the range of 97-99 % for all the composites.

The synthesized materials were analyzed for structural composition, magnetic properties, morphology and organic matter content from precursors. **Figure 4.1** shows the XRD patterns of several materials prepared.

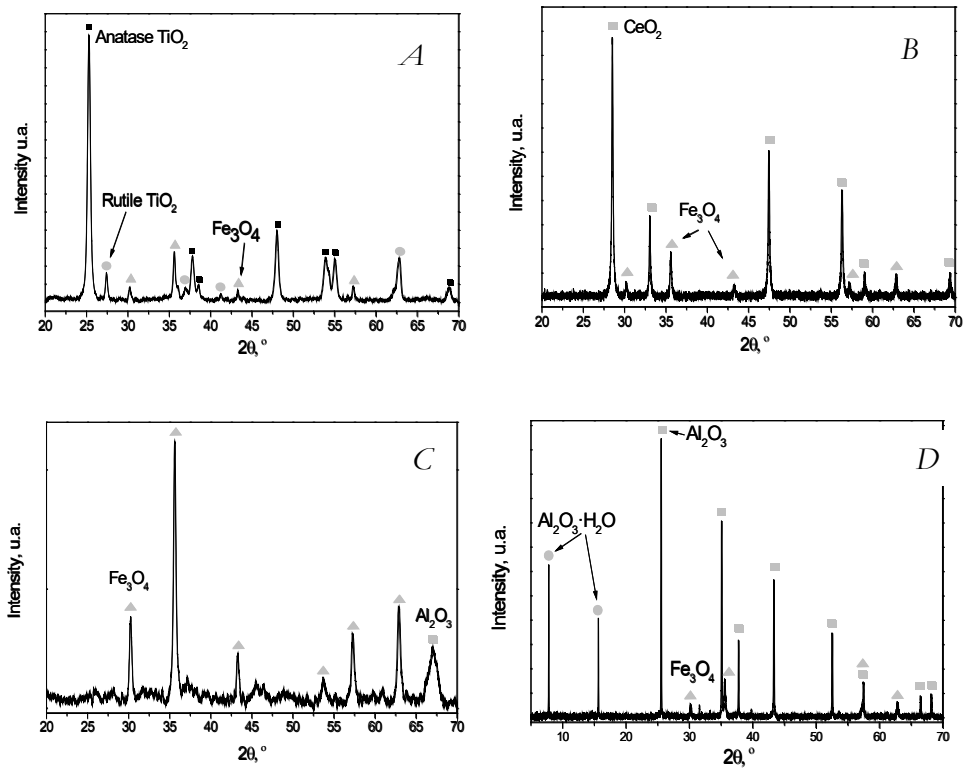

Figure 4.1. XRD patterns of some composites; A) $(TiO_2)_5(Fe)_{20\text{-}3.6}$, B) $(CeO_2)_{1.5}(Fe)_{40\text{-}4}$, C) $(Ru@Al_2O_3)_{3.7}(Fe)_{40\text{-}4}$, D) $(Corundum)_5(Fe)_{40\text{-}4}$.

The presence of the crystalline cubic structure of magnetite Fe_3O_4 in all the materials was proven according to the PDF 01-075-0449 pattern file of the ICCD®. Also, crystalline phases of TiO_2 (PDF 84-1286 and PDF 78-1509 for anatase and rutile, respectively), cubic phase of fluorite structure of CeO_2 (PDF 34-0394) and Al_2O_3 phases (PDF 01-070-0384 and PDF 00-011-0661 for aluminum oxide hydrate and aluminum oxide, respectively) were detected in the corresponding composites. Only Fe_3O_4 magnetite was detected by XRD for the carbon composites due to the amorphous character and/or the small crystallite size of carbon species (not shown here, see Chapter 5).

The magnetic behavior of the composites was examined firstly by their separability from an aqueous suspension using an external magnet (see an example in **Figure 4.2**). All the materials presented this ability, but the optimized composites showed the best performance (see Chapter 6 as an example)

Figure 4.2. Separation of a magnetic composite with an external magnet.

Additional measurements of the magnetic properties of the composite materials were carried out by determining their magnetization hysteresis loops. Some examples of TiO_2-Fe_3O_4 composites are presented in **Figure 4.3**.

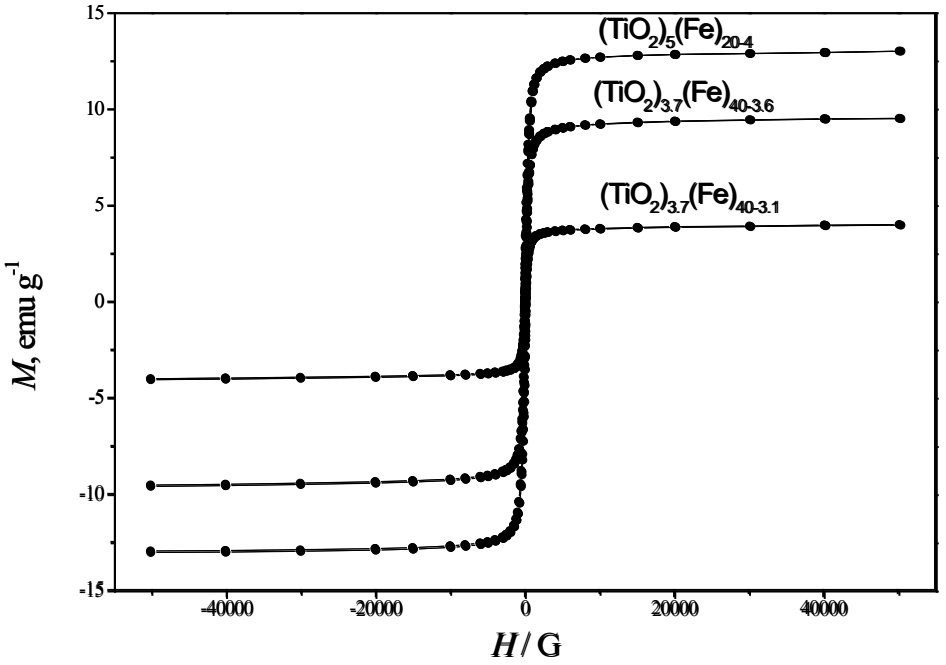

Figure 4.3. Magnetization vs. applied magnetic field at 25ºC, samples: $(TiO_2)_5(Fe)_{20\text{-}4}$, $(TiO_2)_{3.7}(Fe)_{40\text{-}3.6}$ and $(TiO_2)_{3.7}(Fe)_{40\text{-}3.1}$.

The saturation magnetization of bare magnetite is usually in the range of 60-90 emu g^{-1} [25]. The highest saturation magnetization observed in **Figure 4.3** was ca. 13 emu g^{-1} which agrees with the content of iron oxide species (Fe_3O_4) in the composite (15% Fe_3O_4) Lower magnetization values were observed for materials prepared with lower ratios of NaOH.

Optimization in the preparation of composite materials was important to achieve the best magnetic performance. In this sense the excess of alkali (i.e., NaOH) played a key role, followed by the temperature of the synthesis media up to 40 ºC and the final drying temperature at 60 ºC instead 100 ºC to avoid iron (II) species oxidation.

Another important aspect of composite catalytic materials is the distribution of the components. **Figure 4.4** shows the SEM-EDX analysis of the sample

$(TiO_2)_5(Fe)_{20\text{-}3.6}$, with TiO_2 and Fe_3O_4 in its composition. A rather homogeneous distribution of Fe, Ti and O can be seen, which can be advantageous for different applications. In any case, a homogeneous distribution of magnetite undoubtedly will favor the magnetization and the separability of all the inorganic particles.

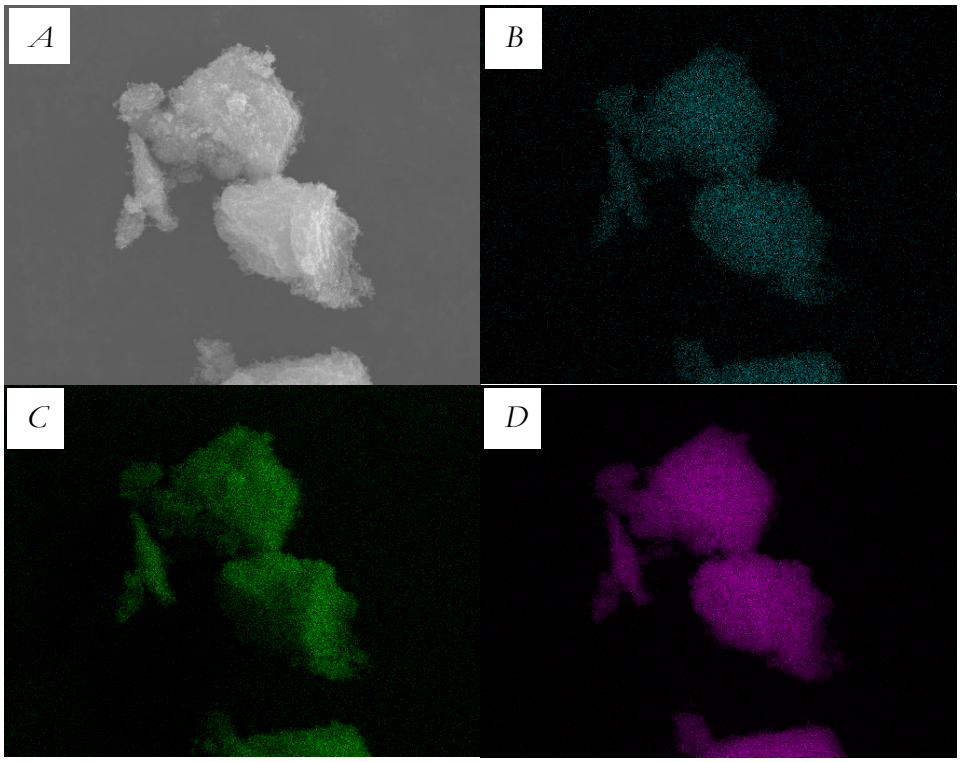

Figure 4.4. SEM and EDX images of the obtained magnetic solid ($(TiO_2)_5(Fe)_{20\text{-}3.6}$). A: image of the sample, B: iron distribution, C: oxygen distribution and D: titanium distribution.

On the other hand, all the materials were thoroughly washed with deionized water to obtain a composite free of organic wastes from the use of terephthalic acid as promoter. The role of the terephthalic acid during the reaction of magnetite formation-coupling is deeply discussed in Chapter 6. Residual H_2BDC could interfere in any catalytic process, but especially for water treatment, could lead to additional contamination. To verify the absence of terephthalic or other

organic intermediates on the catalyst surface, elemental analysis and FTIR were carried out. From the elemental analysis of non-carbonaceous composites, very low carbon contents in inorganic samples were found (lower than 1 wt.%). **Figure 4.5** shows the FTIR spectrum of one washed TiO_2-Fe_3O_4 sample after drying at 60 ºC.

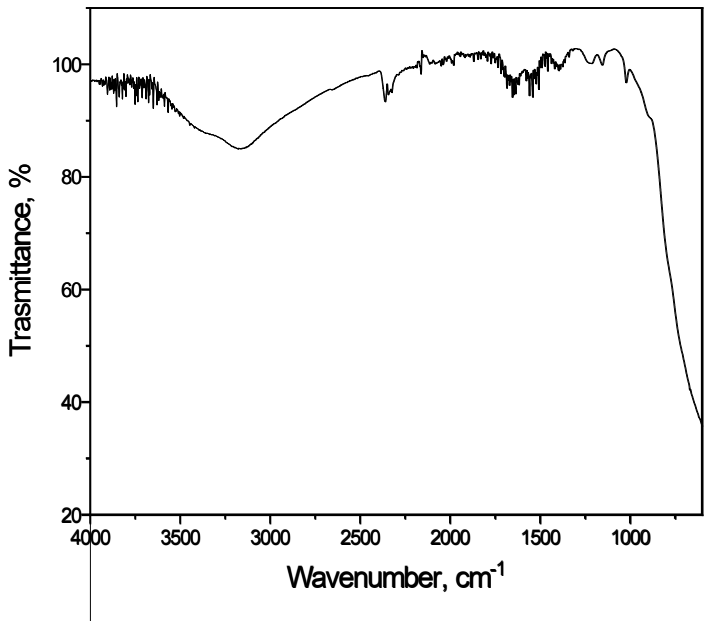

Figure 4.5. FTIR spectrum of the sample $(TiO_2)_5(Fe)_{20\text{-}3.6}$.

From these results, no free terephthalic acid was observed according to the absence of its main band located at 1683 cm^{-1} due to vibration of carboxylic groups v-(C=O) [26]. However, the presence of small amounts of adsorbed terephthalic acid or other organic intermediates formed could not be completely discarded according to the peaks observed in the wavenumber range 1250-1750 cm^{-1}.

Finally, more than 95 wt.% of terephthalic acid could be recovered from the synthesis medium after any composite separation. For this purpose, the supernatant was acidified with HCl until pH lower than 3 to produce the

precipitation of H_2BDC (its solubility at this pH is 0.0015 g/100 mL at 20 °C and pH = 3). The precipitate formed was filtered, washed and dried at 100 ºC. The high purity of the recovered H_2BDC was demonstrated by HPLC, FTIR and XRD (see Chapter 5 for some examples). Also, as an example, **Figure 4.6** shows the identical FTIR spectrum of one batch recovered sample compared with that of pure H_2BDC.

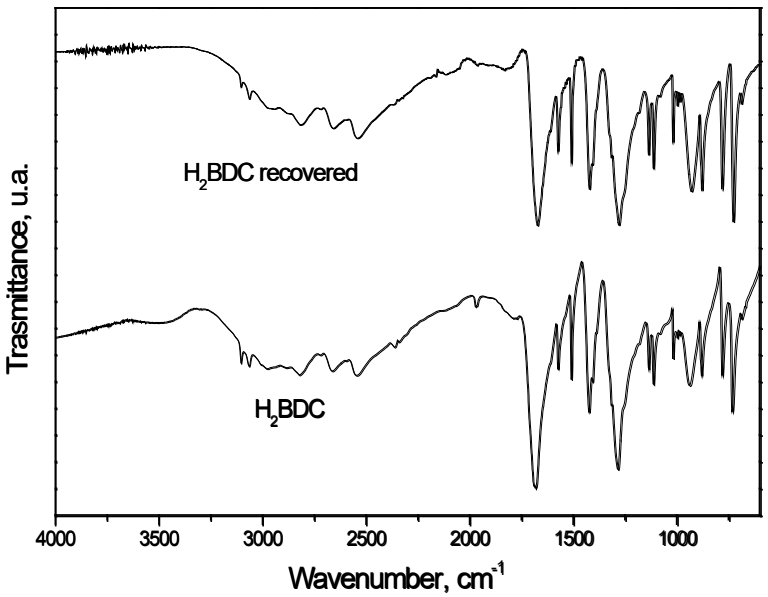

Figure 4.6. FTIR spectra of pure and recovered terephthalic acid.

4.4 CONCLUSIONS

A novel method for the magnetization of inorganic solids was developed and protected under the Spanish Patent ES2884450B2 [22]. The main advantages of the method are the use of water as solvent, the use of non-toxic reagents, mild operating conditions and the recovery of more than 95% of terephthalic acid after the process. All this makes the synthesis attractive from economical and environmental points of view, meeting most of the principles of the "Green Synthesis Methods".

The method led to composites of magnetite with different inorganic materials stable under alkaline conditions (TiO_2, TiO_2-WO_3, CeO_2, Al_2O_3, Ru/Al_2O_3, Pt/Al_2O_3, corundum, activated carbon, graphene and graphene oxide) which presented similar structural properties than the precursors, superior magnetic performance, good components distribution and very low amounts of residual organic compounds. These general characteristics make these materials suitable for different catalytic processes.

References

[1] M. Miceli, P. Frontera, A. Macario, A. Malara. Recovery/reuse of heterogeneous supported spent catalysts. Catal., 11 (**2021**) 591.

[2] Q. Guo, C. Zhou, Z. Ma, X. Yang, Q. Guo, C. Zhou, Z. Ma, X. Yang. Fundamentals of TiO_2 photocatalysis: concepts, mechanisms, and challenges. Adv. Mater., 31 (**2019**) 1901997.

[3] F.J. Beltrán, F.J. Rivas, L.A. Fernández, P.M Álvarez, R. Montero-de-Espinosa. Kinetics of Catalytic Ozonation of Oxalic Acid in Water with Activated Carbon. Ind. Eng. Chem. Res., 41 (**2002**) 6510–6517.

[4] E.M. Rodríguez, A. Rey, E. Mena, F.J. Beltrán, Application of solar photocatalytic ozonation in water treatment using supported TiO_2, Appl. Catal. B Environ., 254 (**2019**) 237–245.

[5] J. Kallas, S. Kamenev, R. Munter. Advanced oxidation processes against phenolic compounds in wastewater treatment. Ozone Sci. Eng., 17 (**1995**) 399-418.

[6] T. Hammedi, M. Triki, M.G. Alvarez, J. Llorca, A. Ghorbel, Z. Ksibi, F. Medina. Heterogeneous fenton-like oxidation of p-hydroxybenzoic acid using Fe/CeO_2-TiO_2 catalyst. Water Sci. Technol., 79 (**2019**) 1276-1286.

[7] Yu, D.; Wu, M.; Hu, Q.; Wang, L.; Lv, C.; Zhang, L. Iron-based metal-organic frameworks as novel platforms for catalytic ozonation of organic pollutant: Efficiency and mechanism. J. Hazard. Mater., 367 (**2019**) 456-464.

[8] W. Huang, N. Liu, X. Zhang, M. Wu, L. Tang. Metal organic framework g-C_3N_4/MIL-53(Fe) heterojunctions with enhanced photocatalytic activity for Cr(VI) reduction under visible light. Appl. Surf. Sci., 425 (**2017**) 107-116.

[9] Xie, W.; Huang, M. Immobilization of Candida rugosa lipase onto graphene oxide Fe_3O_4 nanocomposite: Characterization and application for biodiesel production. Energy Convers. Manag., 159 (**2018**) 42-53.

[10] Ma, R.; Yang, P.; Ma, Y.; Bian, F. Facile synthesis of magnetic hierarchical core–shell structured Fe_3O_4@PDA-Pd@MOF nanocomposites: highly integrated multifunctional catalysts. ChemCatChem., 10 (**2018**) 1446-1454.

[11] Ro, G.; Kim, Y. H_2 generation using Pt nanoparticles encapsulated in Fe_3O_4@SiO_2@TiO_2 multishell particles. Colloids Surfaces A Physicochem. Eng. Asp. 577 (**2019**) 48-52.

[12] M. Savari, A. Varasteh-Moradi, S.Z. Sayyed-Alangi, Z, Hossaini, R. Zafarmehrabian. Ag/Fe_3O_4/TiO_2@MWCNTs as a reusable organometallic nanocatalyst promoted green synthesis of new pyridobenzoazepines: Study of biological activity and reduction of organic pollutants. Appl. Organomet. Chem. (**2021**) 6510.

[13] W. Xie, H. Wang. Immobilized polymeric sulfonated ionic liquid on core-shell structured Fe_3O4/SiO_2 composites: A magnetically recyclable catalyst for simultaneous transesterification and esterifications of low-cost oils to biodiesel. Renew. Energy, 145 (**2020**) 1709-1719.

[14] L. Zhang, X. Liu, M. Zhang, H. Yuan, L. Zhang, J. Lu. Facile construction of dual functional Fe_3O_4@C-MoO_2-Ni composites for catalysis and adsorption. Appl. Surf. Sci., 494 (**2019**) 783-794.

[15] L. Zhu, X. Kong, C. Yang, B. Ren, Q. Tang. Fabrication and characterization of the magnetic separation photocatalyst C-TiO_2@Fe_3O_4/AC with enhanced photocatalytic performance under visible light irradiation. J. Hazard. Mater., 381 (**2020**) 120910.

[16] A. Mirzaie, T. Musabeygi, A. Afzalinia. Sonochemical synthesis of magnetic responsive Fe_3O_4@TMU-17-NH_2 composite as sorbent for highly efficient ultrasonic-assisted denitrogenation of fossil fuel. Ultrason. Sonochem., 38 (**2017**) 664-671.

[17] A.E. Ngo, Sterns et al; Rehabilitation, S.; Corporation, H.; Diego, S.; Majeed et al.; Panyam, J.; Chavanpatil, M. D.; Data, P. P.; Ci, U. S.; Ci, U. S.; Data, R. U. S. A. (12) Patent application publication (10) Pub . No .: US 2013 / 0344194A1. Yeast, 19 (**2010**) 4-6.

[18] S.E. Kim, K.W. Kim, S.W. Lee, S.O. Kim, J.S. Kim, J.K. Synthesis and characterization of TiO_2-Coated magnetite Clusters (NFe_3O_4@TiO_2) as Anode materials for Li-ion Batteries. Curr. Appl. Phys., 13 (**2013**) 1923–1927.

[19] H.P. Qi, H.L Wang, D.Y. Zhao, X.K. Wang. Synthesis of novel magnetic superstructure TiO2 mesocrystal composites with enhanced visible-light photocatalytic activity. Mater. Res. Bull., 118 (**2019**) 110516.

[20] J. Liu, C. Peng, X. Shi. Preparation, characterization, and applications of fe-based catalysts in advanced oxidation processes for organics removal: A Review. Environ. Pollut., 293 (**2022**) 118565.

[21] B. Fan, Y. Tan, J. Wang, B. Zhang, Y. Peng, C. Yuan, C. Guan, X. Gao, S. Cui. Application of magnetic composites in removal of tetracycline through adsorption and advanced oxidation processes (AOPs): A Review. Process., 9 (**2021**) 1644.

[22] J. López, A. Rey, P.M. Álvarez, A.M. Chávez, E. Viñuelas, ES PATENT PUBLICATION Nº ES2884450B2, Método para la magnetización de sólidos inorgánicos, (**2022**).

[23] A. Rey, P. García-Muñoz, M.D. Hernández-Alonso, E. Mena, S. García-Rodríguez, F.J. Beltrán, WO_3–TiO_2 based catalysts for the simulated solar radiation assisted photocatalytic ozonation of emerging contaminants in a municipal wastewater treatment plant effluent, Appl. Catal. B Environ., 154–155 (**2014**) 274–284.

[24] E. Mena, A. Rey, E.M. Rodríguez, F.J. Beltrán, Nanostructured CeO_2 as catalysts for different AOPs based in the application of ozone and simulated solar radiation, Catal. Today., 280 (**2017**) 74–79.

[25] S. Komarneni, W. Hu, Y.D. Noh, A. Van Orden, A.; Feng, S.; Wei, C.; Pang, H.; Gao, F.; Lu, Q.; Katsuki, H. Magnetite syntheses from room temperature to 150°C with and without microwaves. Ceram. Int., 38 (**2012**) 2563–2568.

[26] M.T.H. Nguyen, Q.T. Nguyen. Efficient refinement of a metal-organic framework MIL-53(Fe) by UV-vis irradiation in aqueous hydrogen peroxide solution. J. Photoch. Photobio. A., 288 (**2014**) 55-59.

CHAPTER 5:

GREEN SYNTHESIS OF MAGNETITE-BASED CATALYSTS FOR SOLAR-ASSISTED CATALYTIC WET PEROXIDE OXIDATION

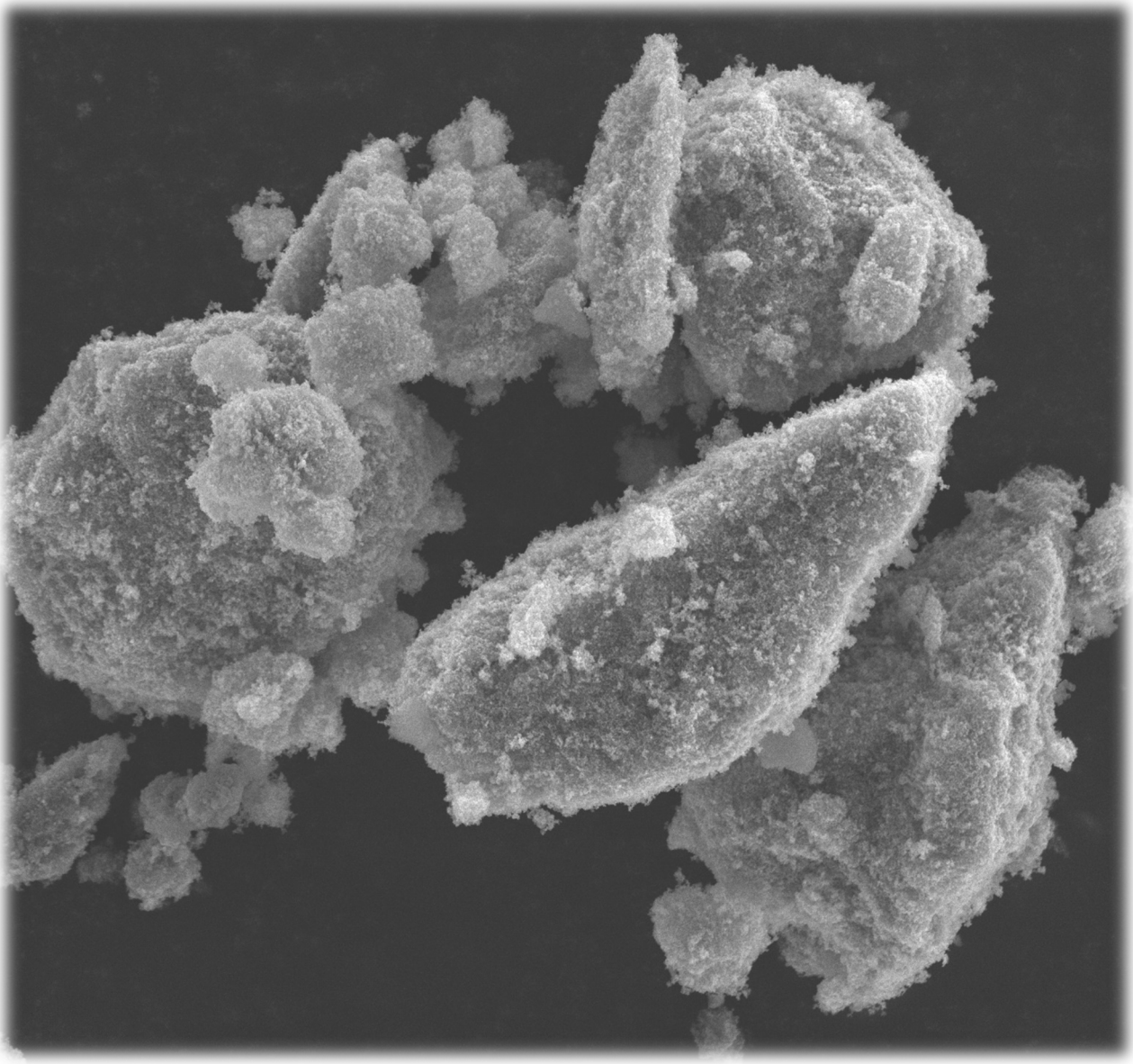

5.1 INTRODUCTION

5.1.1 State of the art

Magnetite-based nanoparticles (NPs) find many applications in several areas such as biomedicine [1–3] and catalysis [4]. Taking advantage of their magnetic properties that allow easy, fast and cost-effective recovery from the reaction medium together with their chemical stability, low toxicity and relatively low cost, a number of magnetite-based catalysts (MBCs) have been proposed to degrade aqueous organic pollutants by different advanced oxidation processes (AOPs) [5]. AOPs are chemical or photochemical processes that triggers the formation of short-lived reactive species (notably hydroxyl radicals, $HO^{\bullet}$) able to degrade water pollutants. By far, since 2008, the most studied AOPs using MBCs have been heterogeneous Fenton and photo-Fenton processes, also called catalytic wet peroxide oxidation (CWPO) [6,7]. Although the mechanism of H_2O_2 decomposition over magnetite (Fe_3O_4) has not been fully elucidated yet, there is general agreement on that surface $\equiv Fe^{2+}$ provokes the decomposition of H_2O_2 into $HO^{\bullet}$ [6–8]. Regeneration of surface $\equiv Fe^{2+}$ is typically the limiting step that control overall process efficiency. When radiation is applied (i.e., heterogeneous photo-Fenton process), the reduction rate of $\equiv Fe^{3+}$ is favored, then increasing the formation rate of $HO^{\bullet}$ [7]. To enhance the catalytic properties of bare magnetite in CWPO reactions, several solids have been used to prepare supported or composite materials [6]. Among them, some carbon materials (e.g. activated carbon, biochar, carbon nanotubes, graphene, graphene oxide or graphitic carbon nitride) have been investigated because of their high surface area and surface chemical properties [7,8]. In addition to providing a greater surface area, favoring the dispersion of magnetite and increasing the adsorption of organic contaminants, carbon structures may promote electron injection towards magnetite thus enhancing the regeneration of $\equiv Fe^{2+}$ sites. Moreover, some carbon materials exhibit catalytic activity in CWPO by themselves [8].

Magnetite can be found in natural minerals or be artificially synthetized [6,7,9]. Synthesis methods are preferred in catalysis to obtain tailored magnetite and MBCs meeting specific properties such as surface area, porosity, particle size or morphology. The most common synthesis procedures followed to prepare magnetic iron oxide NPs are sol-gel [10], hydrothermal or solvothermal reactions [11,12], thermal decomposition [13–16] and co-precipitation [17–20]. Similarly, magnetite-carbon composites are obtained by co-precipitation, hydrothermal and sol-gel syntheses [5]. Temperatures around 80-90 °C were applied to prepare graphene or activated carbon composites by co-precipitation [21,22], whereas a N_2 stream at 90 °C was needed to prepare magnetic activated carbon composites by precipitation [23]. Magnetic activated carbon composites have been also prepared by activation of biowastes in the presence of iron salts in N_2 atmosphere and at temperature as high as 400-800 °C [24]. Generally, all these methods involve the use of organic solvents, moderate to high temperature and/or chemical reagents (e.g., H_2O_2, $NaNO_2$, Na_2SO_3). Even a more environmental-friendly method reported for the synthesis of magnetite NPs using vegetable extracts required moderate temperature (i.e., 80 °C) [25]. Therefore, the search for more sustainable and economic synthesis methods for MBCs is needed to overcome the hurdle for the scale-up and optimization of processes catalyzed by these materials [26,27].

5.1.2 Objectives and scope of this chapter

This work presents the environmental-friendly synthesis method of MBCs based on a terephthalate intermediate as structure director briefly described in Chapter 4 and under the Spanish patent protection ES2884450A1 [28]. Green chemistry philosophy towards circular use of resources has been applied with almost full recovery of the synthesis mediator terephthalic acid (H_2BDC). The method has been successfully used to prepare bare magnetite and different

carbon-magnetite composites with activated carbon, graphene and graphene oxide. Herein, fully characterization of the prepared MBCs and their use as catalysts in solar assisted-CWPO of aqueous solution of the drug metoprolol tartrate (MTP) are reported. Emphasis is placed on catalyst stability, separability, recovery and reusability.

5.2 MATERIALS AND METHODS

5.2.1 Materials

Terephthalic acid (1,4-benzenedicarboxylic acid, $C_6H_4(COOH)_2$, purity ≥ 98%, H_2BDC in this work), iron (II) chloride tetrahydrate ($FeCl_2 \cdot 4H_2O$; purity ≥ 98%), metoprolol tartrate ($(C_{15}H_{25}NO_3)_2 \cdot C_4H_6O_6$, MTP, purity ≥ 99%), sodium hydroxide (NaOH, purity ≥ 98% purity), hydrochloric acid (HCl, 37% wt.), hydrogen peroxide (H_2O_2, 30% wt.) and phosphoric acid (H_3PO_4, 85.5% wt.) were used as received from commercial suppliers (Sigma-Aldrich and Panreac) without any further purification. Ultrapure water (UP) was produced by a Milli-Q academic system (Millipore). Commercial Darco 12-20 granular activated carbon (AC) from Sigma-Aldrich was milled to obtain particle size < 125 μm prior use (specific surface area 650 $m^2\ g^{-1}$); commercial xGnP graphene nanoplatelets (G) from Sigma-Aldrich was used as received (particle size < 2 μm, thickness few nm, specific surface area 750 $m^2 g^{-1}$); and graphene oxide powder (GO) from Graphenea (particle size <25-28 μm, specific surface area > 100 $m^2\ g^{-1}$) were used for catalyst synthesis.

5.2.2 Synthesis of MBCs

Magnetite and composite catalysts were prepared by the novel procedure described in the Spanish Patent ES2884450A1 [28], based in green synthesis philosophy with non-toxic reagents, low energy consumption and reagents

recovery. Four materials were synthesized, bare magnetite (Fe_3O_4) and three carbon magnetic composites (Fe_3O_4-AC, Fe_3O_4-G, Fe_3O_4-GO). Following the procedure depicted in **Figure 5.1**, 1 g of $FeCl_2 \cdot {}_4H_2O$ was dissolved in 50 mL of deionized water (solution A). Then, if required, 0.3 g of AC, G or GO were added and dispersed into solution A by means of 15 min ultrasonication at ambient temperature. For the synthesis of bare magnetite (i.e., Fe_3O_4 sample), no solid was dispersed into solution A. On the other hand, 0.835 g of H_2BDC were dissolved in 20 mL of aqueous NaOH 1 M (solution B). Subsequently, solution A was mechanically stirred at 800 rpm and solution B was added dropwise during 1 min. The mixture was kept at ambient temperature and 800 rpm for 24 h to allow for the formation of the MBC. After that, the solid was separated by means of a neodymium external magnet and then repeatedly washed with 200 mL of deionized water to ensure a solid free of precursors. Iron and terephthalic acid were measured in the washing waters until negligible values were obtained. The solid was finally dried overnight at 60 °C, milled and kept into a desiccator until use. The alkaline solution obtained after the magnetic separation of the catalyst contained terephthalate, Na^+ and Cl^- ions with traces (ppm level) of non-reacted Fe^{2+} or Fe^{3+} ions. Addition of concentrated HCl solution (37 wt.%) to pH < 3 led to the precipitation of H_2BDC (solubility 0.0015 g/100 mL at 20 °C and pH = 3). This solid was recovered by filtration and reused as shown in **Figure 5.1**. A sample of recovered H_2BDC was dried at 100 °C for 24 h and characterized to determine its composition.

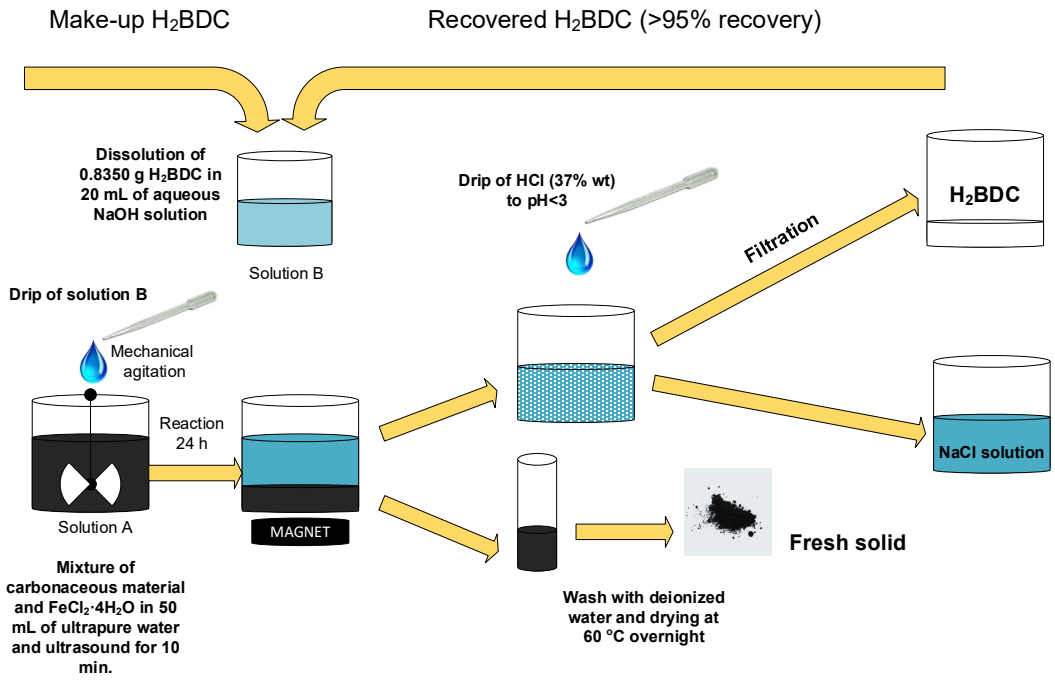

Figure 5.1. Green synthesis of MBCs

5.2.3 Characterization of catalysts

The study of the crystalline phase of solids by X-ray diffraction (XRD) was carried out on a powder Bruker D8 Advance XRD diffractometer with a Cu $K_{\alpha 1}$ radiation (λ=1.541 Å) coupled to a linear detector VANTEC (aperture 3°). The data sets were collected in the range of 2θ = 5 - 70° with a step size of 0.01° and a 0.5 s of sampling per point. Thermogravimetric and differential thermal analyses (TGA-DTA) were carried out with a thermobalance STA 449 F3 Jupiter – Netzsch coupled to mass spectrometer QMS 403D Aëolos III – Netzsch SETSYS Evolution-16 (SETARAM) apparatus using 100 mL min^{-1} of argon and oxygen (80/20, v/v) at a heating rate of 10 °C min^{-1}, from 40 °C to 950 °C. Nitrogen adsorption-desorption isotherms were used to study the BET surface area and pore volume of the materials. The equipment used to acquire them at -196 °C was an Autosorb iQ2-C Series (Quantachrome) apparatus. Before

analysis, the samples were degassed at 150 °C for 10 h under a residual pressure < 10^{-2} mbar. The t-plot method was applied to determine the volume of micropores. The mass percentages of nitrogen, hydrogen and carbon solid samples were determined with a C-H-N-S TRUSPEC MICRO elemental analyzer (LECO). Wavelength dispersive X-ray fluorescence spectroscopy (WDXRF) was performed using a S8 Tiger (Bruker) apparatus to quantify the amount of iron in the samples. Magnetic measurements were performed using a Quantum Design MPMS XL-7 Superconducting Quantum Interference Device (SQUID). Fourier transformed infrared spectroscopy (FTIR) was carried out using the KBr pellet method on a Nicolet iS10 spectrometer. Sampling resolution was set at 1 cm^{-1} and 32 scans from 400 to 4000 cm^{-1} wavenumber range. Surface chemical composition was studied by X-ray photoelectron spectroscopy (XPS) on a PHI VersaProbe II Scanning XPS Microprobe spectrometer equipped with scanning monochromatic X-ray Al K radiation (200 μm area analyzed, 52.8 W and 15 kV and hν = 1486.6 eV) as the excitation source and a multi-channel hemispherical electron analyzer (pass energy of 29.35 eV). Binding energies were calibrated to the C 1 s peak from the carbon signal at 284.8 eV. Raman spectra were acquired using an excitation laser source (λ = 630 nm) on a Thermo Scientific Nicolet Almega XR dispersive Raman spectrometer.

5.2.4 Stability tests

The stability of MBCs in water was tested at different pH (4, 6, 7, 8 and 10) in a 0.01 M phosphate-buffered solution. The experiments were carried out in a thermostatic orbital shaker at 25 °C. MBC samples (1 g L^{-1}) were suspended into 20 mL of buffered solution and kept in 50 mL stoppered glass bottles under stirring for 7 days. After that, the solid was separated by an external magnet and the liquid phase analyzed to determine dissolved and total iron, H_2BDC, TOC and pH. Additionally, catalysts stability was also studied at oxidizing conditions.

Typically, MBC samples (0.2 g L^{-1}) were suspended into 250 mL of ultrapure water in a 300 mL borosilicate glass vessel and allowed for homogenization for 30 min. The, if required, H_2O_2 was added to achieve 50 mM concentration. The vessel was placed in the chamber of a solar box (Suntest CPS+, Atlas Material Testing Technology LLC, Madrid, Spain) equipped with a 1500 W air-cooled Xe lamp. The overall irradiance (λ= 300–800 nm) at the photoreactor level was measured with an UV-Vis spectroradiometer (Black Comet C, StellarNet Inc.) resulting in 581.4 W m^{-2}. The temperature of the simulator chamber was controlled at 40 °C. The experimental set-up has been described in previous works [29,30]. The vessel content was irradiated for 3 h under oxygen bubbling (10 L h^{-1}). After that time, the solid was magnetically separated and dissolved and total iron, H_2BDC, TOC and pH were analyzed in liquid samples.

5.2.5 Catalytic activity tests

CWPO activity tests of magnetic solids in water were performed in a 300 mL borosilicate glass vessel provided with magnetic agitation and liquid sampling. Typically, the vessel was charged with 0.25 L of MTP solution (50 mg L^{-1}) prepared in ultrapure water (Milli-Q) at pH = 7, and 0.2 g L^{-1} of MBC. The suspension was stirred for 30 min for homogenization and MTP adsorption purposes. Then, the reactor vessel was placed in the solar box described above and the required amount of H_2O_2 was added. Immediately, the lamp was turned on if illumination was required. Samples were periodically withdrawn from the reactor, filtered through 0.45 μm PET membranes and analyzed for MTP, pH, H_2O_2, TOC, H_2BDC and dissolved iron. Aliquots of selected samples were analyzed for total iron (non-filtered samples) after separating the catalyst particles with a magnet. The reutilization of Fe_3O_4-AC sample was studied by performing nine consecutive runs under illumination. At the end of each run, the catalyst was

separated magnetically with an external magnet and used without further treatment in the next cycle with a fresh MTP solution.

5.2.6 Analytical methods for reaction monitoring

Total iron concentration was evaluated spectrophotometrically at 565 nm by Spectroquant® iron test (Merck 1.14761.0001). Measurements of pH were made with a pH-meter (Crison GLP21+). Hydrogen peroxide in liquid samples was also measured using the method proposed by Eisenberg [31]. All the spectrophotometric measurements were carried out on a Helios α spectrophotometer from Thermo Spectronic using 1 cm path length cuvettes. TOC was determined on filtered samples using a Shimadzu apparatus (TOC-V CSH model). H_2BDC and MTP concentrations were analyzed by a gradient method on a HPLC apparatus provided with a UV-Vis detector set at 225 nm (HP 1100 Series chromatograph, Agilent Technologies). A Kromasil C-18 column (5 μm, 150 mm length, 4 mm diameter) was used as stationary phase while the mobile phase consisted of a mixture of 0.1% vol. o-phosphoric acid in ultrapure water (solvent A) and acetonitrile (solvent B) at a constant flowrate of 1 mL min^{-1}. The mobile phase program used for the analysis was as follows: start at 20% B; 0–6 min, linear gradient of B in A (20–27.5% B); 6–7 min, hold at 27.5% B, 7–8 min, linear gradient (27.5–20% B); 8–9 min, hold at 20% B. The retention times were 3.4 min (H_2BDC) and 4.1 min (MTP).

5.3 RESULTS AND DISCUSSION

5.3.1 Synthesis of MBCs

Table 5.1 shows the main conditions used for MBCs synthesis, mass yield (i.e., ratio of solid obtained with respect to its theoretical weight) and percentage of terephthalic acid recovered after the synthesis. In **Table 5.1**, G stands for

graphene nanoplatelets, GO for graphene oxide and AC for activated carbon. Subscript R refer to both recovered H_2BDC in each batch synthesis and a MBC sample (Fe_3O_4-AC_R) synthetized with H_2BDC recovered from a previous synthesis batch. Typically, synthesis batches were designed to obtain ca. 0.4 g Fe_3O_4 in each MBC sample (see Section 5.2). In addition, batches intended to procure higher amounts were also carried out for comparative purposes. They are designated with the subscript L (i.e., larger amount). As seen in **Table 5.1**, the mass yield observed after the synthesis of most of the MBC samples was near 100%, meaning almost complete utilization of the limiting reagent (i.e., iron salt) and carbonaceous support. The lower yield observed for the Fe_3O_4-GO composite might be related to the acidic character of GO in aqueous suspension being relatively instable in alkaline solution [32]. The separation of magnetic particles by an external magnet during the washing steps of the synthesis procedure was complete and no turbidity was observed in the washing solution. The use of H_2BDC was crucial for successful synthesis of MBCs. Thus, preliminary tests demonstrated that magnetite was not formed at the conditions given in **Table 5.1** but the absence of terephthalic acid. Therefore, it can be hypothesized that H_2BDC mediates the formation of magnetite through the formation of a terephthalic intermediate which favors the oxidation of Fe^{2+} at alkaline conditions with subsequent precipitation of Fe_3O_4 according to the following simplified set of reactions:

$$3\ FeCl_2 + 3\ H_2BDC + NaOH_{(ex)} \rightarrow 3\ [Fe\text{-}BDC]^*_{(s)} + 6\ HCl + NaOH_{(ex)} \quad (5.1)$$

$$3\ [Fe\text{-}BDC]^*_{(s)} + OH^-_{(ex)} \rightarrow Fe_3O_{4(s)} + 3\ BDC^{2-} + OH^-_{(ex)} \quad (5.2)$$

After separation of the magnetic particles, the aqueous media contained terephthalate (see reaction 5.2) that was almost completely recovered after acidification with HCl to pH < 3 according to:

$$BDC^{2-} + HCl_{(ex)} \rightarrow H_2BDC_{(s)} + HCl_{(ex)} \quad (5.3)$$

Table 5.1. Synthesis conditions, yield and H_2BDC recovery in the preparation of some MBCs.

MBC	Carbon mass (g)	V_{NaOH} (mL)	V_{Total} (mL)	H_2BDC (g)	$FeCl_2 \cdot 4H_2O$ (g)	T (°C)	Yield (%)	$(H_2BDC)_R$ (%)
Fe_3O_4	-	20	70	0.835	1.0	20	99.9	99
Fe_3O_4-G	0.3	20	70	0.835	1.0	20	99.5	98
Fe_3O_4-GO	0.3	20	70	0.835	1.0	20	97.1	97
Fe_3O_4-AC	0.3	20	70	0.835	1.0	20	99.9	96
Fe_3O_4-AC_R	0.3	20	70	0.835	1.0	20	99.9	96
Fe_3O_4-AC_L	6	400	1400	16.7	20	20	99.9	96

The percentage of H_2BDC recovered in any synthesis batch was higher than 95%, as shown in **Table 5.1**. The recovered solid was dried and characterized to check its purity. **Figure 5.2** shows the XRD patterns (A) and FTIR spectra (B) of pure and recovered terephthalic acid. All the diffraction peaks observed are ascribable to triclinic terephthalic acid indexed in the ICCD® (PDF 00-031-1916) with main contributions at 17.4° (110), 25.2° (011) and 27.9° (200) [33]. No other crystalline phases were found in the solid obtained [34]. Moreover, the FTIR spectra of pure H_2BDC and recovered samples show similar profiles with matching bands indicating also similar chemical structure. Th broad band at 2250-3250 cm^{-1} can be attributed to stretching vibration of the -OH (carboxyl group) while other main bands located at 1680, 1575-1420 and 1285 cm^{-1} can be assigned to –C=O (carboxylic group), –C=C/–C–H bonds (aromatic structure), and –C–OH (acid), respectively [33,35]. In order to fully characterize the solid recovered (H_2BDC-R), elemental analysis was performed and compared with that of pure terephthalic acid (H_2BDC-t). As shown in **Table 5.2**, the percentages of C, H and O found in the recovered solid were very close to the theoretical values of pure H_2BDC. Another proof of the purity of the terephthalic acid recovered after the synthesis of MBCs was obtained after dissolving the obtained solid in ultrapure water and analyzing the solution by HPLC, resulting in peak integration that did not differ by more than 2% from the calibration curve obtained with pure H_2BDC. Additionally, the presence of iron compounds in the solid recovered was

ruled out after the analysis of iron at ppb level in the aqueous solution prepared in ultrapure water.

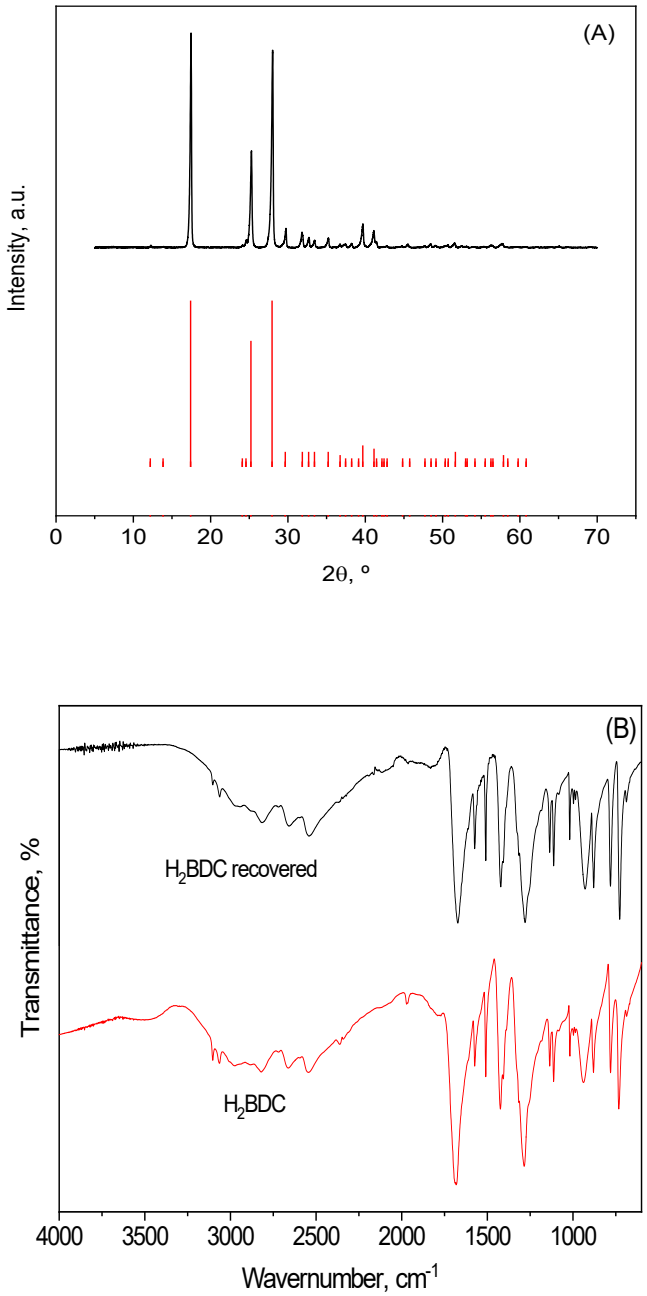

Figure 5.2. XRD patterns of recovered H_2BDC and ICCD PDF 00-031-1916 file (A). FTIR spectra of pure and recovered H_2BDC (B).

Table 5.2. Elemental analysis of recovered H_2BDC

Sample	C (wt.%)	H (wt.%)	N (wt.%)	O (wt.%)
H_2BDC-t	57.84	3.64	0.00	38.52
H_2BDC-R	57.50	3.59	0.03	38.88

All these characterization results pointed out the purity level of the terephthalic acid recovered. Accordingly, some subsequent synthesis batches were performed with the recovered solid and the required amount of make-up pure H_2BDC. As an example, **Table 5.1** shows the MBC labelled as Fe_3O_4-AC_R. Both, the mass yield and the percentage of terephthalic recovered were as high as those for its homologous Fe_3O_4-AC sample obtained with pure commercial H_2BDC only. Furthermore, characterization results of both MBC samples were very alike, as demonstrated by techniques shown in Section 5.3.2.

Another key aspect of the MBCs considered in this work is their easy preparation in large quantities which eventually would lead to a scalable synthesis. As an example, the synthesis procedure proposed was successfully carried out in 1.4 L of total volume to obtain 13.7 g of a Fe_3O_4-AC_L composite, which featured the same characteristics as its counterpart obtained at lower mass scale. See **Table 5.1** for mass yield (99.9%) and terephthalic acid recovery (96%) and Section 5.3.2 for XRD patterns and textural properties of MBC samples.

In summary, the soft experimental conditions, the use of water as a solvent, the low toxicity of the materials used [36–38] and the efficient use of reagents and recovery of terephthalic acid are in clearly line of greener synthesis methods to obtain more environmentally friendly materials to be applied in large scale processes [39–42].

5.3.2 Characterization of MBCs

Elemental analysis (C, H, N) of the as-synthetized MBCs is presented in **Table 5.3** together with the percentage of iron (also calculated as wt.% of Fe_3O_4), and the percentage of carbon calculated from the amounts of CO and CO_2 detected by TGA-DTA-MS.

Table 5.3. Elemental analysis, WDXRF and TG results of some MBCs.

	Elemental analysis			WDXRF		TGA-DTA-MS
MBC	**C (wt.%)**	**H (wt.%)**	**N (wt.%)**	**Fe (wt.%)**	**Fe_3O_4 (wt.%)**	**C (wt.%)**
Fe_3O_4	0.73	0.00	0.00	72.36	100.00	< 0.5
Fe_3O_4-G	37.00	0.47	0.11	44.89	62.04	38.55
Fe_3O_4-GO	22.00	0.91	0.00	55.28	76.40	23.22
Fe_3O_4-AC	32.00	0.71	0.21	45.85	63.36	34.25

The bare iron material prepared (i.e., Fe_3O_4 sample) showed a very low carbon content as measured by elemental analysis and TGA-DTA-MS, indicating that most of the terephthalic acid precursor was removed during the washing procedure. This agrees with the high level of terephthalic acid recovered after the synthesis procedure. On the other hand, the carbon-containing MBCs presented carbon percentages that are consistent with their expected carbon content taking into account the relative amounts of carbon in G (90 wt.%), GO (53 wt.%) and AC (70 wt.%). Besides, the theoretical iron content of these composites is c.a. 41 wt.%, which is close to the actual values for Fe_3O_4-G and Fe_3O_4-AC samples. However, Fe_3O_4-GO sample exhibited a somewhat higher iron content, which might be due to the modification of graphene oxygen groups during the synthesis method. The percentages of carbon in MBC samples were also corroborated by TGA-DTA-MS. The evolution of overall mass loss, and CO, CO_2 and H_2O

released upon heating in air flow are presented in **Figure 5.3**. The first mass loss event observed up to 150 °C can be ascribed to humidity, being more noticeable for the Fe_3O_4-GO sample. Then, there was another weight loss at 200-300 °C with liberation of H_2O, CO and CO_2 that could be attributable to the decomposition of labile surface oxygen groups from the carbonaceous structure like carboxylic acids, with a greater presence in the GO material [43,44]. At higher temperature, desorption of more stable oxygen groups and oxidation of the carbon materials take place. The residue remaining after the TG analysis would most likely be composed of completely oxidized iron and ashes from carbonaceous materials (mostly in AC support).

At this point, it should be mentioned that the presence of minor amounts of residual terephthalic acid in MBC samples cannot be discarded. Sublimation of terephthalic acid takes place as an endothermic process at 300-400 °C according with the TGA-DTA of pure H_2BDC (**Figure 5.4**) in which neither CO_2 nor CO were detected.

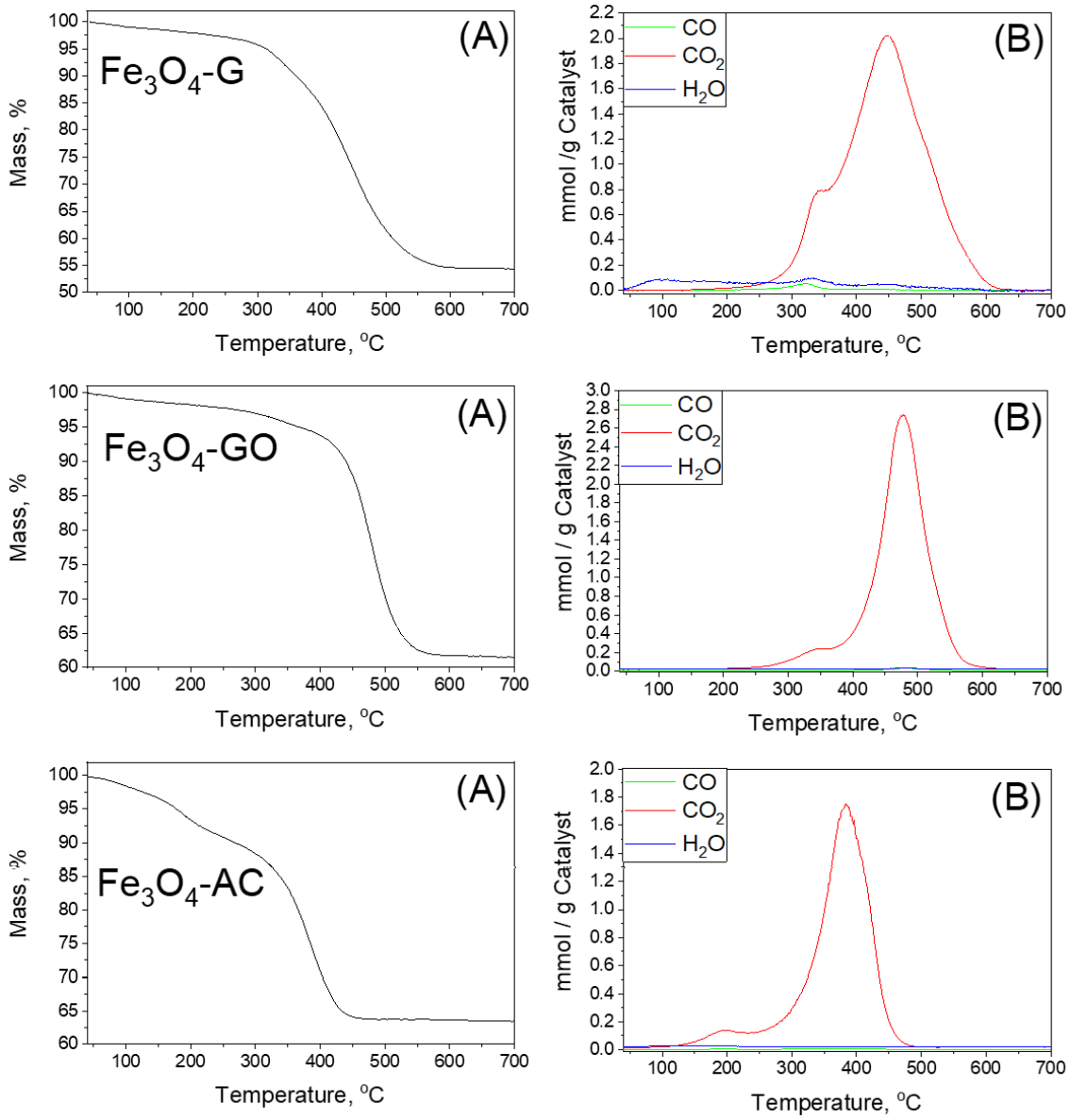

Figure 5.3. TGA-DTA-MS in air: (A) mass loss, and (B) gases released.

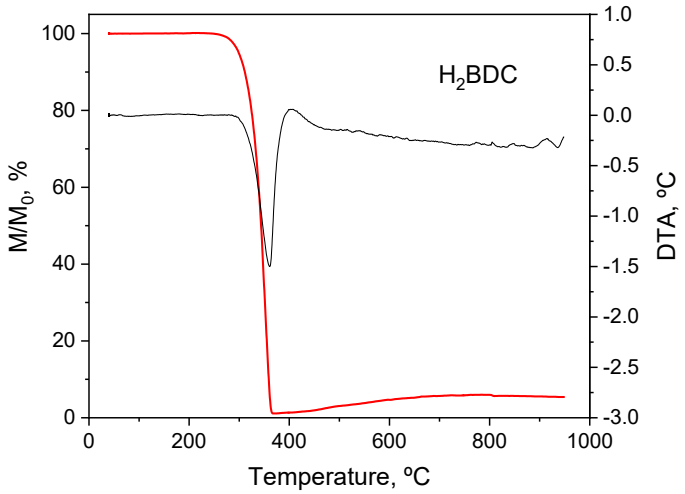

Figure 5.4. TGA-DTA of terephthalic acid in air.

Regarding the crystalline structure of MBC samples, **Figure 5.5** shows the XRD patterns (A) and Raman spectra (B) of some as-synthetized materials. The main reflection peaks observed in XRD at 2θ 30.2°, 35.5°, 43.2°, 53.6°, 57.1° and 62.7° are fully ascribable to cubic structure of magnetite according to PDF 01-075-0449 pattern file of the ICCD®. The presence of other iron species like maghemite would be evidenced by two additional peaks at 23.8° and 26.1° that do not appear in the patterns of **Figure 5.5 (A)** [45]. Thus, although the presence of maghemite in the samples cannot be fully discarded, its content would be negligible. The XRD patterns also pointed out that the Fe_3O_4-GO sample presented the lowest crystallinity among the prepared MBCs with wider peaks even having a high percentage of iron. The crystallite size of magnetite in the materials was determined by the Scherrer's equation from the (311) diffraction peak at 35.5° and the values obtained are shown in **Figure 5.5 (A)**. As seen, they range from 20.1 nm for Fe_3O_4-GO to 29.8 nm for Fe_3O_4 and Fe_3O_4-G samples.

The Raman spectrum of the Fe_3O_4 sample showed their typical bands of magnetite at 630-660 cm^{-1} with a broad band around 1300 cm^{-1}, also ascribable to a second-order peak of magnetite-like materials. Besides, traces of other iron oxide and hydroxide phases were deduced by the presence of the peaks at 219, 281, and 398 cm^{-1}. Nevertheless, it should be kept in mind that the formation of these structures by oxidation during Raman analyses due to the heating of the laser beam cannot be discarded [46]. In addition to these bands related to iron species, the spectra of carbon-containing MBCs showed carbon D and G bands at 1309 and 1595 cm^{-1}, respectively. Typically, the intensity ratio ID/IG from the areas of the corresponding bands are related to the frequency of defects in different carbon materials. In this case, the presence of the magnetite band at 1300 cm^{-1} overlapped with the D contribution, making the ID/IG ratio quantification difficult. Nonetheless, it can be easily noticed that the spectrum of the Fe3O4-G sample exhibited higher intensity of the G band, due to multi-layer arrangement, and the presence of the 2D band at 2646 cm^{-1} [44].

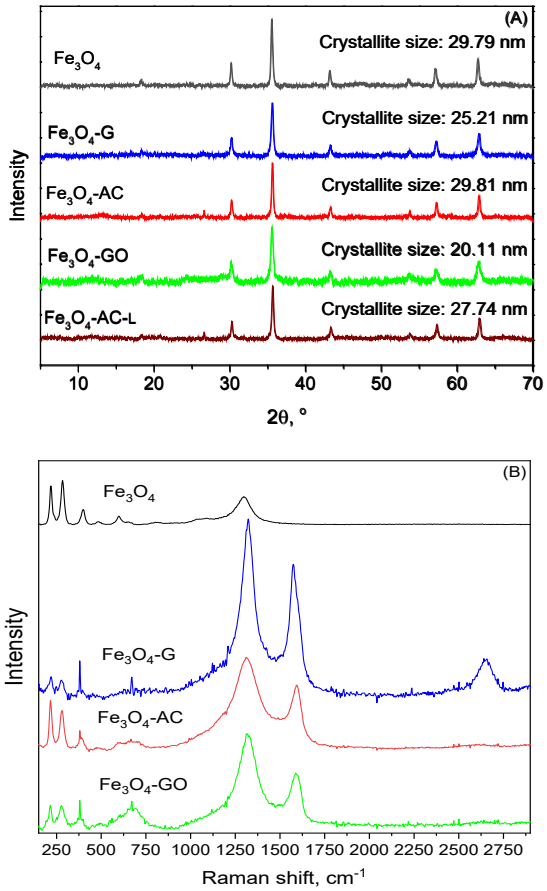

Figure 5.5. XRD patterns (A) and Raman spectra (B) of the as-synthetized MBCs.

FTIR spectra of MBC samples are presented in **Figure 5.6**. This characterization technique might help discriminate between magnetite and maghemite. The intense band located at 570 cm^{-1} is ascribable to Fe—O—Fe from magnetite while the broad shoulder up to 750 cm^{-1} can be assigned to partially oxidized magnetite on the surface, with a stoichiometry approaching maghemite [46,47]. On the other hand, the bands located at 640 cm^{-1} and 725 cm^{-1}, clearly visible in the spectra of Fe_3O_4-G and Fe_3O_4-GO samples but very subtle in that of Fe_3O_4-AC, suggest the presence of maghemite in the surface to some extent. In any case, the relative intensity of these IR bands and the findings from XRD results point out a minor contribution of maghemite to total iron oxide content

in the synthetized samples. No important peaks were observed in the region between 2000-1000 cm^{-1} of the FTIR spectrum of the Fe_3O_4 sample, which indicates the lack of organic compounds on the surface [48]. Then, residual H_2BDC remaining in the catalyst after the synthesis was expected to be of low significance. On the other hand, for the carbon composites the visible bands in the same wavenumber range can be most likely ascribed to different surface oxygen groups in the carbon structures, which are less abundant in the graphene composite [49,50]. Nevertheless, the presence of minor amounts of residual H_2BDC in carbon MBCs, which was revealed in stability tests (see Section 5.3.3), is also consistent with FTIR results.

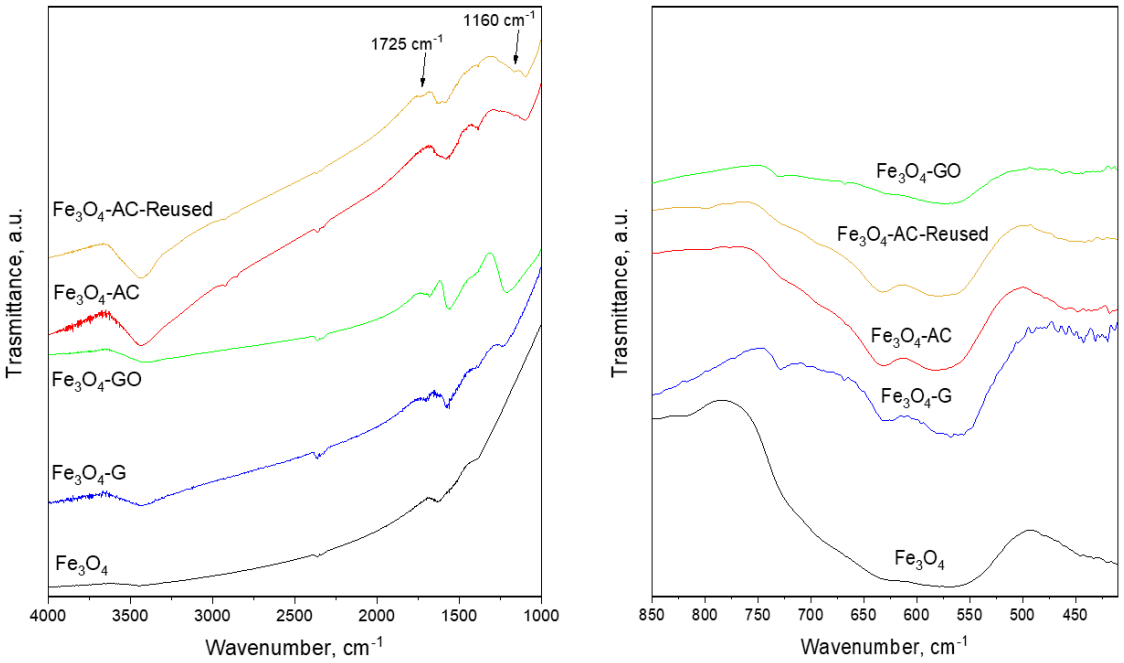

Figure 5.6. FTIR spectra of the as-synthetized materials.

Magnetization hysteresis loops of some MBC samples are plotted in **Figure 5.7**, where it can be seen that saturation magnetization (M_S) ranged from 25.6 emu g^{-1} (Fe_3O_4-GO) to 80.6 emu g^{-1} (Fe_3O_4). This latter value is in the typical range of magnetite NPs, which exhibit saturation magnetization from 60 to 90 emu g^{-1} depending on the morphology and particle size. In general, the higher the

particle size the higher the M_S [47,51,52]. The Fe_3O_4 sample synthetized here, with crystal size near 30 nm, showed a saturation magnetization slightly higher than values reported for other magnetite samples with similar particle size [51]. On the other hand, the carbon-Fe_3O_4 hybrid materials presented lower saturation magnetization values. While the M_S values observed for Fe_3O_4-G (36.1 emu g^{-1}) and Fe_3O_4-AC (38.7 emu g^{-1}) are consistent with the percentage of iron in these materials as determined by WDXRF (see **Table 5.3**), the saturation magnetization of the Fe_3O_4-GO composite was somewhat lower despite its higher content of iron. This can be explained by the smaller magnetite crystal size (see **Figure 5.5 (A)**) and the possible presence of other iron species to some extent.

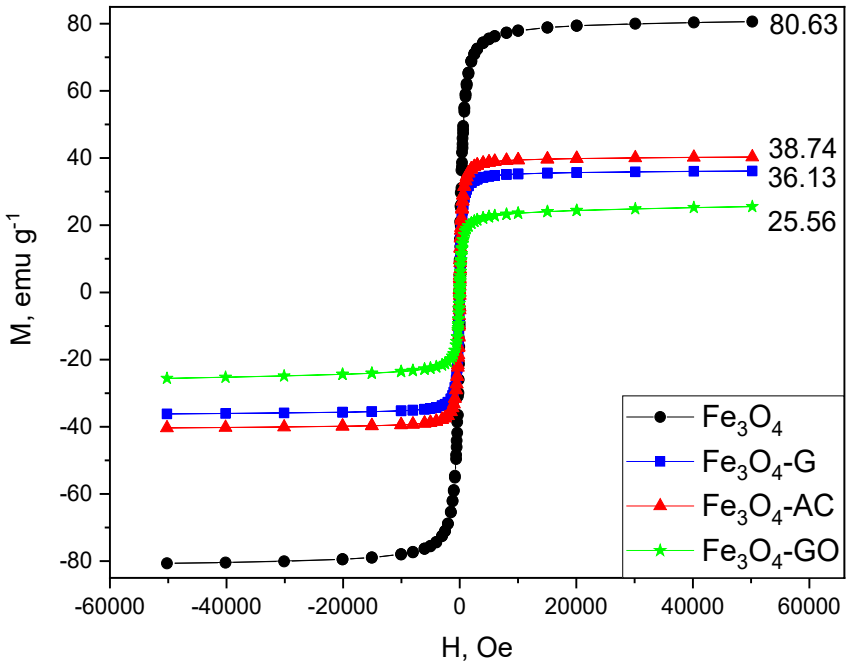

Figure 5.7. Magnetization vs. applied magnetic field at 25 °C.

Finally, some main textural parameters obtained by N_2 adsorption-desorption isotherms plotted in **Figure 5.8**, are summarized in **Table 5.4**. The results of the

carbonaceous materials used as precursors have been added to the table for comparative purposes.

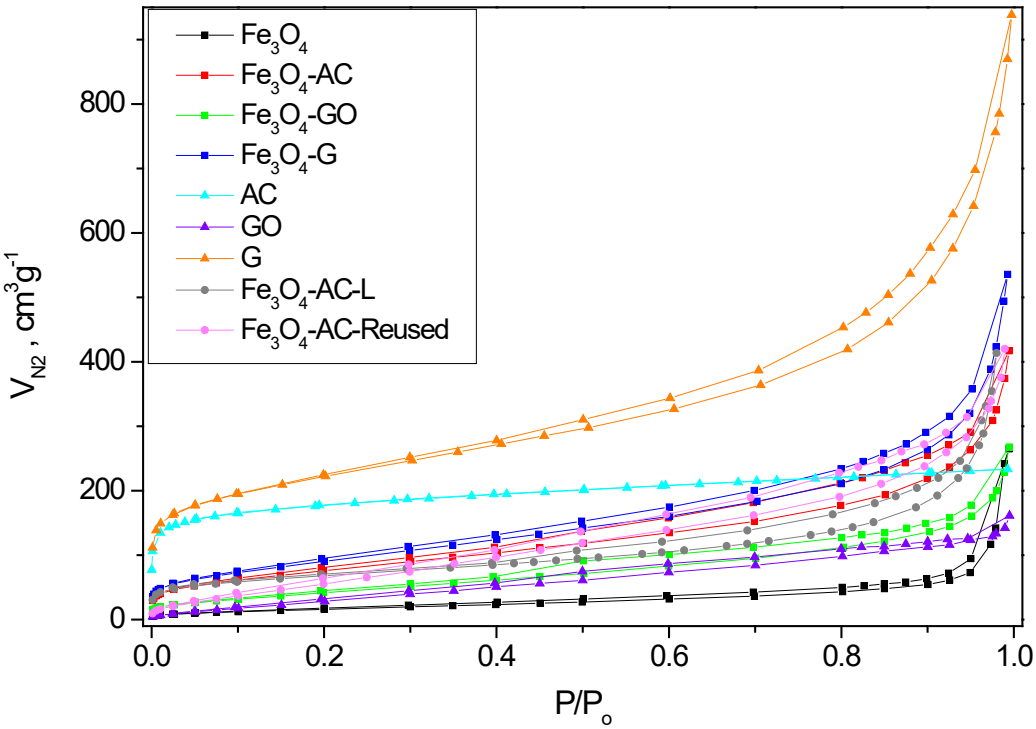

Figure 5.8. N_2 adsorption-desorption isotherms.

First, it is apparent that the Fe_3O_4 sample displayed a type IV isotherm with a hysteresis loop typical of mesoporous materials, with a moderate surface area and very low micropore volume. On the other hand, the combination of magnetite with carbonaceous structures led to composites with higher surface areas according to the porous structure of the supports. These results are consistent with other magnetic-carbon composites reported in the literature [53]. Then, the largest BET area was obtained for Fe_3O_4-G followed by Fe_3O_4-AC and Fe_3O_4-GO. The values of surface area observed for Fe_3O_4-AC and Fe_3O_4-G samples

with respect to their corresponding carbon supports (i.e., AC and G, respectively) were found proportional to the carbon content in the composite material.

Table 5.4. Textural properties of the as-synthetized MBCs and their carbonaceous supports.

Sample	S_{BET} ($m^2\ g^{-1}$)	S_{EXT} ($m^2\ g^{-1}$)	V_{MICRO} ($cm^3\ g^{-1}$)	V_{TOTAL} ($cm^3\ g^{-1}$)
G	760	514	0.118	1.122
GO	142	122	0.024	0.220
AC	644	37	0.303	0.361
Fe_3O_4	63	59	0.005	0.374
Fe_3O_4-G	337	271	0.048	0.764
Fe_3O_4-GO	164	131	0.036	0.353
Fe_3O_4-AC	282	213	0.052	0.578
Fe_3O_4-AC-$_L$	240	181	0.029	0.641
Fe_3O_4-AC-$_{Reused}$	255	255	0.001	0.801

5.3.3 Stability of MBCs in water

The stability of the as-synthetized materials in water was studied at different conditions. First, long-term runs were carried out for 7 days in ultrapure water buffered solution at MBC concentration of 1 g L^{-1}. **Table 5.5** summarizes data of pH, concentration of H_2BDC, Fe and total organic carbon (TOC) after some experiments. Regardless of the pH, the concentration of H_2BDC in solution after the runs carried out with the Fe_3O_4 sample was only about 1 mg L^{-1}, which agrees with a small presence of residual terephthalate in the catalyst after the synthesis procedure (see FTIR results). On the other hand, the values of H_2BDC in solution observed when carbon MBCs were brought into contact with water were significantly larger and they increased with the aqueous pH. This suggests that some amount of H_2BDC adsorbed onto the carbonaceous materials can be favorably desorbed at alkaline conditions. If results of H_2BDC recovery shown in **Table 5.1** are considered, the maxima concentration of H_2BDC observed after stability tests (i.e., at pH = 8-10) accounts for 78%, 62% and 42% of the

maximum releasable H_2BDC from Fe_3O_4-G, Fe_3O_4-GO and Fe_3O_4-AC, respectively. This proves alkaline desorption as a good alternative to remove residual H_2BDC from the catalysts. Then, a sample of Fe_3O_4-AC was submitted to an additional washing step in NaOH solution (pH = 10) and used in catalytic activity tests for comparative purposes (see Section 5.3.4).

A comparison between the concentration of H_2BDC expressed as mg C L^{-1} (TOC_{H2BDC}) and the actual TOC values provides an insight into the leaching of carbon moieties from the materials. In general, $Diff_{TOC}$ was within the experimental error range of the analytical method (i.e. ± 0.5 mg L^{-1}) suggesting that released carbon belonged mostly to H_2BDC. However, much larger $Diff_{TOC}$ values were observed for Fe_3O_4-GO at neutral and alkaline conditions. This can be related to the instability of GO in water and its reaction in alkaline media resulting in the release of humic-like structures to aqueous solution [32]. Iron was analyzed in aqueous solution as dissolved iron (sample filtered through 0.45 μm PET membrane) and total iron (sample obtained by separation of the solid with a magnet). For samples from Fe_3O_4 runs, very low values of iron concentration were found, being no more than 0.2% of the maximum releasable amount according to the catalyst composition. The difference between total and dissolved iron was low, but still appreciable, especially at high pH. This can be due to some instability of the material at alkaline conditions likely because of partial transformation of magnetite into goethite or maghemite in a dissolution-precipitation process [54]. This effect was also observed for Fe_3O_4-AC to a similar extent. However, the difference between total and dissolved iron greatly increased in tests performed with graphene-based materials. In the case of Fe_3O_4-G, at pH = 8 and pH = 10, values of total Fe higher than 4 mg L^{-1} suggests the formation of iron oxide precipitates. Additionally, mechanical breakdown of the small particles (i.e., the graphene used as starting material has a particle size less than 2 μm) must be considered. Finally, in the case of Fe_3O_4-GO, regardless of pH a higher amount of total iron as solid structures (> 4 mg L^{-1}) was detected

compared to dissolved iron (< 0.15 mg L^{-1}). A combination of the above-mentioned effects together with the intrinsic instability of GO in water might be responsible of such iron leaching from the catalyst [32,54].

Table 5.5. Results from MBCs long-term stability tests at different pH.

MBC	pH_0	pH_f	H_2BDC (mg L^{-1})	TOC_{H2BDC} (mg L^{-1})	TOC (mg L^{-1})	[1]$Diff_{TOC}$ (mg L^{-1})	[2]Fe (mg L^{-1})
Fe_3O_4	4.00	4.61	0.93	0.54	0.92	0.38	0.18 / 0.12
	6.00	6.13	1.04	0.60	0.58	-0.02	0.37 / 0.28
	7.00	7.06	0.91	0.53	1.10	0.58	0.99 / 0.16
	8.00	7.96	0.98	0.57	0.81	0.24	1.34 / 0.26
	10.00	9.73	1.02	0.59	1.20	0.61	1.69 / 0.11
Fe_3O_4-G	4.00	4.45	8.22	4.75	5.16	0.41	0.19 / 0.17
	6.00	6.01	27.01	15.61	15.79	0.18	0.39 / 0.10
	7.00	6.93	31.53	18.22	18.36	0.14	0.42 / 0.16
	8.00	7.70	30.62	17.69	18.95	1.26	> 4.00 / 0.16
	10.00	9.57	31.74	18.34	19.85	1.51	> 4.00 / 0.17
Fe_3O_4-GO	4.00	4.59	4.46	2.58	2.25	-0.33	> 4.00 / 0.12
	6.00	6.08	14.48	8.37	9.63	1.26	> 4.00 / 0.09
	7.00	6.90	19.60	11.32	13.93	2.61	> 4.00 / 0.10
	8.00	7.63	22.10	12.77	14.95	2.18	> 4.00 / 0.14
	10.00	8.43	20.77	12.00	16.18	4.18	> 4.00 / 0.11
Fe_3O_4-AC	4.00	4.55	3.30	1.91	2.24	0.33	0.19 / 0.19
	6.00	6.06	9.95	5.75	6.17	0.43	0.16 / 0.16
	7.00	7.02	13.25	7.66	8.17	0.51	0.28 / 0.17
	8.00	7.62	17.11	9.89	9.06	-0.83	0.34 / 0.11
	10.00	8.65	19.48	11.25	10.61	-0.64	0.43/ 0.11

[1] Difference between actual TOC and theoretical TOC calculated from H_2BDC concentration (TOC_{H2BDC})

[2] Fe analyzed after separation with a magnet / after filtration.

A key aspect in the performance of a catalyst is its stability under actual reaction conditions. The MBCs here prepared were intended for CWPO processes. Thus, the stability of the materials in the presence of O_2 and H_2O_2 under simulated solar radiation was explored. For that, MBC samples were brought into contact with ultrapure water under agitation for 30 min. Then, oxygen was bubbled, H_2O_2 was added (if necessary) and the aqueous suspension was irradiated for 3 h. **Table 5.6** shows the concentration of H_2BDC, TOC and pH after some tests. Dissolved iron and total iron were always lower than 0.05 mg L^{-1} and 0.1 mg L^{-1}, respectively. In this regard, it should be noticed that lower solid loadings were used (0.2 g L^{-1}) compared with the previous long-term assays summarized in **Table 5.5**.

Table 5.6. Results from MBCs stability tests under oxidizing conditions.

MBC	Test	Time (min)	H_2BDC (mg L^{-1})	TOC (mg L^{-1})	pH
Fe_3O_4	Rad+O_2	0	0.23	0.12	7.38
		180	0.29	0.52	7.35
	Rad+O_2+H_2O_2	0	0.24	0.11	7.37
		180	0.00	0.55	7.30
Fe_3O_4-G	Rad+O_2	0	3.10	0.16	7.21
		180	3.18	1.27	6.10
	Rad+O_2+H_2O_2	0	3.14	0.17	7.20
		180	1.56	2.52	6.50
Fe_3O_4-GO	Rad+O_2	0	0.53	0.52	7.05
		180	1.02	1.23	6.35
	Rad+O_2+H_2O_2	0	0.60	0.54	7.03
		180	0.00	2.05	5.92
Fe_3O_4-GO	Rad+O_2	0	0.76	0.10	7.63
		180	0.78	0.45	6.32
	Rad+O_2+H_2O_2	0	1.27	0.11	7.65
		180	0.00	0.65	5.84

In general, from **Table 5.6** it can be noticed the desorption of some terephthalic acid from the materials during the initial 30 min dark stage (see

H_2BDC data at time 0). This effect was particularly evident for the Fe_3O_4-G sample. The amount of H_2BDC in solution remained practically unchanged after the treatment with Rad+O_2 experiments but decreased significantly in Rad+O_2+H_2O_2 runs as a result of H_2BDC oxidation by $HO^{\bullet}$ generated in photo-Fenton reactions [29]. Contrarily, TOC increased especially in Rad+O_2+H_2O_2 runs because of breakdown of terephthalate molecule into smaller organic acids (see pH drops in **Table 5.6**) and $HO^{\bullet}$ attack to carbon structures. In any case, Fe_3O_4-AC resulted in the highest stability among the three carbon MBCs synthesized in this work.

5.3.4 Catalytic activity of MBCs in CWPO processes

The catalytic activity of the as-prepared MBCs was studied for the degradation of MTP by heterogeneous Fenton and photo-Fenton processes. According to the accepted mechanism for these AOPs, the following reactions can be considered [7]:

$$\equiv Fe^{2+} + H_2O_2 \rightarrow \equiv Fe^{3+} + OH^- + HO^{\bullet} \quad (5.4)$$

$$\equiv Fe^{3+} + H_2O_2 \rightarrow \equiv Fe^{2+} + H^+ + HO_2^{\bullet} \quad (5.5)$$

$$HO_2^{\bullet} + OH^- \rightarrow H_2O + O_2^{\bullet -} \quad (5.6)$$

where $\equiv Fe^{3+}$ and $\equiv Fe^{2+}$ represents the iron species on the catalyst surface. On the other hand, iron oxides can act as photocatalysts in the presence of UV-vis radiation:

$$\equiv Fe^{3+}/\equiv Fe^{2+} + h\upsilon \rightarrow \equiv Fe^{3+}/\equiv Fe^{2+} + h^+ + e^- \quad (5.7)$$

$$e- + O_2 \rightarrow O_2^{\bullet -} \quad (5.8)$$

$$2\,O_2^{\bullet -} + 2H^+ \rightarrow H_2O_2 + O2 \quad (5.9)$$

$$e^- (O_2^{\bullet-}) + H_2O_2 \rightarrow OH^- + HO^{\bullet} (+ O_2) \quad (5.10)$$

Moreover, radiation favors the regeneration of $\equiv Fe^{2+}$ on the catalyst surface, increasing the generation of hydroxyl radicals:

$$\equiv Fe^{3+} + h\upsilon + OH^- \rightarrow \equiv Fe^{2+} + HO^{\bullet} \quad (5.11)$$

The hydroxyl radicals generated through reactions (5.4), (5.10) and (5.11) will be the main responsible of MTP degradation in aqueous media.

The evolution of MTP during dark CWPO and photo-CWPO using the four materials is depicted in **Figure 5.9**. It should be noticed that prior to oxidation runs, adsorption experiments in the dark were carried out to establish an adequate time for MTP adsorption equilibrium. This was nearly reached in 30 min using any of the four MBCs (not shown), with MTP removals of 17% for Fe_3O_4-G, 12% for Fe_3O_4-AC, 8% for Fe_3O_4-GO and less than 3% for Fe_3O_4. In addition, blank experiments of MTP with H_2O_2 both in the presence and absence of simulated solar radiation were carried out and negligible MTP removal was observed. As is apparent from **Figure 5.9(A)**, the catalytic activity of Fe_3O_4 in dark CWPO at room temperature (i.e., 20 °C) was rather low with only 5% of MTP conversion in 3 h, likely due to a slow $\equiv Fe^{3+}/\equiv Fe^{2+}$ redox cycle (Reaction (5.5)) [55]. The presence of carbon structures in MBCs increased their adsorption capacity (see decrease in MTP concentration from -30 to 0 min in **Figure 5.9**) and the reaction rate of MTP removal to some extent (see data from 0 to 180 min in **Figure 5.9(A)**). However, the activity was still unsatisfactory for practical application at the mild conditions of this work (i.e., ambient temperature and initial pH = 7) with less than 35% overall MTP removal and negligible mineralization (i.e., TOC removal) in 3 h. In this sense, it is well-known that optimum pH for Fenton reactions is near 3 and that higher temperature (i.e., 50-90 °C) would be also required to increase the efficiency of the catalytic activity of MBCs [6]. As expected from reactions (5.7) to (5.11), simulated solar radiation greatly enhanced the process efficiency. Thus, MTP removals between 40% and

95% were observed depending on the MBC used (**Figure 5.9(B)**). In this case, the beneficial effect of carbon structures over bare Fe_3O_4 goes beyond the increase in the adsorption capacity of MTP. **Table 5.7** shows the pseudo-first-order apparent rate constant of MTP removal for the four synthetized materials. As shown, the best results in terms of MTP removal rate were found for Fe_3O_4-GO and Fe_3O_4-AC composites.

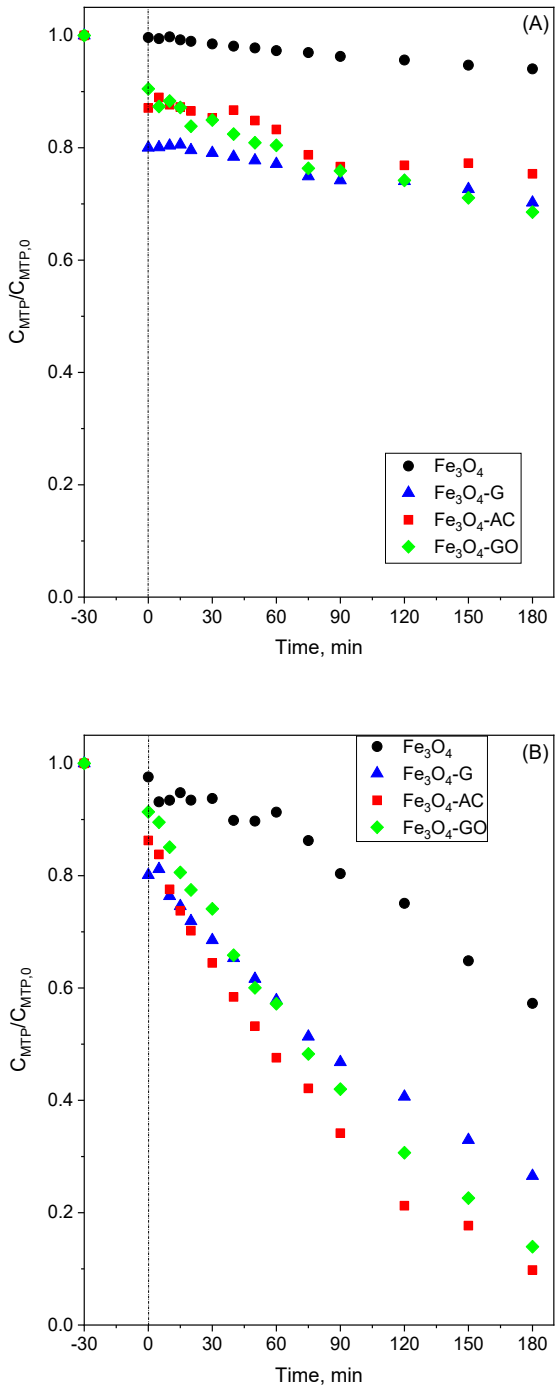

Figure 5.9. Evolution of MTP normalized concentration during (A) dark CWPO and (B) simulated solar radiation-assisted CWPO. Conditions: $C_{MTP,0}$ = 50 mg L^{-1}, C_{MBC}= 0.2 g L^{-1}, pH_0 = 7, T(A) = 20 °C, T(B) = 40 °C, $C_{H2O2,0}$ = 50 Mm, Irradiance = 581 Wm^{-2}.

Table 5.7. Pseudo-first order apparent kinetic constants for MTP degradation and efficiency of H_2O_2 utilization in photo-CWPO runs.

Sample	Conditions	$k_{app\text{-}MTP}$ (min^{-1})	R^2	η-TOC-H_2O_2 (mol C/mol H_2O_2)
Fe_3O_4	50 mM H_2O_2, pH_0 = 7	$2.5x10^{-3}$	0.956	0.074
Fe_3O_4-G	50 mM H_2O_2, pH_0 = 7	$6.0x10^{-3}$	0.997	0.129
Fe_3O_4-GO	50 mM H_2O_2, pH_0 = 7	$9.1x10^{-3}$	0.998	0.079
Fe_3O_4-AC	50 mM H_2O_2, pH_0 = 7	$9.6x10^{-3}$	0.997	0.054
Fe_3O_4-AC	50 mM H_2O_2, pH = 7 (*)	$5.1x10^{-3}$	0.996	0.026
Fe_3O_4-AC	6.5 mM H_2O_2, pH_0 = 7	$1.7x10^{-3}$	0.998	0.205
Fe_3O_4-AC	10 mM H_2O_2, pH_0 = 7	$4.1x10^{-3}$	0.991	0.230
Fe_3O_4-AC	30 mM H_2O_2, pH_0 = 7	$7.4x10^{-3}$	0.974	0.095

(*) pH controlled during the run at 7.0

TOC adsorbed onto the catalysts during the initial dark stage and overall TOC removal after the 180 min photo-treatment are presented in **Figure 5.10**. It is apparent that overall TOC removal achieved in the process catalyzed by Fe_3O_4 was rather low though significantly increased using the carbon composites. Thus, the highest TOC removal (21%) was obtained with the Fe_3O_4-AC catalyst.

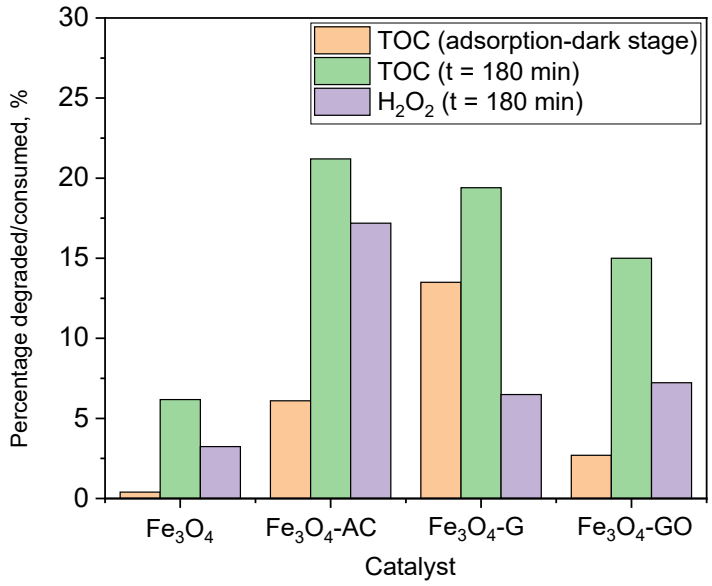

Figure 5.10. Percentages of TOC removal and H_2O_2 depletion during photo-CWPO of MTP. Conditions: $C_{MTP,0}$ = 50 mg L^{-1}, C_{MBC} = 0.2 g L^{-1}, pH_0 = 7, T = 40 °C, $C_{H2O2,0}$ = 50 mM, Irradiance= 581 W m^{-2}.

An efficient use of H_2O_2 is a key aspect in the performance of CWPO processes. In this work, the efficient use of H_2O_2 has been examined by a mineralization efficiency factor defined as TOC removed (mol C) per mol of H_2O_2 consumed, η-TOC-H_2O_2. According to the stoichiometry of the theoretical reaction between MTP and H_2O_2 to yield CO_2 and H_2O (i.e, mineralization) a η-TOC-H_2O_2 value of 0.38 mol C/mol H_2O_2 is calculated. This represents the maximum attainable efficiency factor. As it can be seen in **Table 5.7**, actual η-TOC-H_2O_2 values were well below this maximum because of inefficient H_2O_2 decomposition and $HO^{\bullet}$ reactions (e.g., H_2O_2 auto-scavenging effect, termination steps of the free radical reaction mechanism and $HO^{\bullet}$ reactions with carbon materials). Comparing the different MBCs, the highest efficiency was achieved with Fe_3O_4-G, likely due to its higher surface area and MTP adsorption capacity.

Moreover, higher inefficient consumption of H_2O_2 was expected for Fe_3O_4-AC according to previous studies [56].

As discussed before, the degradation of MTP takes place mainly through the attack of hydroxyl radicals formed from H_2O_2 decomposition. Several steps are expected until complete MTP mineralization, which involve the formation of different intermediate compounds. The final degradation step intermediates are usually short-chain organic acids like oxalic, acetic and formic acids [57,58]. As shown in **Table 5.8**, noticeable concentrations of these acids were found after 3 h of treatment, being formic acid predominant. It should be pointed out that oxalic acid might be fast degraded during iron-photocatalytic treatments through the ligand-charge-metal transition mechanism, which also favor mineralization and reduces the iron leaching [59,60]. Total iron and terephthalic acid released into the reaction medium were also analyzed and presented in **Table 5.8**. As observed, the concentration of total iron was lower than 0.12 mg L^{-1} regardless of the material used. At such low concentration, contribution of homogeneous photo-Fenton reactions to MTP degradation was negligible. The amount of H_2BDC remaining in solution after CWPO runs was also small, the highest value found in the Fe_3O_4-G run in agreement with results discussed in Section 5.3.3.

Table 5.8. Concentrations of short-chain organic acids, iron and terephthalic acid after photo-CWPO runs.

MBC	$C_{Acetic\ acid}$ (mg L^{-1})	$C_{Formic\ acid}$ (mg L^{-1})	$C_{Oxalic\ acid}$ (mg L^{-1})	Fe (mg L^{-1})	C_{H2BDC} (mg L^{-1})
Fe_3O_4	0.44	2.85	0.86	0.12	0.23
Fe_3O_4-G	2.42	12.5	2.16	0.06	3.40
Fe_3O_4-GO	2.10	10.2	2.33	0.07	1.06
Fe_3O_4-AC	1.97	13.4	3.65	0.06	0.88

5.3.5 Improved use of Fe_3O_4-AC catalyst

In view of the above results, Fe_3O_4-AC was the most promising catalyst among the MBCs here studied due to higher MTP and TOC conversions and greater stability in CWPO as well as lower cost of the carbonaceous material (laboratory prices from the suppliers indicates that G and GO are about 4 and 300 times more expensive than AC, respectively). Nevertheless, improvement of the catalyst synthesis and the optimization of CWPO treatment conditions (e.g., pH, temperature, H_2O_2 dosage, treatment time, etc.) might eventually lead to a substantial enhancement of the catalyst performance. In line with this, the impact of further purification of the Fe_3O_4-AC catalyst, its performance in CWPO treatment at circumneutral pH and the effect of H_2O_2 dose were examined.

One of the key aspects of this work is the development of a green synthesis of MBCs with full recovery of the terephthalic acid use a mediator in the procedure. Although low relatively low amounts of H_2BDC remained on the catalyst after the synthesis, a further washing step with NaOH solution (pH = 10) and rinsing water to remove retained H_2BDC to a higher extent was proved useful. In **Figure 5.11**, MTP removal rate and pH evolution during CWPO experiments using the material without the additional alkaline washing step (Fe_3O_4-AC) and after treatment with aqueous NaOH (Fe_3O_4-AC-alkaline washed) are presented. Similar evolution of MTP and a slightly smaller drop in the initial pH during CWPO demonstrated that the process efficiency was not greatly affected by the additional washing step but no accumulation of H_2BDC during the experiment with the Fe_3O_4-AC-alkaline catalyst was observed.

To assess the catalytic process performance of Fe_3O_4-AC in the CWPO of MTP at circumneutral pH, an experiment was completed controlling the pH at 7 throughout the run. **Figure 5.11** shows that MTP removal rate was somewhat slower than in the corresponding pH-free experiment (notice decrease of pH up to 3.5-4) but still higher than that observed with bare Fe_3O_4. This is a promising

result with this material because one of the main drawbacks of CWPO technologies is a relatively low efficiency at circumneutral pH [61].

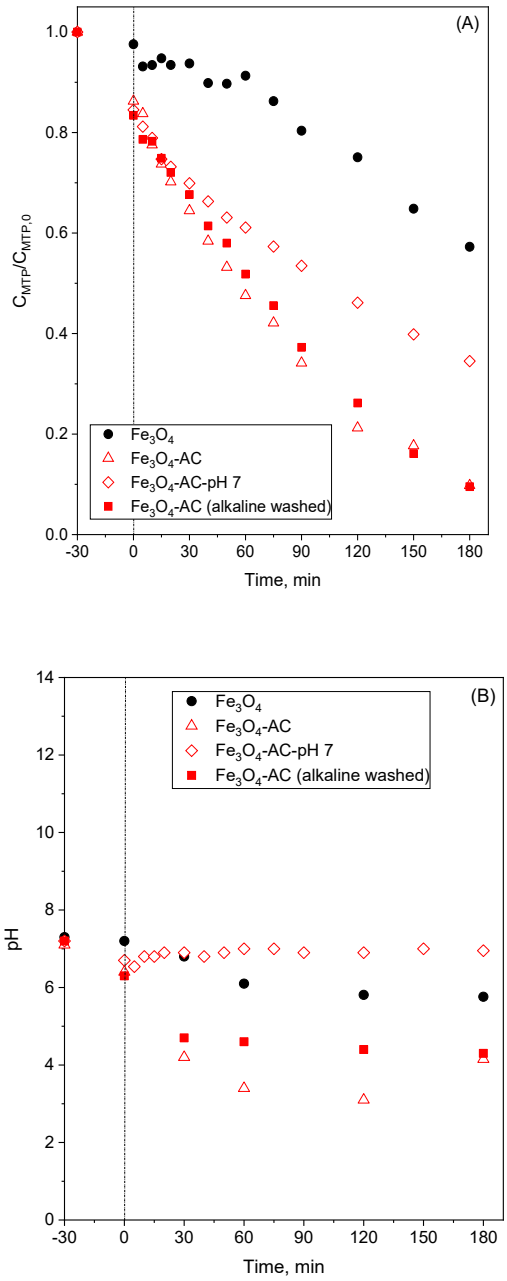

Figure 5.11. Evolution of MTP (A) and pH (B) during photo-CWPO processes with Fe_3O_4 and Fe_3O_4-AC materials. Conditions: $C_{MTP,0}$ = 50 mg L^{-1}, C_{MBC} = 0.2 g L^{-1}, pH_0 = 7, T = 40 °C, $C_{H2O2,0}$ = 50 mM, Irradiance= 581 W m^{-2}.

Another important fact found when carbonaceous materials are used as catalysts or supports in CWPO is the inefficient consumption of H_2O_2 under certain conditions [62,63]. In this sense, the dosage of H_2O_2 applied plays a crucial role. Theoretically, the optimum H_2O_2 dose (stoichiometric dose) to be applied for mineralization of MTP (i.e., complete conversion to CO_2, H_2O and NO_3^-) is 89 mol H_2O_2/mol MTP (as metoprolol tartrate). Since the experiments carried out in this work were completed with an MTP initial concentration of 50 mg L^{-1} (i.e., 0.073 mM), the theoretical initial concentration of H_2O_2 to mineralize MTP is calculated as 6.5 mM. Photo-CWPO experiments with initial H_2O_2 concentration in the 6.5-50 mM range were performed and the obtained results are presented in **Figure 5.12** and **Table 5.7**. Although the rate of MTP removal was clearly influenced by the H_2O_2 dose (the higher the H_2O_2 concentration the higher the apparent rate constant $k_{app\text{-}MTP}$) minor differences were observed in TOC removal. As a consequence, the mineralization efficiency reached a maximum value (η-TOC-H_2O_2=0.23 mol C/mol H_2O_2) for an initial concentration of H_2O_2 10 mM (**Figure 5.12(B)**). Still, this efficiency value is far from the theoretical 0.38 mol C/mol H_2O_2 due to the refractory nature of some MTP degradation intermediates and the auto-scavenging effect of H_2O_2, which also reacts with $HO^{\bullet}$ and other reactive oxygen species [64].

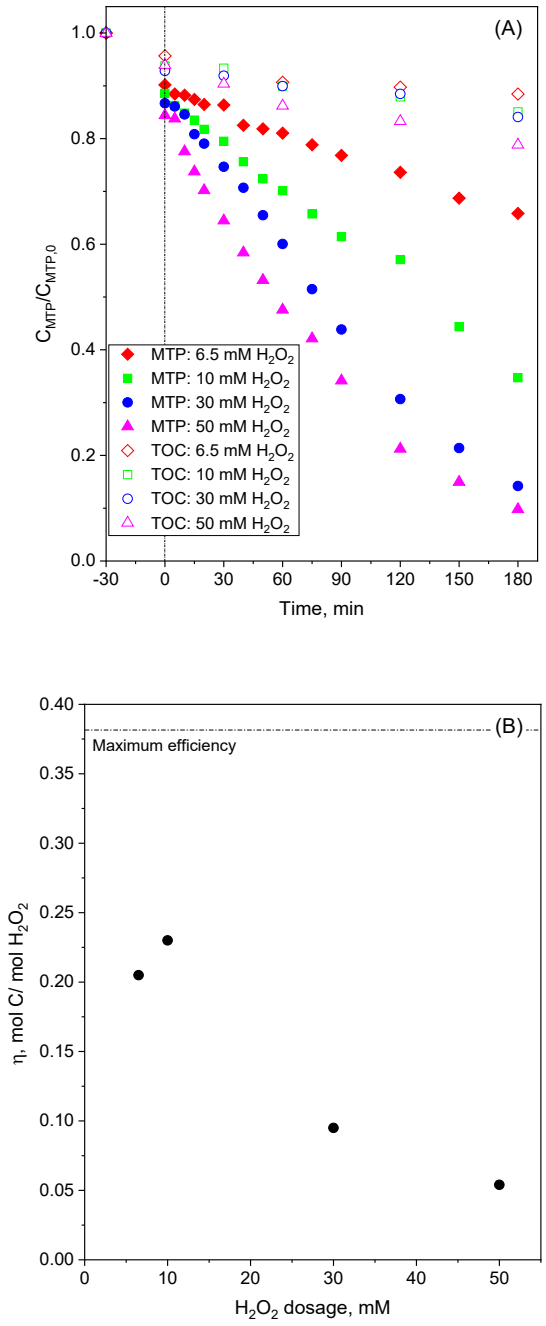

Figure 5.12. (A) MTP and TOC removals and (B) efficiency of H_2O_2 use in MTP mineralization. Effect of H_2O_2 dosage. Conditions: $C_{MTP,0}$ = 50 mg L^{-1}, C_{MBC} = 0.2 g L^{-1}, pH_0 = 7, T = 40 °C, Irradiance = 581 W m^{-2}.

5.3.6 Reuse of Fe_3O_4-AC catalyst

One of the main challenges in developing a catalyst is to ensure good long-term performance. To study the reusability of the Fe_3O_4-AC catalyst, nine consecutive CWPO runs were carried out. The catalyst was recovered with an external magnet after each run and used in the next one without further treatment. Total iron and H_2BDC concentrations at the end of each cycle were always lower than 0.15 mg L^{-1} and 0.5 mg L^{-1}, which proved good catalyst stability. **Figure 5.13** overall MTP and TOC removals by solar assisted CWPO. Additionally, the percentage of MTP adsorbed onto the catalysts after the initial dark stage is presented. It can be seen that overall removal of MTP dropped from 90 to ca. 75% after nine cycles, with a similar trend for TOC (from 21% to 10%). This loss of catalytic performance took place within the first four cycles mainly. It can be related to the loss of the adsorption capacity of the catalyst for MTP, which decreased from 12% (first cycle) to ca. 6% (from second to ninth cycles).

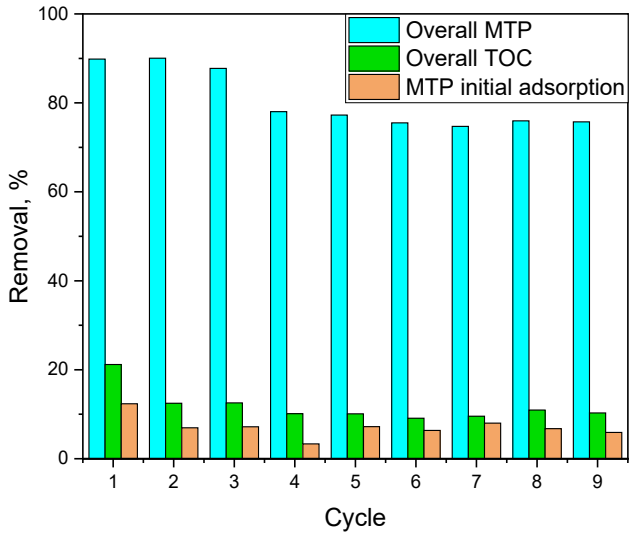

Figure 5.13. Percentage removals of MTP and TOC during CWPO runs reusing the Fe_3O_4-AC catalyst. Conditions: $C_{MTP,0}$ = 50 mg L^{-1}, C_{MBC} = 0.2 g L^{-1}, pH_0 = 7, T = 40 °C, Irradiance = 581 W m^{-2}.

The analysis of the N_2 adsorption-desorption isotherm of a catalyst sample after the fifth cycle, when the main drop of the catalytic activity had already been observed, confirmed a decrease in BET surface area and especially in micropore volume (see **Table 5.4**), which are mainly responsible of adsorption phenomena in activated carbons. This effect is usually related to the presence of organic matter occupying micropores, although may also be due to the collapse of micropores walls due to the oxidation environment of CWPO. In this line, the elemental analysis of the used catalyst showed an increase in the contents of carbon (from 32 to 40%), nitrogen (from 0.2 to 0.4%) and hydrogen (from 0.7 to 1.2%). Besides, although the presence of adsorbed organic matter in carbonaceous materials is difficult to confirm by FTIR due to the overlapping of various bands, in **Figure 5.6**, two visible bands in the reused sample, located at 1160 cm^{-1} and 1725 cm^{-1}, suggest the presence of phenolic and carboxyl moieties adsorbed onto the carbon surface [65]. These results points to the presence of organic compounds (i.e., MTP and degradation products) adsorbed onto the catalyst surface.

On the other hand, at the oxidizing conditions applied in CWPO, some $\equiv Fe^{2+}$ active sites might be oxidized to $\equiv Fe^{3+}$, thus lowering the catalytic activity and the saturation magnetization to some extent. Accordingly, the saturation magnetization decreased from 38.7 to 32.9 emu g^{-1} after the repetitive use of the catalyst, which might be related to the partial transformation of surface magnetite into maghemite. The oxidation state of iron was studied by means of X-ray photoelectron spectroscopy. The high-resolution spectra of Fe 2p spectral region is presented in **Figure 5.14** for fresh and reused catalyst. The peak positions of Fe $2p_{3/2}$ and Fe $2p_{1/2}$ and the satellite signals are consistent with the existence of magnetite and other $\equiv Fe^{3+}$ species in both samples. The spectra were curve-fitted to a combination of Gaussian-Lorentzian functions using a Shirley-type background for peak analysis according to Grosvenor et al. [66]. The ratio between the areas of the Fe^{3+} and Fe^{2+} peaks in the Fe $2p_{3/2}$ zone slightly changed from 4.78 (fresh Fe_3O_4-AC) to 4.97 (reused Fe_3O_4-AC in nine consecutive CWPO

runs), which confirmed that the oxidation takes place to a low extent. Despite these structural changes in the catalyst, its catalytic activity was maintained from the fourth run onwards and was still easily separable with a magnet.

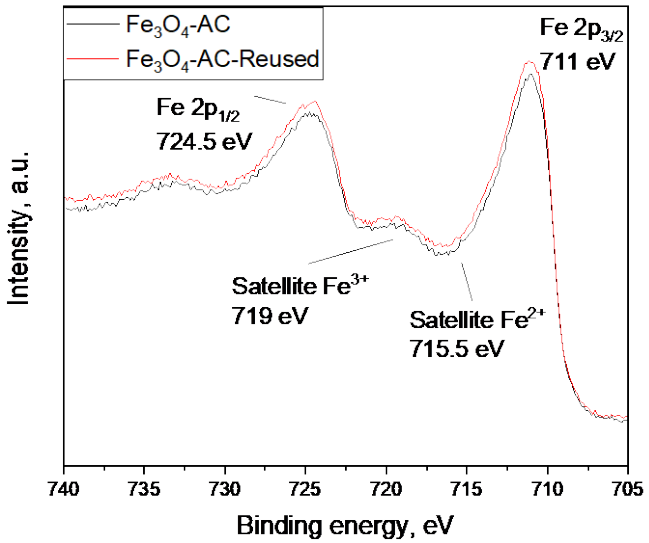

Figure 5.14. High-resolution XPS spectra of Fe 2p region of fresh and reused Fe_3O_4-AC catalyst after CWPO.

5.4 CONCLUSIONS

The synthesis method proposed in this work allowed obtaining mesoporous magnetite and magnetized carbonaceous materials of high purity, with excellent magnetic properties that facilitate their separation, and acceptable textural properties for their possible application as catalysts in different processes. The method proved to be easily scalable, possible to be carried out at ambient conditions and have a high percentage recovery of one of the main reagents (i.e., terephthalic acid), which can be reused into a new synthesis, thus falling within the philosophy of green synthesis to obtain environmentally friendly materials.

The materials thus obtained, bare magnetite and three carbonaceous composites (prepared from activated carbon, graphene and graphene oxide) were active for photo-CWPO, as demonstrated treating an aqueous solution of MTP. Fe_3O_4-G and Fe_3O_4-GO showed low stability compared to Fe_3O_4 and Fe_3O_4-AC. Moreover, the latter presented catalytic activity much superior to bare Fe_3O_4. MTP and TOC conversions higher than 90% and 20%, respectively, were achieved after 3 h of treatment with Fe_3O_4-AC at initial aqueous pH = 7 (pH dropped to ca. 4). At circumneutral pH (pH was controlled about 7 throughout the process) MTP removal was still moderate (> 60%), this being a typical limiting issue in photo-Fenton treatments. The best efficiency in the use of H_2O_2 was 0.23 mol C eliminated per mol H_2O_2 consumed, which is about a 60% of the maximum attainable efficiency. Fe_3O_4-AC could be easily reused in a nine-consecutive CWPO experiment recovering the catalyst with a magnet after each cycle. Moderate catalyst deactivation was observed mainly due to the blockage of some micropores and/or loss of Fe^{2+} catalytic sites. Nevertheless, deactivation from the fourth cycle onwards was negligible and magnetic separability remained quite satisfactory.

References

[1] L.S. Arias, J.P. Pessan, A.P.M. Vieira, T.M.T. De Lima, A.C.B. Delbem, D.R. Monteiro, D. R. Iron oxide nanoparticles for biomedical applications: a perspective on synthesis, drugs, antimicrobial activity, and toxicity. Antibiotics 7 (**2018**) 2.

[2] A.K. Gupta, M. Gupta. Synthesis and surface engineering of iron oxide nanoparticles for biomedical applications. Biomaterials, 26 (**2005**) 3995–4021.

[3] G. Cotin, S. Piant, D. Mertz, D. Felder-Flesch, S. Begin-Colin. Iron oxide nanoparticles for biomedical applications: synthesis, functionalization, and application; Elsevier Ltd., (**2018**).

[4] R.B. Nasir Baig, S. Verma, M.N. Nadagoud, R.S. Varma. Advancing sustainable catalysis with magnetite. surface modification and synthetic applications. Aldrichimica Acta 49 (**2016**) 35–41.

[5] A. Masudi, G.E. Harimisa, N.A. Ghafar, N.W.C. Jusoh. Magnetite-based catalysts for wastewater treatment. Environ. Sci. Pollut. Res., 27 (**2020**) 4664–4682.

[6] M. Muñoz, Z.M. de Pedro, J.A. Casas, J.J. Rodríguez. Preparation of magnetite-based catalysts and their application in heterogeneous fenton oxidation-A Review. Appl. Catal. B Environ., 176-177 (**2015**) 249–265.

[7] N. Thomas, D.D. Dionysiou, S.C. Pillai. Heterogeneous Fenton Catalysts: A Review of Recent Advances. J. Hazard. Mater., 404 (**2021**) 124082.

[8] R.S. Ribeiro, A.M.T. Silva, J.L. Figueiredo, J.L. Faria, H.T. Gomes. Catalytic wet peroxide oxidation: a route towards the application of hybrid magnetic carbon nanocomposites for the degradation of organic pollutants. A Review. Appl. Catal. B Environ., 187 (**2016**) 428–460.

[9] L. Lai, Y. He, H. Zhou, B. Huang, G. Yao, B. Lai. Critical review of natural iron-based minerals used as heterogeneous catalysts in peroxide activation processes: characteristics, applications and mechanisms. J. Hazard. Mater., 416 (**2021**) 125809.

[10] A.S. Teja, P.Y. Koh. Synthesis, properties, and applications of magnetic iron oxide nanoparticles. Prog. Cryst. Growth Charact. Mater., 55 (**2009**)22–45.

[11] Z.J. Zhang, X.Y. Chen, B.N. Wang, C.W. Shi. W. Hydrothermal synthesis and self-assembly of magnetite (Fe_3O_4) nanoparticles with the magnetic and electrochemical properties. J. Cryst. Growth, 310 (**2008**) 5453–5457.

[12] P. V. Nidheesh. Heterogeneous fenton catalysts for the abatement of organic pollutants from aqueous solution: A Review. RSC Adv., 5 (**2015**) 40552–40577.

[13] S. Peng, C. Wang, J. Xie, S. Sun. Synthesis and stabilization of monodisperse Fe nanoparticles. J. Am. Chem. Soc., 128 (**2006**) 10676–10677.

[14] J. Ge, Y. Hu, M. Biasini, C. Dong, J. Guo, W.P. Beyermann, Y. Yin. One-Step synthesis of highly water-soluble magnetite colloidal nanocrystals. Chem. - A Eur. J., 13 (**2007**) 7153–7161.

[15] Z. Li, H. Chen, H. Bao, M. Gao. One-Pot Reaction to synthesize water-soluble magnetite nanocrystals. Chem. Mater., 16 (**2004**) 1391–1393.

[16] X. Lu, M. Niu, R. Qiao, M. Gao. Superdispersible PVP-Coated Fe_3O_4 nanocrystals prepared by a "one-pot" reaction. J. Phys. Chem. B., 112 (**2008**) 14390–14394.

[17] Y. Mizukoshi, T. Shuto, N. Masahashi, S. Tanabe. Preparation of superparamagnetic magnetite nanoparticles by reverse precipitation method: contribution of sonochemically generated oxidants. Ultrason. Sonochem., 16 (**2009**) 525–531.

[18] I. Nedkov, T. Merodiiska, L. Slavov, R.E. Vandenberghe, Y. Kusano, J. Takada. Surface oxidation, size and shape of nano-sized magnetite obtained by co-precipitation. J. Magn. Magn. Mater., 300 (**2006**) 358–367.

[19] S. Qu, H. Yang, D. Ren, S. Kan, G. Zou, D. Li, M. Li. Magnetite nanoparticles prepared by precipitation from partially reduced ferric chloride aqueous solutions. J. Colloid Interface Sci., 215 (**1999**) 190–192.

[20] T. Ozkaya, M.S. Toprak, A. Baykal, H. Kavas, Y. Köseoğlu, B. Aktaş. Synthesis of Fe_3O_4 nanoparticles at 100 °C and its magnetic characterization. J. Alloys Compd., 472 (**2009**) 18–23.

[21] A. Kobyliukh, K. Olszowska, M. Godzierz, A. Kordyka, J. Kubacki, Y. Mamunya, S. Pusz, I. Stoycheva, U. Szeluga. Effect of graphene material structure and iron oxides deposition method on morphology and properties of graphene/iron oxide hybrids. Appl. Surf. Sci., 573 (**2022**) September 2021.

[22] M. Ioffe, M. Long, A. Radian. Systematic evaluation of activated carbon-Fe_3O_4 composites for removing and degrading emerging organic pollutants. Environ. Res., 198 (**2021**) 111187.

[23] K.L. Lopes, H.L. de Oliveira, J.A.S. Serpa, J.A. Torres, F.G.E. Nogueira, V.A.A. de Freitas, K.B. Borges, M.C. Silva. Nanomagnets based on activated carbon/magnetite nanocomposite for determination of endocrine disruptors in environmental water samples. Microchem. J. 168 (**2021**) (May).

[24] S. Rodríguez-Sánchez, B. Ruiz, D. Martínez-Blanco, M. Sánchez-Arenillas, M.A. Diez, J.F. Marco, P. Gorria, E. Fuente. Towards advanced industrial waste-based magnetic activated carbons with tunable chemical, textural and magnetic properties. Appl. Surf. Sci., 551 (**2021**).

[25] M. Stan, I. Lung, M.L. Soran, C. Leostean, A. Popa, M. Stefan, M.D. Lazar, O. Opris, T.D. Silipas, A.S. Porav. Removal of antibiotics from aqueous solutions by green

synthesized magnetite nanoparticles with selected agro-waste extracts. Process Saf. Environ. Prot., 107 (**2017**) 357–372.

[26] Y. Jiang, W.N. Wang, P. Biswas, J.D. Fortner. Facile aerosol synthesis and characterization of ternary crumpled graphene-TiO_2-magnetite nanocomposites for advanced water treatment. ACS Appl. Mater. Interfaces, 6 (**2014**) 11766–11774.

[27] S.E. Kim, K.W. Kim, S.W. Lee, S.O. Kim, J.S. Kim, J.K. Synthesis and characterization of TiO_2-Coated magnetite Clusters (NFe_3O_4@TiO_2) as Anode materials for Li-ion Batteries. Curr. Appl. Phys., 13 (**2013**) 1923–1927.

[28] J. López, A. Rey, P.M. Álvarez, A.M. Chávez, E. Viñuelas, ES PATENT PUBLICATION Nº ES2884450B2, Método para la magnetización de sólidos inorgánicos, (**2022**).

[29] J. López, A.M. Chávez, A. Rey, P.M. Álvarez. Insights into the stability and activity of MIL-53(Fe) in solar photocatalytic oxidation processes in water. Catalysts, 11 (**2021**).

[30] A.M. Chávez, A. Rey, F.J. Beltrán, P.M. Álvarez. Solar photo-ozonation: a novel treatment method for the degradation of water pollutants. J. Hazard. Mater., 317 (**2016**) 36–43.

[31] G.M. Eisenberg. Colorimetric Determination of Hydrogen Peroxide. Ind. Eng. Chem. - Anal. Ed., 15 (**1943**) 327–328.

[32] A.M. Dimiev, L.B. Alemany, J.M. Tour. Graphene Oxide. Origin of Acidity, Its Instability in Water, and a New Dynamic Structural Model. ACS Nano, 7 (**2013**) 576–588.

[33] D.A. Cabrera-Munguia, M.I. León-Campos, J.A. Claudio-Rizo, D.A. Solís-Casados, T.E. Flores-Guia, L.F. Cano Salazar. Potential biomedical application of a new MOF based on a derived PET: synthesis and characterization. Bull. Mater. Sci., 44 (**2021**) 245.

[34] L. Cosimbescu, D.R. Merkel, J. Darsell, G. Petrossian. Simple But Tricky: Investigations of Terephthalic Acid Purity Obtained from Mixed PET Waste. Ind. Eng. Chem. Res., 60 (**2021**) 12792–12797.

[35] K. Varaprasad, M. Pariguana, G.M. Raghavendra, T. Jayaramudu, E.R. Sadiku. Development of biodegradable metaloxide/polymer nanocomposite films based on poly-ε-caprolactone and terephthalic acid. Mater. Sci. Eng. C, 70 (**2017**) 85–93.

[36] G.L. Ball, C.J. McLellan, V.S. Bhat. Toxicological review and oral risk assessment of terephthalic acid (TPA) and its esters: a category approach. Crit. Rev. Toxicol., 42 (**2011**) 28–67.

[37] A. Hoshi, R. Yanai, K. Kuretani. Toxicity of terephthalic Acid. Chem. Pharm. Bull., 16 (**1968**) 1655–1660.

[38] X.X. Zhang, S.L. Sun, Y. Zhang, B. Wu, Z.Y. Zhang, B. Liu, L.Y. Yang, S.P. Cheng. Toxicity of purified terephthalic acid manufacturing wastewater on reproductive system of male mice (mus musculus). J. Hazard. Mater., 176 (**2010**) 300–305.

[39] D. Wang, P. Yang, Y. Zhu. Growth of Fe_3O_4 Nanoparticles with tunable sizes and morphologies using organic amine. Mater. Res. Bull., 49 (**2014**) 514–520.

[40] S.R. Kumar, M.M. Raja, D. Mangalaraj, C. Viswanathan, N. Ponpandian. Surfactant free solvothermal synthesis of monodispersed 3D hierarchical Fe_3O_4 microspheres. Mater. Lett., 110 (**2013**) 98–101

[41] Y. Li, R. Jiang, T. Liu, H. Lv, L. Zhou, X. Zhang. One-Pot Synthesis of Grass-like Fe3O4 Nanostructures by a Novel Microemulsion-Assisted Solvothermal Method. Ceram. Int., 40 (**2014**) 1059–1063.

[42] C.Y. Haw, F. Mohamed, C.H. Chia, S. Radiman, S. Zakaria, N.M. Huang, H.N. Lim. Hydrothermal synthesis of magnetite nanoparticles as MRI contrast agents. Ceram. Int., 4 (**2010**) 1417–1422.

[43] J.L. Figueiredo, M.F.R. Pereira, M.M.A. Freitas, J.J.M. Órfão. Modification of the surface chemistry of activated carbons. Carbon N. Y., 37 (**1999**) 1379–1389.

[44] L.M. Pastrana-Martínez, S. Morales-Torres, V. Likodimos, P. Falaras, J.L. Figueiredo, J.L. Faria, A.M.T. Silva. Role of oxygen functionalities on the synthesis of photocatalytically active graphene–TiO_2 composites. Appl. Catal. B Environ., 158–159 (**2014**) 329–340.

[45] A. Ruíz-Baltazar, R. Esparza, G. Rosas, R. Pérez. Effect of the surfactant on the growth and oxidation of iron nanoparticles. J. Nanomater., 2015 (**2015**).

[46] T.J. Daou, J.M. Grenèche, G. Pourroy, S. Buathong, A. Derory, C. Ulhaq-Bouillet, B. Donnio, D. Guillon, S. Begin-Colin. Coupling Agent Effect on Magnetic Properties of functionalized magnetite-based nanoparticles. Chem. Mater., 20 (**2008**) 5869–5875.

[47] A. Rizzuti, M. Dassisti, P. Mastrorilli, M.C. Sportelli, N. Cioffi, R.A. Picca, E. Agostinelli, G. Varvaro, R. Caliandro. Shape-control by microwave-assisted hydrothermal method for the synthesis of magnetite nanoparticles using organic additives. J. Nanoparticle Res., 17 (**2015**) 408.

[48] J. Niemeyer, Y. Chen, J.-M. Bollag. Characterization of Humic Acids, Composts, and peat by diffuse reflectance Fourier-transform infrared spectroscopy. Soil Sci. Soc. Am. J., 56 (**1992**) 135.

[49] C. Moreno-Castilla, M. V. López-Ramón, F. Carrasco-Marín. Changes in surface chemistry of activated carbons by wet oxidation. Carbon N. Y., 38 (**2000**) 1995–2001.

[50] M. Pakuła, A. Świątkowski, M. Walczyk, S. Biniak. Voltammetric and FT-IR studies of modified activated carbon systems with phenol, 4-chlorophenol or 1,4-benzoquinone adsorbed from aqueous electrolyte solutions. Colloids Surfaces A Physicochem. Eng. Asp., 260 (**2005**) 145–155.

[51] S. Komarneni, W. Hu, Y.D. Noh, A. Van Orden, A.; Feng, S.; Wei, C.; Pang, H.; Gao, F.; Lu, Q.; Katsuki, H. Magnetite syntheses from room temperature to 150°C with and without microwaves. Ceram. Int., 38 (**2012**) 2563–2568.

[52] M.C. Mascolo, Y. Pei, T.A. Ring. Room temperature co-precipitation synthesis of magnetite nanoparticles in a large pH window with different bases. Materials (Basel)., 6 (**2013**) 5549–5567.

[53] R. Ianoș, C. Păcurariu, G. Mihoc. Magnetite/carbon nanocomposites prepared by an innovative combustion synthesis technique—excellent adsorbent materials. Ceram. Int., 40 (**2014**) 13649–13657.

[54] Y.T. He, S.J. Traina. Transformation of magnetite to goethite under alkaline pH conditions. Clay Miner., 42 (**2007**) 13–19.

[55] H. Sun, G. Xie, D. He, L. Zhang. Ascorbic acid promoted magnetite fenton degradation of alachlor: mechanistic insights and kinetic modeling. Appl. Catal. B Environ., 267 (**2020**) 118383.

[56] J. Carbajo, A. Quintanilla, A.L. Garcia-Costa, J. González-Julián, M. Belmonte, P. Miranzo, M.I. Osendi, J.A. Casas. The influence of the catalyst on the co formation during catalytic wet peroxide oxidation process. Catal. Today, 361 (**2021**) 30–36.

[57] A. Rey, D.H. Quiñones, P.M. Álvarez, F.J. Beltrán, P.K. Plucinski. Simulated solar-light assisted photocatalytic ozonation of metoprolol over titania-coated magnetic activated carbon. Appl. Catal. B Environ., 111-112 (**2012**) 246–253.

[58] D.H. Quiñones, A. Rey, P.M. Álvarez, F.J. Beltrán, P.K. Plucinski. Enhanced Activity and Reusability of TiO_2 loaded magnetic activated carbon for solar photocatalytic ozonation. Appl. Catal. B Environ., 144 (**2014**) 96–106.

[59] G. Pliego, P. Garcia-Muñoz, J.A. Zazo, J.A. Casas, J.J. Rodriguez. Improving the fenton process by visible LED irradiation. Environ. Sci. Pollut. Res., 23 (**2016**) 23449–23455.

[60] P. García-Muñoz, N.P. Zussblatt, G. Pliego, J.A. Zazo, F. Fresno, B.F. Chmelka, J.A. Casas. Evaluation of photoassisted treatments for norfloxacin removal in water using mesoporous Fe_2O_3-TiO_2 Materials. J. Environ. Manage., 238 (**2019**) 243–250.

[61] I. Oller, S. Malato. Photo-Fenton applied to the removal of pharmaceutical and other pollutants of emerging concern. Curr. Opin. Green Sustain. Chem., 29 (**2021**) 100458.

[62] C.M. Domínguez, P. Ocón, A. Quintanilla, J.A. Casas, J.J. Rodriguez. Highly Efficient application of activated carbon as catalyst for wet peroxide oxidation. Appl. Catal. B Environ., 140-141 (**2013**) 663–670.

[63] A. Rey, A.B. Hungria, C.J. Duran-Valle, M. Faraldos, A. Bahamonde, J.A. Casas, J.J. Rodriguez. On the optimization of activated carbon-supported iron catalysts in catalytic wet peroxide oxidation process. Appl. Catal. B Environ., 181 (**2016**) 249–259.

[64] A. Rey, A. Bahamonde, J.A. Casas, J.J. Rodríguez. Selectivity of hydrogen peroxide decomposition towards hydroxyl radicals in catalytic wet peroxide oxidation (CWPO) over Fe/AC Catalysts. Water Sci. Technol., 61 (**2010**) 2769–2778.

[65] D. Maity, S.G. Choo, J. Yi, J. Ding, J.M. Xue. Synthesis of magnetite nanoparticles via a solvent-free thermal decomposition route. J Magn. Magn Mater., 321 (**2009**) 1256-1259.

[66] A.P. Grosvenor, B.A. Kobe, M.C. Biesinger, N.S. Mcintyre. Investigation of multiplet splitting of Fe2p XPS spectra and bonding in iron compounds. Surf. Interface Anal., 36 (**2004**) 1564–1574

CHAPTER 6:

PREPARATION OF A NEW GREEN MAGNETIC Fe_3O_4@TIO_2-P25 PHOTOCATALYST FOR SOLAR ADVANCED OXIDATION PROCESSES IN WATER

6.1 INTRODUCTION

6.1.1 State of the art

The awareness of the increasing occurrence of emerging contaminants (ECs) at trace levels in water systems, especially in populated areas of developed countries, has alerted about a high-concern threat to the environment and human health [1]. Conventional biological and physical-chemical treatments usually applied at wastewater treatment plants (WWTPs) have been demonstrated rather ineffective for the removal of different ECs, including pharmaceutical and personal care products (PPCPs), pesticides, nanomaterials and plasticizers, which find their way to surface waters [2]. Moreover, WWTPs are also the main entrance to the environment of new classes of ECs such as antibiotic-resistant bacteria (ARB) and their antibiotic-resistant genes (ARG) [3]. Innovation in wastewater treatment adopting sustainable, cost-efficient technologies to achieve the goal of complete removal of ECs is becoming a must. In this sense, advanced oxidation processes (AOPs) are likely called to lead the battle against ECs in WWTPs. AOPs involve the generation of highly reactive oxygen species (ROS) such as hydroxyl radical ($HO^{\bullet}$, $E°=2.8$ V) or sulfate radical ($SO_4^{\bullet-}$, $E°=2.6$ V) that can degrade EC molecules eventually transforming them into harmless products [4]. Literature extensively reports on the performance of a variety of catalytic AOPs to deal with ECs, though lowering cost and energy consumption, as well as the sustainability and reusability of the catalyst remain as major challenges [5-7]. Among the most promising AOPs, solar heterogeneous photocatalytic oxidation can be highlighted as a method based on renewable energy capable of completely degrading organic ECs, removing inorganic ions (e.g., toxic metal ions) and killing bacteria [8]. Although a number of catalysts have been proposed for solar-driven AOPs so far, TiO_2-P25 is still considered the benchmark catalyst in this field because of its high photosensitivity, stability, non-toxic nature, availability in large quantities and low price [9]. Moreover, despite it is not a visible-light photocatalyst due to its wide band-gap (3.2 eV), TiO_2-P25 typically provides

higher photodegradation rates of aqueous pollutants under sunlight than other classical semiconductors (e.g., ZnO) and alternative new photocatalytic materials (e.g., MOFs) because of larger generation of ROS [10]. Furthermore, ROS production can be improved using TiO_2-P25 in combination with oxidants such as hydrogen peroxide or ozone [11,12]. A main limitation impeding the widespread application of TiO_2-P25 photocatalytic oxidation in WWTPs is the difficulty in the separation of nanosized TiO_2 particles from water suspensions. This is a critical issue regarding the adverse impact associated with the release of nanomaterials into the environment [13]. To overcome this problem, immobilization of TiO_2 on different supports can be considered, though typically at the expense of some loss of photocatalytic activity [14]. Extensive research has also been conducted on the preparation of TiO_2 magnetic reusable materials by in situ formation of anatase TiO_2 and magnetic iron oxides. However, the multi-step synthesis methods for this purpose are usually high energy-consuming and require large amounts of toxic reagents and solvents. Moreover, the activity of the prepared magnetic Fe_3O_4/TiO_2 photocatalysts rarely surpasses that of bare TiO_2-P25 nanoparticles [15]. Particularly interesting seems the direct use of TiO_2-P25 to produce robust magnetic reusable nanoparticles (NPs) [16].

6.1.2 Objectives and scope of this chapter

To achieve a low-carbon fingerprint, sustainable synthesis and reusability of the magnetic catalyst are imperative. In this sense, we have recently developed a green method to magnetize a variety of metal oxides following a green synthesis philosophy with non-toxic reagents, low energy consumption and materials recovery [17]. The method makes use of terephthalic acid (H_2BDC) as additive that favors the formation of magnetite at room conditions by aerial oxidation of Fe(II) at basic pH (i.e, oxidative precipitation method). Almost full recovery of H_2BDC is achieved after the catalyst preparation [18]. In the quest for sustainable

water remediation processes, a Fe_3O_4@TiO_2-P25 composite has been green-synthesized and fully characterized in this work. Possible insights into the formation of this material by oxidative precipitation of Fe(II) in the presence of TiO_2-P25 and BDC^{2-} are addressed. The stability, photocatalytic activity and reusability of the catalyst have been assessed for the removal of the β-blocker metoprolol (MTP), used as probe EC.

6.2 MATERIALS AND METHODS

6.2.1 Materials

Terephthalic acid (1,4-benzenedicarboxylic acid, $C_6H_4(COOH)_2$, purity ≥ 98% wt., H_2BDC in this work), iron (II) chloride tetrahydrate ($FeCl_2 \cdot 4H_2O$, purity ≥ 98% wt.), iron (III) nitrate nonahydrate ($Fe(NO_3)_3 \cdot H_2O$, purity ≥ 99% wt.), titanium (IV) isopropoxide ($Ti[OCH(CH_3)_2]_4$, 97% wt., TISOP in this work), titanium (IV) butoxide ($Ti(OCH_2CH_2CH_2CH_3)_4$, 97% wt., TIBUT in this work), ethylene glycol (C_2H_6O, purity ≥ 99% wt.), ethanol (C_2H_6O, 96% wt.), isopropanol (C_3H_8O, 99.6% wt.), granular activated carbon Darco 12-20 mesh, metoprolol tartrate ($(C_{15}H_{25}NO_3)_2 \cdot C_4H_6O_6$, purity ≥ 99% wt., MTP in this work), sodium hydroxide (NaOH, purity ≥ 98% wt.), hydrochloric acid (HCl, 37% wt.), nitric acid (HNO_3, 69% wt.) hydrogen peroxide (H_2O_2, 30% wt.), acetonitrile (purity ≥ 99.9% wt.) and ortho-phosphoric acid (H_3PO_4, 85.5% wt.) were used as received from commercial suppliers (Sigma-Aldrich and Panreac) without any further purification. Ultrapure water (UP) was produced by a Milli-Q academic system (Millipore). Aeroxide® TiO_2-P25 NPs were directly obtained from the manufacturer (Evonik Industries). Commercial magnetite NPs were kindly provided by Bendix S.A.

6.2.2 Catalyst preparation

Magnetic photocatalysts were prepared by a novel procedure described in the Spanish Patent Nº ES2884450B2 [17]. Following the procedure depicted in **Figure 6.1**, 1 g of $FeCl_2 \cdot 4H_2O$ was dissolved in 50 mL of UP water (solution A). Then, a certain amount of TiO_2-P25 was added and dispersed into solution A by means of 15 min ultrasonication at room temperature. Solution B was prepared by dissolving 0.835 g of H_2BDC in a volume of 1 M NaOH aqueous solution. Subsequently, solution A was stirred at 800 rpm and solution B was added dropwise for 2 min. The mixture was kept under agitation at constant temperature to allow for air oxidation and aging leading to the formation of the catalyst. After that, the solid was separated using a neodymium external magnet and then washed twice with 200 mL of UP water. The solid finally obtained was dried overnight, milled and kept in a desiccator until use. The slightly acidic solution (pH ~5.5) resulting after the magnetic separation of the solid contained BDC^{2-}, Na^+ and Cl^- as well as traces (ppm level) of non-reacted iron. Concentrated HCl solution (37% wt.) was added to bring pH below 3 so that precipitation of H_2BDC (pK_{a1}=3.54, solubility 0.0015 g/100 mL at 20°C and pH=3) took place. The produced solid was recovered by filtration, rinsed with UP water and reused in the catalyst synthesis as shown in **Figure 6.1**. A sample of the recovered solid was dried overnight at 100°C and analyzed by FTIR and elemental analysis to determine its composition as H_2BDC (**Figure 5.2** and **Table 6.1**). Terephthalic acid reuse rate was over 95%. For comparative purposes, samples were also prepared in the absence of TiO_2-P25 and/or H_2BDC following the procedure described above. In addition, samples of magnetic core-shell Fe_3O_4/TiO_2 NPs (CS-Fe_3O_4/TiO_2) and an activated carbon/Fe_3O_4/TiO_2 composite (AC/Fe_3O_4/TiO_2) were prepared by sol-gel methods as detailed previously [19,20]. Briefly, TiO_2 produced from TISOP was deposited onto commercial magnetite NPs and the resulting product calcined at 400 ºC to obtain Fe_3O_4/TiO_2 NPs [19]. A magnetic activated carbon (MAC) sample was prepared by the incipient wetness impregnation

method followed by heat treatment at 550 ºC for 4 h in a reducing atmosphere. Then, MAC particles were dispersed in a TiO_2 sol obtained from TIBUT and subjected to ultrasonic treatment for 1 h to synthesize the AC/Fe_3O_4/TiO_2 ternary composite [20].

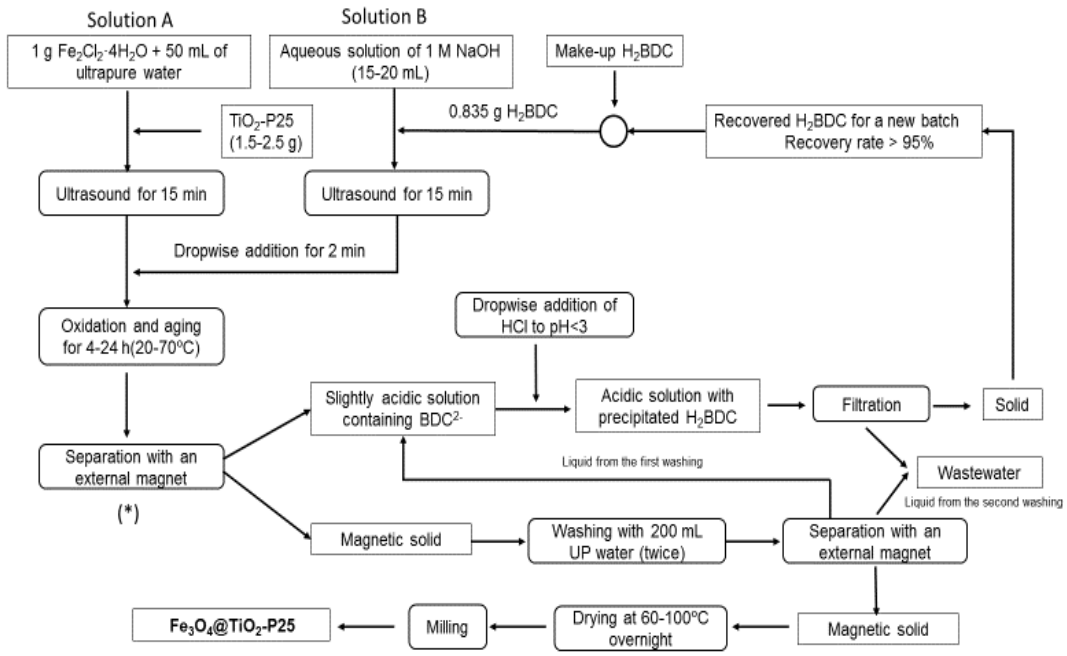

Figure 6.1. Schematic flow chart for the preparation of Fe_3O_4@TiO_2-P25 magnetic catalysts.

Table 6.1. Elemental analysis of pure H_2BDC and the solid recovered and reused in the synthesis of Fe_3O_4@TiO_2-P25.

Sample	% C	% H	% N
Pure H_2BDC	57.78	3.64	0.00
Recovered solid	57.59	3.59	0.03

6.2.3 Characterization of catalysts

X-ray diffraction (XRD) patterns of samples were obtained in the range of 2θ = 5° - 70° with a step size of 0.01° and a 0.5 s of sampling per point using a powder Bruker D8 Advance XRD diffractometer with a Cu $K\alpha_1$ radiation (λ =0.1541 nm) and a linear detector VANTEC (aperture 3º). Thermogravimetric and differential thermal analyses (TGA-DTA) were carried out in air (50 mL min^{-1}) from 20 °C to 800 °C (heating rate of 5 °C min^{-1}) with a thermobalance STA 449 F3 Jupiter-Netzsch coupled to a mass spectrometer QMS 403D Aëolos III-Netzsch SETSYS Evolution-16. The porous structure of catalysts was assessed by nitrogen adsorption–desorption isotherms acquired at -196 ºC in a Quantachrome Autosorb iQ2-C Series apparatus. Before analysis, samples were outgassed at 150 ºC for 10 h under a residual pressure < 10^{-2} mbar. The BET equation and t-plot method were applied to determine surface area and pore volume. Elemental analysis was carried out with a CHNS TruSpec Micro (LECO) elemental analyzer. Wavelength dispersive X-ray fluorescence spectroscopy (WDXRF) (S8 Tiger apparatus, Bruker) was used to determine the amounts of Fe and Ti in the catalyst samples. The morphology and composition of the catalyst particles was examined by scanning electron microscopy fitted to energy dispersive X-ray spectroscopy (SEM-EDX) using a Hitachi S-4800 apparatus working at 20–30 kV accelerating voltage and 500–2000 magnification. Fourier-transformed infrared spectroscopy in attenuated total reflectance mode (ATR-FTIR) analyses were performed on a Nicolet is10 spectrometer (Thermo Scientific). Sampling resolution was set at 4 cm^{-1} and 32 scans from 560 to 4000 cm^{-1} wavenumber range. Spectra were processed using Thermo Scientific Omnic 3.2v software. Magnetic measurements were performed using a Quantum Design MPMS XL-7 Superconducting Quantum Interference Device (SQUID). The magnetic moment *M* was measured as a function of the applied magnetic field *H* at room temperature. Surface chemical composition was studied by X-ray

photoelectron spectroscopy (XPS) on a PHI VersaProbe II Scanning XPS Microprobe spectrometer equipped with scanning monochromatic X-ray Al Kα radiation (hυ = 1486.6 eV) as the excitation source and a multi-channel hemispherical electron analyzer (pass energy of 29.35 eV). Binding energies were calibrated to the C 1 s peak from the carbon signal at 284.6 eV. The resulting XPS peaks were curve-fitted to a combination of Gaussian-Lorentzian functions using a Shirley-type background for peak analysis. Diffuse reflectance UV–vis spectroscopy (DRS) measurements were performed with a UV–vis-NIR Cary 5000 spectrophotometer (Varian-Agilent Technologies) equipped with an integrating sphere device.

6.2.4 Catalyst stability and photoactivity

First, the stability of the prepared catalysts in aqueous solution was studied in the 4-10 pH range. Catalyst samples were suspended in phosphate-buffered ultrapure water to achieve 1 g L^{-1} concentration and kept in tubes under orbital agitation for 7 days at 25 ºC. Catalyst stability under simulated solar radiation and presence of oxidants (O_2, O_3 or H_2O_2) was also tested. **Section 2.4 "Experimental set-up for catalytic activity and stability studies"** shows a schematic picture of the experimental set-up used. Typically, 125 mg of catalyst were suspended in 250 mL of phosphate-buffered ultrapure water in a 300 mL borosilicate glass vessel, which was placed in the chamber of a Suntest CPS+ solar box (Atlas Material Testing Technology LLC) equipped with a 1500 W air-cooled Xe lamp. The overall irradiance (λ= 300–800 nm) at the photoreactor level was measured with a UV-Vis spectroradiometer (Black Comet C, StellarNet Inc.) resulting in 581.4 W m^{-2} (see **Figure 2.4** of **Section 2.4** for complete irradiance spectrum). The temperature of the simulator chamber was controlled at 40 °C throughout the runs. Oxygen (10 L h^{-1}), an ozone-oxygen mixture (10 L h^{-1}, ozone concentration 6 mg L^{-1}) or aqueous H_2O_2 (50 mM) was added to the vessel

containing the catalyst. Once the time programmed for the experiment elapsed, the catalyst was separated by an external magnet and the remaining vessel content was analyzed for total iron, H_2BDC, total organic carbon (TOC) and pH.

Photocatalyst activity was examined under simulated solar radiation using MTP as the target contaminant. The experiments were carried out in batch mode using a 300 mL borosilicate glass vessel provided with magnetic agitation and liquid sampling. Typically, the vessel was charged with 0.25 L of an aqueous solution of MTP (50 mg L^{-1}) and certain amount of catalyst (50-100 mg). Then, the reactor vessel was placed in the solar box described above (see **Figure 2.3** of **Section 2.4**) and kept under stirring in the dark for 30 min to allow for MTP adsorption onto the catalyst. Then, the Xe lamp was switched on and pure oxygen was continuously bubbled at 10 L h^{-1} flowrate. Samples were periodically withdrawn from the reactor, filtered through 0.45 μm PVDF membranes to remove the photocatalyst particles and analyzed for pH, MTP, TOC, H_2BDC and dissolved iron. After the programmed reaction time (typically 3 h), the catalyst particles were separated with an external magnet, and total iron was analyzed in non-filtered samples. Turbidity of the suspension was monitored during the magnetic separation of catalyst particles using a Hanna HI 93414 apparatus. The photocatalytic performance of selected catalyst samples was also tested in the presence of ozone. Then, a mixture of ozone-oxygen (6 mg L^{-1} ozone concentration) produced in a laboratory ozone generator (Anseros Ozomat Com AD02) was bubbled into the reactor instead of pure oxygen. Ozone concentrations at the inlet and outlet reactor were continuously monitored by means of in-line Anseros Ozomat GM analyzers. The amount of ozone actually consumed to degrade MTP in each run was estimated by the mass-balance equation (6.1):

$$\boldsymbol{m}_{O_3} = \int_0^t F_g \left([O_3]_{g,in} - [O_3]_{g,out}\right) dt - [O_3]_{sol} \cdot V \qquad (6.1)$$

where t is the irradiation time, F_g is the gas flowrate, $[O_3]_{g,in}$ and $[O_3]_{g,out}$ are the concentrations of ozone in the gases entering and leaving the reactor, respectively, $[O_3]_{sol}$ is the concentration of dissolved ozone within the reactor and V is the reaction volume.

6.2.5 Analytical methods for reaction monitoring

Samples withdrawn from the reactor during the course of photocatalytic experiments were analyzed to get insights into the reaction progress. H_2BDC and MTP concentrations were analyzed by a gradient method on an HPLC apparatus provided with a UV-Vis detector set at 225 nm (HP 1100 Series chromatograph, Agilent Technologies). A Kromasil C-18 column (5 μm, 150 mm length, 4 mm diameter) was used as the stationary phase while the mobile phase was a mixture of 0.1% vol. ortho-phosphoric acid in ultrapure water (solvent A) and acetonitrile (solvent B) at a constant flowrate of 1 mL min^{-1}. The mobile phase program used for the analysis was as follows: start at 20% B; 0–6 min, linear gradient of B in A (20–27.5% B); 6–7 min, hold at 27.5% B, 7–8 min, linear gradient (27.5–20% B); 8–9 min, hold at 20% B. The retention times were 3.4 min (H_2BDC) and 4.1 min (MTP). TOC was analyzed by catalytic combustion on a TOC-V CSH apparatus (Shimadzu). Spectrophotometric measurements were carried out on a Thermo Spectronic Helios α spectrophotometer using 1 cm path length cuvettes. Spectroquant® iron test (Merck Millipore) was used for iron concentration. H_2O_2 was analyzed by the Eisenberg method [21] while aqueous ozone was measured by the indigo method [22].

6.3 RESULTS AND DISCUSSION

6.3.1 Insights into the formation of magnetically separable Fe_3O_4@TiO_2-P25 composite

The main aim of this study was to investigate a facile, reliable, green method to prepare a robust magnetically separable composite containing Fe_3O_4 and TiO_2-P25, thus offering advantageous photocatalytic properties for the degradation of organic pollutants in water. For this purpose, a method oriented towards the hetero-agglomeration of in-situ synthetized magnetite by oxidative precipitation of Fe(II) and TiO_2-P25 is proposed in this work. In a previous study, related to magnetic carbon materials (e.g., magnetic activated carbon), it was suggested that the presence of H_2BDC favors the generation of magnetite through the formation of terephthalate intermediates which control the oxidation of Fe(II) in alkaline conditions towards Fe_3O_4 [18]. **Figure 6.2** shows pictures of samples of $FeCl_2 \cdot 4H_2O$ in aqueous NaOH (molar ratio, [NaOH]/[Fe(II)]=3.5), in the presence and absence of TiO_2-P25 and/or H_2BDC, aged at room temperature for 24 h (see * in **Figure 6.1**). A brown-black solid, fairly separable by the external magnet, was obtained when neither TiO_2-P25 nor H_2BDC was used in the synthesis, suggesting that a mixture of magnetic and non-magnetic iron oxides was formed (picture A). However, a black magnetic solid, presumably bare magnetite, was obtained in the presence of H_2BDC at 1 mol H_2BDC/ mol Fe (picture B). Furthermore, when this molar ratio was used, the precipitated iron oxide became attached to TiO_2-P25 particles forming a dark grey composite easily separable, designated as Fe_3O_4@TiO_2-P25 in this work (picture C). At 0.5 mol H_2BDC/mol Fe ratio, a light grey solid resulted, which exhibited magnetic properties, though some particles (likely TiO_2-P25) remained in suspension when an external magnetic field was applied (picture D). Finally, in the absence of H_2BDC a brownish mixture of TiO_2-P25 and precipitated iron

oxides/hydroxides was obtained, which was not magnetically recoverable (picture E).

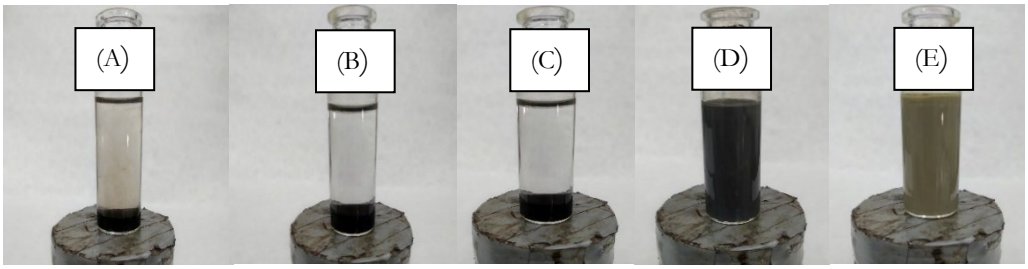

Figure 6.2. Color and magnetic separation of samples prepared in the presence/absence of TiO_2-P25 and/or H_2BDC. Picture A: absence of TiO_2-P25 and H_2BDC; Picture B: absence of TiO_2-P25 and presence of H_2BDC at 1 mol H_2BDC /mol Fe; Picture C: presence of TiO_2-P25 and H_2BDC at 1 mol H_2BDC /mol Fe; Picture D: presence of TiO_2-P25 and H_2BDC at 0.5 mol H_2BDC /mol Fe; Picture E: presence of TiO_2-P25 and absence of H_2BDC.

Solids from samples B, C and E were separated, dried at 100 °C and analyzed by XRD. **Figure 6.3** shows XRD patterns of these solids together with fresh TiO_2-P25. In agreement with the literature, the TiO_2-P25 sample shows characteristic diffraction peaks matching with those of the anatase phase (JCPDS card 21-1272) and the rutile phase (JCPDS card 21-1276) [23]. Average crystallite sizes obtained applying Scherrer's equation were found to be 19.7 nm and 29.6 nm for anatase and rutile phases, respectively. Sample B presents main XRD peaks at 2θ 30.1°, 35.5°, 43.2°, 53.6°, 57.2° and 62.7°, corresponding to crystalline planes of cubic spinel structure of magnetite (JCPDS card 65-3107) [24]. From the diffraction peak at 35.5°, a crystallite size of 25.1 nm was obtained using Scherrer formula. No peak of Fe_3O_4 can be seen in sample E, while characteristics peaks of both TiO_2-P25 and Fe_3O_4 are present in sample C, suggesting a key role

of H_2BDC acid to obtain the Fe_3O_4@TiO_2-P25 composite without destroying the structure of TiO_2 (mean crystallite size anatase 19.8 nm) and Fe_3O_4 (mean crystallite size 24.4 nm). The anatase (1 0 1) to magnetite (3 1 1) peak height ratio was used to estimate the TiO_2/Fe_3O_4 mass ratio in the composite sample [25]. Accordingly, a Ti/Fe mass ratio of 4.6 can be estimated for sample C, which is close to the relative amounts of Ti and Fe used in the synthesis procedure (i.e., 4.44 g Ti/g Fe), suggesting an efficient use of TiO_2-P25 and $FeCl_2 \cdot 4H_2O$ raw materials.

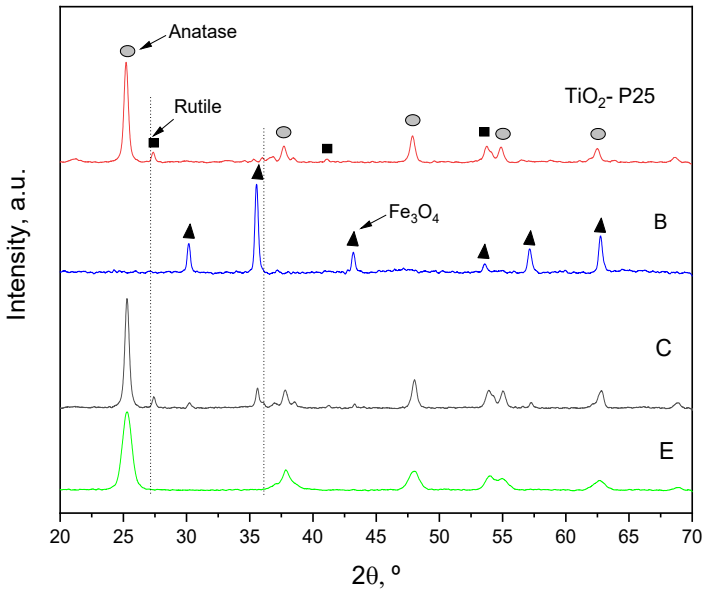

Figure 6.3. XRD patterns of bare TiO_2-P25 and some prepared samples. B: sample prepared in the absence of TiO_2-P25 and presence of H_2BDC at 1 mol H_2BDC/mol Fe; C: sample prepared in the presence of TiO_2-P25 and H_2BDC at 1 mol H_2BDC/mol Fe; E: sample prepared in the presence of TiO_2-P25 and absence of H_2BDC.

To further investigate the mechanism of formation of the Fe_3O_4@TiO_2-P25 composite, solid samples obtained at different aging times were characterized by ATR-FTIR. A first group of samples was produced immediately after the addition

of the alkaline BDC^{2-} solution to the dispersion of TiO_2-P25 particles in aqueous Fe(II) solution (0 h samples). The other samples were collected from the suspension after 1, 3 and 24 h of aging. Samples were filtered and the resulting solids were thoroughly washed with UP water. In addition, a non-washed 24 h sample was used in this study. **Figure 6.4** shows FTIR spectra of these samples together with those corresponding to pure H_2BDC, TiO_2-P25 and Fe_3O_4 as synthesized in this work (picture B in **Figure 6.2**). The spectrum of pristine TiO_2-P25 shows a broad asymmetric band centered at 3400 cm^{-1} due to –OH stretching modes of surface hydroxyl groups and adsorbed water linked by hydrogen bonds. The band at 1620 cm^{-1} is ascribed to the –OH bending mode of vibration of adsorbed water molecules. Also, the broad band at 560-1000 cm^{-1} corresponds to Ti–O stretching vibrations. The FTIR spectrum of pure H_2BDC exhibits main bands located at 1680, 1575-1420, and 1285 cm^{-1} assigned to stretching vibrations of –C=O (carboxylic group), –C=C–, and –C–H bonds (aromatic structure), and–C–OH (acid), respectively [18]. Two 0 h samples were examined by FTIR: one sample taken directly from the alkaline reaction medium (0 h) and another one that was obtained after acidification of the reaction medium to promote H_2BDC precipitation (0 h*). In the spectrum of this latter, the main peaks attributable to H_2BDC can be easily identified (see dotted lines) together with the Ti–O band at 560-1000 cm^{-1}. Contrary, the spectra of the 0 h, 1 h and 3 h samples exhibit various bands in the 1300-1700 cm^{-1} region not matching with those of H_2BDC. These bands are likely due to carboxylate coordination to Fe and/or surface Ti. In fact, the peaks at 1380 and 1577 cm^{-1} are consistent with symmetric and asymmetric stretching vibrations of metal-carboxylate groups in Fe(II)BDC [26-28] and Ti(IV)BDC complexes [29,30]. According to the modification of the spectra with aging time, the initially formed metal-BDC complexes seem to evolve up to complete disappearance. Thus, after 24 h no FTIR bands assigned to these coordination compounds were observed. The spectrum of the unwashed 24 h sample (i.e., 24h*), however, displays typical absorption bands of H_2BDC, attributable to some adsorbed or precipitated H_2BDC, which could be removed

by simply washing with water at room temperature. Spectra of both 24 h and 24 h* samples exhibited a broad band at 560-1000 cm^{-1} which can be due to the overlapping of the characteristic bands of stretching Fe–O, Ti–O and Fe–O-Ti vibrations [31,32].

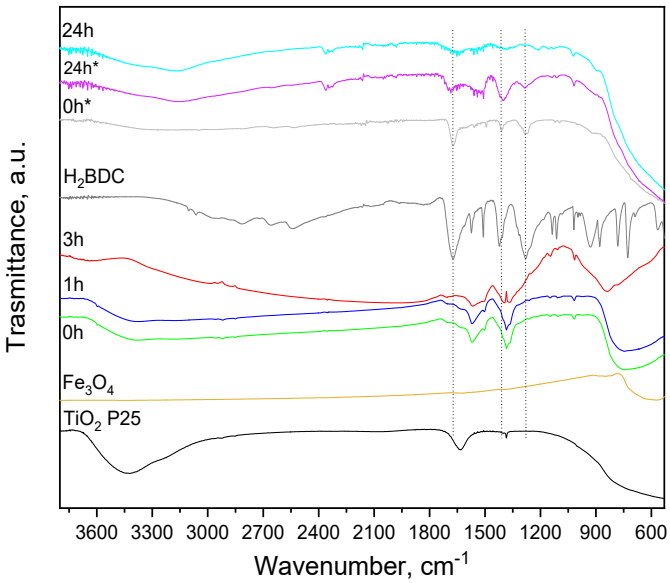

Figure 6.4. ATR-FTIR spectra of TiO_2-P25, H_2BDC and various solid samples at different aging time.

The evolution of pH and color of the aqueous suspension during the course of the synthesis of the Fe_3O_4@TiO_2-P25 material was monitored as shown in **Figure 6.5**. Drastic changes in both pH and suspension appearance took place during the dropwise addition of the alkaline solution of BDC^{2-}. Thus, the suspension evolved from the white aqueous dispersion of TiO_2-P25 particles (picture A) to a brown, viscous dispersion (picture C) as the pH increased from 3.1 to 11.7 (see inset in **Figure 6.5**). At the beginning of the process, while pH is low, chemisorption of H_2BDC onto TiO_2-P25 surface occurred, which led to an increased viscosity of the suspension and cause coagulation of the particles [29]. Different modes of surface complexation at the TiO_2-aqueous solution interface

can be considered, where BDC^{2-} coordinates either one or two neighboring Ti centers [29,33]. In the first case, the second carboxylic group of BDC^{2-} may coordinate to Fe(II) ions, thus serving as a bridge between Ti and Fe centers. The formation of iron terephthalates might be responsible for the brown color of the suspension (picture C) [26]. Upon addition of the alkaline solution, aerial oxidative precipitation of Fe(II) towards Fe_3O_4 was produced at room temperature (picture D). The presence of BDC^{2-} favored the formation of magnetite over other iron oxides/hydroxides species since under identical preparation conditions but in the absence of BDC^{2-} low yield of Fe_3O_4 was obtained (see also picture E in **Figure 6.2**). Terephthalate also facilitated the production of composite particles (i.e., Fe_3O_4@TiO_2-P25) rather than isolated Fe_3O_4 NPs. The oxidative process would proceed through the formation of non-magnetic Fe(III) oxides/hydroxydes [34] and/or mixed-valence iron oxides (i.e., green rust) [35-37] at the early stages of the oxidation and Fe_3O_4 at a longer aging time, which agrees with our experimental observations where intermediate iron oxide species seems to be formed. From **Figure 6.5**, it can be seen that the transformation of iron oxides was accompanied by a dramatic drop of pH from 12 to 5.4 within 4 h of aging, while pH remained practically unchanged thereafter. No difference was observed in the solid obtained at 4 h and 24 h aging time, suggesting that 4 h was enough for the formation of Fe_3O_4@TiO_2-P25.

Figure 6.6 shows results from thermal analysis of pure H_2BDC and some solid samples obtained at different aging times. It can be seen that the total mass loss in samples aged for 0 h and 3 h is around 12% whereas it drops to less than 3% for the sample 24 h. The weight loss in the samples taken at the early stages of the oxidation process is likely related to the breaking up of metal-organic structures upon heating with the release of H_2O, CO and CO_2 at 353 ºC (sample 0 h and 3 h) and 413 ºC (sample 0 h). On the contrary, the mass loss in the sample 24 h is mainly due to desorption of water as no release of CO or CO_2 was observed. From the thermal analysis of pure H_2DBC, it is apparent that this

compound sublimes at about 340 ºC in a single step with neither CO nor CO_2 release. No such effect was observed for any of the reaction samples, suggesting no contribution of free H_2BDC to the mass loss. These results confirm the fast formation of complexes that are further destroyed upon gradual magnetite generation with the release of free terephthalate into solution.

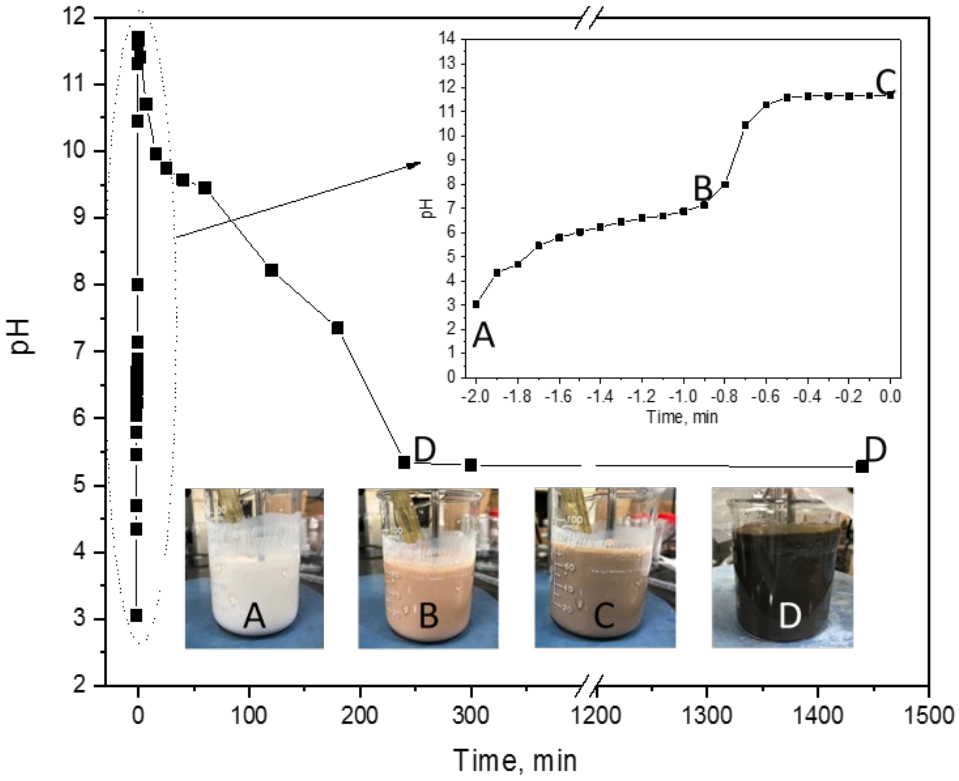

Figure 6.5. Evolution of pH and color of the suspension during the formation of Fe_3O_4@TiO_2-P25.

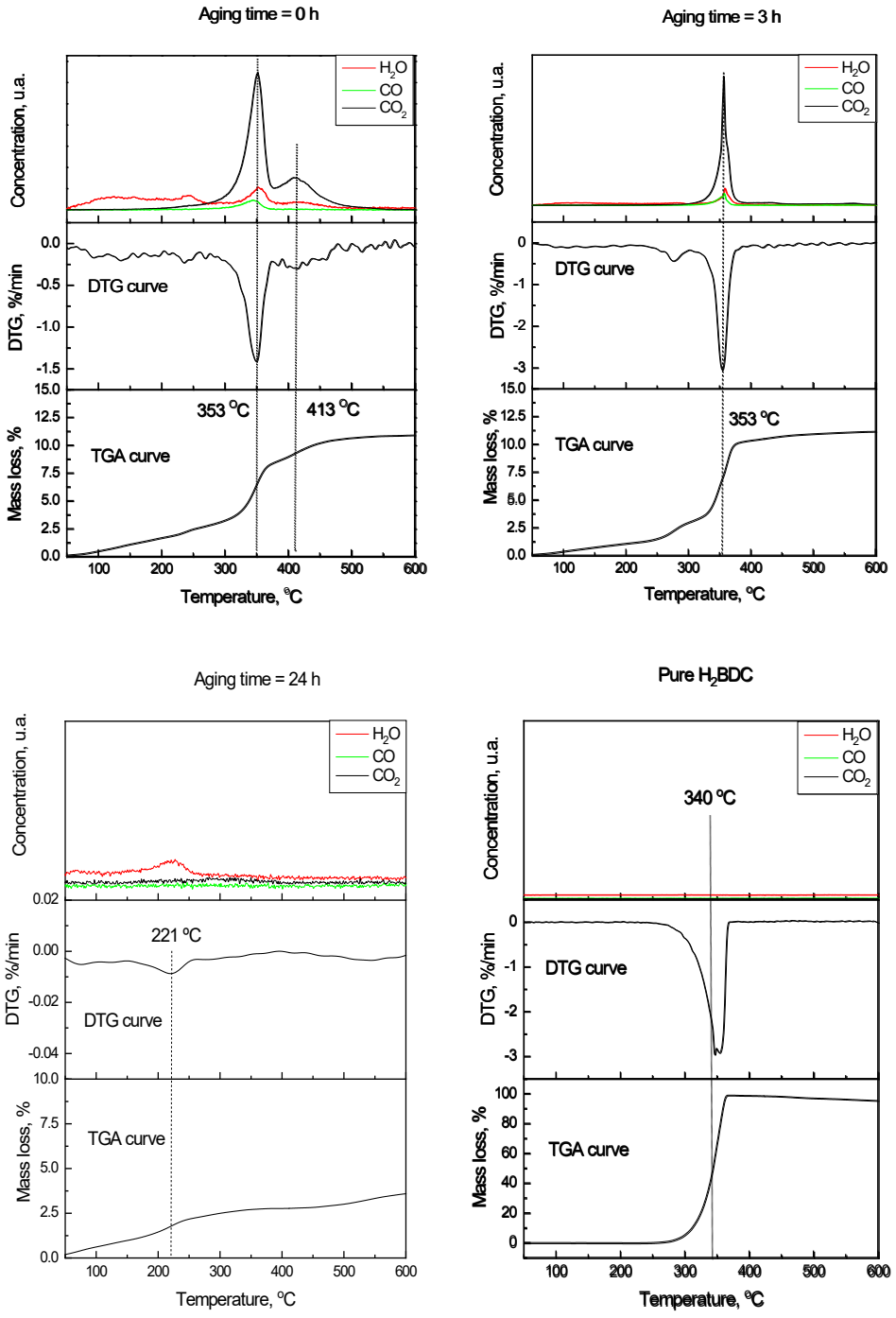

Figure 6.6. TG/DTG-MS of pure H_2BDC and solid samples at different aging times.

Based on the above and the literature on the production of Fe_3O_4 by aerial oxidative precipitation of Fe(II) [34-38], a plausible mechanism of the formation of Fe_3O_4@TiO_2-P25 catalyst can be proposed as follows: (1) fast formation of terephthalate complexes during dropwise addition of the BDC^{2-} alkaline solution to the dispersion containing aqueous Fe(II) and TiO_2-P25 particles; (2) partial oxidation of Fe(II) species to produce intermediate Fe(III) terephthalate complexes, which would further decompose to form iron oxides/hydroxides adsorbed onto or in the vicinity of TiO_2-P25 particles (it is worth noting that titanium terephthalates might become unstable at basic pH [29]); (3) formation of primary magnetite particles nucleated on the surface of those iron intermediate particles; (4) further coagulation of primary Fe_3O_4 particles as pH approaches the isoelectric point of magnetite (i.e., IEP=6.8 [39]) giving rise to agglomerated Fe_3O_4@TiO_2-P25 with release of BDC^{2-} to the aqueous media. The presence of BDC^{2-} would aid controlling the process kinetics, favoring the nucleation and growth of magnetite particles at room temperature and the hetero-agglomeration process.

6.3.2 Influence of the preparation conditions on the magnetic separability and solar photocatalytic performance of the Fe_3O_4@TiO_2-P25 photocatalyst

The distribution of products and particle size and structure of iron oxide NPs obtained by oxidative precipitation of ferrous salts in aqueous media depends on a number of variables, primarily the rate of oxidation, excess of alkali over Fe(II), the reaction temperature and the presence of other ions and/or molecules in the reaction media [34-43]. In this work, the effect of the excess alkali (i.e., R_{OH^-}) and both the reaction and drying temperatures on the magnetic separability and photocatalytic performance of the resulting solids were explored. Also, the influence of the content of TiO_2-P25 in the catalyst was studied. For the analysis

of the excess of [OH^-] over [Fe(II)] the approach of Granath et al. [43] was followed. Accordingly, R_{OH^-} was defined as follows:

$$R_{OH^-} = \frac{[OH^-]-2\cdot[H_2BDC]-2\cdot[Fe(II)]}{[Fe(II)]} \quad (6.2)$$

Table 6.2 shows preparation conditions, solar photocatalytic behavior, magnetic separability and textural properties of some selected catalyst samples obtained according to the scheme of **Figure 6.1**. Photocatalyst activity was analyzed in terms of MTP and TOC removals in batch runs carried out under simulated sunlight in the presence of oxygen as oxidant. Regardless of the catalyst sample used, both MTP and TOC removals obeyed apparent first-order kinetics (see **Figure 6.7** as an example). Accordingly, k_{MTP} and k_{TOC} apparent rate constants were used to compare the photocatalytic activity of different samples.

Table 6.2. Preparation conditions, solar photocatalytic performance, magnetic separability and porous structure of some catalyst samples.

Catalyst sample	Preparation conditions				Solar photocatalytic performance		Magnetic separability		Surface area and pore volume		
	TiO_2-P25 mass (g)	R_{OH^-}	Reaction temperature (°C)	Drying temperature (°C)	$k_{MTP} \times 10^3$ (min^{-1})	$k_{TOC} \times 10^3$ (min^{-1})	Magnetization M_S (emu g^{-1})	Magnetization M_S (emu/g Fe_xO_y)[1]	S_{BET} (m^2 g^{-1})	S_{ext} (m^2 g^{-1})	V_{pore}[2] (cm^3 g^{-1})
(TiFe)$_a$	1.5	-0.45	40	100	9.7 ± 0.2	2.5 ± 0.2	3.5	19.4	75.7	73.3	0.31
(TiFe)$_b$	2.0	-0.45	40	100	11.6 ± 0.4	3.3 ± 0.2	4.0	28.4	72.0	68.4	0.26
(TiFe)$_c$	2.5	-0.45	40	100	12.8 ± 0.6	4.0 ± 0.1	0.6	4.8	70.3	67.7	0.32
(TiFe)$_d$	1.5	-0.35	40	100	9.4 ± 0.1	2.9 ± 0.1	7.5	41.0	67.8	67.5	0.28
(TiFe)$_e$	2.5	-0.35	40	100	13.9 ± 0.8	3.8 ± 0.2	4.0	34.2	67.3	66.9	0.28
(TiFe)$_f$	2.0	-0.20	20	100	11.6 ± 0.2	3.3 ± 0.3	0.6	3.9	76.6	73.3	0.28
(TiFe)$_g$	2.0	-0.20	40	100	10.2 ± 0.3	3.3 ± 0.1	9.5	63.8	57.3	57.3	0.36
(TiFe)$_h$	2.0	-0.20	70	100	10.5 ± 0.3	2.7 ± 0.1	9.5	56.9	63.6	62.7	0.27
(TiFe)$_i$	2.0	0.0	20	100	11.6 ± 0.3	2.8 ± 0.1	11.7	78.0	63.0	55.6	0.25
(TiFe)$_j$	2.0	0.0	40	100	11.9 ± 0.3	3.1 ± 0.1	12.8	75.1	57.0	63.0	0.23
(TiFe)$_k$	2.0	0.0	20	60	12.4 ± 0.5	3.0 ± 0.2	12.2	73.2	67.4	67.9	0.29
(TiFe)$_l$	2.0	0.0	40	60	11.3 ± 0.5	2.7 ± 0.2	13.4	81.2	67.8	67.4	0.28

[1] Fe_xO_y content of catalyst as determined by WDXRF; [2] Pore volume derived from the amount of N_2 adsorbed at P/P_0=0.97

From **Table 6.2**, it is apparent that both rate constants barely depended on the conditions used for the preparation of the catalyst but the amount of TiO_2-P25 used. For instance, all the catalyst samples obtained with 2.0 g TiO_2-P25 (% TiO_2 in the catalyst samples was in the narrow range of 83.4 % to 86.2 %, as measured by WDXRF) exhibited similar photoactivity for the degradation of MTP as deduced from close values of k_{MTP} ($10.2x10^{-3}$-$12.4x10^{-3}$ min^{-1}) and k_{TOC} ($2.7x10^{-3}$-$3.3x10^{-3}$ min^{-1}). However, an enhancement in the rate of MTP removal and mineralization was observed with the increasing percentage of TiO_2-P25 in the catalyst. These results suggest that the photocatalytic activity of the synthesized materials for the degradation of MTP under simulated sunlight is primarily due to the TiO_2 content while the iron oxides does not seem to play a key role. Accordingly, bare TiO_2-P25 NPs showed higher photocatalytic performance (k_{MTP} = $2.7x10^{-2}$ min^{-1} and k_{TOC} = $7.2x10^{-3}$ min^{-1}) than any of the photocatalyst samples listed in **Table 6.2** (see **Figure 6.8**).

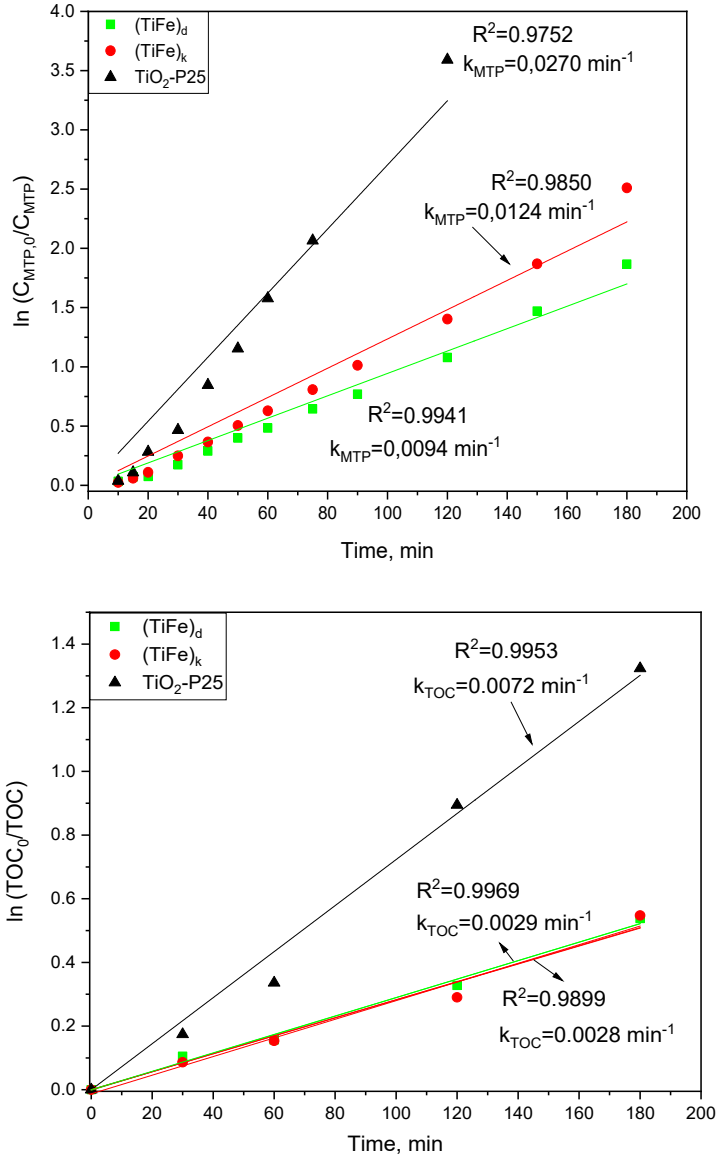

Figure 6.7. Apparent first-order kinetics plots for photocatalytic degradation of MTP under simulated sunlight. a) MTP removal; b) TOC removal. Catalyst samples as designated in **Table 6.2** of the main text.

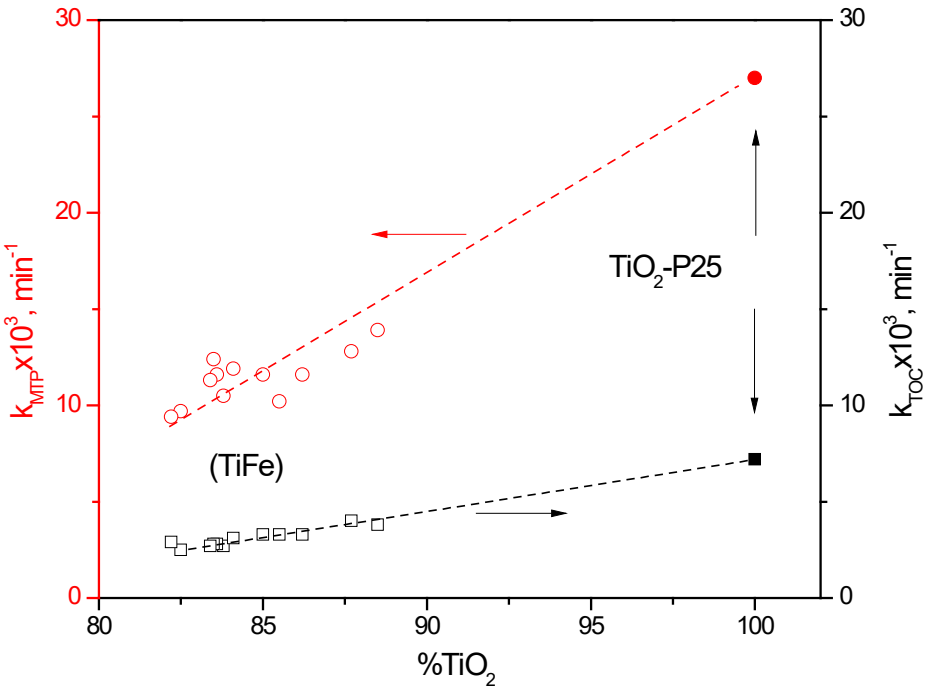

Figure 6.8. Relationship between apparent first-order rate constants for the removal of MTP (k_{MTP}) and TOC (k_{TOC}) under sunlight and the TiO_2 content of the catalyst samples (as measured by WDXRF).

On the other hand, the saturation magnetization of catalyst samples (M_S) strongly depended on their synthesis conditions (see **Figure 6.9** for SQUID magnetization curves), which suggests the formation of different magnetic and non-magnetic iron oxides depending on the actual conditions applied. In this sense, R_{OH^-} has been identified as a critical parameter influencing the reaction products from oxidative precipitation of Fe(II) [36-38,40-41]. After some preliminary experiments, the R_{OH^-} range of study in this work was limited to values from -0.45 to 0 so that almost complete conversion of aqueous Fe(II) without excess of alkali was achieved. From **Table 6.2** it is clearly seen that, within this range, R_{OH^-} favored the formation of magnetic particles at any of the

contents of TiO_2-P25 and reaction temperatures tested. Moreover, at R_{OH-}=0 M_S values reached a upper limit about 12-13 emu g^{-1} (~70-80 emu/g Fe_xO_y), which suggests quantitative conversion of aqueous Fe(II) into Fe_3O_4. Notice that M_S normalized to the Fe_xO_y content as determined by XRF approaches the value found for bare magnetite as obtained in this work (80.6 emu g^{-1}). It should be mentioned that at R_{OH-}>0 magnetization was not improved with respect to R_{OH-}=0.

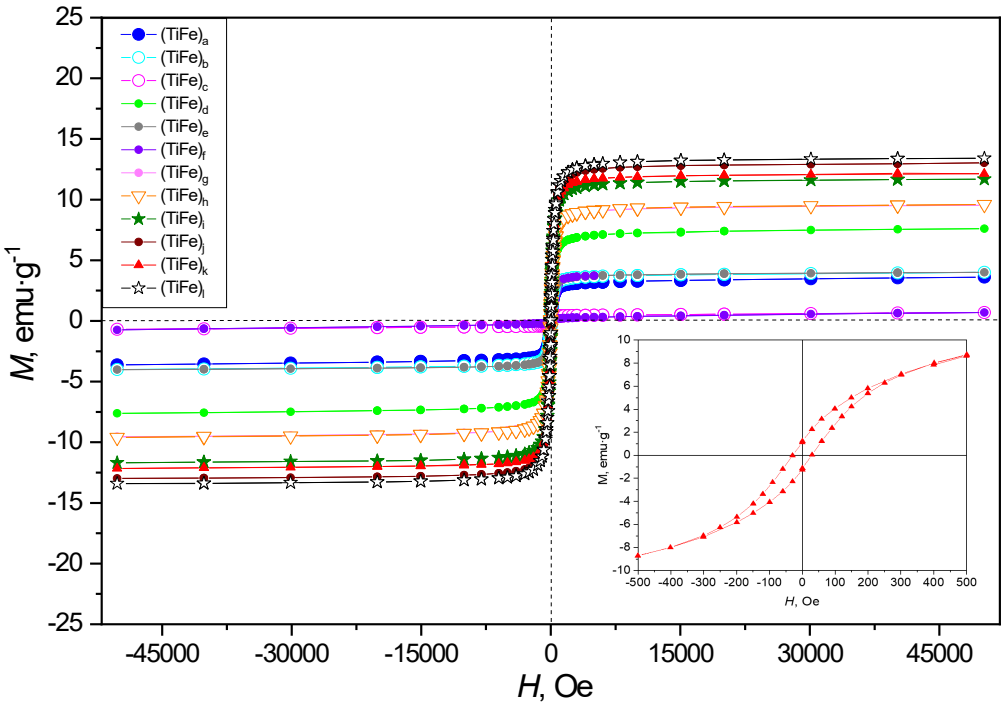

Figure 6.9. SQUID magnetization curves of selected catalyst samples. Nomenclature as in **Table 6.2** of the main text.

In any case, particles of catalyst samples with M_S higher than 9 emu g^{-1} were easily separated from aqueous solution by means of an external magnet, leaving a clear solution after a few minutes (see **Figure 6.10** and **Figure 6.11**). The higher presence of magnetite in the samples obtained at R_{OH-}=0 was also observed in

their XRD patterns where a more intense peak at 35.5º can be seen than in diffractograms of samples produced at negative R_{OH^-} (**Figure 6.12**). The reaction temperature is reported to exert a key influence on the nature, size and morphology of the particles formed during the course of aerial oxidative precipitation of $Fe(OH)_2$. In general, Fe_3O_4 can be preferentially precipitated over other iron oxides/hydroxides at 40-70 ºC, though the distribution of iron oxide/hydroxides products also depends on the aqueous pH (i.e., excess of alkali used) [34-38]. In line with this, as shown in **Table 6.2**, the solid obtained at R=-0.2 and 20 ºC presented a low saturation magnetization being not magnetically recoverable while those prepared at the same reaction temperature but R=0 exhibited M_S values around 12 emu g^{-1}. At R=-0.2, an increase of temperature from 20 to 40 ºC clearly favored the precipitation of magnetic iron oxide (i.e., Fe_3O_4) whereas a further increase up to 70 ºC caused no effect on the magnetization saturation of the resulting product. When the synthesis of the catalyst was carried out at R=0, a small favoring effect of the reaction temperature on M_S was observed in the 20-40 ºC range. On the contrary, the drying temperature (from 60 to 100 ºC) had a negative impact on the magnetic recoverability of the prepared catalysts, likely due to the partial oxidation of Fe_3O_4 to γ-Fe_2O_3 [34]. In line with this, slight browning of the material was observed after drying at 100 ºC.

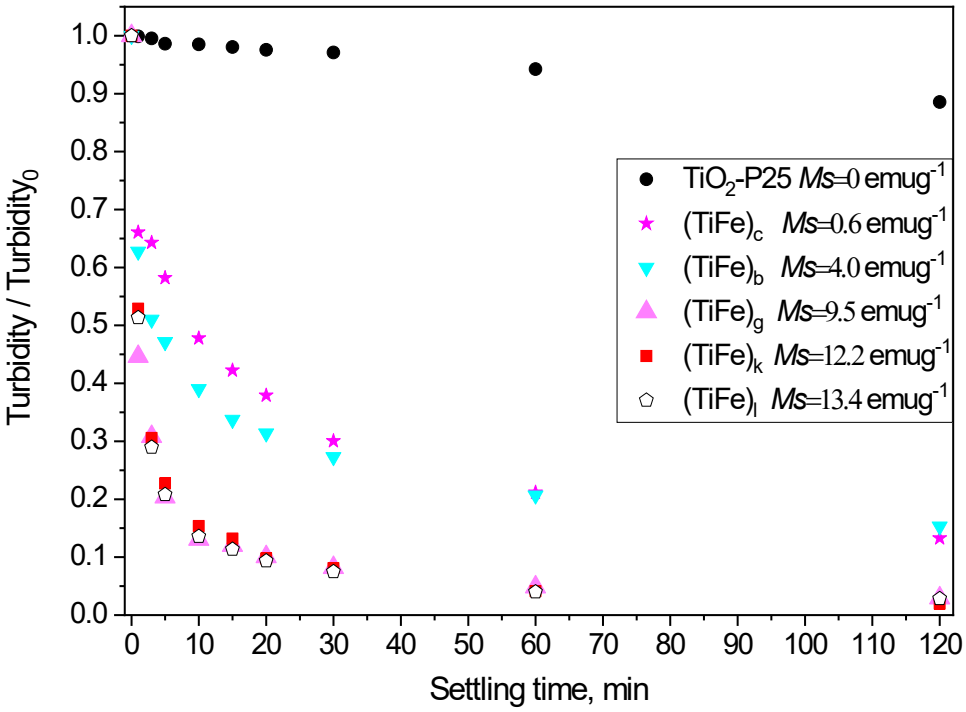

Figure 6.10. Turbidity removal during magnetic separation of catalyst particles from aqueous suspension.

Figure 6.11. Pictures showing the appearance of a suspension of the Fe_3O_4@TiO_2-P25 under the influence of an external magnetic field. Effect of settling time.

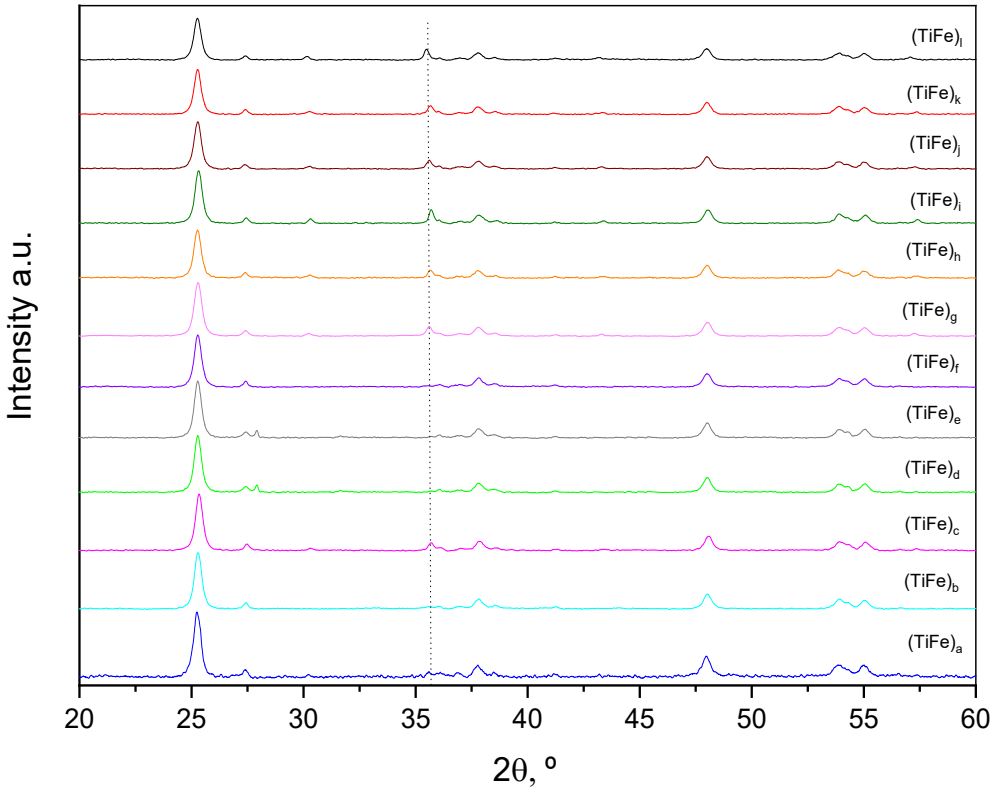

Figure 6.12. XRD patters of selected catalyst samples. Nomenclature as in **Table 6.2** of the main text.

Chemical surface analysis of catalyst samples was carried out by XPS. The XPS survey spectra (**Figure 6.13**) confirmed the presence of Ti, Fe and O from TiO_2 and iron oxides, in addition to trace amount of C, which is likely a result of an instrumental contamination (i.e., adventitious carbon) and minimal amount of residual BDC^{2-} on the sample surface.

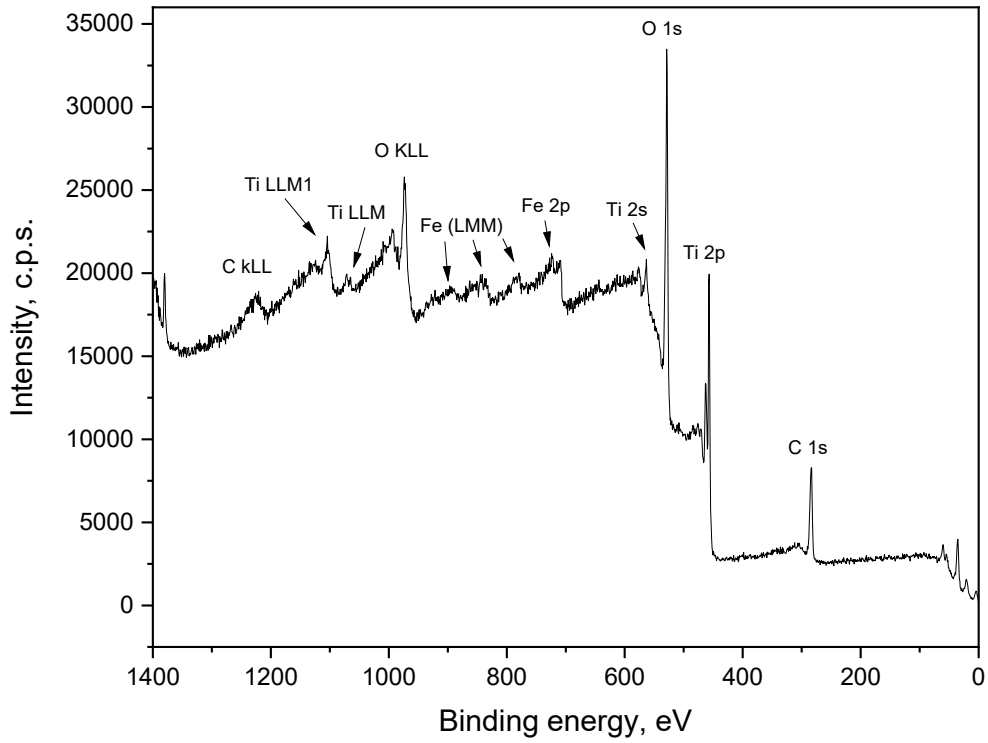

Figure 6.13. XPS survey spectrum of $(TiFe)_k$ sample. Nomenclature as in **Table 6.2** of the main text.

As an example, **Figure 6.14** shows the Fe 2p, Ti 2p, O 1s and C 1s core-level photoelectron spectra of sample $(TiFe)_k$. The Ti 2p spectrum exhibits characteristics signals, Ti $2p_{3/2}$ and Ti $2p_{1/2}$, centered at 458.6 eV and 464.1 eV, which correspond to the Ti^{4+} valence state of TiO_2 [44] The curve-resolved O 1s spectrum resulted in three peaks: the broad band centered at 529.7 eV can be assigned to Ti-O, Fe-O and Ti-O-Fe bonds, while the subtler signals at 531.1 eV and 532.5 eV might be ascribed to C=O and C-O bonds, respectively. This agrees with the C 1s spectrum where signals associated to C=O and C-O bonding can be seen positioned at 288.4 eV and 286.0 eV, respectively. The high-resolution Fe 2p spectrum was deconvoluted into four main peaks at 711.2 eV (Fe $2p_{3/2}$) and 725.5 eV (Fe $2p_{1/2}$) for Fe^{3+} and at 709.5 eV (Fe $2p_{3/2}$) and 723.3 eV (Fe $2p_{1/2}$)

for Fe^{2+}. Fe $2p_{3/2}$ peak areas were used to estimate the surface Fe^{2+}/Fe^{3+} atomic ratio of the catalyst samples [45].

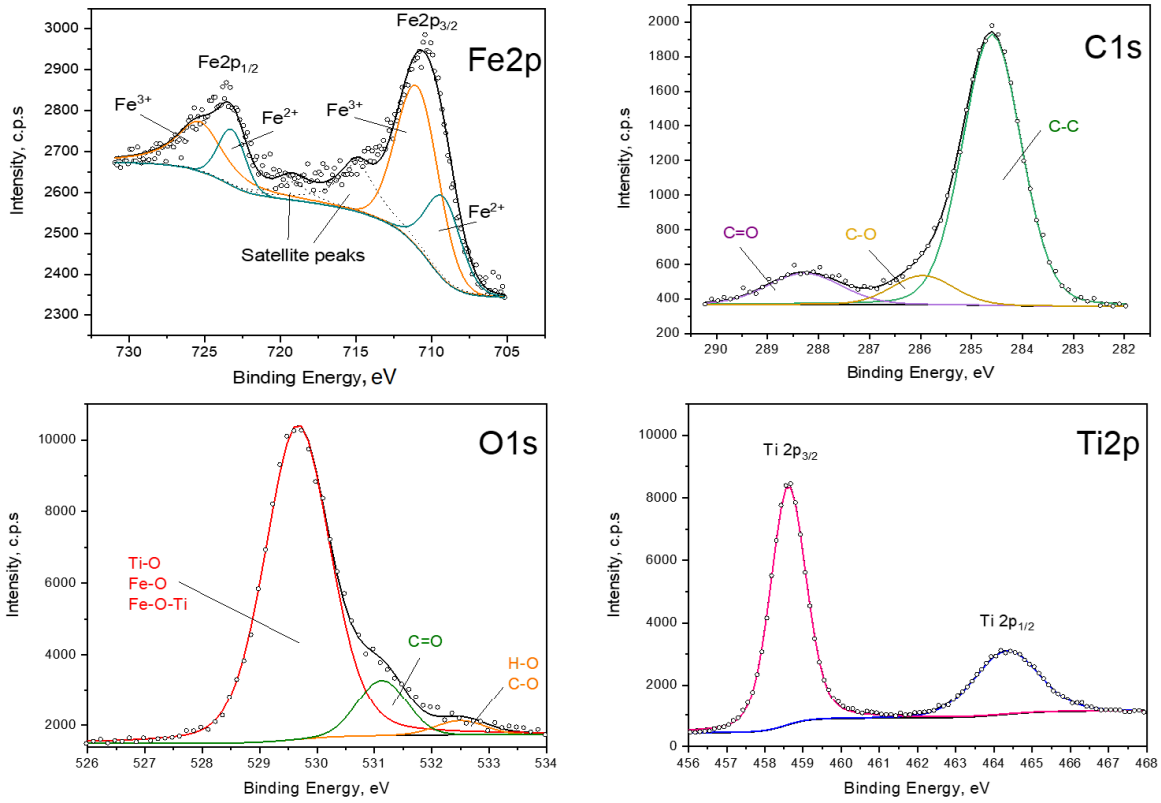

Figure 6.14. High resolution Fe2 p, C 1s, O 1s and Ti 2p of a Fe_3O_4@TiO_2-P25 sample ($(TiFe)_k$ as designated in **Table 6.2**).

Figure 6.15 reveals a linear relationship between the saturation magnetization (measured as per gram of Fe_xO_y) and the surface Fe^{2+}/Fe^{3+} ratio of some catalyst samples. It is clearly seen that maximum M_S (~ 80 emu/g Fe_xO_y) was reached as the Fe^{2+}/Fe^{3+} ratio approached 0.5, which is consistent with the stoichiometry of Fe_3O_4. Lower ratios were found for samples with lower saturation magnetization, suggesting either incomplete transformation of Fe(II) into magnetite or surface oxidation of Fe_3O_4 NPs.

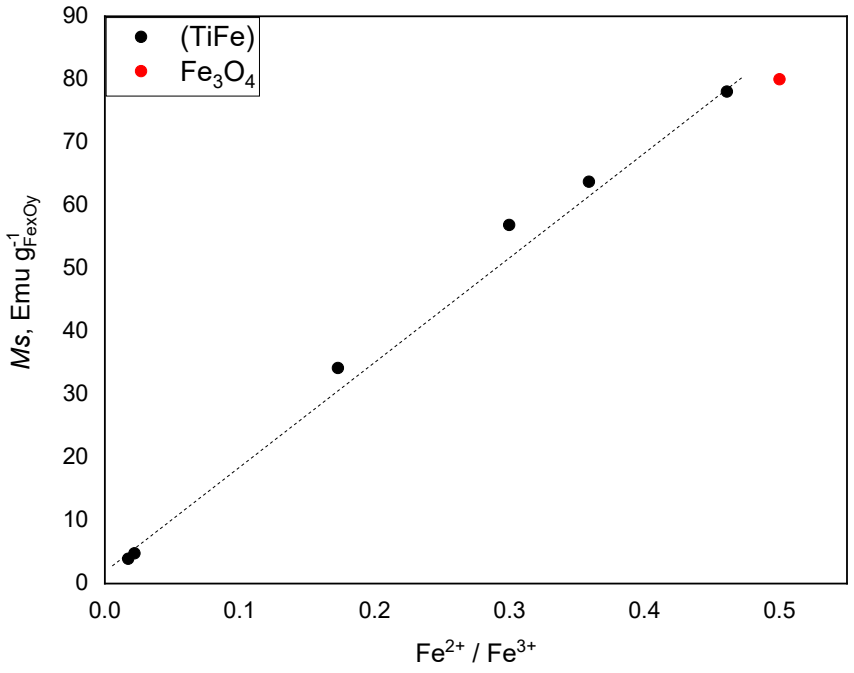

Figure 6.15. Effect of the surface Fe^{2+}/Fe^{3+} ratio on the saturation magnetization of catalyst samples.

6.3.3 Characterization of Fe_3O_4@TiO_2-P25 photocatalyst

Some characterization methods were used to assess the most important properties of the Fe_3O_4@TiO_2-P25 photocatalyst synthetized in this work at 20 ºC and dried at 60 ºC (i.e., $(TiFe)_k$ in **Table 6.2**). As discussed above, XRD patterns of the catalyst show the presence of both Fe_3O_4 and TiO_2 nanocrystals (see **Figure 6.2**, sample C). Average chemical composition of the catalyst was 50.8% Ti and 10.8% Fe as determined by WDXRF spectroscopy. Then, 84.8% TiO_2 and 14.9% Fe_3O_4 composition is deduced assuming that all Fe in the catalyst belongs to Fe_3O_4 NPs. Minimal presence of organic compounds in the catalyst samples was observed by elemental analysis (<0.2% C in samples), suggesting that

almost all residual H_2BDC was successfully removed in the recovery and washing steps (see **Figure 6.1**). **Figure 6.16** shows SEM images of the Fe_3O_4@TiO_2-P25 composite, where the aggregation behavior of particles is apparent, giving rise to irregularly shaped, micrometric grain aggregates of different sizes (**Figure 6.16a**). EDX analysis revealed the presence of surface Ti and Fe in a mass ratio of 4.54 (**Figure 6.16b**), which matches with WDXRF spectroscopy results. Moreover, effective homogeneous coupling of Fe_3O_4 and TiO_2-P25 particles is demonstrated from the elemental mapping using EDX (**Figure 6.16c**). The presence of Fe_3O_4 in the composite is responsible for the magnetic behavior of the Fe_3O_4@TiO_2-P25 photocatalyst. In addition to high saturation magnetization (M_S=12.2 emu g^{-1}), the magnetization curve of Fe_3O_4@TiO_2-P25 (see inset in **Figure 6.9**) revealed a narrow hysteresis loop with very low coercivity (H_C=55.1 Oe) and remanence magnetization (M_R=1.8 emu g^{-1}), suggesting near superparamagnetic behavior of the nanocomposite. These magnetic properties allowed the easy recovering of the photocatalyst from treated water by the action of a magnet and further redispersion in solution for recycling.

Figure 6.17 displays the nitrogen adsorption/desorption isotherm of a Fe_3O_4@TiO_2-P25 sample compared to those of bare TiO_2-P25 and Fe_3O_4. According to the IUPAC classification, all samples exhibited a typical type IV-a isotherm with a type H3 hysteresis loop [46]. This type of adsorption-desorption behavior is characteristic of materials with a mesoporous structure. As a consequence, the BET surface area (S_{BET}) and the external surface area, as calculated by the t-plot method, (S_{ext}) were quite similar in all the samples studies (see **Table 6.2**), being the volume of micropores negligible (< 5 mm^3 g^{-1}). The BET surface area and the pore volume of the $(TiFe)_k$ sample (S_{BET}=67.4 m^2 g^{-1}; V_{pore}=0.29 cm^3 g^{-1}) were slightly higher than those of bare TiO_2-P25 (S_{BET}=60.4 m^2 g^{-1}; V_{pore}=0.19 cm^3 g^{-1}) and bare Fe_3O_4 (S_{BET}=63.0 m^2 g^{-1}; V_{pore}=0.18 cm^3 g^{-1}), reflecting the creation of new mesopores upon Fe_3O_4@TiO_2-P25 preparation.

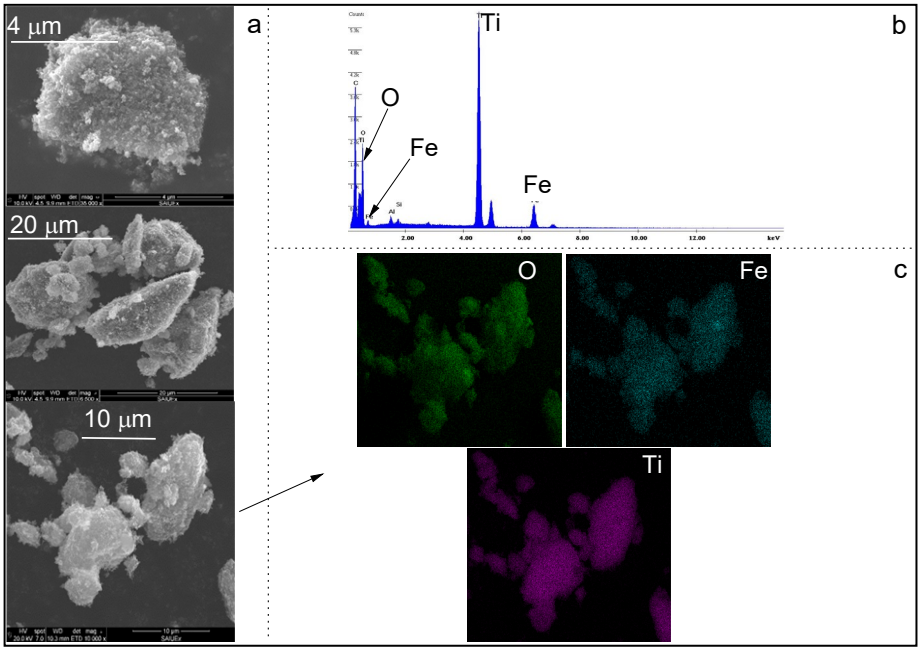

Figure 6.16. SEM and EDX elemental mapping of a Fe_3O_4@TiO_2-P25 sample ($(TiFe)_k$ as designated in **Table 6.2**). (a) SEM images; (b) EDX analysis; (c) EDX elemental mapping.

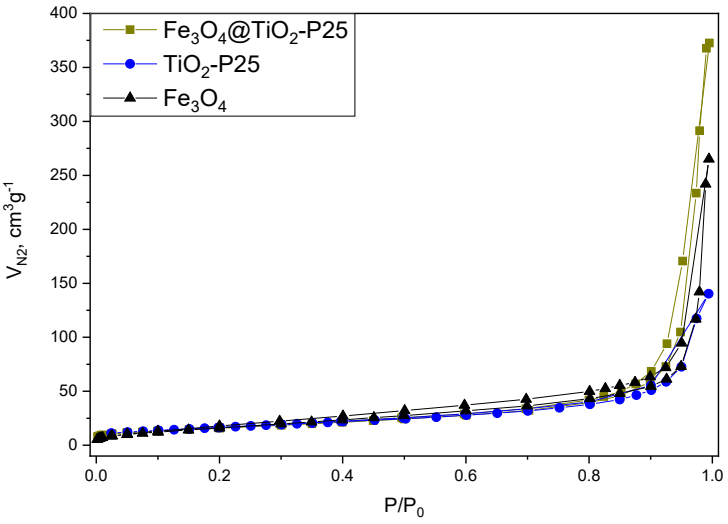

Figure 6.17. The N_2 adsorption-desorption isotherm of a Fe_3O_4@TiO_2-P25 sample ($(TiFe)_k$ as designated in **Table 6.2**) compared to those of Aeroxide TiO_2-P25 and Fe_3O_4 (as synthetized in this work).

The diffuse reflectance spectra (DRS) of TiO_2-P25 and Fe_3O_4@TiO_2-P25 samples are shown in **Figure 6.18**. The optical band gap energy (E_g) of both materials was evaluated using the Kubelka-Munk function and the plot shown as inset in **Figure 6.18**. Light absorption of TiO_2-P25 is limited to the wavelength region below 400 nm leading to an estimated band gap energy of 3.15 eV, while the spectrum of the Fe_3O_4@TiO_2-P25 composite also displays a strong absorption band in the visible region due to the presence of Fe_3O_4. Therefore, Fe_3O_4@TiO_2-P25 combines the wide band gap TiO_2-P25 with Fe_3O_4, resulting in a hybrid material with two-stage band-gap energies of 3.07 eV and 1.85 eV, able to absorb light in the UV-vis wavelength range of 200-800 nm. Therefore, the coupling of Fe_3O_4 and TiO_2 phases might result beneficial in solar photocatalytic removal of water pollutants due to the stronger light absorption properties of the Fe_3O_4@TiO_2-P25 photocatalyst compared to their single components. Equations (6.3) and (6.4) were used to estimate the conduction band energy (E_{CB}) and the valence band energy (E_{VB}) of Fe_3O_4@TiO_2-P25:

$$E_{CB} = \chi - E^C - 0.5E_g \tag{6.3}$$

$$E_{VB} = E_{VB} + E_g \tag{6.4}$$

where χ stands for the absolute electronegativity (5.81 eV for TiO_2 and 5.77 eV for Fe_3O_4), E^C=4.5 eV is a factor to convert energy from the absolute vacuum scale to the normal hydrogen electrode scale (NHE) and E_g is the band gap energy. Following this calculation, **Figure 6.19** depicts a scheme of the energy band set-up of the Fe_3O_4@TiO_2-P25 composite, which corresponds to that of a type-I heterojunction photocatalyst [47]. As a consequence, photogenerated carriers would transfer across the heterojunction interface and accumulate on the Fe_3O_4 semiconductor, which might act as an electron-hole recombination center. However, different authors have observed an enhanced photocatalytic activity of type-I TiO_2/Fe_3O_4 heterostructures under UV-vis radiation due to the favorable effect of the carrier transfer mechanism (i.e., enhanced charge separation

efficiency) provided that an appropriate percentage of Fe_3O_4 in the composite is used [32,48-51].

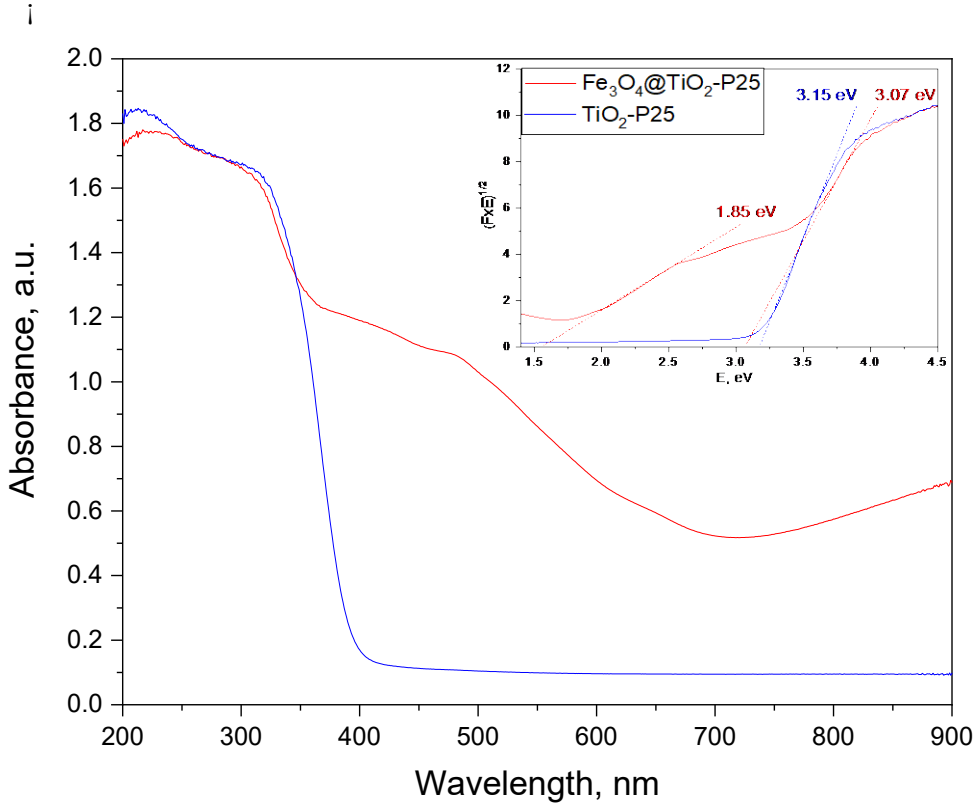

Figure 6.18. UV-vis DRS spectra obtained for Fe_3O_4@TiO_2-P25 ($(TiFe)_k$ as designated in **Table 6.2**) and TiO_2-P25 and their corresponding plots based on the Kubelka-Munk function (inset Figure).

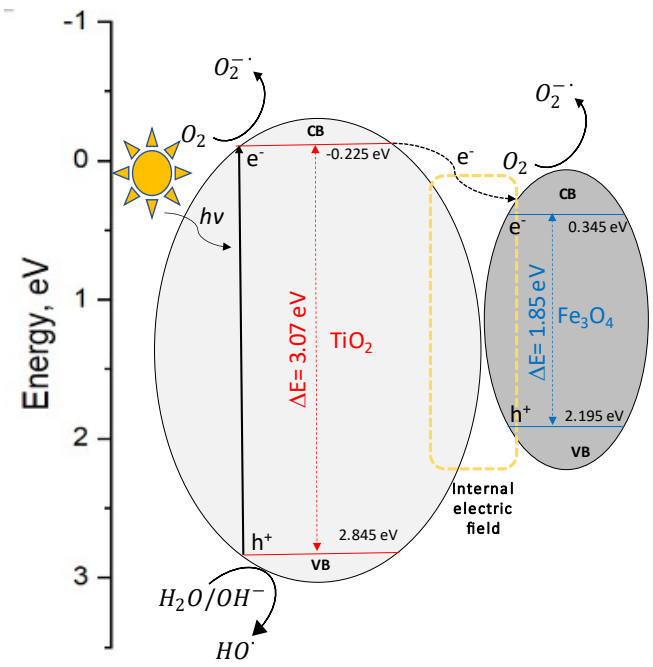

Figure 6.19. Schematic energy diagram of the hybrid Fe_3O_4@TiO_2-P25 material Proposed mechanism of migration of charge carriers under solar irradiation and generation of ROS.

6.3.4 Stability of the Fe_3O_4@TiO_2-P25 photocatalyst in aqueous media

The stability of the Fe_3O_4@TiO_2-P25 heterostructure was first examined in the dark in phosphate buffered UP water in the pH range of 4-10. No leaching of Fe and Ti species into the solution was found at any pH after 7 days, which confirms the stability of the catalyst in aqueous media in the absence of radiation. Besides, negligible TOC was observed in solution, corroborating the efficient separation of residual terephthalate in the washing steps (see **Figure 6.1**). Even so, concerns about Fe_3O_4@TiO_2 photocatalysts designed for UV-vis water treatment processes are related to: (i) the iron photodissolution induced by

electronic migration from the TiO_2 to the Fe_3O_4 phase and subsequent reduction of Fe^{3+} to Fe^{2+}, which is transferred to the solution [19,52] and (ii) the surface oxidation of Fe_3O_4 to γ-Fe_2O_3 at the reaction conditions [15]. To examine these issues, a series of stability test was carried out in non-buffered UP water under simulated solar radiation in the presence of different oxidants (O_2, H_2O_2 and O_3). Again, the release of Fe ions into solution observed after the 15-hour tests was found negligible at < 0.05 mg L^{-1}. As the injection of electrons from TiO_2 into Fe_3O_4 is favored by the relative positions of their conduction bands in the energy diagram of the Fe_3O_4@TiO_2-P25 composite (**Figure 6.19**), the absence of dissolved iron after irradiation suggests that either electrons in the conduction band of Fe_3O_4 are quickly captured by oxidants to produce ROS or the Fe_3O_4 phase acts as an electron-hole recombination center. Some minor loss of saturation magnetization (< 10%) was observed in the Fe_3O_4@TiO_2-P25 photocatalyst after prolonged irradiation (**Figure 6.20**), likely due to partial oxidation of surface Fe_3O_4 to γ-Fe_2O_3 under the strong oxidizing environment of photogenerated ROS.

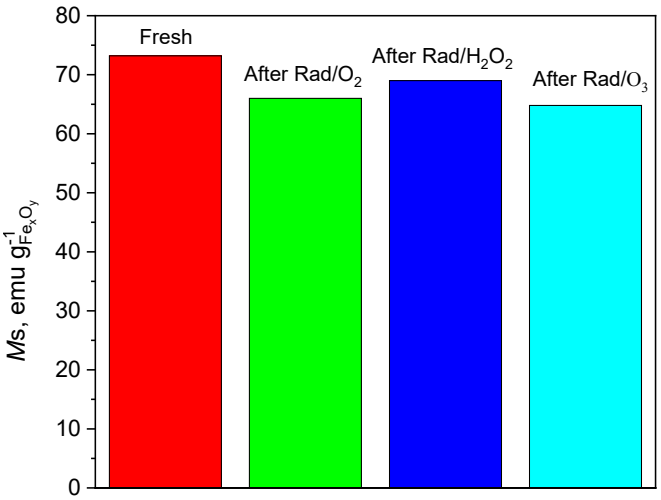

Figure 6.20. Saturation magnetization of fresh Fe_3O_4@TiO_2-P25 and after its exposure to simulated sunlight and oxidants.

6.3.5 Photocatalytic performance of the Fe_3O_4/TiO_2-P25 hybrid structures

The photocatalytic performance of the Fe_3O_4@TiO_2-P25 composite was evaluated by monitoring the degradation of MTP under simulated solar radiation in the presence of O_2 and an O_2/O_3 mixture as electron acceptors. For the sake of comparison, experiments with bare Fe_3O_4, bare TiO_2-P25 and other two Fe_3O_4/TiO_2 hybrid structures (i.e., CS-Fe_3O_4/TiO_2 and AC/Fe_3O_4/TiO_2) were also carried out. **Table 6.3** shows the composition, surface area and saturation magnetization of these materials compared to those of the Fe_3O_4@TiO_2-P25 composite.

Table 6.3. Composition, surface area and saturation magnetization of hybrid Fe_3O_4/TiO_2 samples.

Sample	% Fe_3O_4	% TiO_2	S_{BET} (m^2g^{-1})	M_S (emu g^{-1})
Fe_3O_4@TiO_2-P25	14.9	84.8	67	12.2
CS-Fe_3O_4/TiO_2	57.1	42.9	27	44.3
AC/Fe_3O_4/TiO_2	12.7	66.4	263	4.4

Figure 6.21 presents plots of the evolution of the MTP concentration and TOC with time in photocatalytic runs using O_2 and O_3/O_2. As it is apparent from these Figures, MTP was not adsorbed significantly on any of the solids used as photocatalyst. Thus, only the AC/Fe_3O_4/TiO_2 material could remove about 5% MTP during the thirty-minute dark stage due to its activated carbon content. The degradation of MTP by direct photolysis under simulated sunlight was also negligible as expected from its UV-vis absorption spectrum [53]. Contrary, MTP concentration declined rapidly upon ozonation and complete conversion of MTP was achieved in less than 2 h of treatment in the absence of any catalyst. Such removal rate is explained by two contributing reactions pathways: direct reaction

of MTP with molecular ozone given the relatively high ozone-MTP rate constant ($k_{O3\text{-}MTP}$ = 2.9×10^2 M^{-1} s^{-1} at pH = 6) [54] and the reactions of the ROS generated from the decomposition of ozone in aqueous media. In this sense, it is important to recall that, in addition to the decomposition reaction initiated by hydroxide ion, aqueous ozone also undergoes photolysis at UVA-vis wavelengths (λ> 300 nm) to eventually yield HO$^{\bullet}$ [55]. Hydroxyl radical, in turns, reacts fast with MTP through three possible parallel pathways with an average reported rate constant around 8.0×10^9 $M^{-1}s^{-1}$ [56]. The various photocatalysts used in this investigation enhanced the degradation of MTP in both oxygen and ozone-driven experiments to different extents. **Table 6.4** summarizes their performance in terms of pseudo-first order rate constants (k_{MTP} and k_{TOC}) and ozone utilization factors (OUF). OUF_{MTP} was measured as moles of ozone consumed for the disappearance of 80% MTP whereas OUF_{TOC} was evaluated at 50% TOC removal. According to the stoichiometry of the reaction of metoprolol tartrate with O_3 to yield NO_3^-, CO_2 and H_2O (i.e., mineralization) a theoretical OUF_{TOC} value can be calculated to be 0.87 mol O_3/mol C. As seen in **Table 6.4**, OUF_{TOC} in the non-catalytic ozonation was close to this Figure. However, in some catalyzed runs, OUF_{TOC} deviated from the theoretical value due to (i) the enhancement the ozone utilization rate because of free-radical mechanisms leading to MTP mineralization (TiO_2-P25 and Fe_3O_4@TiO_2 catalysts) and/or (ii) ineffective ozone decomposition on the catalyst surface or in the water bulk (CS-Fe_3O_4/TiO_2 and AC/Fe_3O_4/TiO_2).

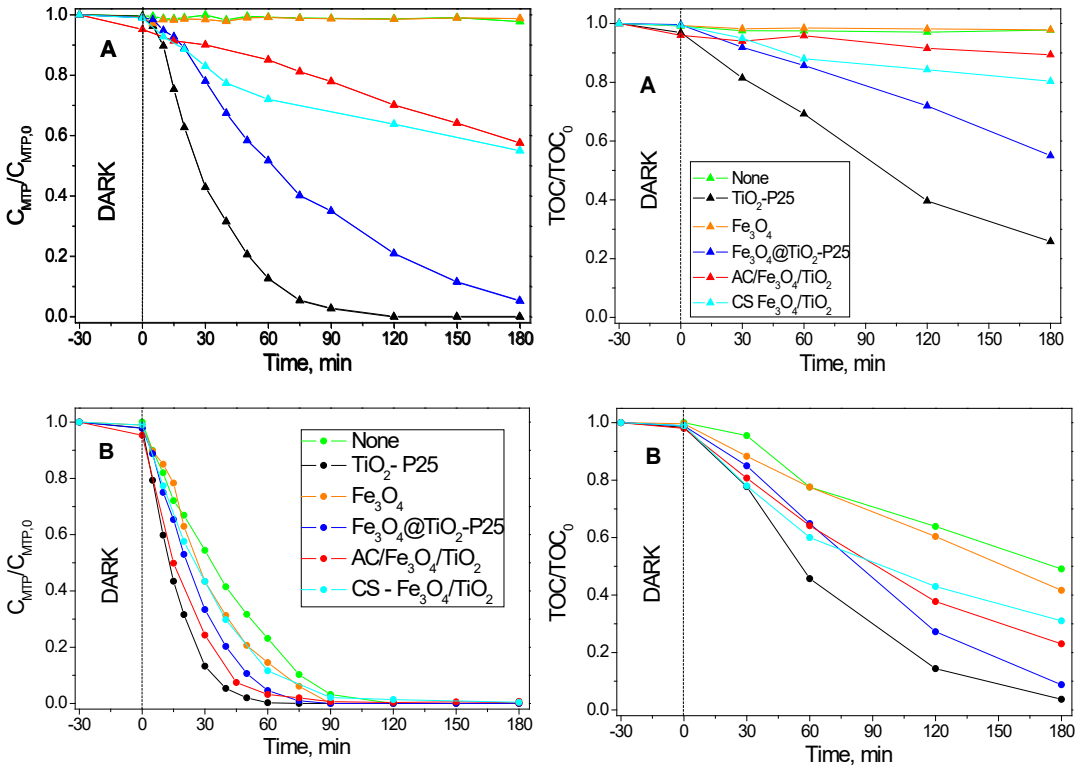

Figure 6.21. Degradation of aqueous MTP under simulated solar radiation in the presence of O_2 (A) and O_2/O_3 (B). Effect of different photocatalysts. Reaction conditions: $CMTP_{,0}$=50 mg L^{-1}; T=40ºC; pH_0=6 (non-buffered); Gas flow rate = 10 L h^{-1}; Ozone concentration (inlet gas) = 6 mg L^{-1} (if used); Overall irradiance ~580 W m^{-2}. Catalyst dose as indicated in **Table 6.4** of the main text.

As derived from **Figure 6.21** and k_{MTP} and k_{TOC} values in **Table 6.4**, the photocatalytic effect of bare Fe_3O_4 was weak while TiO_2-P25 showed higher photocatalytic degradation rate of MTP than any of the hybrid composite materials tested. In agreement with previous research, the poor photoactivity of bare Fe_3O_4 under sunlight can be attributed to a low quantum yield due to fast electron-hole recombination [52,57]. Even though magnetite is recognized as a heterogeneous catalyst in ozonation reactions in water giving rise to ROS [58,59],

the presence of Fe_3O_4 barely improved MTP degradation in our solar photo-ozonation experiments. Moreover, OUF_{MTP} and OUF_{TOC} decreased to a little extent in the Fe_3O_4 catalyzed experiment with respect to the ozone alone run. Therefore, the magnetite prepared in this work can be considered as an inefficient photocatalyst for the degradation of MTP under simulated sunlight. Contrary, the benchmark photocatalyst TiO_2-P25 exhibited the greatest degradation rate of MTP amongst the catalysts tested, with complete removal of the target compound in about 2 h (oxygen as electron acceptor) or 1 h (ozone as electron acceptor). TOC elimination was also remarkable in the TiO_2-P25 catalyzed experiments, reaching almost full MTP mineralization (>95% TOC removal) after 3 h when ozone was used as electron acceptor. In addition to fast degradation of MTP, TiO_2-P25 significantly improved the ozone utilization efficiency with low values of OUF_{MTP} and OUF_{TOC}.

Table 6.4. Photocatalytic performance of different photocatalyst: apparent rate constants for MTP degradation and efficiency on the use of oxidants.

Catalyst sample (dose)	Oxidant/dose	$k_{MTP} \times 10^3$ (min^{-1})	$k_{TOC} \times 10^3$ (min^{-1})	Ozone utilization factor	
				OUF_{MTP}[(1)] (mol O_3/ mol MTP)	OUF_{TOC}[(2)] (mol O_3/ mol C)
None	Oxygen	< 0.5	< 0.1	-	-
	O_3 / 60 mg h^{-1}	22.9±0.5	3.9±0.2	3.42	0.94
Fe_3O_4 (0.2 g L^{-1})	Oxygen	< 0.5	< 0.1	-	-
	O_3 / 60 mg h^{-1}	29.8±1.3	4.6±0.2	3.25	0.91
TiO_2-P25 (0.2 g L^{-1})	Oxygen	27.0±1.5	7.2±0.3	-	-
	O_3 / 60 mg h^{-1}	61.1±2.9	15.0±1.2	1.95	0.53
Fe_3O_4@TiO_2-P25 (0.2 g L^{-1})	Oxygen	12.4±0.5	3.0±0.2	-	-
	O_3 / 60 mg h^{-1}	39.6±2.0	12.1±1.0	2.63	0.47
CS-Fe_3O_4/TiO_2 (0.4 g L^{-1})	Oxygen	3.7±0.3	1.3±0.1	-	-
	O_3 / 60 mg h^{-1}	33.6±1.5	6.8±0.3	3.87	1.09
AC/Fe_3O_4/TiO_2 (0.3 g L^{-1})	Oxygen	2.6±0.1	0.7±0.1	-	-
	O_3 / 60 mg h^{-1}	41.1±1.6	7.9±0.2	3.46	1.15

[(1)] OUF_{MTP} evaluated at 80% MTP removal; [(2)] OUF_{TOC} evaluated at 50% TOC removal.

The photocatalytic activity of TiO_2-P25 was not improved with the Fe_3O_4@TiO_2-P25 heterostructure. Thus, k_{MTP} decreased by a factor of 2.2 (O_2 as oxidant) or 1.5 (O_3 as oxidant) when TiO_2-P25 was substituted by Fe_3O_4@TiO_2-P25 as photocatalyst. Similar decreasing factors were found for the rate constant of TOC decay (see **Table 6.4**). The deceleration of the MTP degradation process could be attributed to a combination of factors: i) first, the amount of TiO_2 phase in the experiments carried out with Fe_3O_4@TiO_2-P25 was somewhat lower than that with pure TiO_2-P25 because of about 15% Fe_3O_4 in the hybrid material (see **Table 6.3**); ii) second, the agglomeration of particles in Fe_3O_4@TiO_2-P25 might produce a shading effect, thus provoking a reduction of TiO_2 light absorption in the composite material [49]; iii) finally, the particle agglomeration might also make the active sites in the catalyst surface less accessible for both MTP and the electron acceptors adsorption, hence favoring electron-hole recombination.

Despite the loss of photocatalytic activity compared to TiO_2-P25, the Fe_3O_4@TiO_2-P25 composite showed markedly better photocatalytic behavior than the other Fe_3O_4/TiO_2 structures tested (CS-Fe_3O_4/TiO_2 and AC/Fe_3O_4/TiO_2). Generally speaking, Fe_3O_4@TiO_2-P25 led to faster MTP degradation, both in the presence of O_2 and O_2/O_3, than its analogous hybrid materials. It should be noted that similar amount of TiO_2 phase was used in the experiments carried out with different Fe_3O_4/TiO_2 heterostructures (see **Table 6.4** for catalyst dose). The core-shell Fe_3O_4/TiO_2 NPs suffered from iron photodissolution since iron concentration as high as 3.7 and 4.5 mg L^{-1} was found in solution after three-hour photocatalytic runs in the presence of O_2 and O_2/O_3, respectively. These amounts of iron released from the catalyst account for 2.2% (O_2) and 2.7% (O_2/O_3) of the iron in the Fe_3O_4 core. These are likely underestimated Figures as some of the Fe ions produced from the Fe_3O_4 phase could have precipitated or remained adsorbed on the surface of the NPs [52]. The high level of photodissolution had a detrimental impact on the photoactivity of the CS-Fe_3O_4/TiO_2 catalyst due to the inefficient utilization of (i) photogenerated

electrons of TiO_2 to reduce Fe(III) to Fe(II) in the Fe_3O_4 phase and (ii) primary oxidants (i.e., O_2 or O_3) and/or generated ROS participating in side reactions in the liquid bulk to oxidize dissolved Fe(II) to Fe(III) [19]. An intermediate layer of an insulator (e.g., SiO_2, amorphous carbon) between TiO_2 and Fe_3O_4 phases has been proposed in capped photocatalysts (e.g., core-shell NPs) to prevent iron photodissolution [19,52,60]. Fe_3O_4@TiO_2-P25 and AC/Fe_3O_4/TiO_2, being coupled photocatalysts where the magnetite is not fully surrounded by the TiO_2, did not undergo iron photodissolution under solar simulated illumination (negligible amounts of iron leached out of the catalysts). Despite this, the photocatalytic activity of the AC/Fe_3O_4/TiO_2 composite towards MTP degradation in the absence of ozone was even lower than that of CS-Fe_3O_4/TiO_2 NPs. Although the activated carbon component in AC/Fe_3O_4/TiO_2 provided high surface area favoring the adsorption of MTP and oxidants (much higher than those of Fe_3O_4@TiO_2-P25 and CS-Fe_3O_4/TiO_2 as shown in **Table 6.3**), its lower photocatalytic activity could be mainly attributed to a low photoactivity of the TiO_2 phase in this catalyst. In fact, pure anatase TiO_2 was prepared as in AC/Fe_3O_4/TiO_2 and tested as photocatalyst for the degradation of MTP under simulated solar illumination, resulting in $k_{MTP} = 2.2 \times 10^{-3}$ min^{-1} and $k_{TOC} = 3.4 \times 10^{-4}$ min^{-1}, which are well below the values corresponding to TiO_2-P25.

Form **Figure 6.21** it is seen that for all the Fe_3O_4/TiO_2 catalyst used, the experiments using ozone brought about a much faster MTP degradation than those carried out bubbling pure oxygen. As a result, k_{MTP} and k_{TOC} greatly increased upon ozonation (see **Table 6.4**). Moreover, the presence of any Fe_3O_4/TiO_2 catalyst improved the MTP degradation rate compared to the ozone alone experiment (i.e., without catalyst). This is a logical consequence of the enhanced generation of ROS due to various catalytic routes: (i) ozone traps photogenerated electrons on the catalyst surface to generate $O_3^{\bullet-}$, which is eventually transformed into $HO^{\bullet}$ [61]; (ii) ozone decomposes on the catalyst surface. In this sense, TiO_2, Fe_3O_4 and activated carbon are reported to provide

active sites for aqueous ozone decomposition into H_2O_2 and other ROS [62]; (iii) aqueous ozone is transformed into $HO^{\bullet}$ through the classical water bulk chain reaction mechanism initiated by OH^- and the generated H_2O_2 [63]. Generally, the increased generation of ROS improves the utilization rate of ozone to some extent [62]. This improvement is clearly seen in **Table 6.4** for TiO_2-P25 and Fe_3O_4@TiO_2-P25, OUF_{MTP} and OUF_{TOC} decreasing markedly with respect to the uncatalyzed experiment. However, the ozone utilization was not enhanced by the presence of CS-Fe_3O_4/TiO_2 and AC/Fe_3O_4/TiO_2 catalysts because of undesirable side ozone reactions such as oxidation of aqueous Fe(II) leached out of CS-Fe_3O_4/TiO_2 NPs and attack to the activated carbon structure of the AC/Fe_3O_4/TiO_2 composite.

6.3.6 Reusability of the Fe_3O_4@TiO_2-P25 photocatalyst

Reusability of the catalyst is a critical issue affecting technical, economic and environmental aspects of industrial applications of heterogeneous photocatalysts. **Figure 6.22** shows the evolution of MTP concentration and TOC during the course of six consecutive solar photocatalytic ozonation runs reusing the Fe_3O_4@TiO_2-P25 sample. No apparent loss of activity was appreciated with the repeated use of the photocatalyst. Thus, MTP invariably disappeared in less than 1 h and TOC removal in 3 h was always above 85%. No important structural changes other than some surface oxidation of the Fe_3O_4 phase were observed in the Fe_3O_4@TiO_2-P25 composite after being reused. As result, the saturation magnetization decreased from 12.8 to 9.6 emu g^{-1}, without appreciable impact on the magnetic separation of the catalyst.

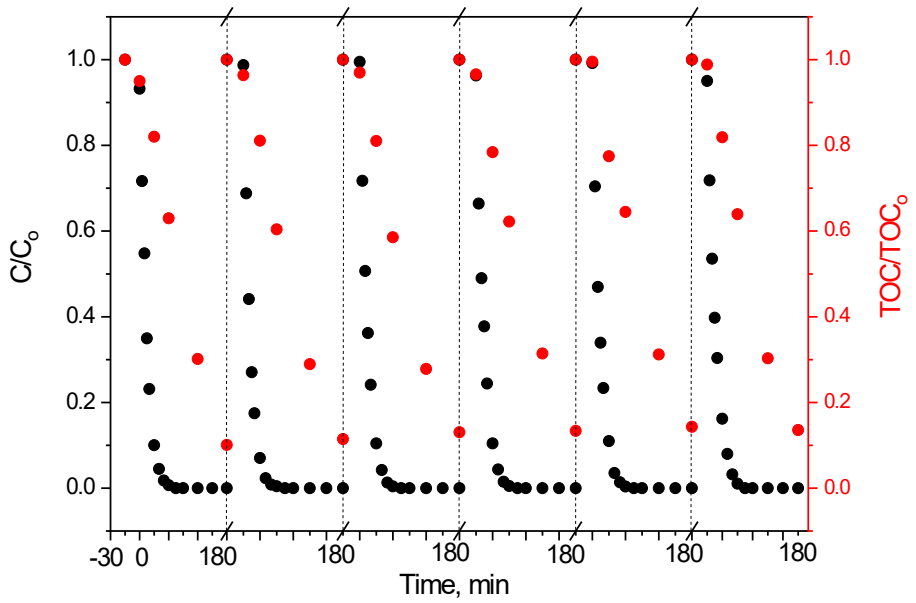

Figure 6.22. Degradation of aqueous MTP in six consecutive solar photocatalytic ozonation runs reusing the Fe_3O_4@TiO_2-P25 catalyst sample. Reaction conditions: Catalyst dose = 0.2 g L^{-1}; $CMTP_{,0}$= 50 mg L-1; T=40ºC; pH_0=6 (non-buffered); Gas flow rate = 10 L h^{-1}; Ozone concentration (inlet gas) = 6 mg L^{-1}; Overall irradiance ~580 W m^{-2}.

6.4 CONCLUSIONS

A new magnetic Fe_3O_4/TiO_2 composite aimed at being used as a UV-vis photocatalyst in solar AOPs has been successfully synthesized by in situ formation of Fe_3O_4 nanoparticles in the presence of commercial TiO_2-P25 NPs. H_2BDC mediated the synthesis towards the formation of the heterojunction structure. The method is attractive as mild conditions are applied, thus avoiding the use of toxic reagents and high-temperature treatment required in conventional sol-gel methods usually followed to obtain photoactive Fe_3O_4/TiO_2 composites. While the TiO_2 phase in Fe_3O_4@TiO_2-P25 was responsible for the photocatalytic

activity under UV-vis illumination, the Fe_3O_4 phase conferred the catalyst with superparamagnetic behavior at room temperature. The Fe_3O_4@TiO_2-P25 was proven fairly stable under solar illumination and presence of strong oxidants such as hydrogen peroxide and ozone, though some surface oxidation of Fe_3O_4 to γ-Fe_2O_3 at the reaction conditions led to a decrease in the saturation magnetization. Photocatalytic activity studies using MTP as target pollutant revealed that Fe_3O_4@TiO_2-P25 shows better photocatalytic performance than an AC/Fe_3O_4/TiO_2 composite and core-shell Fe_3O_4/TiO_2 NPs. Finally, the reusability of the Fe_3O_4@TiO_2-P25 was demonstrated through six photocatalytic ozonation cycles reusing the catalyst sample. Therefore, the synthesized Fe_3O_4/TiO_2 structure can be regarded as a promising sustainable, effective and recyclable photocatalyst for AOPs.

References

[1] X. Tong, S. Mohapatra, J. Zhang, N.H. Tran, L. You, Y. He, K.Y.-H. Gin, Source, fate, transport and modelling of selected emerging contaminants in the aquatic environment: Current status and future perspectives, Water Res., 217 (**2022**) 118418.

[2] M.F.T. Sá, V. Castro, A.I. Gomes, D.F.S. Morais, R.V.P.S. Silva Braga, I. Saraiva, B.M. Souza-Chaves, M. Park, V. Fernández-Fernández, R. Rodil, R. Montes, J.B. Quintana, V.J.P. Vilar, Tracking pollutants in a municipal sewage network impairing the operation of a wastewater treatment plant, Sci. Total Environ., 817 (**2022**) 152518.

[3] M. Pazda, J. Kumirska, P. Stepnowski, E. Mulkiewicz, Antibiotic resistance genes identified in wastewater treatment plant systems - A review, Sci. Total Environ., 697 (**2019**) 134023.

[4] A. Tufail, W.E. Price, M. Mohseni, B.K. Pramanik, F.I. Hai, A critical review of advanced oxidation processes for emerging trace organic contaminant degradation: Mechanisms, factors, degradation products, and effluent toxicity, J. Water Process Eng., 40 (**2021**) 101778.

[5] A. El Golli, M. Fendrich, N. Bazzanella, C. Dridi, A. Miotello, M. Orlandi, Wastewater remediation with ZnO photocatalysts: Green synthesis and solar concentration as an economically and environmentally viable route to application, J. Environ. Manage., 286 (**2021**) 112226.

[6] E.K. Radwan, H.H. Abdel Ghafar, M. Ibrahim, A.S. Moursy, C.K. Emad Radwan, Recent trends in treatment technologies of emerging contaminants, Environ. Qual. Manag., (**2022**) 1-19.

[7] B. Panda, A survey on the present status of sustainable technologies for water pollutant abatement, Desalin. Water Treat., 57 (**2016**) 28705-28714.

[8] S.N. Ahmed, W. Haider, Heterogeneous photocatalysis and its potential applications in water and wastewater treatment: a review, Nanotechnology, 29 (**2018**) 342001.

[9] J.M. Coronado, M.D. Hernández-Alonso, The Keys of Success: TiO_2 as a benchmark photocatalyst, Green Energy Technol., 71 (**2013**) 85-101.

[10] J. Carbajo, M. Jiménez, S. Miralles, S. Malato, M. Faraldos, A. Bahamonde, Study of application of titania catalysts on solar photocatalysis: Influence of type of pollutants and water matrices, Chem. Eng. J., 291 (**2016**) 64-73.

[11] J. Kelly, C. McDonnell, N. Skillen, P. Manesiotis, P.K.J. Robertson, Enhanced photocatalytic degradation of 2-methyl-4-chlorophenoxyacetic acid (MCPA) by the addition of H_2O_2, Chemosphere, 275 (**2021**) 130082.

[12] D. Bertagna Silva, A. Cruz-Alcalde, C. Sans, J. Giménez, S. Esplugas, Performance and kinetic modelling of photolytic and photocatalytic ozonation for enhanced micropollutants removal in municipal wastewaters, Appl. Catal. B Environ., 249 (**2019**) 211-217.

[13] L.K. Limbach, R. Bereiter, E. Müller, R. Krebs, R. Gälli, W.J. Stark, Removal of oxide nanoparticles in a model wastewater treatment plant: Influence of agglomeration and surfactants on clearing efficiency, Environ. Sci. Technol., 42 (**2008**) 5828-5833.

[14] A.Y. Shan, T.I.M. Ghazi, S.A. Rashid, Immobilisation of titanium dioxide onto supporting materials in heterogeneous photocatalysis: A review. Appl. Catal. A: Gen., 389 (**2010**) 1–8.

[15] R. Krakowiak, R. Frankowski, K. Mylkie, D.T. Mlynarczyk, M. Ziegler-Borowska, A. Zgoła-Grześkowiak, T. Goslinski, TiO_2–Fe_3O_4 composite systems. Preparation, physicochemical characterization, and an attempt to explain the limitations that arise in catalytic applications. Appl. Sci., 12 (**2022**), 8826.

[16] S. Sultana, A. Amirbahman, C.P. Tripp, A method to produce robust magnetic particles coated with TiO_2 nanoparticulates, Appl. Catal. B Environ., 273 (**2020**) 118935.

[17] J. López, A. Rey, P.M. Álvarez, A.M. Chávez, E. Viñuelas, ES Patent Publication N° ES2884450B2, Método para la magnetización de sólidos inorgánicos, (**2022**).

[18] J. López, A. Rey, J.F. García-Araya, P.M. Álvarez, Green synthesis of magnetite-based catalysts for solar-assisted catalytic wet peroxide oxidation, Catalysts, 12 (**2022**), 271.

[19] P.M. Álvarez, J. Jaramillo, F. López-Piñero, P.K. Plucinski, Preparation and characterization of magnetic TiO_2 nanoparticles and their utilization for the degradation of emerging pollutants in water, Appl. Catal. B Environ., 100 (**2010**) 338-345.

[20] D.H. Quiñones, A. Rey, P.M. Álvarez, F.J. Beltrán, P.K. Plucinski, Enhanced activity and reusability of TiO_2 loaded magnetic activated carbon for solar photocatalytic ozonation. Appl. Catal. B Environ., 144 (**2014**) 96–106.

[21] G.M. Eisenberg, Colorimetric determination of hydrogen peroxide, Ind. Eng. Chem. - Anal. Ed., 15 (**1943**) 327-328.

[22] H. Bader, J. Hoigné, Determination of ozone in water by the indigo method, Water Res. 15 (**1981**) 449-456.

[23] D.M. Tobaldi, R.C. Pullar, M.P. Seabra, J.A. Labrincha, Fully quantitative X-ray characterisation of Evonik Aeroxide TiO_2P25®, Mater. Lett., 122 (**2014**) 345-347.

[24] J.C. Aphesteguy, G. V. Kurlyandskaya, J.P. De Celis, A.P. Safronov, N.N. Schegoleva, Magnetite nanoparticles prepared by co-precipitation method in different conditions, Mater. Chem. Phys. 161 (**2015**) 243-249.

[25] R.E. Kalan, S. Yaparatne, A. Amirbahman, C.P. Tripp, P25 titanium dioxide coated magnetic particles: Preparation, characterization and photocatalytic activity, Appl. Catal. B Environ., 187 (**2016**) 249-258.

[26] F.G. Sherif, Heavy Metal Terephthalates, Ind. Eng. Chem. Prod. Res. Dev., 9 (**1970**) 408-412.

[27] H.H. Lee, Y. Park, S.H. Kim, S.-H. Yeon, S.K. Kwak, K.T. Lee, S.Y. Hong, Mechanistic studies of transition metal-terephthalate coordination complexes upon electrochemical jithiation and delithiation, Adv. Funct. Mater., 25 (**2015**) 4859-4866.

[28] X. Ou, S. Lei, X. Zhang, K. Wan, Y. Wang, W. Zhou, Y. Xiao, B. Cheng, Hydrothermal growth of ferrous hydroxide terephthalate as a new positive electrode material for supercapacitors, Dalt. Trans., 47 (**2018**) 12056-12060.

[29] A.M. Johnson, S. Trakhtenberg, A.S. Cannon, J.C. Warner, Effect of pH on the viscosity of titanium dioxide aqueous dispersions with carboxylic acids, J. Phys. Chem. A., 111 (**2007**) 8139-8146.

[30] X. Chen, X. Peng, L. Jiang, X. Yuan, J. Zhang, H. Yu, Terephthalate acid decorated TiO_2 for visible light driven photocatalysis mediated via ligand-to-metal charge transfer (LMCT), Colloids Surf. A: Physicochem. Eng. Asp., 603 (**2020**) 125188.

[31] S. Khashan, S. Dagher, N. Tit, A. Alazzam, I. Obaidat, Novel method for synthesis of Fe_3O_4@TiO_2 core/shell nanoparticles, Surf. Coatings Technol., 322 (**2017**) 92-98.

[32] M. Xiao, R. Li, J. Yin, J. Yang, X. Hu, H. Xiao, W. Wang, T. Yang, Enhanced photocatalytic oxidation of As(III) by TiO_2 modified with Fe_3O_4 through Ti-O-Fe interface bonds, Colloids Surf. A: Physicochem. Eng. Asp., 651 (**2022**) 129678.

[33] A.E. Regazzoni, P. Mandelbaum, M. Matsuyoshi, S. Schiller, S.A. Bilmes, M.A. Blesa, Adsorption and photooxidation of salicylic acid on titanium dioxide: A surface complexation description, Langmuir, 14 (**1998**) 868-874.

[34] M. Kiyama, Conditions for the formation of Fe_3O_4 by the air oxidation of $Fe(OH)_2$ suspensions, Bull. Chem. Soc. Jpn., 47 (**1974**) 1646–1650.

[35] S. Hamada, K. Kuma, Preparation of γ-FeOOH by aerial oxidation of iron(II) chloride solution, Bull. Chem. Soc. Jpn., 49 (**1976**), 3695–3696.

[36] Y. Tamaura, G.S. Chyo, T. Katsura, The Fe_3O_4 formation by the "Ferrite Process": oxidation of the reactive $Fe(OH)_2$ suspension induced by sucrose, Water Res., 13 (**1979**) 21–31.

[37] Y. Tamaura, P. V. Buduan, T. Katsura, Studies on the oxidation of iron(II) ion during the formation of Fe3O4 and α-FeO(OH) by air oxidation of $Fe[OH]_2$ suspensions, J. Chem. Soc. Dalt. Trans., (**1981**) 1807-1811.

[38] J. Wang, T. Deng, Y. Dai, Study on the processes and mechanism of the formation of Fe_3O_4 at low temperature, J. Alloys Compd., 390 (**2005**) 127-132.

[39] S. Laurent, D. Forge, M. Port, A. Roch, C. Robic, L. Vander Elst, R.N. Muller, Magnetic iron oxide nanoparticles: Synthesis, stabilization, vectorization, physicochemical characterizations and biological applications, Chem. Rev., 108 (**2008**) 2064–2110.

[40] C. Domingo, R. Rodríguez-Clemente, M.A. Blesa, Kinetics of oxidative precipitation of iron oxide particles, Colloids Surf. A: Physicochem. Eng. Asp., 79 (**1993**) 177–189.

[41] F. Vereda, J. De Vicente, R.Hidalgo-Álvarez, Influence of a magnetic field on the formation of magnetite particles via two precipitation methods, Langmuir, 23 (**2007**) 3581–3589.

[42] T. Asimakidou, A. Makridis, S. Veintemillas-Verdaguer, M.P. Morales, I. Kellartzis, M. Mitrakas, G. Vourlias, M. Angelakeris, K. Simeonidis, Continuous production of magnetic iron oxide nanocrystals by oxidative precipitation, Chem. Eng. J., 393 (**2020**) 124593.

[43] T. Granath, P. Löbmann, K. Mandel, Oxidative precipitation as a versatile method to obtain ferromagnetic Fe_3O_4 nano- and mesocrystals adjustable in morphology and magnetic properties, Part. Part. Syst. Charact., 38 (**2021**) 2000307.

[44] B. Erdem, R.A. Hunsicker, G.W. Simmons, E.D. Sudol, V.L. Dimonie, M.S. El-Aasser, XPS and FTIR surface characterization of TiO_2 particles used in polymer encapsulation. Langmuir, 17 (**2001**) 2664–2669.

[45] T. Yamashita, P. Hayes, Analysis of XPS spectra of Fe^{2+} and Fe^{3+} ions in oxide materials, Appl. Surf. Sci., 254 (**2008**) 2441-2449.

[46] K.S.W. Sing, D.H. Everett, R.A.W. Haul, L. Moscou, R.A. Pierotti, J. Rouquerol, T. Siemieniewska, Reporting physisorption data for gas/solid systems with special reference to the determination of surface area and porosity, Pur. and Appl. Chem., 57 (**1985**) 603-619.

[47] L. Xie, T. Du, J. Wang, Y. Ma, Y. Ni, Z. Liu, L. Zhang, C. Yang, J. Wang, Recent advances on heterojunction-based photocatalysts for the degradation of persistent organic pollutants, Chem. Eng. J., 426 (**2021**) 130617.

[48] L. Gnanasekaran, R. Hemamalini, S. Rajendran, J. Qin, M.L. Yola, N. Atar, F. Gracia, Nanosized Fe_3O_4 incorporated on a TiO_2 surface for the enhanced photocatalytic degradation of organic pollutants, J. Mol. Liq., 287 (**2019**) 110967.

[49] D. Beketova, M. Motola, H. Sopha, J. Michalicka, V. Cicmancova, F. Dvorak, L. Hromadko, B. Frumarova, M. Stoica, J.M. Macak, One-step decoration of TiO_2 nanotubes with Fe_3O_4 nanoparticles: Synthesis and photocatalytic and magnetic properties. ACS Appl. Nano Mater., 3 (**2020**) 1553–1563.

[50] N. Madima, K.K. Kefeni, S.B. Mishra, A.K. Mishra, A. T. Kuvarega, Fabrication of magnetic recoverable Fe_3O_4/TiO_2 heterostructure for photocatalytic degradation of Rhodamine B dye. Inorg. Chem. Commun., 145 (**2022**) 109966.

[51] A. Aguinaco, J.M. Mánuel, E. Blanco, M Domínguez, R. Litrán, J.J. Delgado, M. Ramírez-del-Solar, Fe_3O_4-TiO_2 thin films in solar photocatalytic processes, Mater., 15 (**2022**) 6718.

[52] D. Beydoun, R. Amal, G.K.C. Low, S. McEvoy, Novel photocatalyst: Titania-coated magnetite. Activity and photodissolution, J. Phys. Chem. B, 104 (**2000**) 4387–4396.

[53] V. Romero, O. González, B. Bayarri, P. Marco, J. Giménez, S. Esplugas, Performance of different advanced oxidation technologies for the abatement of the beta-blocker metoprolol, Catal. Today, 240 (**2015**) 86–92.

[54] F.J. Benitez, J.L. Acero, F.J. Real, G. Roldán, G. Ozonation of pharmaceutical compounds: Rate constants and elimination in various water matrices, Chemosphere, 77 (**2009**) 53–59.

[55] A.M. Chávez, A. Rey, F.J. Beltrán, P.M. Álvarez, Solar photo-ozonation: A novel treatment method for the degradation of water pollutants, J. Hazard. Mater., 317 (**2016**) 36–43.

[56] K. Kovácsa, T. Tóth, L. Wojnárovits, Evaluation of advanced oxidation processes for β-blockers degradation: a review, Water Sci. Technol., 85 (**2022**) 685-705.

[57] Z.J. Li, Z. W. Huang, W.L. Guo, L. Wang, L.R. Zheng, Z.F. Chai, W.Q. Shi, Enhanced photocatalytic removal of uranium(VI) from aqueous solution by magnetic TiO_2/Fe_3O_4 and its graphene composite, Environ. Sci. Technol., 51 (**2017**) 5666–5674.

[58] J. Wang, Z. Bai, Fe-based catalysts for heterogeneous catalytic ozonation of emerging contaminants in water and wastewater, Chem. Eng. J., 15 (**2017**) 79–98.

[59] L. Yan, J. Bing, H. Wu,. The behavior of ozone on different iron oxides surface sites in water, Sci. Rep., 9 (**2019**) 14752.

[60] R.E. Kalan, S. Yaparatne, A. Amirbahman, C.P. Tripp, P25 titanium dioxide coated magnetic particles: Preparation, characterization and photocatalytic activity, Appl. Catal. B Environ., 187 (**2016**) 249–258.

[61] T.E. Agustina, H.M. Ang, V.K. Vareek, A review of synergistic effect of photocatalysis and ozonation on wastewater treatment, J. Photochem. Photobio. C: Photochem. Reviews., 6 (**2005**) 264–273.

[62] J. Wang, H. Chen, Catalytic ozonation for water and wastewater treatment: Recent advances and perspective, Sci. Total Environ. 704 (**2020**) 135249.

[63] J. Staehelin, J. Holgné, Decomposition of ozone in water: Rate of initiation by hydroxide ions and hydrogen peroxide, Environ. Sci. Technol. 16 (**1982**) 676–681.